Durham E-Theses

Synthesis, Structure and Properties of Metal Oxychalcogenides

TUXWORTH, ANDREW,JAMES

Abstract

"**Synthesis, Structure and Properties of Metal Oxychalcogenides**"

PhD Thesis   Andrew J. Tuxworth   December 2013

Chapter 1 gives a brief review of oxychalcogenide materials and their properties, with particular focus on structures similar to the systems discussed in the later chapters. These oxychalcogenides, are of interest due to their potentially interesting magnetic and electronic properties.

Chapter 2 discusses the synthetic methods and characterisation techniques used throughout this thesis. The theory behind both single crystal and powder diffraction techniques used in this work is described.

Chapter 3 describes the synthesis of a new ZrCuSiAs-related transition metal containing oxychalcogenide $La_2O_2ZnSe_2$. The structure of $La_2O_2ZnSe_2$ is reported, deduced from symmetry adapted distortion mode analysis of laboratory X-ray powder diffraction data, and confirmed by Rietveld analysis of combined X-ray and neutron powder diffraction data. The variable temperature structural properties of $La_2O_2ZnSe_2$ are also reported alongside diffuse reflectance measurements.

Chapter 4 discusses the variable temperature structural, electronic and magnetic properties of $A_4O_4TiSe_4$ (A = Sm, Gd, Tb, Dy, Ho, Er, & Y). The variable temperature structural properties of the compounds are also reported. Electronic measurements show these materials are semiconductors while SQUID magnetometry measurements suggest these materials order antiferromagnetically at low temperatures.

Chapter 5 reports the synthesis of an extended family of ternary oxychalcogenides with $A_4O_4Se_3$ composition. Three new structures for this composition have been solved using a combination of single crystal and powder X-ray diffraction. The new γ and δ-structures have been shown to contain a highly disordered layer of selenium anions. The variable temperature structural properties of the series are also reported.

Chapter 6 discusses the synthesis of single crystals of $La_2O_2Se_2Fe_2O$, $La_2O_2Se_2Mn_2O$ and $Pr_2O_2Se_2Mn_2O$. A comparison of the structural properties of the $A_2O_2Se_2Mn_2O$ materials is given, alongside determination of the incommensurately modulated cell of $La_2O_2Se_2Mn_2O$.

Chapter 7 reports synthesis a new 3D oxychalcogenide $LaInS_2O$. Its structure is solved from X-ray powder diffraction measurements.

Chapter 8 describes the method of temperature calibration used for variable temperature X-ray powder diffraction measurements used in this work.

Synthesis, Structure and Properties of Metal Oxychalcogenides

Andrew J. Tuxworth M.Chem (Dunelm)

Durham University

Supervisor: Prof. John S. O. Evans

A thesis submitted in partial fulfilment of the requirements

for the degree of Doctor of Philosophy

Department of Chemistry

Durham University

2013

Table of Contents

Abbreviations

ADP	Anisotropic thermal displacement parameter
AFM	Antiferromagnetic
BVS	Bond Valence Sum
CCR	Closed circuit refrigerator
CIF	Crystallographic information file
DFT	Density functional theory
EDX	Energy dispersive X-ray (analysis)
FC	Field cooled
GOF	Goodness of Fit
HRPD	High resolution powder diffractometer
ICSD	Inorganic crystal structure database
XRPD	X-ray powder diffraction
RT	Room temperature
SEM	Scanning electron microscopy
SHG	Second harmonic generation
TEM	Transmission electron microscopy
TOF	Time-of-flight
VT	Variable temperature
XRD	X-ray diffraction
ZFC	Zero-field cooled

Declaration & Statement of Copyright

The work described in this thesis is entirely my own, except where I have acknowledged help from, or collaboration with, a named person, or given reference to a published source or thesis. Aspects of research on the materials described in Chapter 3 were performed with Dr. Emma McCabe (Durham University), and led to a joint publication. Selected results are included in the text for clarity, and attribution is given at the relevant points.

The research presented was performed in the Department of Chemistry, Durham University, between October 2010 and December 2013, the result of which have not been submitted for a degree in this or any other university.

Acknowledgments

Chapter 1: Introduction and Literature Review

1.1 Introduction

Oxychalcogenides are mixed anion systems which contain both oxide ions and anions of another group 16 element, typically S, Se or Te. To date there are only three known naturally occurring oxychalcogenides: kermesite, sarabauite and cetineite,[1-3] presumably due to preferential formation of sulphates and selenates under natural conditions. There has been significant interest in the study of synthetic mixed anion compounds since the discovery of high temperature superconductivity in iron-arsenide systems in 2008.[4] Superconducting transition temperatures of up to 55 K have been reported for F^- doped $SmO_{1-x}F_xFeAs$ ($x = 0.1$).[5] Many oxychalcogenide materials with interesting electronic, magnetic and optical properties have been synthesised. These properties, along with the frequent structural similarity of oxychalcogenides and oxypnictide, make oxychalcogenides worthy of further study. These aspects will be reviewed in this chapter where the following nomenture will be used: "A" for trivalent rare earths (including Bi & Y); "Q" for chalcogen (S, Se, Te); "M" for transition metals (including In) and all other cations will be labelled "B".

This chapter is divided into two sections: oxychalcogenides with layered structures and those with extended three dimensional structures. Emphasis is placed on compounds with structures similar to those discussed in the later chapters of this thesis. A review of layered oxychalcogenides was written by Clarke *et al.* in 2008.[6]

1.2 Layered oxychalcogenides

1.2.1 Ternary materials, $A_xO_yQ_z$ and $B_xO_yQ_z$

Ternary oxychalcogenides are most common for rare-earth metals, although a small number of transition metal and actinoid containing phases have also been reported. The most widely studied series have the general formula A_2O_2Q and contain layers of distorted A_4O tetrahedra separated by a layer containing Q atoms (figure 1.1a). There is an extensive series of compositions with this structure: S^{2-} (A=La-Ce, Nd-Lu, Y, Bi); Se^{2-} (A=La, Pr, Nd, Sm, Gd, Ho, Er, Yb, Y, Bi); and Te^{2-} (A=La–Nd, Sm–Ho).[7-13] A_2O_2S and A_2O_2Se adopt a trigonal unit cell with P-$3m1$ space group and $a = b \sim 4$ Å, $c \sim 7$ Å. The A_4O tetrahedra share 3 edges to form infinite layers that alternate along the c axis with layers of Q^{2-} ions. The A^{3+} site is found in a 7 fold AQ_3O_4 environment, figure 1.1a.

A_2O_2Te adopts a tetragonal unit cell, $a = b \sim 4$ Å, $c \sim 13$ Å, and the structure consists of alternating layers of A_4O tetrahedra and layers of Q^{2-} along the c axis of the material. In contrast to the S and Se analogues the A_4O tetrahedra share 4 edges producing fluorite-like

layers of $[A_2O_2]^{2+}$. The A^{3+} site is found in a 8 fold AQ_4O_4 4+4 square antiprismatic coordination environment, figure 1.1b. Bi_2O_2Se also adopts the A_2O_2Te structure. Bi_2O_2S adopts a very closely related structure (*Pnnm* orthorhombic space group) a = 3.874(1) Å, b = 11.916(2) Å, c = 3.840(1) Å. The structure consists of distorted fluorite-like layers of $[Bi_2O_2]^{2+}$ alternating with layers of S^{2-} ions. The BiQ_4O_4 4+4 square antiprism environment of Bi is distorted due to the loss of 4 fold symmetry, figure 1.1c.

a) A_2O_2Q (Q = S & Se)
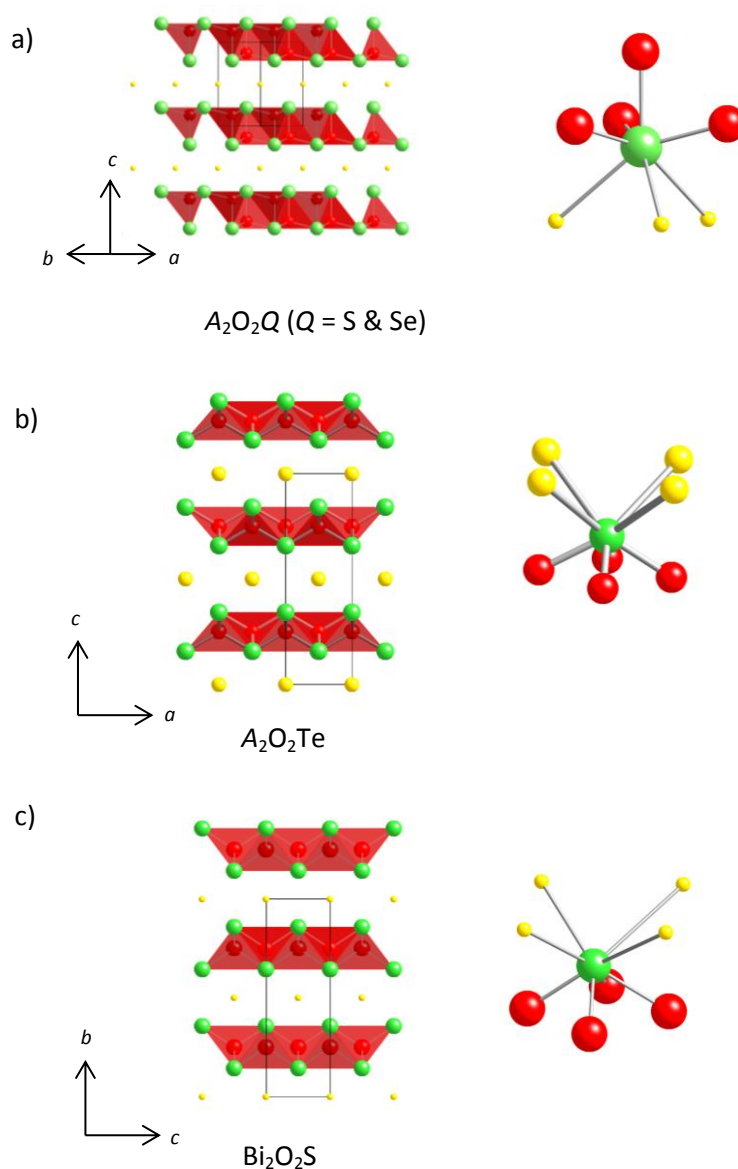
b) A_2O_2Te

c) Bi_2O_2S

Figure 1.1: *Crystal structures and A^{3+} coordination environment of a)* A_2O_2Q *(Q = S & Se), b)* A_2O_2Te, *c)* Bi_2O_2S. *A = green, O = red, Q = yellow.*

Other ternary rare-earth containing oxychalcogenides include $A_4O_4Se_3$ (La–Nd, Sm)[12, 14-16] systems which crystallises in space group *Amm*2 with unit cell dimensions $a \sim$ 8.5 Å, $b \sim$ 4 Å, $c \sim$ 13 Å. The structure contains infinite fluorite-type $[A_2O_2]^{2+}$ layers which alternate along the c axis with layers consisting of Se^{2-} and Se_2^{2-} anions, figure 1.2, this structure is described in

greater detail in Chapter 5. Figure 1.3 shows there is a smooth decrease in unit cell volume with decreasing A^{3+} ionic radii, with perhaps $Ce_4O_4Se_3$ falling slightly below the trend.
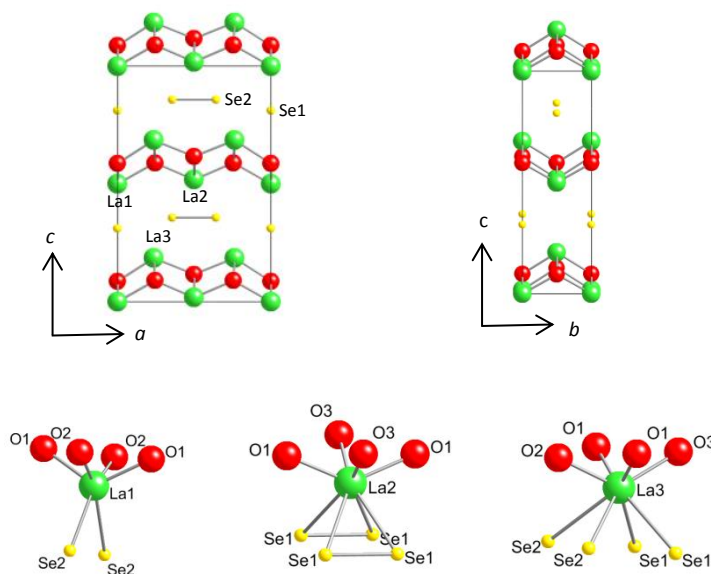
Figure 1.2: *Structure of $A_4O_4Se_3$ (A = La, Ce, Pr, Nd & Sm) and coordination environments of A^{3+} cations. A = green, O = red, Q = yellow.*

Figure 1.3: *The effect of rare-earth cation radii of the cell volume of $A_4O_4Se_3$ material, ionic radii are the values reported by Shannon.[17]*

Recently nano particles with $A_4O_4Se_3$ (A = Nd , Sm, Gd, Tb, Dy, Ho) composition have been reported, although the structures have not been reported for the A = Gd-Ho members of the series. Light extinction properties of $A_4O_4Se_3$ (A = Nd, Sm, Gd–Ho) nano particle dispersions in cyclohexane show absorption edges for $Nd_4O_4Se_3$ and $Sm_4O_4Se_3$ at ~1.95 eV and $A_4O_4Se_3$ (A = Sm, Gd–Ho) at ~1.75 eV.[18] Band gaps of ~1.9 eV for A = La, Pr, Nd, Sm and 1.7 eV for A = Ce have also been observed.[15] No evidence of magnetic ordering down to 1.8 K for $Ce_4O_4Se_3$ and

$Nd_4O_4Se_3$ has been observed, but negative values for θ_w suggest the presence of antiferromagnetic interactions.[15]

Two compositionally similar sulphides, $A_4O_4S_3$, have been reported: $Ce_4O_4S_3$ and $Bi_4O_4S_3$. $Ce_4O_4Se_3$ crystallises in the orthorhombic space group *Pbam* with a = 6.856 Å, b = 14.558 Å, c = 3.9848 Å. The structure consists of chains rather than layers of $[Ce_4O_4]^{6+}$ along [001] linked by shared S^{2-} ions, thus the structure contains a mixture of Ce^{3+} and Ce^{4+} as opposed to the A^{3+} of the Se phases. The compound is reported to be semiconducting.[19]

$Bi_4O_4S_3$ crystallises in the tetragonal space group *I4/mmm* with unit cell dimensions of a = b = 3.9592(1) Å and c = 41.241(1) Å. The structure of this material is, however, very different and thought to consist of fluorite-type $[Bi_2O_2]^{2+}$ layers stacking with rock salt type Bi_2S_4 and SO_4^{2-} layers. The chemical composition can thus be better described as $Bi_6O_4S_4(SO_4)_{1-x}$ with partial occupancy of the sulphate layer, and $Bi_4O_4S_3$ corresponds to x = 0.5.[20] There has been much interest in this materials due to the observation of superconductivity at T_c ~ 4.5 K.[20-27] No Te containing $A_4O_4Q_3$ phases have been reported.

Two other selenium containing $A_xO_yQ_z$ compositions are known: $A_{10}OSe_{14}$ (A = La-Nd),[16, 28, 29] and A_2OSe_2 (A = Pr & Gd)[16, 30]. $A_{10}OSe_{14}$ adopts a tetragonal space group *I4₁/acd* with a = b = 15.9204(9) Å, c = 21.0648(14) Å. The structure contains isolated A_4O tetrahedra separated by Se ions, figure 1.4a. Pr_2OSe_2 and Gd_2OSe_2 adopt different structures figure 1.4a & b. Pr_2OSe_2 has a monoclinic *P2₁/c* cell with a = 8.8205(6) Å, b = 7.3289(5) Å, c = 7.3294(5) Å and β = 100.288(7)°, it contains edge and corner sharing A_4O tetrahedra to produce chains along [010]. These chains are separated by rows of Se^{2-}. Gd_2OSe_2 adopts an orthorhombic cell with *Pnma* symmetry a = 16.0500(30) Å, b = 3.9375(8) Å, c = 7.0309(14) Å. The structure consists of La_4O tetrahedra which share 2 edges to form chains along [010] which are separated by Se^{2-} ions.
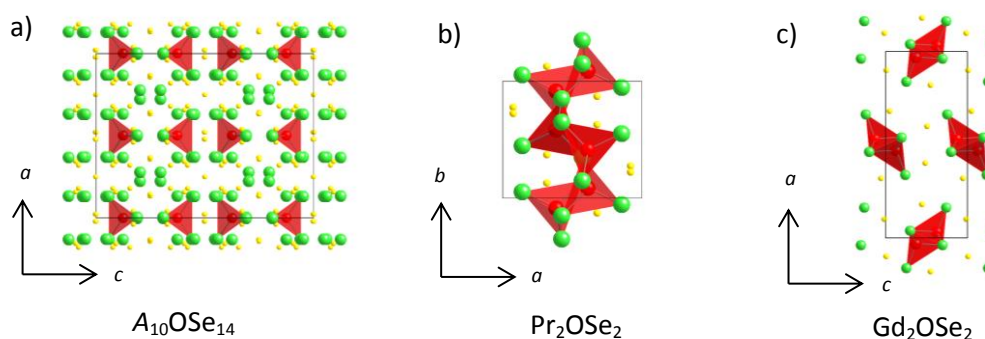
Figure 1.4: *Crystal structure of a) $A_{10}OSe_{14}$, b) Pr_2OSe_2 & c) Gd_2OSe_2. A = green, O = red, Se = yellow.*

Materials with the composition BOQ are known for: S^{2-} (B =Th, U, Np); Se^{2-} (B = Th, U, Np); and Te^{2-} (Th, U). These materials contain edge sharing $[B_2O_2]^{2+}$ layers constructed of B_4O tetrahedra which share 4 edges to produce fluorite-type infinite layers perpendicular to the c axis, these fluorite-like layers are separated by two Q layers.[31-36] The materials adopt a tetragonal structure with space group $P4/nmm$. The B^{4+} cation is found in a 9-fold coordination in a BO_4Q_5 environment, similar to the 8-fold coordination of A^{3+} in A_2O_2Te, i.e. a 4+4 square antiprism-like environment with an additional Q ion above the B site, figure 1.5.

BOQ
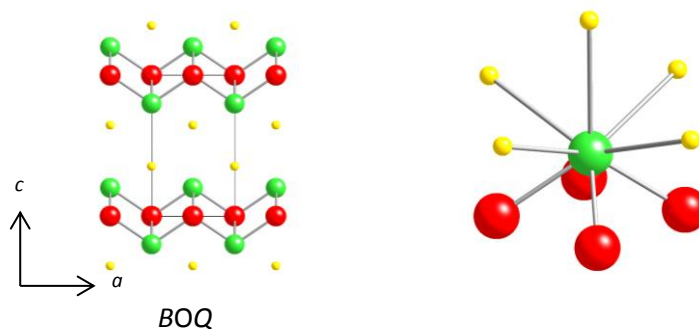
Figure 1.5: *Crystal structure of BOQ, including coordination environment of B site. B = green, O = red, Q = yellow.*

Several transition metal ternary oxychalcogenides have also been reported, namely: HfOS, ZrOS, and Sc_2O_2S.[37-39] HfOS and ZrOS are isostructural and, in contrast to the materials discussed previously, do not contain A_4O (or M_4O) tetrahedra. The transition metal (M) is found in a 7 coordinate MQ_4O_3 environment. Sc_2O_2S adopts a similar structure to A_2O_2S consisting of layers of edge and corner-sharing M_4O tetrahedra alternating with layers of S^{2-} ions. The A_4O tetrahedra share 3 edges like in A_2O_2S, but every second layer is shifted along [110], resulting in a different stacking arrangement along c axis.
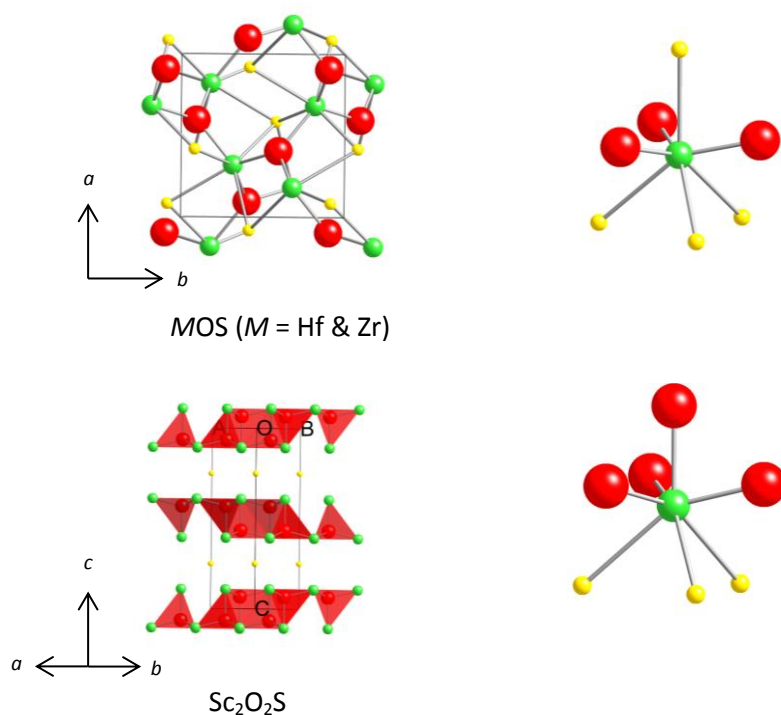
Figure 1.6: *Crystal structure of a) MOS (M = Hf, Zr) and b) Sc$_2$O$_2$S. including coordination environment of M site. M = green, O = red, Q = yellow.*

1.2.2 Quaternary *AOMQ* materials with the ZrCuSiAs structure

Many quaternary and higher stoichiometric oxychalcogenides form two dimensional layered structures, such as the ZrCuSiAs structure type, due to the differing bonding preferences of oxygen and chalcogen anions. Oxygen ions generally bond to "harder" metal cations, while the chalcogenide ions in the structure coordinate to the "softer" metal, resulting in the separation of oxygen and chalcogenide ions into different layers.[40]

The ZrCuSiAs structure type is found for many quaternary oxychalcogenides and has strong similarities to the $A_4O_4Se_3$ structures of section 1.2.1. It contains layers of fluorite-like $[A_2O_2]^{2+}$ and antifluorite-like $[M_2Q_2]^{2-}$ units, constructed from distorted edge sharing of A_4O and MQ_4 tetrahedra. These layers stack alternately along the *c* axis, with space group *P*4/*nmm*, see figure 1.7. The *A* cation is coordinated in an 8 fold AO_4Q_4 4+4 square antiprism environment. This structure is found for the *AO*Cu*Q* series: S^{2-} (La–Eu, Bi); Se^{2-} (La–Nd, Sm–Er, Y, Bi); & Te^{2-} (La, Ce, Nd, Bi).[41-47] By 2008 there were more than 150 mixed anion systems reported with the tetragonal ZrCuSiAs structure.[48]
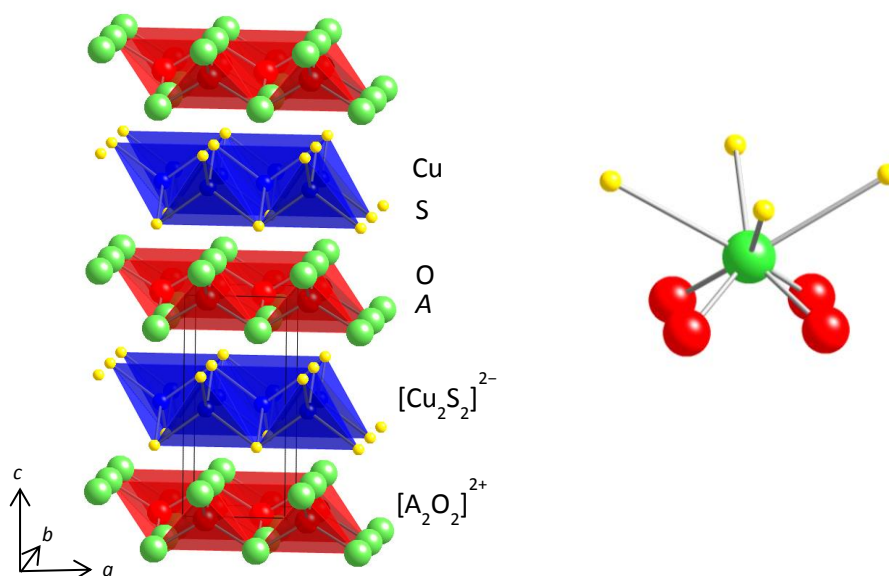
Figure 1.7: *ZrCuSiAs type structure of AOCuQ with P4/nmm symmetry, A = green, O = red, Cu = blue, Q = yellow.*

1.2.2.1 Structural trends

Figure 1.8 shows the variation in the reported unit cell volumes for each of the AOCuS, AOCuSe and AOCuTe series of materials, relative to the ionic radii of the corresponding lanthanide.[48] The unit cell volumes decrease regularly with decreasing rare-earth cation radius. Bi^{3+} materials contain shorter A-O and A-Q bond lengths and smaller volumes than the lanthanides containing materials, despite the large ionic radius of bismuth. This is presumably because Bi^{3+} is more electronegative than La^{3+} meaning, Bi-O bonds are therefore more covalent and shorter than La-O bonds.[17] The *a* cell parameter is decreased while *c* is increased relative to the lanthanum containing materials. This can be rationalised in terms of the electronic configuration of Bi^{3+} which has a lone pair of electrons which repel the bound oxide ions.
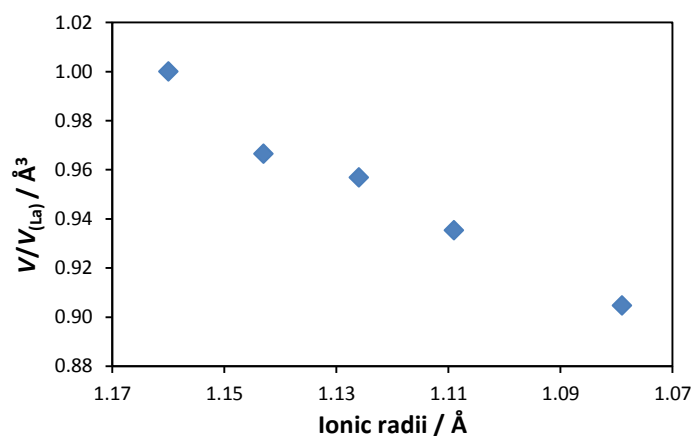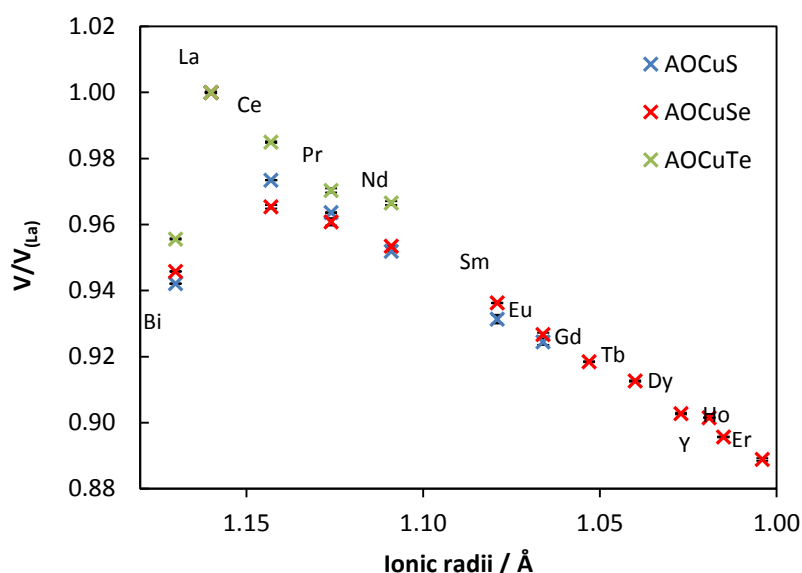
Figure 1.8: *The effect of rare-earth cation radii on the cell volume of AOCuQ material, ionic radii are the values reported by Shannon.*[17]

Over resent years there has been considerable controversy concerning the unit cell volume of CeOCuS. This material has been shown to readily accept a copper deficiency, which leads to either the formal oxidation of Ce^{3+} or to losing electrons from antibonding states at the top of the Cu-3d/S-3p band.[40, 45] In 2009 Clarke *et al.* attempted to clarify the situation by synthesising CeOCuS with a precisely known copper deficiency, $CeOCu_{0.987}OS$.[47] This almost-stoichiometric material has a unit cell volume in line with the series trend, suggesting that the earlier materials were not stoichiometric.[45] Figure 1.4 actually suggests that rather than Ce^{3+} being below the trend, La^{3+} is above the Q = S trend, although the reason for this is unknown. Clarke *et al.* also showed that a linear relationship exists between unit cell volume and accurately determined copper deficiency for CeOCuS.[47]

1.2.2.2 Electronic and magnetic properties

Materials with *AOCuQ* composition are of interest due to their transparent p-type semiconducting properties, and large band gaps (LaOCuS 3.1 eV), which make blue photoluminescence possible.[49-51] The band structure of LaOCuS has been calculated by Ueda *et al*. and shows the highly conducting copper-chalcogenide layers are separated by insulating $[A_2O_2]^{2+}$ layers. The valence band maxima and conduction band minima consist of Cu 3d and *S* 3p and Cu 4s states, respectively.[52] The valence band is formally full and the conduction band empty, therefore conduction is contained within the $[Cu_2Q_2]^{2-}$ layers, bound by $[A_2O_2]^{2+}$ insulating layers. [52]

The band gap of these materials can easily be tuned by varying the rare-earth and chalcogen. The decrease in electronegativity from S^{2-} (2.58) to Se^{2-} (2.55) results in greater hybridisation in the valence band maximum state, consequently the band gap is decreased from LaOCuS (3.1

eV) to LaOCuSe (2.8 eV).[53, 54] The band gap is further decreased to 2.3 eV for LaOCuTe due to the higher energy of the Te 5p level compared to the S 3p and Se 4p levels.[42] Substitution of the A site for a smaller rare-earth results in a decrease in band gap, as the unit cell shrinks from LaOCuS (3.1 eV) to NdOCuS (3.05 eV) to SmOCuS (2.8 eV)[55, 56]. The lanthanide ions do not affect the valence band maxima and conduction band minima directly. Instead, decreasing the A^{3+} radii reduces the size of the $[A_2O_2]^{2+}$ layer and consequently the $[Cu_2Q_2]^{2-}$ layer. This reduces Cu-Q bond lengths, leading to an increase in hybridisation between Cu 3d and Q np giving rise a higher valence bond maximum and hence a decreased band gap.

The efficient UV-blue photoluminescence from room temperature excitons and controllable p-type conductivity make AOCuQ materials promising for short wavelength opto-electronic devices. One drawback in implementing these devices has been the impossibility of fabricating homo pn junctions due to a difficultly obtaining suitable n-type conductors. Despite this a LaOCuSe pn hetero junction was demonstrated in 2006, using n-type amorphous indium gallium zinc oxide (a-InGaZn$_5$O$_8$). Electrons injected into the a-InGaZn$_5$O$_8$ layer combine with holes in the p-type LaOCuSe layer giving blue emission.[57]

AOAgS (A = La & Ce) can also be synthesised, LaOAgS is a fast ion conductor. Rietveld refinement of neutron diffraction data has shown anisotropic temperature factors which indicate enhanced silver mobility in the ab plane of the tetragonal cell. The silver ion density suggests that the conduction is via interstitial (4e, ½ ½ ½) sites in the ab plane between the occupied Ag sites at (0.25 0.75 0.5).[58] The optical band gaps for LaOAgS and CeOAgS are 0.22 eV and 0.71 eV respectively, correspond to a change from green to black.[40, 58-60]

Magnetic susceptibility data for AOCuQ compounds data show that A = Pr, Nd, Sm, Eu materials remain paramagnetic to low temperature. While in LaOCuQ, La^{3+} ions are diamagnetic.[55, 61-63]

1.2.2.3 ZrCuSiAs derived oxychalcogenides

There are several materials structurally and compositionally closely related to AOCuQ where the monovalent transition metal is substituted for divalent metal ions and charge balance is achieved through half occupancy of this site. This results in distinct but related structures with fluorite-like $[A_2O_2]^{2+}$ layers separated by half occupied transition metal-chalcogenide layers. Prior to this work three compounds of this type had been reported (CeOMn$_{0.5}$Se, Ce$_2$O$_2$FeSe$_2$ and La$_2$O$_2$CdSe$_2$); each contains a different arrangement of M^{2+} ions.[64-66] In CeOMn$_{0.5}$Se the transition metal ions in the $[M$Se$_2]^{2-}$ layers have been reported to be randomly arranged, with 50% statistical occupancy on each site, thus the symmetry remains $P4/nmm$ as in LaOCuS. An

optical band gap of 2.01 eV has been measured for this compound; however electrical and magnetic properties have not been reported.[64]

$Ce_2O_2FeSe_2$ has been reported to have an enlarged unit cell relative to LaOCuS of $\sim\sqrt{2}a_{tet}$ x $\sim\sqrt{2}a_{tet}$ x $\sim2c_{tet}$. The transition metal chalcogenide layers contain chains of edge linked $FeSe_4$ tetrahedra running along the shorter a axis of the material. This structure is shown in figure 1.9. The Fe^{2+} moments order upon cooling with a Néel temperature, T_N, of 171 K. Ferromagnetic chains of Fe^{2+} form along [100] with moments oriented along [010], perpendicular to the chain direction. The interaction between the chains is anti-ferromagnetic, $Ce_2O_2FeSe_2$ is a semiconductor with an electronic band gap of 0.64 eV.[66]
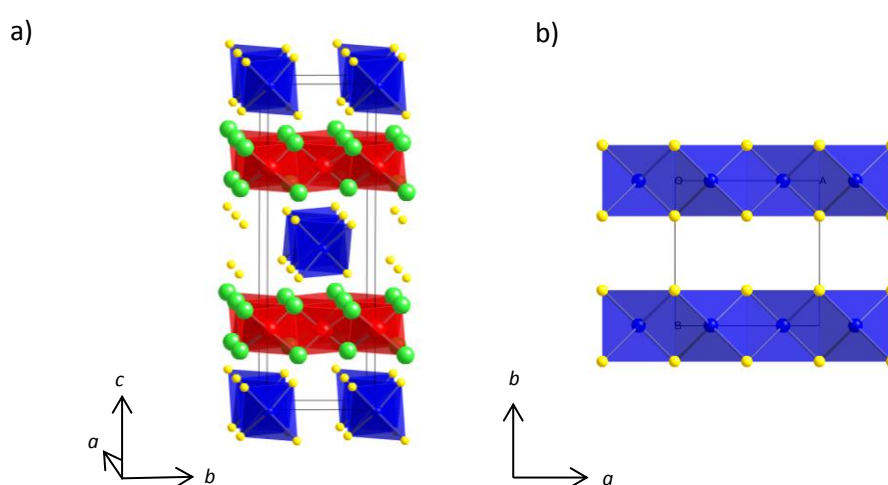
Figure 1.9: *a) Structure of $Ce_2O_2FeSe_2$ in Imcb symmetry b) $[FeSe_2]^{2-}$ layer viewed along [001]; Ce = green, O = red, Se= yellow and Fe = blue.*

In $La_2CdO_2Se_2$ the $[CdSe_2]^{2-}$ metal chalcogenide layer contains corner-sharing $CdSe_4$ tetrahedra, as opposed to the edge sharing tetrahedra in LaOCuS. This results in a "checkerboard" arrangement of $CdSe_4$ tetrahedra shown in figure 1.10. The material has a reported optical band gap of 3.3 eV at room temperature, larger than any $AOCuQ$ material reported to date, and much higher than CdSe (1.8 eV). The wide band gap is a result of the layered structure, which reduces the interlayer hybridisation of Cd 5s orbitals, thus the band gap of $La_2O_2CdSe_2$ is determined by the $(CdSe_2)^{2-}$ layers, where the conduction band minimum is mainly composed of Cd 5s and the valence band maximum by Se 4p.[67] $La_2O_2CdSe_2$ is reported to be electrically insulating with resistivities greater than 10^{10} Ωcm; Hiramatsu *et al.* attempted to generate electron carriers by Al^{3+} substitution for Cd^{2+} and Zr^{4+} for La^{3+}; however, all doped samples remained insulating.[65]
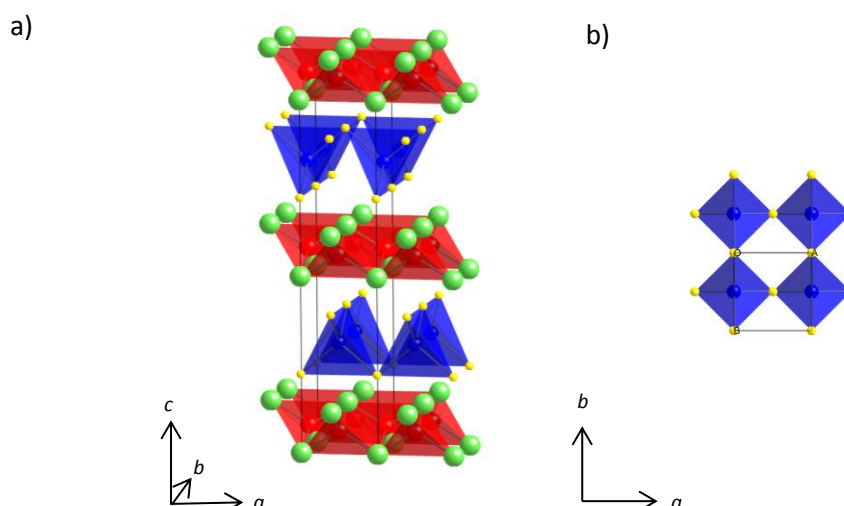
Figure 1.10: *a) La$_2$O$_2$CdSe$_2$ crystal structure with P4$_2$/nmc symmetry, b) [CdSe$_2$]$^{2-}$ layer viewed along [001]; La = green, O = red, Cd = blue, Se = yellow.*

Two more complex materials which are structurally related to *AOCuQ* are La$_5$Cu$_6$O$_4$S$_7$ and (NdO)$_4$Ga$_2$S$_5$. La$_5$Cu$_6$O$_4$S$_7$ contains [La$_5$O$_4$S]$^{5+}$ layers which are separated by undulating layers of edge sharing [Cu$_6$S$_6$]$^{5-}$, alternating along the [001] direction. The [La$_5$O$_4$S]$^{5+}$ are conceptually related to the [La$_2$O$_2$]$^{2+}$ found in *AOMQ* by the O atom in every fifth tetrahedron being replaced with a S atom, leading to discrete [La$_2$O$_2$]$^{2+}$ blocks of 4 edge sharing tetrahedra, see figure 1.11a. The larger size of sulfur compared to oxygen causes the layer to distort. La$_5$Cu$_6$O$_4$S$_7$ crystallises in space group *Imma* a = 5.667 Å, b = 15.666 Å, c = 17.534 Å. The distorted layers allows the material to contains extra S when compared [AO]$_n$$MQ_n$. The average oxidation state of copper is $+^7/_6$ and this compound is reported to be a metallic conductor in the [100] direction, with a room temperature conductivity of 2.6 x10^4 S/cm.[68]

(NdO)$_4$Ga$_2$S$_5$ also contains additional S relative to [AO]$_2$$MQ_2$ (i.e. [NdO]$_2$GaS$_{2.5}$) and crystallises in space group *Pbca* with a = 18.293(3) Å, b = 22.586(4) Å, c = 5.737(2) Å. This material contains undulating layers of fluorite-like [Nd$_2$O$_2$]$^{2+}$ edge-sharing tetrahedra which alternate with sheets of GaS$_4$ corner-sharing tetrahedra perpendicular to the [100] direction, see figure 1.11b. The corner-sharing tetrahedra, as opposed to edge shared MQ_4 tetrahedra, allows the accommodation of the additional Q atoms. No physical properties for this system have been reported.[69]
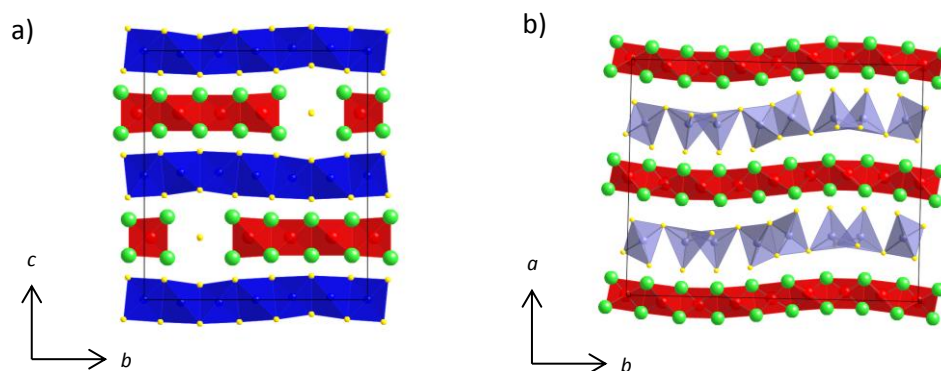
Figure 1.11: *Structures of a) $La_5Cu_6O_4S_7$ with Imma symmetry and b) $(NdO)_4Ga_2S_5$ with Pbca symmetry; La/Nd = green, O = red, S = yellow, Cu = blue, Ga = purple.*

1.2.2.4 Other *AOBQ* Materials

There are several quaternary materials with a similar composition to LaOCuS but with different structures. For example the structure of BaZnOS (figure 1.12a) contains Zn atoms in a tetrahedral geometry, coordinated by two oxygen and two sulfur atoms. [70] The ZnO_2S_2 tetrahedra share all of their vertices and form two sets of parallel chains along the *a* and *c* axes. Ba is 8 fold coordinated in a BaO_4S_4 environment, which resembles the 4+4 square antiprism environment of La found in LaOCuS, but with some distortion due to the loss of 4 fold symmetry. The band gap is reported to be 3.9 eV.[70] BaZnOS has shown promise as a luminescent host material and has shown blue and red luminescence when doped with Cu and Mn respectively.[71-73] While it has not been possible to synthesise the Sr analogue, CaZnOS has been made, and contains layers of ZnS_3O tetrahedra with their Zn-O bonds aligned parallel to the *c* axis of the material and linked at all their S vertices to create layers, figure 1.12b. [71] The Ca sites are 7 coordinate in a CaS_4O_3 environment, similar to that found for the ternary compound HfOS. CaZnOS has a reported room temperature band gap of 3.7 eV, consistent with the white colour of the compound.[74] Mn^{2+}-activated CaZnOS shows potential as a red-emitting phosphor.[71]
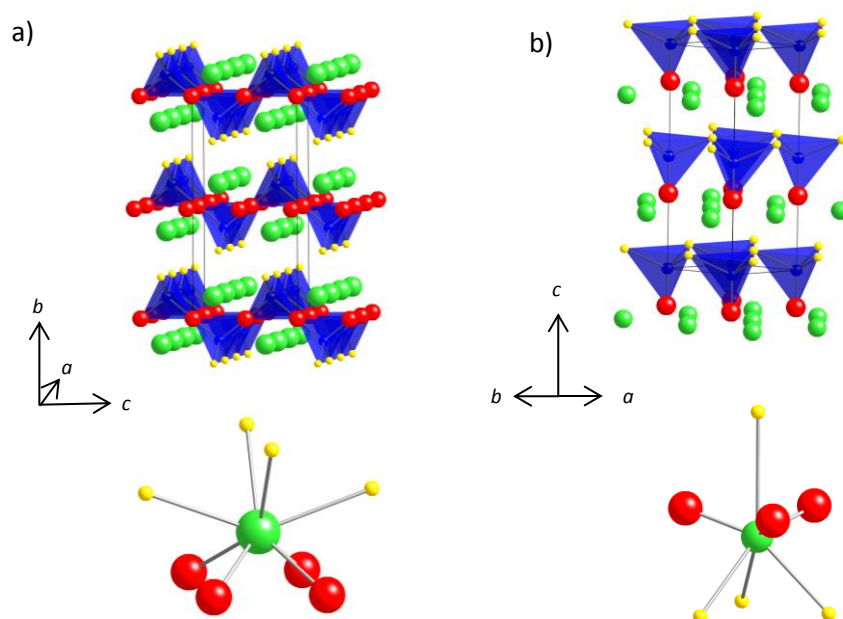
Figure 1.12: Structures of a) BaZnOS in Cmcm symmetry and b) CaZnOS in P6₃mc; Ba/Ca = green , S = yellow, O = red, Zn = blue.

1.2.3 $A_2O_2Q_2M_2O$ type materials

Another important class of layered oxychalcogenides have the $A_2O_2Q_2M_2O$ structure, first reported in 1992 from single crystal studies by Mayer *et al.* for $La_2O_2Se_2Fe_2O$ and $La_2O_2S_2Fe_2O$.[75] In recent years the series has been expanded to include a wide range of rare earths and a number of different divalent transition metals. Table 1.1 shows reported compositions of the $A_2O_2Se_2M_2O$ series.[76-79] This structure is thermodynamically stable for nine Mn, Fe and Co containing compositions with the Fe-containing materials forming with the widest range of rare-earth radii. This is presumably a result of an optimum match between the size of the $[FeO_2Se_4]^{2-}$ and $[A_2O_2]^{2+}$ layers.

Table 1.1: *Reported compositions for $A_2O_2Se_2M_2O$ series.*

M^{2+}	A^{3+}	Ref
Mn	La Ce Pr	78, 79
Fe	La Ce Pr Nd Sm	75, 79, 80
Co	La	81

The $A_2O_2Se_2M_2O$ structure can be described as containing fluorite-type $[A_2O_2]^{2+}$ layers of edge sharing tetrahedra, as found in the ZrCuSiAs structure, which are separated from anti-CuO$_2$ type $[M_2O]^{2+}$ layers by layers of Se^{2-} ions (figure 1.13). This unusual geometry, with two-coordinate transition metals and four-coordinate oxide ions, is not found in oxide materials. There is, however, significant bonding between M^{2+} and Se^{2-} ions such that 4 Se^{2-} ions coordinate around each transition metal ion. The transition metal layers can thus be described as containing face-sharing octahedra with two axial oxide ions and four equatorial selenide ions. The structure adopts a tetragonal unit cell at room temperature $a = b \sim 4$ Å, $c \sim 18.5$ Å, and $I4/mmm$ symmetry.
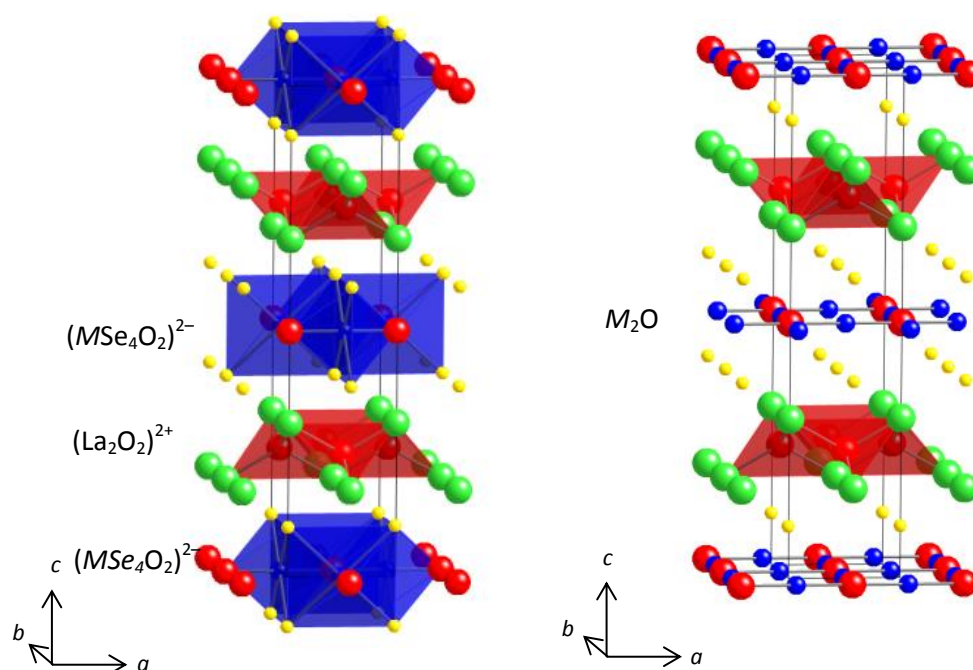
Figure 6.13: *Crystal structure of $A_2O_2Se_2M_2O$ I4/mmm symmetry, A = green, O = red, Q = yellow, M = blue.*

1.2.3.1 Structural trends in $A_2O_2Se_2M_2O$ materials

Figure 1.14 shows a decrease in unit cell volume with decreasing rare earth size, as observed in the $AOCuQ$ series of materials, due to contraction of the $[A_2O_2]^{2+}$ layers. The lanthanum-containing materials also show the expected decrease in cell volume with decreasing size of M^{2+} ion: $La_2O_2Se_2Mn_2O$ (313.860(3) Å^3), $La_2O_2Se_2Fe_2O$ (310.268(8) Å^3) and $La_2O_2Se_2Co_2O$ (306.52(3) Å^3).[79] However, $La_2O_2Se_2Co_2O$ shows a significantly smaller c/a ratio than the Mn and Fe containing materials (figure 1.14). A substantial decrease in the height of the M_2OSe_2 layers is observed which is not compensated by an increase in the height of the $[A_2O_2]^{2+}$ layers.

Extra structural reflections are observed in X-ray and neutron powder diffraction patterns for $A_2O_2Se_2Mn_2O$ (A = La, Pr) upon cooling.[79, 82] Chapter 6 will discuss the low temperature structures of $A_2O_2Se_2Mn_2O$ (A = La, Pr) determined from single crystal X-ray diffraction. The effect of temperature on the M_2OSe_2 and $[A_2O_2]^{2+}$ layers will be discussed.
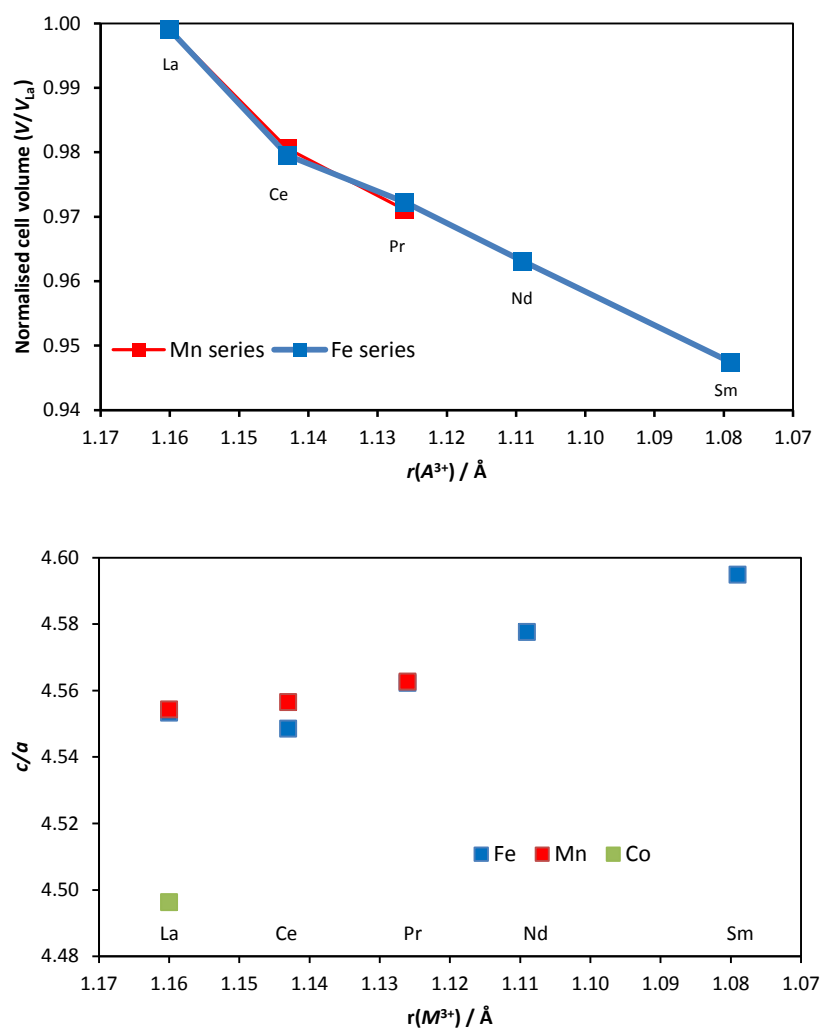
Figure 1.14: Structural trends in $A_2O_2Se_2M_2O$ series, ionic radii are the values reported by Shannon.[17]

1.2.3.2 Electronic properties of $A_2O_2Se_2M_2O$ materials

$La_2O_2Se_2Fe_2O$, $La_2O_2Se_2Mn_2O$ and $La_2O_2Se_2Co_2O$ are semiconductors at room temperature with band gaps for $La_2O_2Se_2Mn_2O$ and $La_2O_2Se_2Co_2O$ being 0.24 eV and 0.35 eV, consistent with a change in sample colour from olive green to light grey.[79, 81] Room temperature resistivities are 10^4 Ωcm, 3.65 x 10^4 Ωcm and 2.24 x 10^7 Ωcm for the Fe, Mn and Co materials respectively. Electronic structure calculations by Zhu for $La_2O_2Se_2Fe_2O$ and $La_2O_2S_2Fe_2O$ show a partially filled conduction band with the Fe 3d electrons contributing most to the density of states near the Fermi level. The Fe d electron band width (3.2 eV) is appreciably narrower than for LaOFeAs (4.4 eV) thus these materials can be described as Mott insulators.[83] Studies by Wu show that the Co 3d bandwidth in $La_2O_2Se_2Co_2O$ is appreciably narrower again, at 2.8 eV. Electrical properties have not been reported on the other members of this series.[84]

1.2.3.3 Magnetic properties of $A_2O_2Se_2M_2O$ materials

25

$A_2O_2Se_2M_2O$ materials show antiferromagnetic (AFM) transitions upon cooling and represent rare examples of frustrated AFM checkerboard spin-lattices. The magnetic structures for several members of the family have been reported and are shown in figure 1.15.

In $A_2O_2Se_2Mn_2O$ (A = La, Ce, Pr) Mn^{2+} magnetic moments order antiferromagnetically with moments directed along [001] and a k vector k = (0,0,0) and T_N = 168.1(4), 174.1(2) and 180.3(4) K for La, Ce, Pr ions respectively. The in-plane spin arrangement is shown in figure 1.15b. The increase in T_N is approximately linear with respect to decreasing A^{3+} radius. The refined magnetic moments for $La_2O_2Se_2Mn_2O$ is ~4.2 μ_B at low temperature.[78, 79] Magnetic moment for $Ce_2O_2Se_2Mn_2O$ and $Pr_2O_2Se_2Mn_2O$ at 12 K are 4.023(7) μ_B and 4.219(8) μ_B respectively.[79]

$A_2O_2Se_2Fe_2O$ has been reported to have a propagation vector k = (1/2,0,1/2). This corresponds to two independent Fe sites with AFM coupling along a doubled a axis [100], and FM coupling along [010] figure 1.15c.[82] A T_N ~90 K is observed for $A_2O_2Se_2Fe_2O$ (A = La, Ce, Pr, Nd) with a refined Fe^{2+} moment of 2.83(3) μ_B and 2.21(6) μ_B for the La and Pr analogues at 12 and 40 K respectively.[80, 82, 85] Recently an alternative 2-k structure has been proposed, figure 15.5d, which gives equivalent neutron scattering. Here moments point orthogonal to Fe-O bonds with nearest neighbour moments perpendicular to one another.[86] The magnetic structure has not been published for $Ce_2O_2Se_2Fe_2O$. It is reported to have a propagation vector (1/4,1/4,0). Unpublished work from this group, however, suggests a structure similar to the La material.

For $La_2O_2Se_2Co_2O$ two magnetic structures have been proposed which cannot be distinguished from powder data, figure 15.5 e & f. The orientation of the nearest neighbour cobalt moments are orthogonal to each other in the ab plane with propagation vector k = (1/2,1/2,0). Two different studies have reported Co^{2+} moment of 3.29(3) and 3.53(1) μ_B.[79, 87]
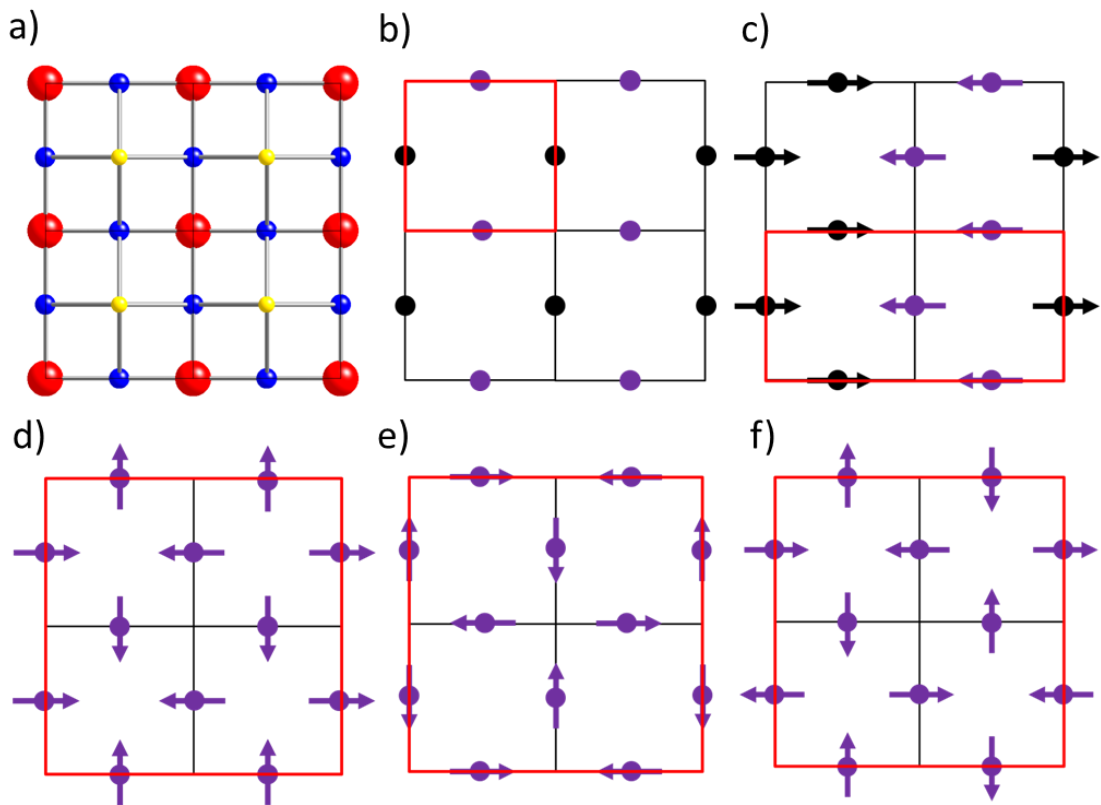
Figure 1.15: *a) Nuclear structure of $A_2O_2Se_2M_2O$ viewed down [001], observed magnetic structures of b) $A_2O_2Se_2Mn_2O$, c) & d) $A_2O_2Se_2Fe_2O$, e & f) $La_2O_2Se_2Co_2O$, the black and purple colour represents M^{2+} moments, similar colours represents similarly orientated moments, magnetic unit cell highlighted in red.*

1.2.3.4 Other M_2O containing systems

The systems $B_2F_2Fe_2OQ_2$ (B = Sr, Ba; Q = S, Se) and $B_2F_2Mn_2OSe_2$ contain the same $[M_2O]^{2+}$ square planar layers as $A_2O_2Se_2M_2O$. These anti-CuO_2 type layers are separated by layers of Se^{2-} from fluorite-like $[F_2B_2]^{2+}$ layers constructed from edge sharing $[FB_4]$ tetrahedra. (figure 1.16a). The iron containing compounds are known to order antiferromagnetically below 83.6 and 106.2 K for Sr and Ba analogues respectively. Another material which contains M_2O layers is $Na_{1.9}Cu_2Se_2Cu_2O$. This material consists of layers of edge sharing $CuSe_4$ tetrahedra (as found in LaOCuS) and layers of square planar CuO_2 separated by sodium ions, figure 1.16b.[88]
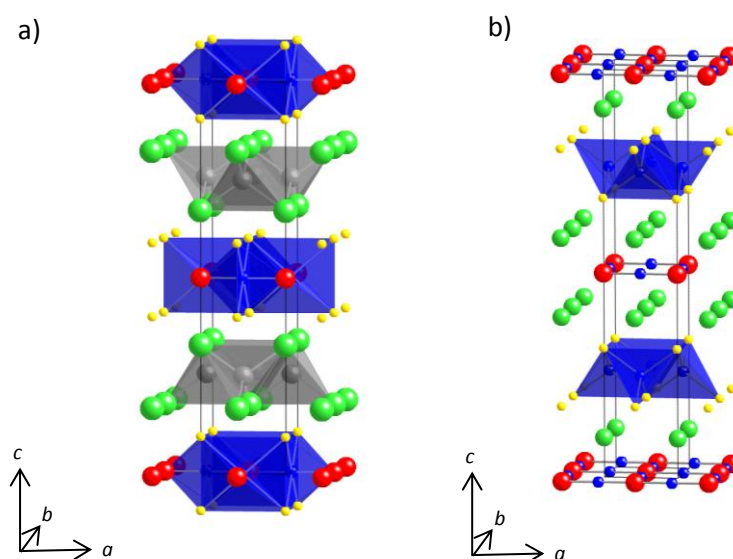
Figure 1.16: Structures of a) $B_2F_2Fe_2OQ_2$ (B = Sr, Ba; Q = S, Se) and b) $Na_{1.9}Cu_2Se_2Cu_2O$, Sr, Ba, Na = green, Fe,Cu =blue, O = red, Se, S = yellow, F = grey.

1.3 3-Dimensional oxychalcogenides $A/O/M/Q$

Whilst many oxychalcogenides adopt layered structures as discussed in section 1.2, there are many other oxychalcogenides related to those discussed above which contain fragments of the infinite $[A_2O_2]^{2+}$ layers but in more 3-dimensional structures. Some of these materials are investigated in Chapter 4 ($A_4O_4TiSe_4$) and Chapter 7 (LaInS$_2$O) of this thesis. One way to systematise these is by considering the number of A_4O tetrahedra the fragment contains between breaking points, e.g. 2, 3 or 4 units; here we quantify this by the value x in xA_4O. In the following sections quaternary 3D materials relevant to the systems explored in this thesis are introduced. They are discussed in order of the non-lanthanide (M site) metal they contain.

1.3.1 $A/O/Ti/Q$ compounds

There are two reported titanium-containing quartenerary oxychalcogenides with A_4O fragments: La$_{16}$TiS$_{17.75}$O$_{17}$ and Gd$_4$O$_4$TiSe$_4$.[89, 90] Figure 1.17a shows the structure of Gd$_4$O$_4$TiSe$_4$ which contains fragments of A_4O and A_3TiO 4 tetrahedra in length i.e. 4A_4O units. These 4A_4O units are linked by octahedrally coordinated titanium ions, TiSe$_4$O$_2$, which edge-share to produce chains along b. The tetrahedra share edges to form 1D ribbons which run parallel to the b-axis. There are two crystallographically independent A^{3+} ions which have either ASe$_4$O$_4$ or ASe$_5$O$_3$ 4+4 square antiprismatic coordination environments similar to that found in LaOCuS, though with a small distortion due to the loss of 4-fold symmetry in this system. Due to the finite width of the tetrahedral ribbons, one oxygen atom is replaced by selenium in the coordination sphere around one A site forming ASe$_5$O$_3$ units.

Magnetic susceptibility measurements shows Gd$_4$O$_4$TiSe$_4$ remains paramagnetic upon cooling to 4 K, below which a large increase susceptibility is observed, thought to be a result of Gd^{3+} ordering.[89] It has not been possible to investigate the origin of this magnetic anomaly by neutron diffraction due to Gd being a high neutron absorber. Compounds structurally related to Gd$_4$O$_4$TiSe$_4$ and their properties are discussed in Chapter 4.

A second 3D quaternary oxychalcogenide containing Ti is La$_{16}$TiS$_{17.75}$O$_{17}$. As with Gd$_4$O$_4$TiSe$_4$, the $[A_2O_2]^{2+}$ layers in La$_{16}$TiS$_{17.75}$O$_{17}$ are broken by Ti, but into units 3 tetrahedra in width, 3A_4O. The units are coordinated in a *cis* fashion around octahedrally coordinated TiO$_4$S$_2$ to form rings which surround TiS$_6$ octahedra, figure 1.17b.
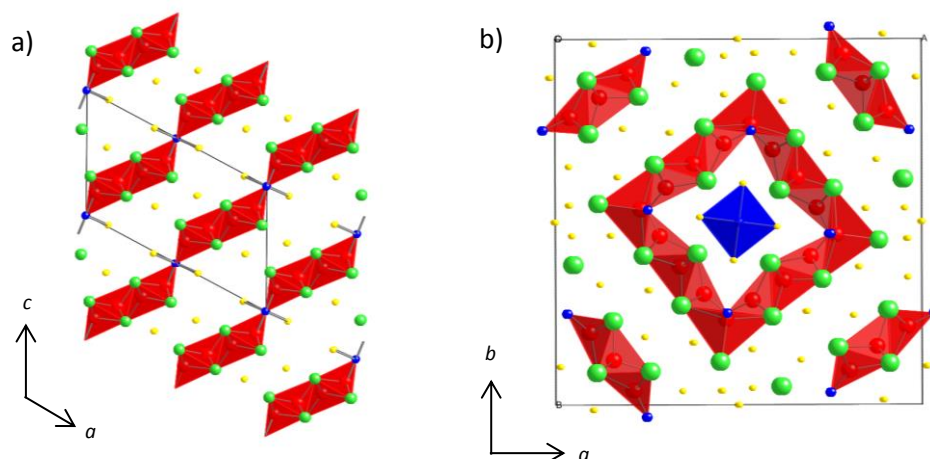
Figure 1.17: *Crystal structures of a) $Gd_4O_4TiSe_4$ in C2/m symmetry and b) $La_{16}TiS_{17.75}O_{17}$ in I4/m symmetry; A = green, Ti = blue, Q = yellow, O = red.*

1.3.2 *A/O/V/Q* compounds

There are 2 different compositions reported for *A*/O/V/*Q* materials: $A_5V_3O_7S_6$ (*A* = La, Ce, Pr, Nd, Eu)[91-93] which adopts *Pmmn* symmetry and $A_7VO_4Se_8$ (*A* = Nd, Sm, Gd)[94] which adopts *Pbam* symmetry.

$A_5V_3O_7S_6$ materials contain fragments of edge sharing tetrahedra of A_4O and A_3VO coordination both 2 and 3 tetrahedra in width, therefore we can categorise this material as a 2.5A_4O system, figure 1.18a. These different sized tetrahedral fragments again edge-share to produce 1D ribbons along *b* and are interconnected by discrete vanadium containing octahedra, VS_4O_2, which themselves edge-share to produce chains along *b*; these are similar to the MQ_4O_2 octahedra as found in $Gd_4O_4TiSe_4$ discussed in Section 1.3.1. The vanadium sites have a mixed valence of V^{3+}/V^{4+} distributed randomly throughout the structure.

$A_7VO_4Se_8$ also contains ribbons of edge-sharing A_4O and A_3VO tetrahedra, but only 2 tetrahedra wide, 2A_4O, interrupted by chains of edge-sharing VSe_4O_2 octahedra along *c*. The remaining A^{3+} ions are in chains of edge-sharing octahedra of $GdSe_6$ along *c*, figure 1.18b. Magnetic measurements show that $Gd_7VO_4Se_8$ is paramagnetic down to 5 K.[94] The vanadium ions are all in a V^{3+} oxidation state.
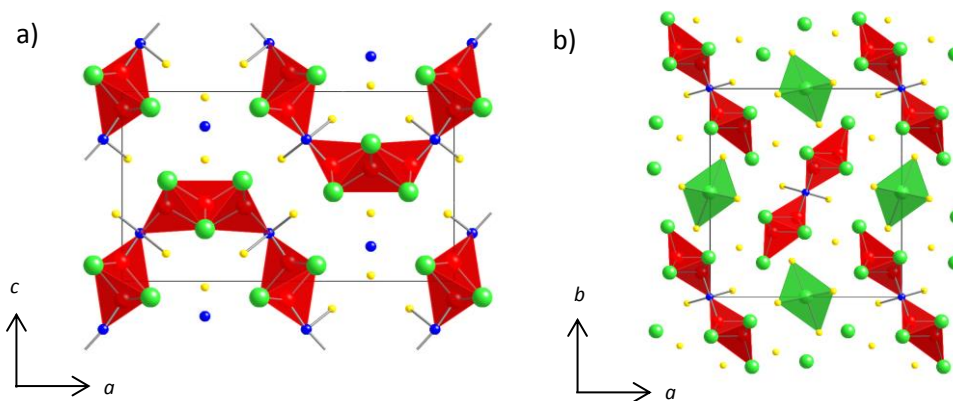
Figure 1.18: *Structure of a) $A_5V_3S_6O_7$ in Pmmn symmetry and b) $A_7VO_4Se_8$ in Pbam symmetry; A = green, Q = yellow, V = blue, O = red.*

1.3.3 ACrOQ_2 compounds

The ACrOS$_2$ (A = La, Ce, Pr, Nd) and ACrOSe$_2$ (A = La, Ce, Nd) compounds fall into two structural groups. When A = La a *Pbnm* space group is adopted while the remaining A containing compounds have $B2/m$ symmetry. [95-99] In both structures the lanthanoid atoms are found in the same environment, with ribbons along c of edge-sharing A_3CrO tetrahedra two units in width, therefore we can describe these as 2A_4O structures. The differences lie in the chromium coordination environment. In LaCrOQ_2, two parallel chains of CrOQ_5 octahedra edge share to produce 1D chains. In ACrOQ_2 ($A \neq$ La) there are two M-containing chains, one of CrQ_6 and one of CrO$_2Q_4$ octahedra, which are connected by edges and corners to form layers, figure 1.19. Both of these chromium containing structures the A^{3+} cation is 9 fold coordinated in an AQ_6O_3 environment based on a 4+4 square antiprism with an additional Q atom directly above the A site completing the coordination sphere, figure 1.19c.
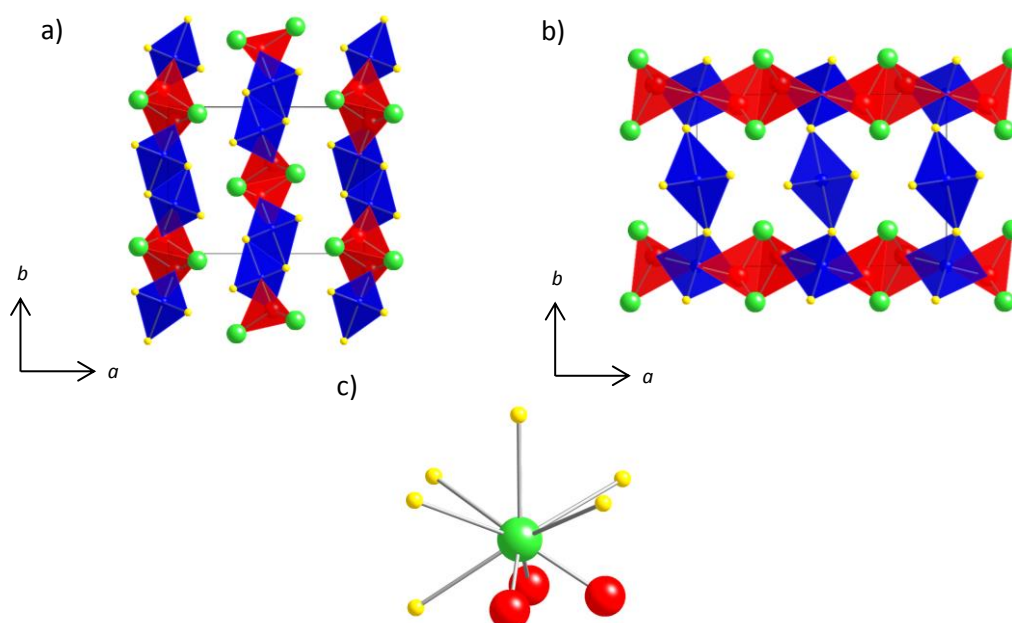
Figure 1.19: *Crystal structure of a) LaCrOQ$_2$ in Pbmm symmetry, b) ACrOQ$_2$ (A = Ce, Pr, Nd, Sm) in B2/m symmetry , c) local coordination environment of A^{3+} cations in ACrOQ$_2$; A = green, Cr = blue, Q = yellow, O = red.*

1.3.4 A/O/M/Q (M = Mn, Fe) compounds

There are three different compositions known for A/O/M/Q (M = Mn, Fe): A_4MOQ_6, $A_2O_2MSe_2$, and $Sr_2Mn_2O_4Se$ with non-layered structures.[100-102] These materials and their space groups are given in table 1.2

Table 1.2: *A/O/M/Q (M = Mn, Fe) materials and their space groups.*

Compound	Space group
La$_4$MnOS$_6$	$P6_3mc$
La$_4$MnOSe$_6$	$P6_3$mc
La$_4$FeOSe$_6$	$P6_3mc$
Ce$_4$MnOSe$_6$	$P6_3mc$
Ce$_4$FeOSe$_6$	$P6_3mc$
Nd$_4$MnOSe$_6$	$P6_3mc$
Sm$_4$FeOSe$_6$	$P6_3mc$
La$_2$O$_2$MnSe$_2$	$Ama2$
La$_2$O$_2$FeSe$_2$	$Ama2$
Sr$_2$Mn$_2$O$_4$Se	$Pnma$

A_4MOSe_6 (M = Mn, Fe) materials crystallise in the hexagonal $P6_3mc$ space group and contain discrete A_4O tetrahedra separated by layers of MSe$_6$ edge-shared octahedra. The remaining Se sites complete the ASe$_7$O coordination sphere, figure 1.20a. The physical properties of these materials have not been reported.

The structure of β-$La_2O_2MSe_2$ (M = Mn, Fe) contains ribbons of A_4O and A_3MO edge-shared tetrahedra 4 units in width, i.e. $4A_4O$. These fragments are connected by an octahedrally coordinated MSe_4O_2 transition metals, which themselves form edge-sharing MSe_4O_2 chains along c (figure 1.20b). The structure is therefore similar to $Gd_4O_4TiSe_4$, and further comparison will be given in Chapter 4. A second tetrahedrally coordinated M^{2+} ion is present linking the MO_2Se_4 octahedra, producing chains of alternating MO_2Se_4 and MSe_4 units. $La_2O_2MnSe_2$ is an insulator at room temperature with an optical band gap of 1.6 eV, while $La_2O_2FeSe_2$ is an semiconductor over the range 150 to 300 K with a band gap of 0.7 eV. Both compounds are reported to be antiferromagnetic at low temperatures.[101]

$Sr_2Mn_2O_4Se$ has recently been reported and, like A_4MOSe_6, does not contain edge-sharing A_4O tetrahedra. The structure contains chains of distorted face-sharing MnO_4Se_2 with Sr^{2+} ions in 6 coordinate SrO_4Se_2 sites between the manganese layers, figure 1.20c.
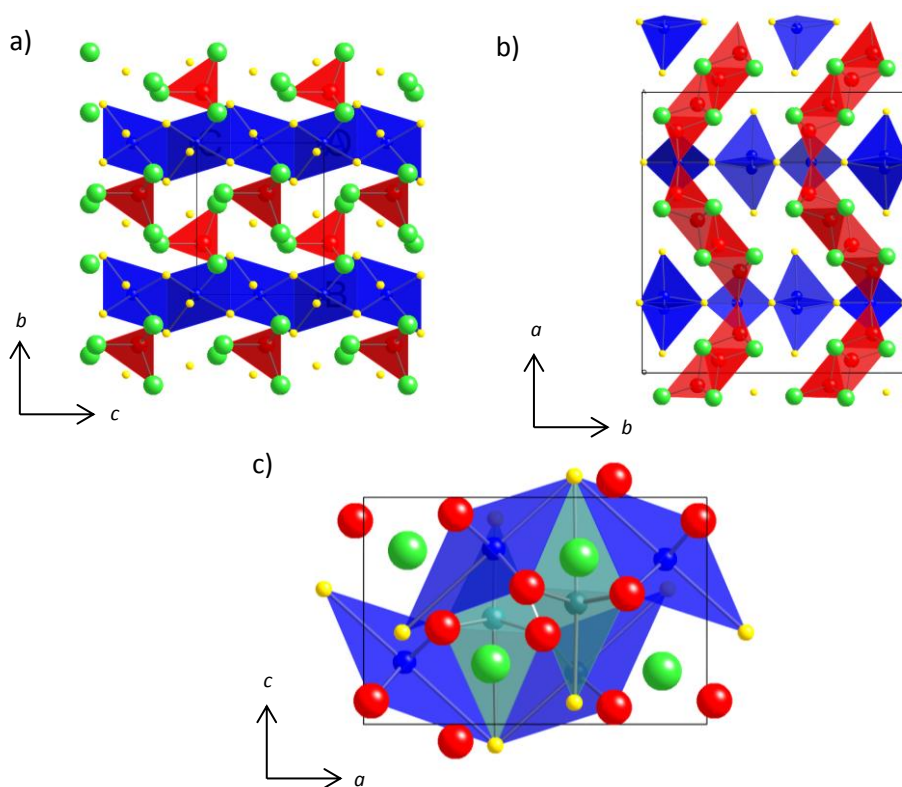
Figure 1.20: *Structures of a) A_4MOSe_6 in $P6_3mc$ symmetry, b) β-$La_2O_2MSe_2$ in Ama2 symmetry c) $Sr_2Mn_2O_4Se$ in Pnma symmetry; A = green, Mn, Fe = blue, Q = yellow, O = red.*

1.3.5 La/O/In/S compounds
Three 3-dimensional lanthanum indium oxysulfides: $La_5In_3O_3S_9$, $La_{10}In_6S_{17}O_6$ and $LaInS_2O$, have been reported.[103, 104] In $La_5In_3O_3S_9$ the indium atoms are coordinated in all sulfur environments in either distorted tetrahedra or octahedra. The octahedra edge-share to produce indium

sulphide layers. Figure 1.21 shows that these layers are separated by ribbons of fluorite-like La_4O edge-shared tetrahedra, 3 units in width, we can therefore describe the materials as a $3A_4O$ structure. The fluorite blocks edge-share to produce ribbons of A_4O along a. $La_{10}In_6S_{17}O_6$ can be described in a similar way, with ribbons of $3A_4O$ fluorite-type $[La_2O_2]^{2+}$ tetrahedra, separated by octahedrally and tetrahedrally coordinated indium sulfide layers.

A structural model has yet to be reported for $LaInS_2O$. This compound has been demonstrated to catalyse the reduction of H^+ to H_2 and the oxidation of H_2O to O_2 under visible light and in the presence of an electron donor or acceptor respectively. $Na_2S–Na_2SO_3$ and Ag^+ have been used as donors and acceptors for this process.[105] The structure determination of $LaInS_2O$ is the subject of Chapter 7 of this thesis.
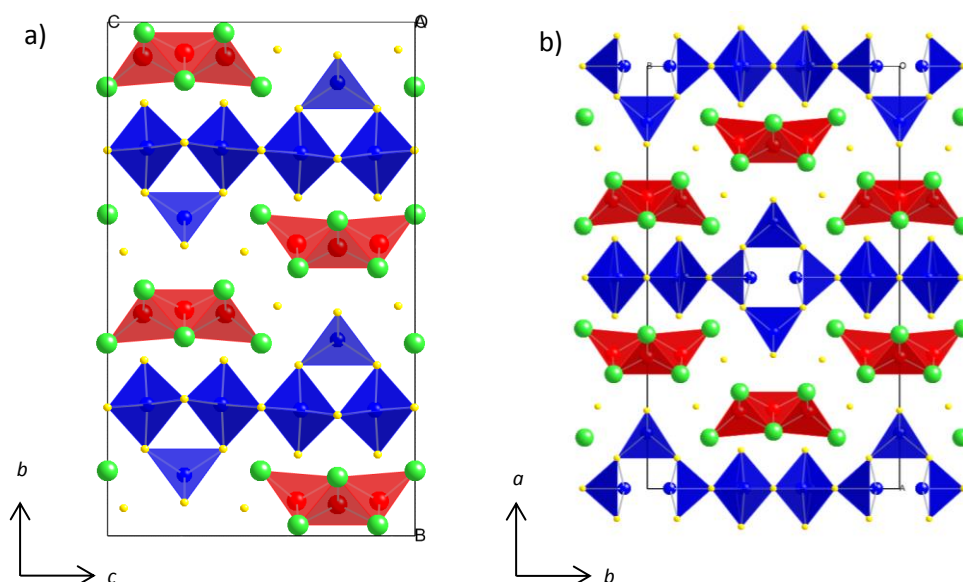
Figure 1.21: *Crystal structures of a) $La_5In_3O_3S_9$ in Pbcm symmetry and b) $La_{10}In_6S_{17}O_6$ in Immm symmetry; La =green, O = red, S = yellow, In = blue.*

1.4 Conclusions and project aims

Whist a range of structure types are adopted by oxychalcogenide systems, this review has tried to highlight the features which are common across a wide range of compositions and structures. A unit common to many ternary and quaternary systems are distorted A_4O tetrahedra. These tetrahedra often share edges to create 1D ribbons or 2D layers and systems of reverence to the work presented in later chapters have been chosen to highlight these units. The aim of the project described in this thesis was to prepare new oxychalcogenide materials, and to measure and control their electronic and magnetic properties. The long-term goal is to relate the crystal structures of these compounds to their physical properties, so that ultimately we may be able to understand how to design better materials for applications. Chapter 3 will build upon the ZrCuSiAs structure of LaOCuS and will investigate related oxychaogenides with the general formula A_2O_2MSe$_2$ where A is a lanthanide ion and M is a divalent transition metal. Chapter 4 explores the structure and physical properties of materials with A_4O_4TiSe$_4$ composition, which crystallise with a structure containing 1D ribbons of fluorite-like units linked by 1D chains of octahedrally coordinated transition metal. In Chapter 5 the structural properties of the ternary series with A_4O_4Se$_3$ composition will be discussed with decreasing A^{3+} ionic radii. Three new structures which we define as β, γ and δ-A_4O_4Se$_3$ are presented which are all structurally related to the α-A_4O_4Se$_3$ structure discussed in section 1.2.1. The structural properties of materials with the La$_2$O$_2$Se$_2$Fe$_2$O structure will be discussed in Chapter 6. The structures of several members of the series will be studied using low temperature single crystal X-ray diffraction. Chapter 7 presents the structure solution of LaInS$_2$O from powder data. Chapters 2 and 8 contain technical details.

References

1. Nakai, I., Koto, K., Nagashima, K., and Morimoto, N., *Chemistry Letters*, 1977, 275-276
2. Nakai, I., Nagashima, K., Koto, K., and Morimoto, N., *Acta Crystallographica Section B-Structural Science*, 1978, **34**, 3569-3572
3. Sabelli, C., Nakai, I., and Katsura, S., *American Mineralogist*, 1988, **73**, 398-404
4. Kamihara, Y., Watanabe, T., Hirano, M., and Hosono, H., *Journal of the American Chemical Society*, 2008, **130**, 3296-3297
5. Ren, Z. A., Lu, W., Yang, J., Yi, W., Shen, X. L., Li, Z. C., Che, G. C., Dong, X. L., Sun, L. L., Zhou, F., and Zhao, Z. X., *Chinese Physics Letters*, 2008, **25**, 2215-2216
6. Clarke, S. J., Adamson, P., Herkelrath, S. J. C., Rutt, O. J., Parker, D. R., Pitcher, M. J., and Smura, C. F., *Inorganic Chemistry*, 2008, **47**, 8473-8486
7. Zachariasen, W. H., *Acta Crystallographica*, 1949, **2**, 60-62
8. Eick, H. A., *Journal of the American Chemical Society*, 1958, **80**, 43-44
9. Eick, H. A., *Acta Crystallographica*, 1960, **13**, 161-161
10. Ballestr.R, *Comptes Rendus Hebdomadaires Des Seances De L Academie Des Sciences Serie B*, 1967, **264**, 1736-1738
11. Benz, R., *Acta Crystallographica Section B-Structural Crystallography and Crystal Chemistry*, 1971, **B 27**, 853-855
12. Weber, F. A. and Schleid, T., *Zeitschrift Fur Anorganische Und Allgemeine Chemie*, 1999, **625**, 1833-1838
13. Raccah, P. M., Longo, J. M., and Eick, H. A., *Inorganic Chemistry*, 1967, **6**, 1471-1473
14. Dugue, J., Adolphe, C., and Khodadad, P., *Acta Crystallographica Section B-Structural Crystallography and Crystal Chemistry*, 1970, **B 26**, 1627-1628
15. Strobel, S., Choudhury, A., Dorhout, P. K., Lipp, C., and Schleid, T., *Inorganic Chemistry*, 2008, **47**, 4936-4944
16. Weber, F. A. and Schleid, T., *Zeitschrift Fur Anorganische Und Allgemeine Chemie*, 2001, **627**, 1383-1388
17. Shannon, R. D., *Acta Crystallographica Section A*, 1976, **32**, 751-767
18. Gu, J., Zhao, Z.-Q., Ding, Y., Chen, H.-L., Zhang, Y.-W., and Yan, C.-H., *Journal of the American Chemical Society*, 2013, **135**, 8363-8371
19. Wichelhaus, W., *Angewandte Chemie-International Edition*, 1978, **17**, 451-452
20. Mizuguchi, Y., Fujihisa, H., Gotoh, Y., Suzuki, K., Usui, H., Kuroki, K., Demura, S., Takano, Y., Izawa, H., and Miura, O., *Physical Review B*, 2012, **86**, 220510
21. Tan, S. G., Li, L. J., Liu, Y., Tong, P., Zhao, B. C., Lu, W. J., and Sun, Y. P., *Physica C-Superconductivity and Its Applications*, 2012, **483**, 94-96
22. Singh, S. K., Kumar, A., Gahtori, B., Shruti, Sharma, G., Patnaik, S., and Awana, V. P. S., *Journal of the American Chemical Society*, 2012, **134**, 16504-16507
23. Takatsu, H., Mizuguchi, Y., Izawa, H., Miura, O., and Kadowaki, H., *Journal of the Physical Society of Japan*, 2012, **81**, 125002
24. Tan, S. G., Tong, P., Liu, Y., Lu, W. J., Li, L. J., Zhao, B. C., and Sun, Y. P., *European Physical Journal B*, 2012, **85**, 414-417
25. Phelan, W. A., Wallace, D. C., Arpino, K. E., Neilson, J. R., Livi, K. J., Seabourne, C. R., Scott, A. J., and McQueen, T. M., *Journal of the American Chemical Society*, 2013, **135**, 5372-5374
26. Sathish, C. I., Feng, H. L., Shi, Y. G., and Yamaura, K., *Journal of the Physical Society of Japan*, 2013, **82**, 074703
27. Shruti, Srivastava, P., and Patnaik, S., *Journal of Physics-Condensed Matter*, 2013, **25**, 312202
28. Wu, L.-B. and Huang, F.-Q., *Zeitschrift Fur Kristallographie-New Crystal Structures*, 2007, **222**, 175-176
29. Weber, F. A., Schurz, M. C., Frunder, S., Kuhn, C. F., and Schleid, T., *Crystals*, 2012, **2**, 1136-1145

30. Tougait, O. and Ibers, J. A., *Acta Crystallographica Section C-Crystal Structure Communications*, 2000, **56**, 623-624

31. Zachariasen, W. H., *Acta Crystallographica*, 1949, **2**, 291-296

32. Deye, R. W. M., Sellman, P. G., and Murray, J. R., *Journal of the Chemical Society*, 1952, 10.1039/jr95200025552555-2555

33. Ferro, R., *Zeitschrift Fur Anorganische Und Allgemeine Chemie*, 1954, **275**, 320-326

34. Jin, G. B., Raw, A. D., Skanthakumar, S., Haire, R. G., Soderholm, L., and Ibers, J. A., *Journal of Solid State Chemistry*, 2010, **183**, 547-550

35. Deye, R. W. M. and Sellman, P. G., *Journal of the Chemical Society*, 1954, 10.1039/jr95400037603760-3766

36. Haneveld, A. J. K. and Jellinek, F., *Journal of Inorganic & Nuclear Chemistry*, 1964, **26**, 1127-1128

37. Julienpouzol, M., Jaulmes, S., Guittard, M., and Laruelle, P., *Journal of Solid State Chemistry*, 1978, **26**, 185-188

38. Stocks, K., Eulenberger, G., and Hahn, H., *Zeitschrift Fur Anorganische Und Allgemeine Chemie*, 1980, **463**, 105-109

39. McCullough, J. D., Brewer, L., and Bromley, L. A., *Acta Crystallographica*, 1948, **1**, 287-289

40. Chan, G. H., Deng, B., Bertoni, M., Ireland, J. R., Hersam, M. C., Mason, T. O., Van Duyne, R. P., and Ibers, J. A., *Inorganic Chemistry*, 2006, **45**, 8264-8272

41. Charkin, D. O., Akopyan, A. V., and Dolgikh, V. A., *Russian Journal of Inorganic Chemistry*, 1999, **44**, 833-837

42. Liu, M. L., Wu, L. B., Huang, F. Q., Chen, L. D., and Ibers, J. A., *Journal of Solid State Chemistry*, 2007, **180**, 62-69

43. Hiramatsu, H., Yanagi, H., Kamiya, T., Ueda, K., Hirano, M., and Hosono, H., *Chemistry of Materials*, 2008, **20**, 326-334

44. Ohtani, T., Hirose, M., Sato, T., Nagaoka, K., and Iwabe, M., *Japanese Journal of Applied Physics Part 1-Regular Papers Short Notes & Review Papers*, 1993, **32**, 316-318

45. Ueda, K., Takafuji, K., and Hosono, H., *Journal of Solid State Chemistry*, 2003, **170**, 182-187

46. Kusainova, A. M., Berdonosov, P. S., Akselrud, L. G., Kholodkovskaya, L. N., Dolgikh, V. A., and Popovkin, B. A., *Journal of Solid State Chemistry*, 1994, **112**, 189-191

47. Pitcher, M. J., Smura, C. F., and Clarke, S. J., *Inorganic Chemistry*, 2009, **48**, 9054-9056

48. Pottgen, R. and Johrendt, D., *Zeitschrift Fur Naturforschung Section B-a Journal of Chemical Sciences*, 2008, **63**, 1135-1148

49. Kamioka, H., Hiramatsu, H., Hirano, M., Ueda, K., Kamiya, T., and Hosono, H., *Excitonic properties related to valence band levels split by spin-orbit interaction in layered oxychalcogenide LaCuOCh(Ch = S,Se)*. in *6th International Conference on Excitonic Processes in Condensed Matter (EXCON 04)*. 2004. Cracow, POLAND: Elsevier Science Bv.

50. Kamiya, T., Ueda, K., Hiramatsu, H., Kamioka, H., Ohta, H., Hirano, M., and Hosono, H., *Thin Solid Films*, 2005, **486**, 98-103

51. Ramasubramanian, S., Rajagopalan, M., Kumar, J., and Thangavel, R., *Journal of Applied Physics*, 2009, **106**, 023720

52. Ueda, K., Hiramatsu, H., Ohta, H., Hirano, M., Kamiya, T., and Hosono, H., *Physical Review B*, 2004, **69**, 155305

53. Ueda, K. and Hosono, H., *Journal of Applied Physics*, 2002, **91**, 4768-4770

54. Allred, A. L., *Journal of Inorganic & Nuclear Chemistry*, 1961, **17**, 215-221

55. Llanos, J. and Pena, O., *Journal of Solid State Chemistry*, 2005, **178**, 957-960

56. Hiramatsu, H., Kamioka, H., Ueda, K., Hirano, M., and Hosono, H., *Journal of the Ceramic Society of Japan*, 2005, **113**, 10-16

57. Hiramatsu, H., Kamioka, H., Ueda, K., Ohta, H., Kamiya, T., Hirano, M., and Hosono, H., *Physica Status Solidi a-Applications and Materials Science*, 2006, **203**, 2800-2811

58. Wilmer, D., Jorgensen, J. D., and Wuensch, B. J., *Solid State Ionics*, 2000, **136**, 961-966
59. Palazzi, M., Carcaly, C., and Flahaut, J., *Journal of Solid State Chemistry*, 1980, **35**, 150-155
60. Palazzi, M. and Jaulmes, S., *Acta Crystallographica Section B-Structural Science*, 1981, **37**, 1337-1339
61. Llanos, J., Cortes, R., Guizouarn, T., and Pena, O., *Materials Research Bulletin*, 2006, **41**, 1266-1271
62. Llanos, J., Cortes, R., and Sanchez, V., *Materials Research Bulletin*, 2008, **43**, 320-325
63. Nakao, H., Takano, Y., Takase, K., Sato, K., Hara, S., Ikeda, S., Takahashi, Y., and Sekizawa, K., *Journal of Alloys and Compounds*, 2006, **408**, 104-106
64. Ijjaali, I., Mitchell, K., Haynes, C. L., McFarland, A. D., Van Duyne, R. P., and Ibers, J. A., *Journal of Solid State Chemistry*, 2003, **176**, 170-174
65. Hiramatsu, H., Ueda, K., Kamiya, T., Ohta, H., Hirano, M., and Hosono, H., *Journal of Materials Chemistry*, 2004, **14**, 2946-2950
66. McCabe, E. E., Free, D. G., and Evans, J. S. O., *Chemical Communications*, 2011, **47**, 1261-1263
67. Hiramatsu, H., Ueda, K., Kamiya, T., Ohta, H., Hirano, M., and Hosono, H., *Journal of Physical Chemistry B*, 2004, **108**, 17344-17351
68. Chan, G. H., Liu, M. L., Chen, L. D., Huang, F. Q., Bugaris, D. E., Wells, D. M., Ireland, J. R., Hersam, M. C., Van Duyne, R. P., and Ibers, J. A., *Inorganic Chemistry*, 2008, **47**, 4368-4374
69. Dugue, J. and Guittard, M., *Acta Crystallographica Section B-Structural Science*, 1982, **38**, 2368-2371
70. Broadley, S., Gal, Z. A., Cora, F., Smura, C. F., and Clarke, S. J., *Inorganic Chemistry*, 2005, **44**, 9092-9096
71. Duan, C. J., Delsing, A. C. A., and Hintzen, H. T., *Chemistry of Materials*, 2009, **21**, 1010-1016
72. Xia, Y. J., Huang, F. Q., Wang, W. D., Wang, A. B., and Shi, J. L., *Solid State Sciences*, 2007, **9**, 1074-1078
73. Xia, Y. J., Huang, F. Q., Wang, W. D., Wang, Y. M., Yuan, K. D., Liu, M. L., and Shi, J. L., *Optical Materials*, 2008, **31**, 311-314
74. Sambrook, T., Smura, C. F., Clarke, S. J., Ok, K. M., and Halasyamani, P. S., *Inorganic Chemistry*, 2007, **46**, 2571-2574
75. Mayer, J. M., Schneemeyer, L. F., Siegrist, T., Waszczak, J. V., and Vandover, B., *Angewandte Chemie-International Edition in English*, 1992, **31**, 1645-1647
76. Fuwa, Y., Wakeshima, M., and Hinatsu, Y., *Journal of physics. Condensed matter : an Institute of Physics journal*, 2010, **22**, 346003
77. Fuwa, Y., Wakeshima, M., and Hinatsu, Y., *Solid State Communications*, 2010, **150**, 1698-1701
78. Ni, N., Climent-Pascual, E., Jia, S., Huang, Q., and Cava, R. J., *Physical Review B*, 2010, **82**, 214419
79. Free, D. G., Withers, N. D., Hickey, P. J., and Evans, J. S. O., *Chemistry of Materials*, 2011, **23**, 1625-1635
80. Fuwa, Y., Wakeshima, M., and Hinatsu, Y., *Journal of Physics-Condensed Matter*, 2010, **22**, 346003
81. Wang, C., Tan, M. Q., Feng, C. M., Ma, Z. F., Jiang, S. A., Xu, Z. A., Cao, G. H., Matsubayashi, K., and Uwatoko, Y., *Journal of the American Chemical Society*, 2010, **132**, 7069-7073
82. Free, D. G. and Evans, J. S. O., *Physical Review B*, 2010, 214433
83. Zhu, J.-X., Yu, R., Wang, H., Zhao, L. L., Jones, M. D., Dai, J., Abrahams, E., Morosan, E., Fang, M., and Si, Q., *Physical review letters*, 2010, **104**, 216405
84. Wu, H., *Physical Review B*, 2010, **82**, 4

85.   Ni, N., Jia, S., Huang, Q., Climent-Pascual, E., and Cava, R. J., *Physical Review B*, 2011, **83**, 224403

86.   SO Evans, J., *Submitted for publication*, 2013

87.   Fuwa, Y., Endo, T., Wakeshima, M., Hinatsu, Y., and Ohoyama, K., *Journal of the American Chemical Society*, 2010, **132**, 18020-18022

88.   Park, Y. B., Degroot, D. C., Schindler, J. L., Kannewurf, C. R., and Kanatzidis, M. G., *Chemistry of Materials*, 1993, **5**, 8-10

89.   Meerschaut, A., Lafond, A., Meignen, V., and Deudon, C., *Journal of Solid State Chemistry*, 2001, **162**, 182-187

90.   Meignen, V., Lafond, A., Cario, L., Deudon, C., and Meerschaut, A., *Acta Crystallographica Section C-Crystal Structure Communications*, 2003, **59**, I63-I64

91.   Vovan, T., Dugue, J., and Guittard, M., *Comptes Rendus De L Academie Des Sciences Serie Ii*, 1981, **292**, 957-959

92.   Meerschaut, A., Lafond, A., Palvadeau, P., Deudon, C., and Cario, L., *Materials Research Bulletin*, 2002, **37**, 1895-1905

93.   Dugue, J., Vovan, T., and Laruelle, P., *Acta Crystallographica Section C-Crystal Structure Communications*, 1985, **41**, 1146-1148

94.   Tougait, O. and Ibers, J. A., *Journal of Solid State Chemistry*, 2000, **154**, 564-568

95.   Dugue, J., Vovan, T., and Villers, J., *Acta Crystallographica Section B-Structural Science*, 1980, **36**, 1291-1294

96.   Wintenberger, M., Dugue, J., Guittard, M., Dung, N. H., and Tien, V. V., *Journal of Solid State Chemistry*, 1987, **70**, 295-302

97.   Dugue, J., Vovan, T., and Villers, J., *Acta Crystallographica Section B-Structural Science*, 1980, **36**, 1294-1297

98.   Van, T. V. and Huy, D. N., *Comptes Rendus De L Academie Des Sciences Serie Ii*, 1981, **293**, 933-936

99.   Wintenberger, M., Tien, V., Guittard, M., and Dugue, J., *Journal of Solid State Chemistry*, 1989, **79**, 285-287

100.   Ijjaali, I., Deng, B., and Ibers, J. A., *Journal of Solid State Chemistry*, 2005, **178**, 1503-1507

101.   McCabe, E. E., Free, D. G., Mendis, B. G., Higgins, J. S., and Evans, J. S. O., *Chemistry of Materials*, 2010, **22**, 6171-6182

102.   Free, D. G., Herkelrath, S. J. C., and Clarke, S. J., *Zeitschrift Fur Anorganische Und Allgemeine Chemie*, 2012, **638**, 2532-2537

103.   Kabbour, H., Cario, L., Moelo, Y., and Meerschaut, A., *Journal of Solid State Chemistry*, 2004, **177**, 1053-1059

104.   Gastaldi, L., Carre, D., and Pardo, M. P., *Acta Crystallographica Section B-Structural Science*, 1982, **38**, 2365-2367

105.   Ogisu, K., Ishikawa, A., Teramura, K., Toda, K., Hara, M., and Domen, K., *Chemistry Letters*, 2007, **36**, 854-855

Chapter 2: Synthetic Methods and Analytical Techniques

2.1 Introduction

This chapter will discuss the methods and techniques used in the synthesis and analysis of the materials reported in this thesis. The structures of polycrystalline materials were studied using powder X-ray diffraction and in some cases neutron powder diffraction and transmission electron diffraction. Materials which could be prepared as single crystals were studied using single crystal X-ray diffraction. Magnetic properties were investigated via SQUID magnetometry, and electronic properties using a 4-probe conductivity method.

2.2 Experimental details

The synthetic work undertaken can be broken down into two categories: preparation of starting materials and the synthesis of the target phases. A List of all reagents used in this project is given in table 2.1.

Table 2.1: Table of reagents used during synthetic work.

	Compound	Supplier	Purity
	La_2O_3	Alfa Aesar	99.99 %
	CeO_2	Alfa Aesar	99.99 %
	Pr_6O_{11}	Alfa Aesar	99.99 %
	Nd_2O_3	Electronic materials	99 %
	Sm_2O_3	Alfa Aesar	99.99 %
	Eu_2O_3	Alfa Aesar	99.99 %
A_xO_y	Gd_2O_3	Alfa Aesar	99.99 %
	Tb_4O_7	Alfa Aesar	99.9 %
	Dy_2O_3	Sigma-Aldrich	99.9 %
	Ho_2O_3	Alfa Aesar	99.9 %
	Er_2O_3	Sigma-Aldrich	99.9 %
	Yb_2O_3	Sigma-Aldrich	99.9 %
	Y_2O_3	Sigma-Aldrich	99.99 %
	Ti	BDH	Unknown
	Mn	Avocado	99 %
M	Fe	Sigma-Aldrich	99.9 %
	Zn	Alfa Aesar	99.9 %
	In	Alfa Aesar	99.99 %
Q	S	Sigma-Aldrich	99.98 %
	Se	Alfa-Aesar	99.999 %

2.2.1 Preparation of A_xO_y starting reagents

Apart from Pr_2O_3 and Tb_2O_3 all other A_2O_3 reagents (A = La, Nd, Sm, Eu, Gd, Dy, Ho, Er, Yb, and Y) were treated in the same way prior to use: the supplied powder was heated to ~1000 ˚C in an alumina crucible to remove any absorbed H_2O or CO_2, then cooled to room temperature. Samples were then either used immediately or stored in a nitrogen filled glovebox. A small amount of material was analysed by XRPD to confirm purity. CeO_2 was prepared by an identical method. Pr_2O_3 and Tb_2O_3 were prepared by reducing Pr_6O_{11} and Tb_4O_7 respectively in a tube furnace under a stream of 5% hydrogen in 95% nitrogen gas at 1000 ˚C for 12 hours, before cooling to room temperature and storing in an inert atmosphere. All these A_2O_3 samples were stable in air for a few hours therefore these materials were used on the bench.

2.2.2 Synthesis of $TiSe_2$ starting reagent

$TiSe_2$ was prepared by heating Ti (0.1163 g) and Se (0.3837 g) powders together in a sealed and evacuated quartz ampoule at 800 °C for 120 hours, before being allowed to cool to room temperature, the material was then reground and stored in a sample vial. A small amount of material was kept for analysis by XRPD to confirm purity.

2.2.3 Synthesis of $La_2O_2ZnSe_2$

Stoichiometric amounts of La_2O_3, Zn and Se powders were weighed out to within ±0.0001g (masses given in table 2.2) and ground together using an agate pestle and mortar before placing in a 7 mm diameter high density alumina crucible. The crucible was placed inside an 11 mm (inner diameter) quartz tube along with a crucible containing an aluminium getter to remove excess oxygen (forming Al_2O_3 during the reaction). A 10% stoichiometric molar excess of Al was typically used as this gave higher purity products. The experimental setup is shown in figure 2.1. The quartz tube was evacuated for ~15 min at ~0.1 mbar and flame sealed before heating in a muffle furnace under the following heat conditions: ramp at 5 °C min^{-1} to 600 °C and dwell for 12 hours, ramp at 0.5 °C min^{-1} to 800 °C and dwell for 1 hour, ramp at 1 °C min^{-1} to 1000 °C and dwell for 12 hours before cooling to room temperature in the furnace. The ampoules were removed from the furnace at room temperature and broken open using a hammer, and the contents of the crucibles reground, the resulting white powder was analysed using XRPD.[1]
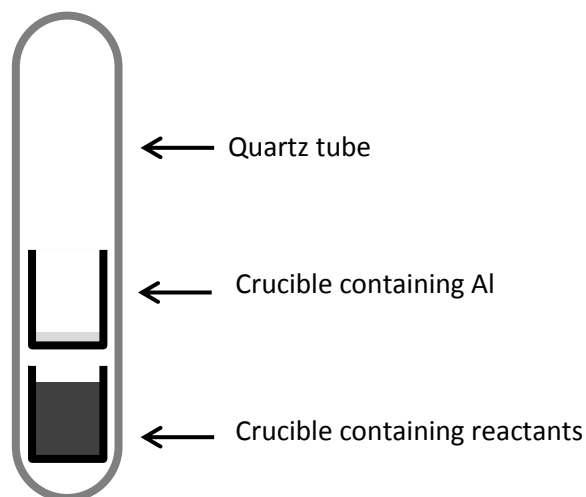
Figure 2.1: *Arrangement of experimental setup for reactions involving Al getter.*

The equation for this reaction is given by:

$$La_2O_3 + Zn + 2Se + \tfrac{2}{3}Al \rightarrow La_2O_2ZnSe_2 + \tfrac{1}{3}Al_2O_3 \qquad Eqn\ 2.1$$
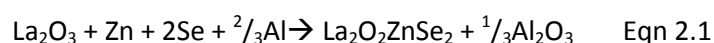
A variety of closely related compositions were also synthesised to help assess phase purity with an identical synthetic method to the stoichiometric samples; the exact masses used are given in table 2.2.

Table 2.2: *Table of compositions, masses and moles used for stoichiometric and non-stoichiometric compositions closely related to La$_2$O$_2$ZnSe$_2$.*

Composition	La$_2$O$_3$ / g	La$_2$O$_3$ / mmol	Zn / g	Zn / mmol	Se / g	Se / mmol	Al / g	Al / mmol
La$_2$O$_2$ZnSe$_2$	0.3056	0.9379	0.0613	0.9376	0.1481	1.8756	0.0186	0.6894
La$_{2.2}$O$_2$ZnSe$_2$	0.3195	0.9806	0.0583	0.8916	0.1408	0.8487	0.0229	0.8487
La$_2$O$_{2.2}$ZnSe$_2$	0.3037	0.9321	0.0610	0.9319	0.1472	0.5485	0.0148	0.5485
La$_2$O$_2$Zn$_{1.2}$Se$_2$	0.2983	0.9156	0.0718	1.9800	0.1446	0.6708	0.0181	0.6708
La$_2$O$_2$ZnSe$_{2.2}$	0.2968	0.9110	0.0596	0.9115	0.1582	0.6671	0.0180	0.6671

A larger sample of La$_2$O$_2$ZnSe$_2$, ~4g, was synthesised for powder neutron diffraction. La$_2$O$_3$ (2.6343 g, 8.0854 mmol), Zn (0.5287 g, 8.0853 mmol) and Se (1.2769 g, 16.1314 mmol) were ground together using a agate mortar and pestle, and placed in four 7 mm high density alumina crucibles. 0.1600 g of Al powder was placed in two 7 mm crucibles, and all 6 crucibles sealed inside an evacuated quartz ampoule. The same heat cycle was applied as used for the smaller sample. Rietveld analysis of a XRPD pattern showed an approximately 5 % weight present impurity of La$_2$O$_2$Se. The sample was reground and placed back in the furnace in a

sealed tube with the following heat cycle: ramp at 5 °C min^{-1} to 600 °C and dwell for 12 hours, ramp at 0.5 °C min^{-1} to 800 °C and dwell for 1 hour, ramp at 1 °C min^{-1} to 1100 °C and dwell for 24 hours then cool to room temperature. Analysis of the XRPD pattern showed an essentially pure phase had been obtained.

Single crystals of La$_2$O$_2$ZnSe$_2$ were grown from a polycrystalline sample prepared as above. Approximately 0.2 g of polycrystalline La$_2$O$_2$ZnSe$_2$ was placed in an alumina crucible inside a sealed quartz ampoule evacuated to 0.1 mbar then filled with 10 mbar of argon. The sealed ampoule was placed in muffle furnace and the following heat cycle applied: Ramp to 1300 ˚C at 5 ˚C min^{-1} and dwell for 10 hours, cool to 800 ˚C at 0.12 ˚C min^{-1}, cool to room temperature by switching off the furnace. Single crystals were identified at the bottom of the crucible. Clear and colourless plates ≈ 0.08 mm x 0.08 mm x 0.008 mm were formed.

2.2.4 Synthesis of $A_4O_4TiSe_4$ (A = Sm, Gd, Tb, Dy, Ho, Er and Y)

A_2O_3, TiSe$_2$ and Se powders were weighed according to the masses given in Table 2.3, and thoroughly ground together using an agate pestle and mortar, and placed in a quartz tube along with the Al getter using the method described in section 2.2.3. The quartz tube was evacuated for ~15 min at ~ 10^{-4} mbar and flame sealed before placing a muffle furnace with the following heat cycle: ramp at 5 °C min^{-1} to 600 °C and dwell for 12 hours, ramp at 0.5 °C min^{-1} to 800 °C and dwell for 1 hour, ramp at 1 °C min^{-1} to 900 °C and dwell for 3 days then cool to room temperature in the furnace. The sealed tube was then broken open with a hammer, and the resulting product reground and analysed using XRPD.

The equation for this reaction is given by:

$$2A_2O_3 + TiSe_2 + 2Se + {}^4/_3Al \rightarrow A_4O_4TiSe_4 + {}^2/_3Al_2O_3 \qquad \text{Eqn 2.2}$$

Table 2.3: *Reagent masses and moles used in synthesis of $A_4O_4TiSe_4$.*

Composition	A_2O_3 / g	A_2O_3 / mmol	TiSe$_2$ / g	TiSe$_2$ / mmol	Se / g	Se / mmol	Al / g	Al / mmol
Sm$_4$O$_4$TiSe$_4$	0.3388	0.9716	0.1000	0.4859	0.0767	0.9714	0.0192	0.7116
Gd$_4$O$_4$TiSe$_4$	0.3430	0.9462	0.0974	0.4733	0.0747	0.9460	0.0187	0.6931
Tb$_4$O$_4$TiSe$_4$	0.3440	0.9403	0.0968	0.4704	0.0743	0.9410	0.0186	0.6894
Dy$_4$O$_4$TiSe$_4$	0.3461	0.9279	0.0955	0.4641	0.0733	0.9283	0.0184	0.6819
Ho$_4$O$_4$TiSe$_4$	0.3475	0.9197	0.0946	0.4597	0.0726	0.9195	0.0182	0.6745
Er$_4$O$_4$TiSe$_4$	0.3488	0.9118	0.0938	0.4558	0.0720	0.9119	0.0180	0.6671
Y$_4$O$_4$TiSe$_4$	0.2883	1.2767	0.1314	0.6385	0.1008	1.2766	0.0253	0.9377

2.2.5 Synthesis of $A_4O_4Se_3$ (A = Nd, Sm-Er, Yb, Y)

$A_4O_4Se_3$ (A = Nd, Sm-Er, Yb and Y) materials were synthesised from stoichiometric amounts of A_2O_3 and Q powders. The reagents were weighed out to within ±0.0001 g (table 2.4) and ground together using an agate pestle and mortar, and placed in a quartz tube along with an Al getter using the method described in section 2.2.3. The tube was then evacuated for ~15 min at 0.01 mbar before flame sealing. The sealed tubes were placed in a muffle furnace, with the following heat cycle: Ramp at 5 °C min^{-1} to 600 °C and dwell for 12 hours, ramp at 0.5 °C min^{-1} to 800 °C and dwell for 1 hour, ramp at 1 °C min^{-1} to X °C and dwell for Y hours then cool to room temperature in the furnace. Values of X between 900 °C and 950 °C and Y between 12 and 72 hours were used depending on the sample (table 2.4). Compositions $A_4O_4Se_3$ (A = La-Nd, Sm) have previously been reported via solid state methods and single crystals obtained from CsI fluxes after prior reaction of the corresponding rare-earth metal, Se and SeO$_2$ at 750 °C for 168 hours.[2]

For the Eu$_4$O$_4$Se$_3$ composition it was also possible to grow single crystals. 0.2 g of polycrystalline Eu$_4$O$_4$Se$_3$ was placed in an alumina crucible along with 0.1143 g of CsI to act as a flux. The crucible was then sealed inside an evacuated quartz ampoule and placed in a muffle furnace with the following heat cycle: ramp at 1 °C min^{-1} to 900 °C and dwell for 72 hours, ramp at 0.05 °C min^{-1} to 400 °C, before furnace cooling to room temperature. The tube was broken open using a hammer and the contents washed with water to remove CsI. Plate-like crystals were formed suitable for single crystal X-ray diffraction.

Table 2.4: Reagent masses and synthetic conditions used for A$_4$O$_4$Se$_3$ materials.

Composition	A_2O_3 / g	A_2O_3 / mmol	Se / g	Se / mmol	Al / g	Al / mmol	X / °C	Y / hrs
Nd$_4$O$_4$Se$_3$	0.3833	1.1392	0.1349	1.7085	0.0205	0.7598	900	24
Sm$_4$O$_4$Se$_3$	0.3865	1.1083	0.1313	1.6629	0.0199	0.7375	900	24
Eu$_4$O$_4$Se$_3$	0.3873	1.1005	0.1303	1.6502	0.0198	0.7338	900	72
Gd$_4$O$_4$Se$_3$	0.3898	1.0753	0.1274	1.6135	0.0193	0.7153	900	12
Tb$_4$O$_4$Se$_3$	0.3906	1.0677	0.1265	1.6021	0.0192	0.7116	950	12
Dy$_4$O$_4$Se$_3$	0.3923	1.0517	0.1246	1.5780	0.0189	0.7005	900	12
Ho$_4$O$_4$Se$_3$	0.3934	1.0411	0.1233	1.5616	0.0187	0.6931	900	12
Er$_4$O$_4$Se$_3$	0.3944	1.0311	0.1222	1.5476	0.0185	0.6857	900	24
Yb$_4$O$_4$Se$_3$	0.3968	1.0069	0.1193	1.5109	0.0181	0.6708	950	12
Y$_4$O$_4$Se$_3$	0.3440	1.5234	0.1804	2.2847	0.0274	1.0155	950	12

2.2.6 Synthesis of $A_2O_2Se_2M_2O$ (A = La, Pr, M = Fe, Mn)

Polycrystalline and single crystal samples of $La_2O_2Se_2Fe_2O$, $Pr_2O_2Se_2Fe_2O$, and $La_2O_2Se_2Mn_2O$ were prepared following the methods of Free and Chen.[3, 4] A_2O_3, Se and M powders were weighed out according to the masses give in table 2.5 and thoroughly ground together in an agate pestle and mortar before being pressed into two 5 mm diameter pellets using a pellet press with a force of ~2 tonnes. The pellets were placed inside an 11 mm (internal diameter) quartz tube which was evacuated for ~15 minutes at ~0.1 mbar before flame sealing. The evacuated quartz ampoule was placed in a muffle furnace and heated with the following cycles. $La_2O_2Se_2Fe_2O$: ramp to 1000 ˚C at 2 ˚C min^{-1} dwell for 40 hours, before furnace cooling to room temperature. $La_2O_2Se_2Mn_2O$ and $Pr_2O_2Se_2Fe_2O$: ramp at 5 ˚C min^{-1} to 600 ˚C and dwell for 12 hours, ramp at 0.5 ˚C min^{-1} to 800 ˚C and dwell for 1 hour, ramp at 1 ˚C min^{-1} to 1000 ˚C and dwell for 12 hours, furnace cool to room temperature. The samples were removed at room temperature and the ampoule broken open using a hammer. The pellets were reground after removing surface impurities (presumably from reaction with the quartz) with a scalpel. The samples were analysed by XRPD before being pressed back into two pellets and a second heat cycle applied.

Table 2.5: *Reagent masses and moles used in synthesis of $A_2O_2Se_2M_2O$.*

Composition	A_2O_3 / g	A_2O_3 / mmol	Se / g	Se / mmol	M / g	Fe / mmol
$La_2O_2Se_2Fe_2O$	0.2736	0.8397	0.1326	1.6794	0.0938	1.6794
$La_2O_2Se_2Mn_2O$	0.2744	0.8422	0.1330	1.6844	0.0925	1.6844
$Pr_2O_2Se_2Mn_2O$	0.2759	0.8365	0.1321	1.6730	0.0919	1.6730

Single crystals were grown from the as formed pellets by placing them in an alumina crucible inside a sealed quartz ampoule evacuated to 0.1 mbar then filled with 10 mbar of argon. For $La_2O_2Se_2Fe_2O$ the sample was ramped to 1300 ˚C at 5 ˚C min^{-1} and held for 10 hours, cooled to 1000 °C at 0.12 ˚C min^{-1}, then left to cool to room temperature in the furnace. For $La_2O_2Se_2Mn_2O$ and $Pr_2O_2Se_2Mn_2O$ the sample was ramped to 1250 ˚C at 5 ˚C min^{-1} and held for 10 hours, cooled to 950 ˚C at 0.12 ˚C min^{-1}, then left to cool to room temperature in the furnace. The ampoule was broken open and the pellet carefully removed with tweezers, the pellet was lightly crushed with an agar pestle and mortar, until single crystals were seen under a polarising microscope.

2.2.7 Synthesis of LaInS$_2$O

A synthesis of polycrystalline LaInS$_2$O has previously been reported by Meerschaut *et al.*,[5] from the reaction of La$_2$S$_3$, La$_2$O$_3$ and In$_2$O$_3$ powders in an evacuated silica tube at 800 °C for 12 hours. We adopted a synthetic method involving the use of an Al getter, as this method had proved successful at synthesising other quaternary oxychalcogenides. La$_2$O$_3$ (0.2440 g, 0.7489 mmol), S (0.0960 g, 2.9953 mmol) and In (0.1720 g, 1.4978 mmol) powders were weighed out to within ±0.0001 g, and ground together using a agate pestle and mortar and sealed in an evacuated quartz tube using the method described in section 2.2.3 with 0.0135 g of Al powder as getter. The sealed tube was then heated with the following cycle: ramp at 2 ˚C min^{-1} to 800 ˚C, dwell for 12 hours, cool to room temperature in the furnace. The sealed tube was then broken open with a hammer, and the resulting product reground and analysed using XRPD.

2.3 X-ray diffraction

Diffraction is a powerful tool for the characterisation of crystalline material and gives information about the positions of atoms within, and the dimensions of the unit cell. This section will discuss the theory behind diffraction and the instruments and specific methods used in this work.

2.3.1 Diffraction from commensurate materials

Diffraction is an interference phenomenon caused when waves interact with a suitable grating. The grating causes the waves to act as if they were emanating from a series of point sources, which then interfere with one another. When the waves are in phase and interfere constructively we observe an increase in their amplitude, and conversely if the waves are out of phase we observe a decrease in amplitude. Crystalline materials can be described in terms of a regular 3D periodic array of lattice points, where each point has an identical environment to the next. By associating a motif (e.g. a set of atoms or molecules) with each lattice point one builds up the crystal structure of a material. This leads to the concept of the unit cell, a convenient small block from which the crystal structure can be built up through solely translational displacements. In crystalline materials the resulting periodic arrangement of atoms will act as a diffraction grating if the atoms are separated by a distance comparable to the wavelength of the radiation or particle being scattered. As such crystalline materials diffract neutrons, electrons and X-rays.

Although diffraction occurs due to interference phenomena between atoms which act as point sources of X-rays (or neutrons/electrons) it is often convenient to think of the process in terms of reflections from lattice planes; this is not a strictly physical description but provides a good model. We can label these lattice planes using Miller indices, hkl, which intercept the three unit cell axes at positions a/h, b/k and c/k. This hkl defines a set of lattice planes with a constant distance between them, d_{hkl}. When an integer number (n) of wavelengths of the incident beam equals the path difference ($2d_{hkl}\sin\theta$) of X-rays reflected from adjacent planes, constructive interference occurs and we observe intensity in the diffraction pattern. By convention we can introduce imaginary planes and only consider the case when $n = 1$. This leads to Bragg's law, equation 2.3, which describes the scattering of X-rays by lattice planes within a crystalline material (figure 2.2).

$$\lambda = 2d_{hkl}\sin\theta_{hkl} \qquad\qquad \text{eqn 2.3}$$

Where λ is the wavelength of incident radiation, d_{hkl} is the spacing between the lattice planes and θ_{hkl} is the angle of the incident radiation with respect to the lattice planes.
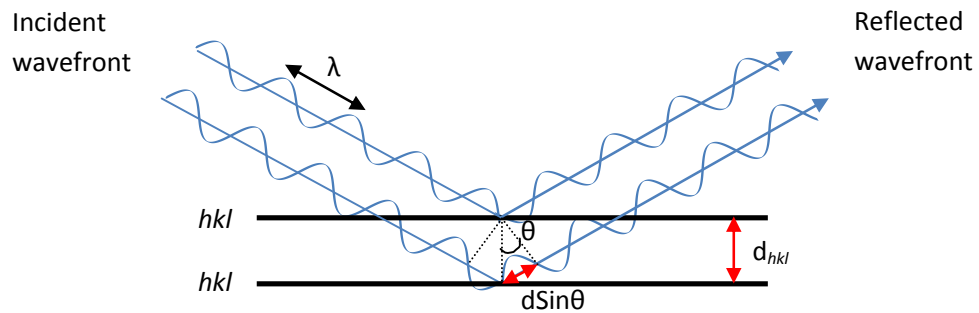
Figure 2.2: A schematic representation of *Bragg's law.*

The intensity of a specific reflection *hkl* is related to the unit cell contents by the structure factor equation (equation 2.4), summed over all atoms in the unit cell. The structure factor relates the fractional coordinates of individual atoms (*xyz*), the indices (*hkl*), and the atomic scattering factors (f_j) to the observed intensities. The intensity of diffraction observed is proportional to the square of the structure factor, modified by other factors (e.g. geometric) which depend on the specific experiment being performed.

$$F_{hkl} = \sum_j f_j exp\left[2\pi i \left(hx_j + ky_j + lz_j\right)\right] \qquad \text{eqn 2.4}$$

2.3.2 Incommensurate materials

The formal definition of a crystal is; "a material is a crystal if it has essentially a sharp diffraction pattern".[6] There are four types of structures with long range order which show sharp diffraction peaks:

-   Structures which contain translational symmetry (described in section 2.3.1)
-   Incommensurately modulated structures
-   Incommensurate composite crystals
-   Quasicrystals

This section will discuss incommensurately modulated structures; composite crystals and quasicrystals will not be discussed further. An incommensurately modulated structure contains electron density (or atomic arrangements) where the function which describes the modulation of distortions from a simple parent structure is a non-integral factor of the lattice periodicity. If we consider an atomic displacement for which the periodicity is equal to 2*a*, as in figure 2.3, we can describe the structure by a unit cell doubled in the *a* direction but still constructed of purely translations. If the periodicity of the modulation is not an integral number of lattice periodicity, as in figure 2.4, then we have an incommensurately modulated structure, but which still contains long range order.
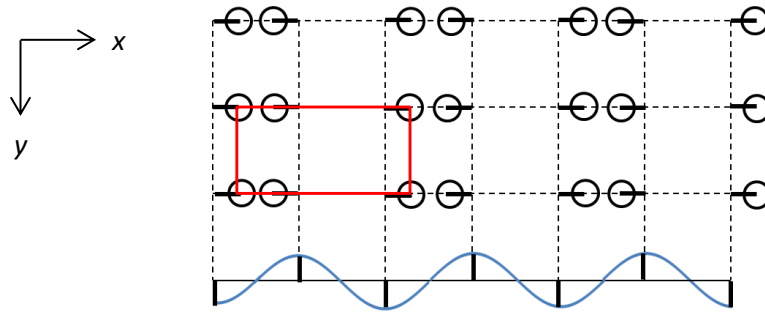
Figure 2.3: *A crystal structure in which atoms are displaced from (0,0) to (x,0) according to the value of a modulation function the modulation has twice the lattice periodicity, and we can describe as a twofold superstructure. Dashed line is the original 2D unit cell, blue line is a displacive modulation wave with a period of double the lattice period, red rectangle is the new unit cell (supercell), circles represent the new atomic positions.*
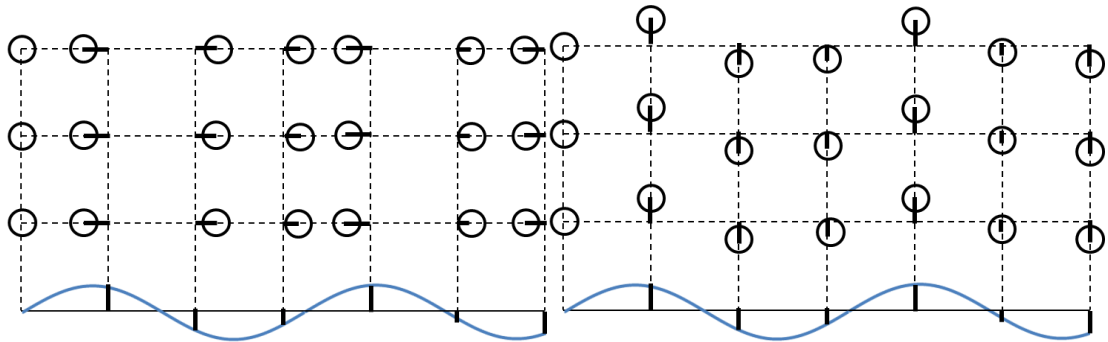
Figure 2.4: *Incommensurately modulated structure with displacive modulation wave length (blue) equal to a non-integer number of lattices periods, resulting in either transverse or longitudinal displacements of atoms from the vertices of the 2D unit cell (dashed lines), circles represent the new atomic positions.*

Incommensurately modulated structures can be described using the concept of superspace, with up to 3 additional dimensions orthogonal to the 3 physical space dimensions. This is represented in figure 2.5 for one dimension in physical space and one in superspace. In figure 2.5 the modulation along *a* is rotated about each basic lattice point so that it is orthogonal to physical space, producing a periodic structure of so called "strings" in superspace. Atomic positions are given by the intersection between these strings and physical space. In this description an atom in superspace is a wave one period in length, which repeats by purely translational displacements within superspace.
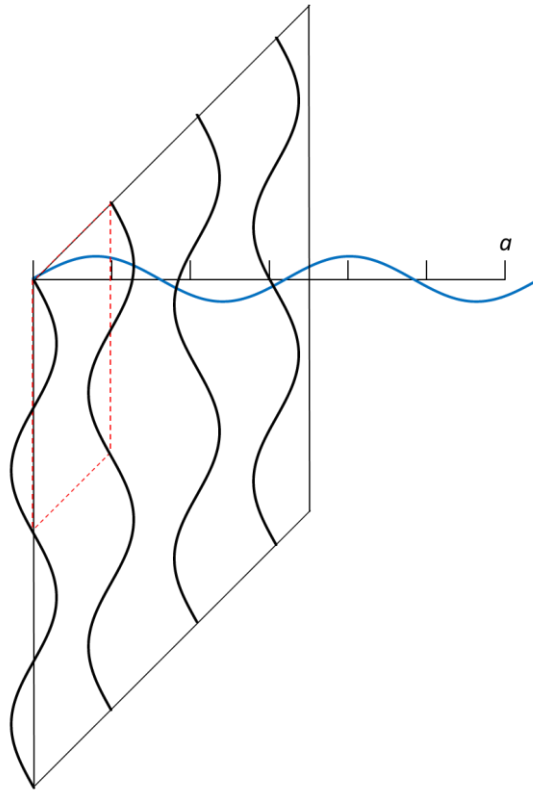
Figure 2.5: *Diagram displaying one physical space dimension (a) horizontally with an orthogonal superspace dimension. An incommensurate modulation wave along a is shown in blue and its corresponding positions in superspace directions in black, basic lattice points are represented by vertical marks, the red dashed box represents the unit which translates within superspace.*

For weakly modulated structures we observe Bragg reflections of the basic structure surrounded in a regular pattern by satellite reflections. These satellite reflections are spaced at distances of ± the index of the modulation (m) × the modulation vector (q). When the amplitude of the modulation is small only low order satellite reflections are often observed. In many crystals with multi-dimensional modulations the modulation wave vectors are not independent and are related by symmetry, but must be included in order to index all Bragg reflections. Therefore a diffraction pattern which requires d modulations to index is described as a d-dimensionally modulated structure and indexing of Bragg reflections requires up to d integers. The letters *hklmnp* are commonly used to describe the indices in physical and superspace.

2.4 Single crystal X-ray diffraction

Single crystal X-ray diffraction is a powerful technique for structure determination of crystalline solids. A single crystal of the material of interest is required so that we see spots of diffracted intensity from a single domain, as opposed to cones observed from powder diffraction. The crystal and detector are rotated to observe each of these reflections. Indices (*hkl)* can be assigned to each reflection which indicate its position within reciprocal space. A schematic diagram of the relationship between single crystal and powder diffraction is shown in figure 2.6.
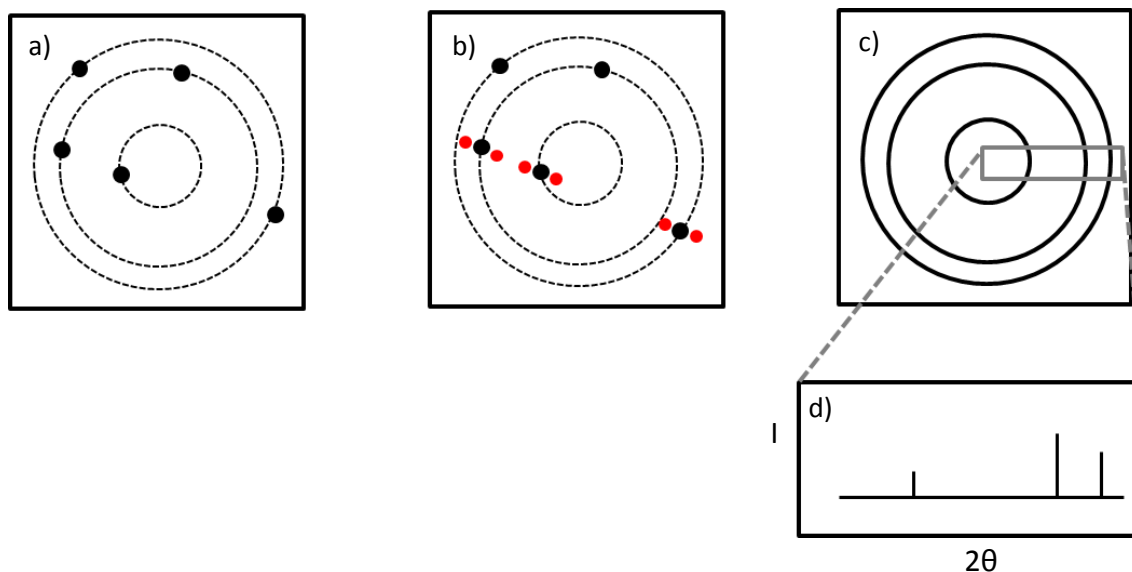
Figure 2.6: *Schematic diagrams of diffraction from a) an orientated single crystal, b) an incommensurately modulated single crystal, with satellite reflections shown in red, c) a polycrystalline material. One dimensional powder pattern (d) obtained by scanning across the cones of diffracted intensity.*

2.4.1 Instruments

Two laboratory based single crystal X-ray diffractometers were routinely used during this project, and were controlled using Bruker's SMART software and used molybdenum radiation.[7] The first was a Bruker SMART-6000 CCD area detector diffractometer (known locally as the "6K") with a sealed tube molybdenum source with graphite monochromator, fitted with an Oxford Cryosystems Nitrogen Cryostream 600, giving an accessible temperature range from 80 to 500 K, with a stated temperature accuracy of 0.1 K. The second was a Bruker SMART-CCD 1K area detector diffractometer (known locally as the "1K") with the same source as the SMART-6000, fitted with an Oxford Cryosystems Nitrogen Cryostream and an Oxford Cryosystems HELIX cooling device, which allows a temperature range of 28-300 K, with a stated temperature accuracy of 0.3 K. The Helix operates by passing bottled helium gas though heat exchangers mounted on a closed cycle helium cooler.

2.4.2 Crystal mounting procedure and selection

The first step in collecting single crystal diffraction data is to select a suitable crystal, typically by visual observation using a polarizing microscope. The crystal is then mounted on a fibre made of glass, composite or hair. For data collections where the temperature was maintained below 200 K for the duration of the experiment the crystals were mounted to the fibre using perfluoropolyether oil. This substance is a liquid at room temperature but freezes below 200 K forming an amorphous glass with no additional Bragg reflections. This method is a non-permanent way of mounting crystals.

For data collections at multiple temperatures or above 200 K crystals were attached to the fibre using a small amount of epoxy resin. It is important to use a small amount of epoxy resin as it can increase the background scattering, and, due to the difference between the thermal expansion of the crystal and the resin, strain can be introduced with large amounts.

The crystal is then mounted on the diffractometer and centred in the X-ray beam so that it rotates without translation during the experiment. Next a few initial diffraction frames are collected to determine an orientation matrix. This also allows determination of the unit cell parameters, assessment of the quality of the diffraction spots, and enables a data collection strategy to be established. Multiple crystals were often screened before a full data collection, to assess the quality of each crystal and to check the crystal was representative of the batch.

2.4.3 Indexing, symmetry determination and integration

The frames collected were harvested for diffraction spots which were then indexed using the Bruker SMART diffractometer software.[7] The frames were then integrated to give a list of intensities and their standard uncertainties. The Saint+ software package was used for the integration step, and an absorption correction was applied to correct for differences in path length through the crystal for each reflection.[8, 9] The SADABS absorption correction used compares the intensities of equivalent reflections and uses this to estimate the absorption anisotropy present in the data.[10] Integration also involves reducing the amount of data present by merging symmetry equivalent reflections along with those measured more than once using the XPrep software within Saint+. Space group symmetry is determined by looking at systematic absences in the indexed reflections. Two output files are generated at this stage, the first of these is a '.*hkl*' file which contains a list of the intensity and its standard uncertainty for each of the independent reflections; the second is a '.ins' file which contains information on experimental details, cell parameters, space group, etc.

2.4.4 Structure solution and least squares refinement

Structure solution involves finding estimates for the phase of each reflection. Two methods of structure solution were used during this work: direct methods and charge flipping.

Direct methods exploits statistical connections between phases of reflections and relies on assumptions such as the scattering density being real and positive throughout the unit cell and arising from discrete isolated ("atom like") objects. Direct methods were implemented using the SIR92 software package interfaced with the Crystals package.[8, 11]

Charge flipping is a *ab initio* structure solution technique which can be applied to both single crystal and powder data without any prior knowledge of unit cell contents or symmetry. The technique was developed by Oszlányi and Süto in 2008.[12] A random set of phases is applied to the measured structure factor amplitudes and a Fourier transform carried out to produce an electron density map. Sites on the density map which are less than a specified value δ, are multiplied by -1 and hence "charged flipped". A Fourier transform of this map is then carried out to produce a set of temporary phases and structure factor amplitudes. These new phases are then combined with the observed amplitudes and the process is repeated. Charge flipping of single crystal data was carried out using Superflip interfaced through either the Crystals or Jana2006 packages.[11, 13, 14]

After the initial structure solution, rounds of Fourier difference maps and least squares refinement were carried out until a low R factor model was achieved, there were minimal fluctuations in the difference electron density map and the model was deemed chemically sensible.

2.5 Powder diffraction

A powder contains a large number of randomly oriented small crystals or crystallites. Therefore we can assume that all possible sample orientations are presented to the incident X-ray beam. Consequently a powder diffraction pattern contains cones of intensity rather than beams which we slice through with a detector, producing a 1D pattern. The pattern is recorded by collecting the intensity present, y_i, at small increments of i, where i is the 2θ angle between the beam and detector. In powder diffraction there is often overlap of reflections in the pattern, thus some structure information is lost. Structure solution from powder diffraction data is not routine, but some of the methods used are described 2.5.8. In powder diffraction patterns the 2θ position of the reflections is related to the geometry and symmetry of the unit cell, the intensity of the reflections is related to the position of atoms within the unit cell, and peak width is influenced by instrumental and microstructural factors.

2.5.1 X-ray powder diffraction instruments

For samples analysed by X-ray powder diffraction, two laboratory based X-ray powder diffractometers were routinely used: a Bruker D8 Advance (colloquially known as the "d9") and a Bruker D8 Advance (colloquially known as the "d7"). Both diffractometers were used to collect rapid data collections for phase identification and to collect high quality data for Rietveld analysis. Powder patterns were given a systematic naming scheme of dx_$nnnnn$ (where x defines the diffractometer used and $nnnnn$ the pattern serial number. Both instruments used CuK$_{\alpha 1,2}$ X-ray sources with operating conditions of 40 kV and 40 mA.

2.5.1.1 Bruker D8 Advance ("d9") and PheniX

 The d9 was used for both routine phase analysis and for high quality data collections and variable temperature experiments in Bragg-Brentano geometry. The X-ray beam passes through a series of slits, including a Soller slit, an antiscatter slit a programmable variable divergent slit. A Lynx-Eye detector is fitted to this instrument, which contains 192 silicon strip detectors allowing it to rapidly collect very high resolution diffraction patterns. A Ni filter is used to remove CuK$_{\beta}$ from the X-ray beam and the system was controlled using "Bruker AXS: XRD commander" software.[15]

The "d9" was equipped with an Oxford Cryosystems PheniX CCR cryostat to carry out variable temperature (VT) experiments between 310 and 12 K. It is controlled independently of the diffractometer control software using 'CryoPad' software.[16] As there is no direct link between the PheniX and the diffractometer control software, data were collected while the temperature was slowly ramped, therefore each diffraction pattern represents a small temperature range. The sample temperature was logged every 30 seconds, allowing the average temperature for each scan to be extracted using the local program 'phenixlogfile'.[17]

The PheniX uses a liquid helium CCR compressor system to cool the base of the sample holder, which is surrounded by an inner heat shield and a vacuum to reduce heat transfer to the sample. The use of the PheniX cryostat leads to two broad low intensity peaks at low angle which were typically modelled as two extra pseudo-Voigt peaks in the Rietveld refinement.

2.5.1.2 Bruker D8 advance ("d7") and Cryostream

The d7 advance was also used for routine phase analysis and high quality data collections at room temperature in Bragg-Brentano geometry. In this geometry the optics were identical to those described in section 2.6.1.1. Experiments were also carried out in Debye-Scherrer transmission geometry where the primary optics consists of a Goebel mirror and fixed incident slit and a series of Soller slits. The diffracted beam goes through a Soller slit before being detected by a Lynx-Eye detector. The system was controlled using "Bruker AXS: DIFFAC.SUITE" software.[18]

Temperature control in Debye-Scherrer geometry was achieved through a newly installed Oxford Cryrosystems 'Cryostream plus' nitrogen flow cooling system, between 80 and 500 K. The cryostream is controlled independently of the diffractometer control software using 'CryoPad' software.[16] Data were again collected while the temperature was slowly ramped, such that each diffraction pattern represents a small temperature range. The Cryostream uses a 60 L liquid nitrogen delwar which can be top up during the experiment. Information on the temperature calibration of the system is reported in Chapter 8.

2.5.2 Sample preparation

Slides for reflection measurements were prepared by grinding the sample into a fine powder using a pestle and mortar. The powder was passed through a sieve (100 or 120 mesh) onto a silicon slide lightly covered with Vaseline® to act as an adhesive. These slides were made of a single crystal of silicon cut parallel to the (511) crystallographic plane so that no diffracted intensity from the sample holder was recorded. By sprinkling the samples onto the slide rather than preparing them as a bulk, one can reduce preferred orientation. For flat plate variable temperature work the silicon disk was attached to an aluminium sample base using highly heat conductive grease in order to get good thermal contact with the PheniX cryostat.

For capillary transmission measurements the sample was ground and then packed into borosilicate or kapton capillaries of appropriate diameter based on absorption considerations. If the absorption was especially high the sample was mixed with crystalline Si or amorphous SiO_2 to reduce to average absorption of the sample. Capillaries were tapped on the bench during the preparation process to ensure adequate and even packing of the sample, and sealed using either heat or epoxy resin.

2.5.3 Analysis of X-ray powder diffraction data

Phase identification was carried out using the Bruker EVA interface to the Powder Diffraction File (PDF) database[19], allowing the peak positions and approximate intensity from the scan file to be compared to the database. More detailed analysis of selected samples was undertaken using Rietveld or Pawley analysis with TOPAS Academic (referred from now on as TOPAS)[20, 21] or Jana2006.[13]

2.5.4 Rietveld refinement

The Rietveld method is a structure refinement technique that requires a reasonable starting model so that the global minimum is found. A powder diffraction pattern is a collection of many individual refection profiles, each with its own intensity, position, and width, with the integrated area proportional to the Bragg intensity, I_k. The Bragg intensity is itself proportional to the square of the structure factor. Rietveld refinement works by fitting the experimental y_i intensities measured by a diffractometer, using a non-linear least squares method. The difference between the calculated model and the observed data are minimised and thus we can derive structural information about a given material. The residual minimised is given by:[15, 16]

$$S_y = \sum_i w_i (y_i(obs) - y_i(calc))^2 \qquad \text{eqn 2.5}$$

where w_i is typically $1/y_i$(obs), y_i(obs) is the observed intensity at the ith step and y_i(calc) is the calculated intensity at the ith step. S_y is summed over all data points in the pattern.

Examples of parameters which can be refined are given in table 2.6, these have been split up into global parameters and phase-specific parameters. Sufficient parameters are required in the structural model for the observed pattern to be reproduced, whilst ensuring that refined parameters lead to a chemically sensible model.

Table 2.6: *Example of parameters which can be refined during a Rietveld refinement.*

Parameters for each phase present	Global parameters
Lattice parameters	Background
Atomic coordinates	Instrumental profile
Scale factor	2θ –Zero
Isotropic thermal parameters	Specimen displacement
Anisotropic thermal parameters	
Preferred orientation	
Sample contribution to peak shape	

Several indicators (R factors) are used to judge the progress of a refinement to observe and determine when convergence is reached. The most meaningful of these is R_{wp}, because it contains the residual S_y in the numerator, and thus provides the most direct indication of the progress of the refinement.

$$R_{wp} = \left\{ \frac{\sum w_i (y_i(obs) - y_i(calc))^2}{\sum w_i (y_i(obs))^2} \right\}^{\frac{1}{2}}$$
eqn 2.6

R_{exp} is a measure of the expected fit achievable from statistics, and is given by:

$$R_{exp} = \left\{ \frac{(N-P)}{\sum w_i y_i(obs)^2} \right\}^{\frac{1}{2}}$$
eqn 2.7

where, N is the total number of data points, P is the number of refined parameters. Note that N-P should always be positive if we are refining an appropriate number of parameters from the collected data.

We can then define the 'goodness of fit' S as:

$$S = \frac{R_{wp}}{R_{exp}}$$
eqn 2.8

An S value of significantly less than 1 therefore indicates that an inappropriate set of parameters has been included. The goodness of fit is also sometimes described via the "chi-squared". Where:

$$\chi^2 = \left[\frac{R_{wp}}{R_{exp}} \right]^2$$
eqn 2.9

2.5.5 Methodologies for analysis of multiple datasets

Sequential Rietveld refinements have been automated using a local DOS command line program Multitopas.[22] Multitopas enables multiple refinements to be run one after another using a single input file (seed.inp). A batch file is created which can read in experimental data on temperatures etc, and processes the scans sequentially, with the parameter values for the second refinement based on the results of the first convergence, and so on. The input file can include a list of parameters to output to a text file that can be imported into spread sheet programs for analysis. This methodology was applied in this work to powder diffraction patterns collected at multiple temperatures.

2.5.6 Peak fitting and indexing in TOPAS

All peak fitting in this work was performed in TOPAS and the positions and intensities refined to their optimal values by least squares. Indexing of peaks was then carried out using the

indexing method of Coelho.[21, 23] Indexing outputs a list of possible unit cell and space groups ranked by figure of merit (FOM).[23] Cells were favoured which accounted for all of the observed reflections and which have a high FOM. A Pawley fit was used to check if all of the peaks in the powder diffraction pattern were predicted by candidate cells.

2.5.7 Pawley refinement

Pawley analysis is a curve fitting technique where the model contains a list of allowed reflections for the selected unit cell and space group.[24] Each of these reflections is then given intensity which is refined against the observed data, and thus no information on the unit cell contents is required. After indexing peaks from an unknown phase the space group of lowest symmetry in that crystal class was used, if this fit is successful at modelling all of the required reflections it is possible to limit the number of potential space groups for the material by considering the systematic absences. As with Rietveld refinement, lattice parameters, peak shapes and background parameters can also be refined. A Pawley refinement therefore gives a good indication the quality of Rietveld fit that could be expected for a given data set.

2.5.8 Structure solution from powder diffraction data

Structure solution from X-ray powder diffraction data was carried out using direct methods and charge flipping, these methods are described in section 2.4.4. Direct methods were implemented through the EXPO2013 software package and charge flipping of powder X-ray diffraction data was implemented using the algorithms present in Topas.[25, 26]

2.6 Neutron powder diffraction

2.6.1 Neutron diffraction

The de Broglie relation states that particles have associated wavelengths, and therefore may undergo diffraction. Thermal neutrons have wavelengths similar to those of X-rays and consequently can be used for diffraction studies of crystalline materials. Neutron diffraction differs from X-ray diffraction in a number of ways: firstly the neutrons interact with the nuclei of atoms/ions, thus the scattering factor does not vary lineally with atomic number, allowing us to distinguish between adjacent atoms in the Periodic Table; a second consequence is that high atomic number atoms in the structure do not dominate the diffraction pattern. In addition the scattering factor of neutrons does not fall off with $\sin\theta/\lambda$ as found for X-ray diffraction, allowing measurement to short d spacing. Finally neutrons have spin ½ and therefore possess a magnetic moment, which can couple with a magnetic moment of atoms or ions in the structure.

Neutron spallation sources (such as ISIS at RAL) produce neutron fluxes ideally suited for time-of-fight studies. H^- ions are generated and pass through a chain of linear accelerators, before being stripped of their electrons to form H^+ and stored in an accumulator ring. They are then directed at a heavy metal Ta target for spallation. This process causes the target to emit pulses of neutrons which are slowed to useful energies by moderators before being directed to the beam lines.

2.6.2 Time-of-flight (TOF) neutron diffractometers

Time-of-flight (TOF) difractometers use fixed detector positions, where the interplanar (d_{hkl}) spacing is explored by a discrete wavelengths (λ_{hkl}) in the pulse. Bragg's law becomes:

$$\lambda_{hkl} = 2d_{hkl}sin\theta \qquad \text{eqn 2.10}$$

where θ is the fixed detector angle, λ_{hkl} is the discrete wavelength and d_{hkl} is the interplaner spacing.

Each pulse contains neutron with a considerable range of wavelengths, and thus velocities, so structures are probed by the time it takes neutrons to reach fixed detector positions. Data are recorded as the number of neutrons as a function of time-of-flight typically in microseconds.

The wavelength of neutrons is related to TOF by:

$$\lambda = \frac{ht}{mL} \qquad \text{eqn 2.11}$$

where h is Plank's constant, t is the time of flight, m is the neutron mass and L is the total neutron flight path.

Substituting 2.10 into 2.11 gives:

$$d_{hkl} = \frac{ht}{2mLsin\theta}$$

eqn 2.12

2.6.3 GEM

Time-of-flight neutron diffraction studies were carried out on the GEM diffractometer at the ISIS spallation source in Oxfordshire. Approximately 4 g of sample was loaded into a cylindrical vanadium can. GEM has a very large detector array of 7.270 m^2 constructed of individual ZnS/^{6}Li scintillator detectors and can measure a wide range of scattering angles.[27]

2.7 Synchrotron X-ray sources

Synchrotron X-ray sources were used during this work to solve problems which could not be tackled using laboratory based sources. Both the high intensities and high X-ray energies available have been exploited

2.7.1 Synchrotron radiation

When electrons traveling at approximately the speed of lights are accelerated, e.g. by changing their trajectory, they emit synchrotron radiation tangentially at a variety of wavelengths, some of which are useful for studying the diffraction of crystalline solids. At synchrotron sources electrons are injected into a linear accelerator and then into a booster ring which accelerates them to nearly the speed of light. Periodically the electrons are transferred to a larger storage ring, where they are kept in the ring by bending magnets. The storage ring must be kept under a very high vacuum to prevent energy loss. The 'ring' is actually constructed from a series of straight sections. During each turn of the ring photons are produced which exit the ring and are directed towards target stations through optics which include slits, mirrors and monochromators. Each beamline has specific individual optics to ensure the required radiation wavelength and collimation are achieved. Intensities higher than those produced by bending magnets can be achieved through the use of undulators and wigglers, which change the direction of the storage ring electrons sinusoidally.

2.7.2 Synchrotron beamlines

The I19 beamline at the Diamond Light Source, is a single crystal beamline equipped with a Rigaku Saturn 724+ CCD detector and typically operated at a wavelength of 0.6889 Å. Temperature control was achieved by use of an Oxford Cryosystems Helix. Synchrotron single crystal studies were also carried out on the BL02B1 beamline at Spring-8 located in Hyogo Japan. BL01B1 was operated at 0.34958 Å and is equipped with a large cylindrical image-plate (IP) camera, and an helium open flow cooling device. Synchrotron powder diffraction measurements were made at the 11-BM beamline at the APS, USA, via the mail in service.

2.8 Other characterisation methods

2.8.1 Electron diffraction

Electrons, unlike X-rays or neutrons interact with mater through strong Coulomb forces due to their charge. As a consequence electron diffraction, especially in transmission geometry, requires very thin samples. Samples were prepared by dispersing the material over a holey carbon grid. Braggs' law can be applied to electron diffraction, but, as the de Broglie wavelength of the electrons is very short, only small diffraction angles need to be measured. Another consequence of the very short electron wavelength is that the radius of the Ewald sphere in reciprocal space is large compared to the crystal lattice, so a large number of reflections can be recorded at each Bragg angle. Electron diffraction was carried out on a JEOL 2100F FEG TEM in transmission mode operating at 200 eV.

2.8.2 SEM-EDX

Energy dispersive X-ray spectroscopy (EDX) allows quantitative elemental analysis. An electron beam within a scanning electron microscope is used to remove an electron from the inner shell of an atom within the sample, producing an electron hole. An electron from a higher energy shell then falls down to fill the hole, and in the process emits X-rays of characteristic wavelengths. Providing the energy of the electron beam is greater than the energy required to remove an electron from the inner shell of all the elements present in the sample, quantitative analysis is possible. Measurements were performed on pelletised samples which were carbon coated to increase electrical conductance using a Hitachi Su-70 FEG SEM.

2.8.3 Second Harmonic Generation (SHG)

Second harmonic generation (SHG) tests were carried out on polycrystalline samples to detect the presence/absence of a centre of symmetry. SHG or frequency doubling involves the conversion of photons of a specific light wavelength to one of half the wavelength, or double the frequency. SHG is a good technique for investigating extended inorganic solids as electric fields interact strongly with polarisable atoms, such as oxygen atoms. Therefore even if the heavy atoms are arranged centrosymmetrically, the lighter oxygen atoms are still able to generate an SHG signal.

An induced polarisation, P, occurs in a material due to the large optical fields. In a centrosymmetric material the linear electric polarisation is proportional to the applied electric field, equation 2.13. In a non centrosymmetric material this is not the case and it is necessary to include high order terms and thus the electric polarisation is given by equation 2.14. The electric field can be described in terms of a wavevector, equation 2.15, where t is the time and ω is the angular frequency.

$$P = \varepsilon_0 \chi E \qquad \text{eqn 2.13}$$

$$P = \varepsilon_0[\chi^1 E + \chi^2 E^2] \qquad \text{eqn 2.14}$$

$$E = E_0 \sin \omega t \qquad \text{eqn 2.15}$$

Where ε_0 is the dielectric constant of vacuum, χ^i electric susceptibilities of 'i' order, and E electric field.

Substituting equation 2.15 into equation 2.14, leads to equation 2.16, which for an acentric materials generates a wave with double the frequency of the incident electromagnetic radiation, or second harmonic generation.

$$P = \varepsilon_0\chi^1 E_0 \sin \omega t + \frac{\varepsilon_0\chi^2}{2}E_0^2 - \frac{\varepsilon_0\chi^2}{2}E_0^2 \cos 2\omega t \qquad \text{eqn 2.16}$$

The samples were tested for second-harmonic generation (SHG) using the experimental setup described by Halasyamani et al..[28] Approximately 50 mg of sample was placed in a fused silica tube. A pulsed 1064 nm Nd-YAG laser was used and activity assessed by 532 nm green light production. SHG efficiency was compared to α-SiO_2 as a standard.

2.8.4 SQUID magnetometry

Magnetic properties of materials were investigated using a Quantum Design Magnetic Properties Measurement System (MPMS). In a SQUID magnetometer the sample is moved through an external magnetic field, and monitored by a pickup coil linked to a superconducting ring which contains two parallel Josephson junctions. The Josephson junctions couple two superconductors via a small insulating gap, through which superconducting electrons can tunnel. The magnetic flux from the moving sample induces a current in the pickup coil which interrupts the superconducting loop. The detection coil is located in a uniform region of magnetic field generated by a superconducting magnet. The output is recorded as a change in voltage across the superconducting ring and is proportional to the magnetic moment of the sample.

Samples were loaded into the larger end of a gelatin capsule and then compacted with the smaller end which was upturned. A thin layer of varnish was then applied to the outside of the capsule to seal the two halves together, figure 2.6. The varnish used was a mixture of "G" varnish and 10:1 ethanol-toluene solution. The capsule was then mounted within a plastic straw and mounted within the magnetometer.
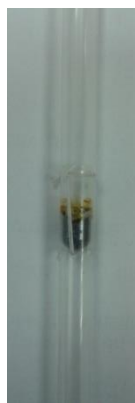
Figure 2.6: *Sample setup of for SQUID magnetometry, sample in grey.*

Data were recorded as text files which were analysed using Excel. Experimental moments were converted to molar susceptibility via equation 2.17. The susceptibility was corrected for diamagnetic contributions due to core electrons in the sample, and any temperature independent paramagnetic contributions and the sample holder by plotting χ_{mol} vs 1/T and extrapolating to infinite temperature to give $\chi_{mol}^{measured}$. For a Curie-Weiss paramagnet a plot of $1/\chi_{mol}^{measured}$ vs *T* should give a straight line and the Curie constant *C* is given by 1/gradient of this line and the Weiss constant θ by the intercept divided by the gradient. The effective magnetic moment, μ_{eff} can be determined via equation 2.18

$$\chi_{mol} = \frac{long\ moment}{field \times (mass/RMM)}$$ eqn 2.17

$$\mu_{eff} = 2.828\sqrt{C}$$ eqn 2.18

2.8.5 Conductivity measurements

Electronic properties of materials were investigated by a Quantum Design Physical Properties Measurement System (PPMS), equipped with a 4-probe conductivity puck. Data were collected on cooling and warming between 295 K and the temperature where the resistance became too high to measure. Materials were first pressed into 5 mm diameter cylindrical pellets using a a pellet press and 2 tonnes of load. The pellet was then prepared into a rectangular prism and the dimensions recorded using a pair of digital callipers. The pellets were mounted on the conductivity puck using a small amount of a mixture of "G" varnish and 10:1 ethanol-toluene solution to hold it in position, a cigarette paper was used to insulate the sample from the puck. Copper wires were attached to the sample using silver paste.
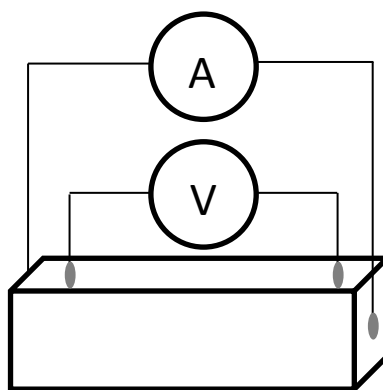
Figure 2.7: Schematic diagram of resistivity measurement geometry

Data were output as a text files with temperature (K) the resistance (Ω) along with its standard uncertainty. The resistivity (Ω m) of the samples was obtained using the orientation and dimensions of the sample. For a semiconducting material a plot of ln(conductivity) vs 1/T is a straight line where the activation energy, E_a, in eV can be deduced by equation 2.19 where the electronic band gap is $2E_a$.

$$E_a = \frac{gradient \times k}{N_a} \qquad \text{eqn 2.19}$$

where k is the Boltzmann constant and N_a is Avogadro's constant.

2.8.6 Diffuse reflectance spectroscopy

Diffuse reflectance spectra were obtained by illumination of the sample using an Energetiq LDLS EQ-99 broadband lamp and collected at 20° to the excitation, using an Ocean Optics Maya Pro 2000 spectrometer. Integration times were adjusted to afford maximum response of the spectrometer without saturation of the detector. The sample was dispersed in NaCl which was also used as the white standard. Data for the standard and sample were collected multiple times and the intensities averaged. Data were output as a text file of wavelength (nm) and intensity (arbitrary units). The reflectance R, is giving by the intensity of the sample divided by the intensity of the reference at any given wavelength, equation 2.20. The optical band gap of the material was calculated by plotting the Kubelka-Munk function, given by equation 2.21 against energy, and the intercept of the slope of the function with the baseline was taken as the optical band gap.[29, 30]

$$R = \frac{I_{sample}}{I_{reference}} \qquad \text{eqn 2.20}$$

$$F = \frac{(1-R)^2}{2R} \qquad \text{eqn 2.21}$$

References

1. Tuxworth, A. J., McCabe, E. E., Free, D. G., Clark, S. J., and Evans, J. S. O., *Inorganic Chemistry*, 2013, **52**, 2078-2085

2. Strobel, S., Choudhury, A., Dorhout, P. K., Lipp, C., and Schleid, T., *Inorganic Chemistry*, 2008, **47**, 4936-4944

3. Free, D., *PhD thesis: Synthesis and Properties of New Oxychalcogenide materials*, Durham University, 2010

4. Liu, R. H., Zhang, J. S., Cheng, P., Luo, X. G., Ying, J. J., Yan, Y. J., Zhang, M., Wang, A. F., Xiang, Z. J., Ye, G. J., and Chen, X. H., *Physical Review B*, 2011, **83**, 174450

5. Kabbour, H., Cario, L., Moelo, Y., and Meerschaut, A., *Journal of Solid State Chemistry*, 2004, **177**, 1053-1059

6. *Acta Crystallographica Section A*, 1992, **48**, 922-946

7. *SMART V5.625, Bruker AXS, Madison, WI, USA*, 2005

8. Altomare, A., Cascarano, G., Giacovazzo, C., and Guagliardi, A., *Journal of Applied Crystallography*, 1994, **27**, 1045-1050

9. *SAINT V6.02, Bruker AXS, Madison, WI, USA*, 2005

10. *G. M. Sheldrick, SADABS, University of Gottingen, Germany*, 1996

11. CRYSTALS, Betteridge, P. W., Carruthers, J. R., Cooper, R. I., Prout, K., Watkin, D. J. (2003). J. Appl. Cryst. 36, 1487-1487

12. Oszlanyi, G. and Suto, A., *Acta Crystallographica Section A*, 2004, **60**, 134-141

13. *Jana2006. The crystallographic computing system, Petricek,V., Dusek,M. & Palatinus,L., 2006*,

14. Palatinus, L. and Chapuis, G., *Journal of Applied Crystallography*, 2007, **40**, 786-790

15. Bruker-AXS, *DiffracPlus XRD Commander v2.3: Software for Controlling Bruker Diffractometers, 2000*,

16. Oxford Cryosystems Cryopad v1.484, Oxford, 2007

17. Evans, J. S. O., *'Phenixlogfiles', 1999*,

18. Bruker-AXS, *Diffrac.Suite v2.27: Software for Controlling Bruker Diffractometers, 2011*,

19. *Powder Diffraction File, International Centre for Diffraction Data, Pennsylvania*, 1998

20. *Bruker AXS, Diffrac^{plus} Basic Evaluation Package: EVA 10.0, Karlsruhe*, 2004

21. Coelho, A. A., *TOPAS Academic: General Profile and Structure Analysis Software for Powder Diffraction Data, Bruker AXS*, 2010

22. Evans, J. S. O., *'Multitopas'*, 1999

23. Coelho, A. A., *Journal of Applied Crystallography*, 2003, **36**, 86-95

24. Pawley, G. S., *Journal of Applied Crystallography*, 1981, **14**, 357-361

25. Coelho, A. A., *TOPAS Academic: General Profile and Structure Analysis Software for Powder Diffraction Data*, 2012.

26. Altomare, A., Cuocci, C., Giacovazzo, C., Moliterni, A., Rizzi, R., Corriero, N., and Falcicchio, A., *Journal of Applied Crystallography*, 2013, **46**, 1231-1235

27. Hannon, A. C., *Nuclear Instruments & Methods in Physics Research Section a-Accelerators Spectrometers Detectors and Associated Equipment*, 2005, **551**, 88-107

28. Ok, K. M., Chi, E. O., and Halasyamani, P. S., *Chemical Society Reviews*, 2006, **35**, 710-717

29. Tandon, S. P. and Gupta, J. P., *Physica Status Solidi*, 1970, **38**, 363-367

30. Kortum, G., Braun, W., and Herzog, G., *Angewandte Chemie-International Edition*, 1963, **75**, 653-404

Chapter 3: Synthesis and Characterisation of a New ZrCuSiAs-Related Material – La$_2$O$_2$ZnSe$_2$

3.1 Introduction

As discussed in Chapter 1, there have been many interesting mixed-anion materials prepared with the ZrCuSiAs structure. Several oxychalcogenides adopt the ZrCuSiAs structure and the study of these materials has been fuelled by their interesting optical and electronic properties. These materials formally contain fluorite-like $[A_2O_2]^{2+}$ layers, separated by antifluorite-like $[M_2Q_2]^{2-}$ layers which alternate along the long axis of a ~4 Å x 4 Å x 9 Å tetragonal unit cell. The most studied oxychalcogenide materials are those with a copper-chalcogenide layers where the transition metal is formally in a +1 oxidation state.

In an attempt to prepare potentially interesting new ZrCuSiAs-related oxychalcogenides, our group has prepared various new ZrCuSiAs-related oxychalcogenides containing divalent transition metals.[1, 2] Prior to our work the only bulk sample prepared was La$_2$O$_2$CdSe$_2$ which adopts a superstructure of the LaOCuS (ZrCuSiAs) structure in which half of the tetrahedral sites in the $[CdSe_2]^{2-}$ layer are vacant such that there are only corner-sharing CdSe$_4$ tetrahedra. La$_2$O$_2$CdSe$_2$ has a band gap of 3.3 eV and has been investigated as a possible transparent conductor, but the conductivities of La$_2$O$_2$CdSe$_2$, have been found to be very low (>10^{10} Ω cm) compared to compounds containing copper chalcogenide layers.[3]

In this chapter the synthesis, structure solution from X-ray powder diffraction data, variable temperature structural properties and optical properties of La$_2$O$_2$ZnSe$_2$ will be described. Attempts to synthesize a material of this composition were first reported in 1996 but were unsuccessful, resulting in a mixture of La$_2$O$_2$Se and ZnSe.[4] Structure solution of La$_2$O$_2$ZnSe$_2$ from laboratory X-ray powder diffraction data was carried out via symmetry adapted distortion mode refinements complemented by single crystal X-ray diffraction, powder neutron diffraction and electron diffraction. The relationship to other quaternary oxychalcogenide materials will be discussed. This work, along with electronic structure calculations, has been reported in a joint publication with Dr Emma McCabe.[5]

3.2 Synthesis

An off white powder of La$_2$O$_2$ZnSe$_2$ was synthesised according to the method outlined in Section 2.2.3. Powder X-ray diffraction data collected at room temperature showed that a ZrCuSiAs related phase had been obtained. Additional reflections were present in the diffraction pattern, most notably at 5.32, 4.45, 3.63, 3.52, 2.81 and 2.53 Å (Figure 3.1). As the origin of these additional reflections could not be identified, initial Rietveld refinements were performed in a ~4 Å x 4 Å x 9 Å cell with the parent tetragonal space group *P*4/*nmm* and the Zn^{2+} half occupied, as in CeOMn$_{0.5}$Se (figure 3.12a); a Rietveld plot in this space group is shown in figure 3.1.[6] Attempts to index the weak superstructure reflections observed required a very large unit cell (at least 2√2$a_{subcell}$ × √2$a_{subcell}$ × 2$c_{subcell}$). Work by Free investigated the origin of these additional diffraction peaks which indicated that they could not be explained by known impurity phases. It was tentatively suggested that the origin of the peaks was due to a complex ordering pattern of Zn^{2+}, but it was not possible to index the peaks to a sensible unit cell.[7] Masters project work by this author showed that as composition was varied the additional reflections scale with the main phase, and therefore could most likely be attributed to a superstructure.[8] During this work further off-stoichiometric samples with La$_{2.2}$O$_2$ZnSe$_2$, La$_2$O$_{2.2}$ZnSe$_2$, and La$_2$O$_2$Zn$_{1.2}$Se$_2$ compositions were synthesised to investigate if a small change in stoichiometry affected the additional peaks' intensities (relative to the main reflections) or introduced additional impurity phases. Figure 3.2 shows this further synthesis of off-stoichiometric compositions confirms that the additional peaks' intensities scale with the percentage of the main phase, and therefore should be attributed to superstructure.
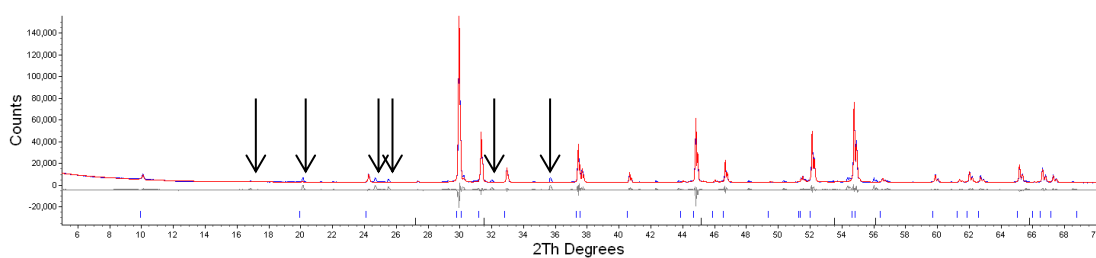
Figure 3.1: *Rietveld plot of La$_2$O$_2$ZnSe$_2$ at room temperature, performed in P4/nmm with the Zn^{2+} sites half occupied; observed = blue, calculated = red, difference = grey; additional unindexed reflections are indicated by black arrows. Sample AJT039, d9_06009.*
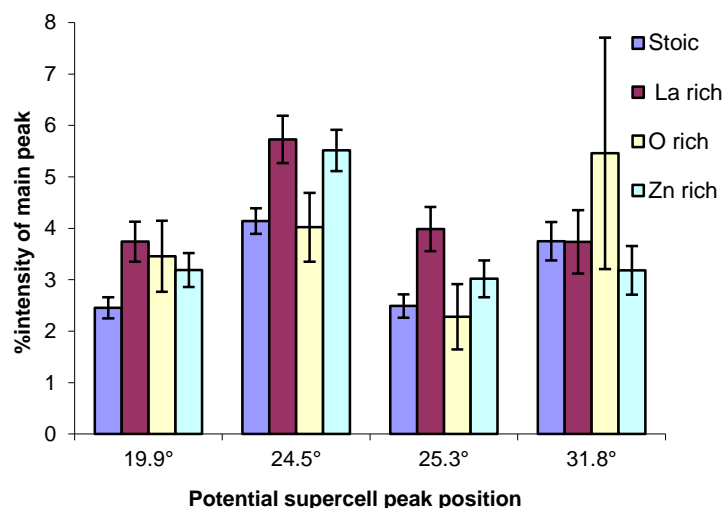
Figure 3.2: *Intensity of several unindexed arrowed peaks in figure 3.1 for different sample preparations relative to the intensity of the 012 reflection at 30° 2θ, La$_2$O$_2$ZnSe$_2$ d9_04315 (AJT022a), La$_{2.2}$O$_2$ZnSe$_2$, d9_04913 (AJT028a), La$_2$O$_{2.2}$ZnSe$_2$ d9_04914 (AJT028b), La$_2$O$_2$Zn$_{1.2}$Se$_2$ d9_04915 (AJT028c).*

3.3 EDX atomic ratios

Backscattered secondary electron images of La$_2$O$_2$ZnSe$_2$ carbon coated pellets indicate that the sample composition is homogeneous (figure 3.3). EDX analysis collected using an incident electron beam energy of 15 kV gave the following atomic percentages: La 26(1)%, O 30(1)%, Zn 15.8(4)% and Se 27.9(4)%, where the figure in parentheses is the standard deviation of 30 data points; data are given in Appendix 1. This gives an La:O:Zn:Se atomic ratio of 1.86(7):2.15(7):1.132(3):2.000(4) close to the target composition.
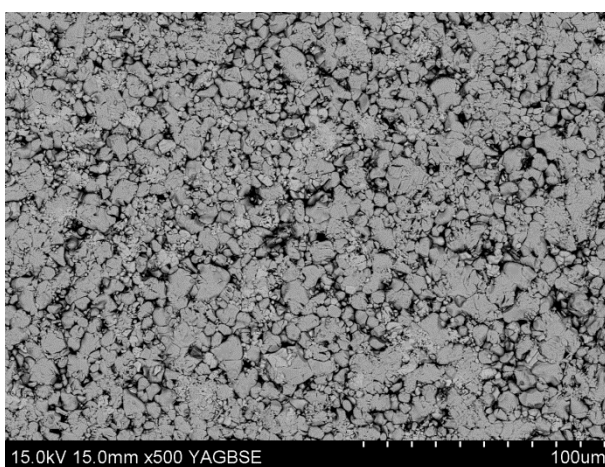
Figure 3.3: *Backscattered secondary electron image of La$_2$O$_2$ZnSe$_2$.*

69

3.4 Supercell determination by X-ray and electron diffraction

Selected area electron diffraction (SAED) images taken along the [001] and [110] zone axes confirmed the presence of superstructure reflections. Figure 3.4a shows strong reflections consistent with the *P*4/*nmm* parent structure were observed down the [001] zone axis, with weak superstructure reflections observed along [1$\bar{1}$0] but not [110] directions, indicating the loss of tetragonal symmetry in the superstructure. These additional reflections can be indexed as 100, 200, *h*00 (*h* = *n*) in a 2√2*a*$_{subcell}$ × √2*a*$_{subcell}$ × 2*c*$_{subcell}$ unit cell, or 200, 400, *h*00 (*h* = 2*n*) in a 4√2*a*$_{subcell}$ × √2*a*$_{subcell}$ × 2*c*$_{subcell}$ unit cell. Figure 3.4c shows the diffraction pattern taken down the [110] zone axis, weak superstructure reflections are again observed indicating an increased unit cell size in the *ab* plane. The SAED images shown have zone axes and *hkl* indices relative to the parent *P*4/*nmm* tetragonal structure, reflections consistent with the parent structure are shown in white, and those which are inconsistent are shown in red.
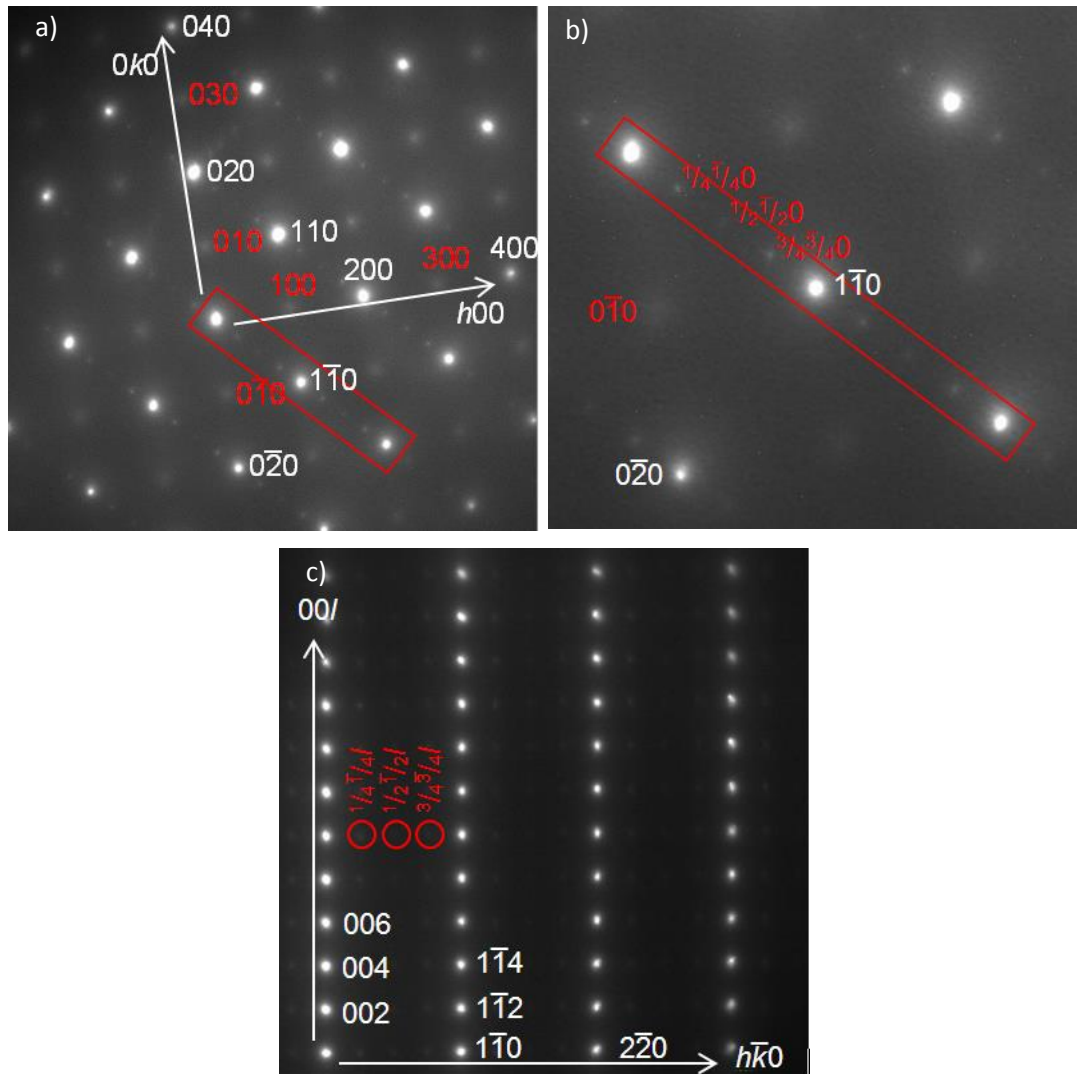
Figure 3.4: *Selected area electron diffraction images for La$_2$O$_2$ZnSe$_2$ taken down the (a) [001] zone axis, (b) [001] enlarged region showing supercell reflections, (c) [110] zone axis; zone axes and hkl indices relative to the parent P4/nmm tetragonal structure, reflections consistent with P4/nmm structure are shown in white, and those which are inconsistent are shown in red.*

Single crystals of $La_2O_2ZnSe_2$ were grown using the procedure outlined in section 2.2.3. Single-crystal X-ray diffraction data were collected on a plate-like crystal of 0.08 mm x 0.08 mm x 0.008 mm, at 150 K using Mo Kα_1 radiation. Generator settings of 35 kV and 50 mA were selected to reduce problems with $\lambda/2$ contamination. A total of 2070 frames were collected in ω steps of 0.3° using a frame collection time of 10 seconds. Raw images confirmed the need for a large supercell of $4\sqrt{2}a_{subcell} \times \sqrt{2}a_{subcell} \times 2c_{subcell}$. With single crystal data the loss of tetragonal symmetry, clear in figure 3.3, was not observed, indicating that the larger X-ray crystals are heavily twinned, which is unsurprising given the relationship between the parent and actual structure of $La_2O_2ZnSe_2$. It was not possible to solve the structure from these twinned data.

Figure 3.5 shows that a Pawley refinement of powder data with a supercell of $4\sqrt{2}a_{subcell} \times \sqrt{2}a_{subcell} \times 2c_{subcell}$ and space group $P222$ successfully accounts for all observed reflections in the XRPD data.
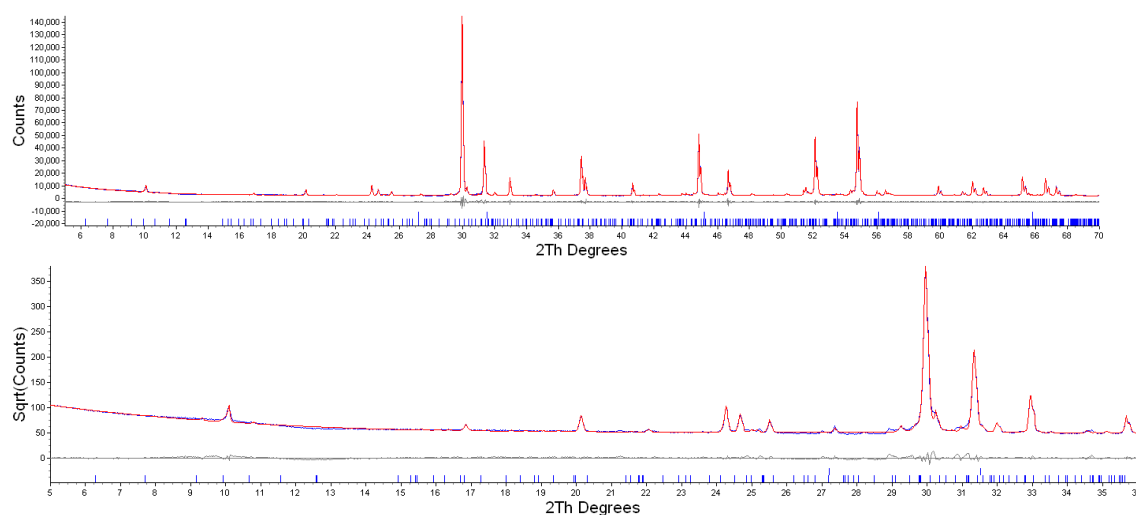
Figure 3.5: a) *Pawley plot of $La_2O_2ZnSe_2$ at room temperature, performed in P222 with a supercell of $4\sqrt{2}a_{subcell} \times \sqrt{2}a_{subcell} \times 2c_{subcell}$; b) zoom of low angle region on square route scale; AJT039, d9_06009.*

3.5 Structure determination

3.5.1 Symmetry-adapted distortion mode analysis - occupancies

Based on the ZrCuSiAs related structure and the composition of $La_2O_2ZnSe_2$ relative to LaOMSe (M = monovalent transition metal), the most likely source of the observed superstructure is a ordering of Zn^{2+} ions within the $[ZnSe_2]^{2-}$ antifluorite-like layer. To investigate the symmetry of the material and hence deduce the structure, a symmetry-adapted distortion mode approach was applied. For crystal structures that can be viewed as a low-symmetry structural distortion of a higher-symmetry parent structure, the details of the distorted structure can be described in terms the parent structure with symmetry-adapted distortion modes imposed on it, rather

than using traditional atomic *xyz* coordinates. A similar approach can be used for site occupancy ordering modes.[9] These modes can be treated as binary (on/off) parameters, within a supercell in $P1$ symmetry. If the symmetry change from the parent to the distorted structure involves activation if a given mode it must be turned "on" and its amplitude adjusted to described the magnitude of the distortion. If the mode is not activated it remains "off" and its amplitude is zero. The web-based ISODISTORT software was used to create a symmetry-adapted distortion mode description of the $La_2O_2ZnSe_2$ superstructure in $P1$ symmetry including all allowed zinc occupancy modes and displacive modes for all sites.[10] The 32 allowed modes acting on zinc site occupancies are given in table 3.1, each distortion mode is given a mode label such as Σ1 or S2 and is associated with a particular *k* point and order parameter direction. The distortion mode amplitudes influence site occupancy, for example:

Zn1 occupancy = 0.5 + Zn1_do

Where:

Zn1_do = 0.17678*b1 + 0.17678*b2 + 0.25000*b3 + 0.25000*b5 + 0.25000*b7 + 0.25000*b9 + 0.25000*b11 + 0.25000*b13 + 0.17678*b15 - 0.17678*b16 + 0.17678*b17 - 0.17678*b18 + 0.17678*b19 + 0.17678*b20 + 0.25000*b21 + 0.25000*b23 + 0.25000*b25 + 0.25000*b27 + 0.25000*b29 + 0.25000*b31

Zn2 occupancy = 0.5 + Zn2_do

Where:

Zn2_do = 0.17678*b1 + 0.17678*b2 + 0.25000*b4 + 0.25000*b6 - 0.25000*b7 - 0.25000*b9 - 0.25000*b12 - 0.25000*b14 + 0.17678*b15 - 0.17678*b16 + 0.17678*b17 - 0.17678*b18 + 0.17678*b19 + 0.17678*b20 + 0.25000*b22 + 0.25000*b24 - 0.25000*b25 - 0.25000*b27 - 0.25000*b30 - 0.25000*b32

Where b*n* corresponds to the amplitude of mode number *n* in table 3.1, and hence only certain distortion modes affect each site within the structure.

Table 3.1: Occupancy mode number, label, k-point and order parameter directions corresponding to occupancy modes acting upon zinc sites in La$_2$O$_2$ZnSe$_2$, in P1 symmetry with a 4√2a$_{subcell}$ × √2a$_{subcell}$ × 2c$_{subcell}$ supercell.

Mode number	Mode label	k point	order parameter direction
1	GM1+	[0,0,0]	(a)
2	GM4-	[0,0,0]	(a)
3	SM1	[1/8,1/8,0]	(a,0,0,b)
4	SM1	[1/8,1/8,0]	(a,0,0,b)
5	SM4	[1/8,1/8,0]	(a,0,0,b)
6	SM4	[1/8,1/8,0]	(a,0,0,b)
7	SM1	[1/4,1/4,0]	(a,0,0,b)
8	SM1	[1/4,1/4,0]	(a,0,0,b)
9	SM4	[1/4,1/4,0]	(a,0,0,b)
10	SM4	[1/4,1/4,0]	(a,0,0,b)
11	SM1	[3/8,3/8,0]	(a,0,0,b)
12	SM1	[3/8,3/8,0]	(a,0,0,b)
13	SM4	[3/8,3/8,0]	(a,0,0,b)
14	SM4	[3/8,3/8,0]	(a,0,0,b)
15	M2	[1/2,1/2,0]	(a,b)
16	M2	[1/2,1/2,0]	(a,b)
17	A1	[1/2,1/2,1/2]	(a,b)
18	A1	[1/2,1/2,1/2]	(a,b)
19	Z2+	[0,0,1/2]	(a)
20	Z3-	[0,0,1/2]	(a)
21	S2	[1/8,1/8,1/2]	(a,0,0,b)
22	S2	[1/8,1/8,1/2]	(a,0,0,b)
23	S3	[1/8,1/8,1/2]	(a,0,0,b)
24	S3	[1/8,1/8,1/2]	(a,0,0,b)
25	S2	[1/4,1/4,1/2]	(a,0,0,b)
26	S2	[1/4,1/4,1/2]	(a,0,0,b)
27	S3	[1/4,1/4,1/2]	(a,0,0,b)
28	S3	[1/4,1/4,1/2]	(a,0,0,b)
29	S2	[3/8,3/8,1/2]	(a,0,0,b)
30	S2	[3/8,3/8,1/2]	(a,0,0,b)
31	S3	[3/8,3/8,1/2]	(a,0,0,b)
32	S3	[3/8,3/8,1/2]	(a,0,0,b)

Initially the zinc occupancy modes were analysed using the "repeated local minimisation from random starting values" or RLM method.[9] The amplitudes of the 32 allowed occupancy modes (displacive modes were fixed) acting on Zn sites in the supercell were randomised and the model refined against laboratory powder diffraction data (5-50° 2θ) until convergence. As well distortion modes, parameters were also included to model phase specific and instrumental factors including: 18 terms of a Chebyshev polynomical to model the background, a sample height parameter, and scale factor, and parameters to model a ZnSe impurity phase. Unit cell

parameter and a pseudo-Voigt peak shape function for La$_2$O$_2$ZnSe$_2$ were fixed at the values obtained from a Pawley refinement. Upon convergence the mode amplitudes and crystallographic agreement factors such as R$_{wp}$ were output to a text file. The process was then repeated from random starting amplitudes to build up histograms of mode amplitudes. The RLM method suggested that several occupancy modes (four S2, six S3 modes, two Σ4 modes and a Γ4– mode) had non-zero amplitudes in the distorted structure, and thus are "on". Mode amplitude histograms are shown in figure 3.6.

The mode amplitudes of the best solution gave zinc site occupancies close (but not equal) to either 0 or 1. Therefore the RLM method was repeated with all 32 occupancy modes refining and penalties applied to the 32 zinc site occupancies to favour this criterion. The number of active modes identified was reduced with non-zero amplitudes for four S2, two S3 modes, and a Γ4– mode, mode amplitude histograms using these criteria are shown in figure 3.7. The penalty applied was of the form:

Penalty = (0.5 - ((Zn*n*_do^2)^0.5))^2

Where Zn*n*_do is the magnitude the site occupancy differs from 0.5.

Figure 3.6: Results from RLM analysis showing multi-convergence histograms for each of the occupancy mode amplitudes in P1 symmetry for a 4√2a$_{subcell}$ × √2a$_{subcell}$ × 2c$_{subcell}$ model of La$_2$O$_2$ZnSe$_2$ based on refinements using XRPD data (d9_06009).
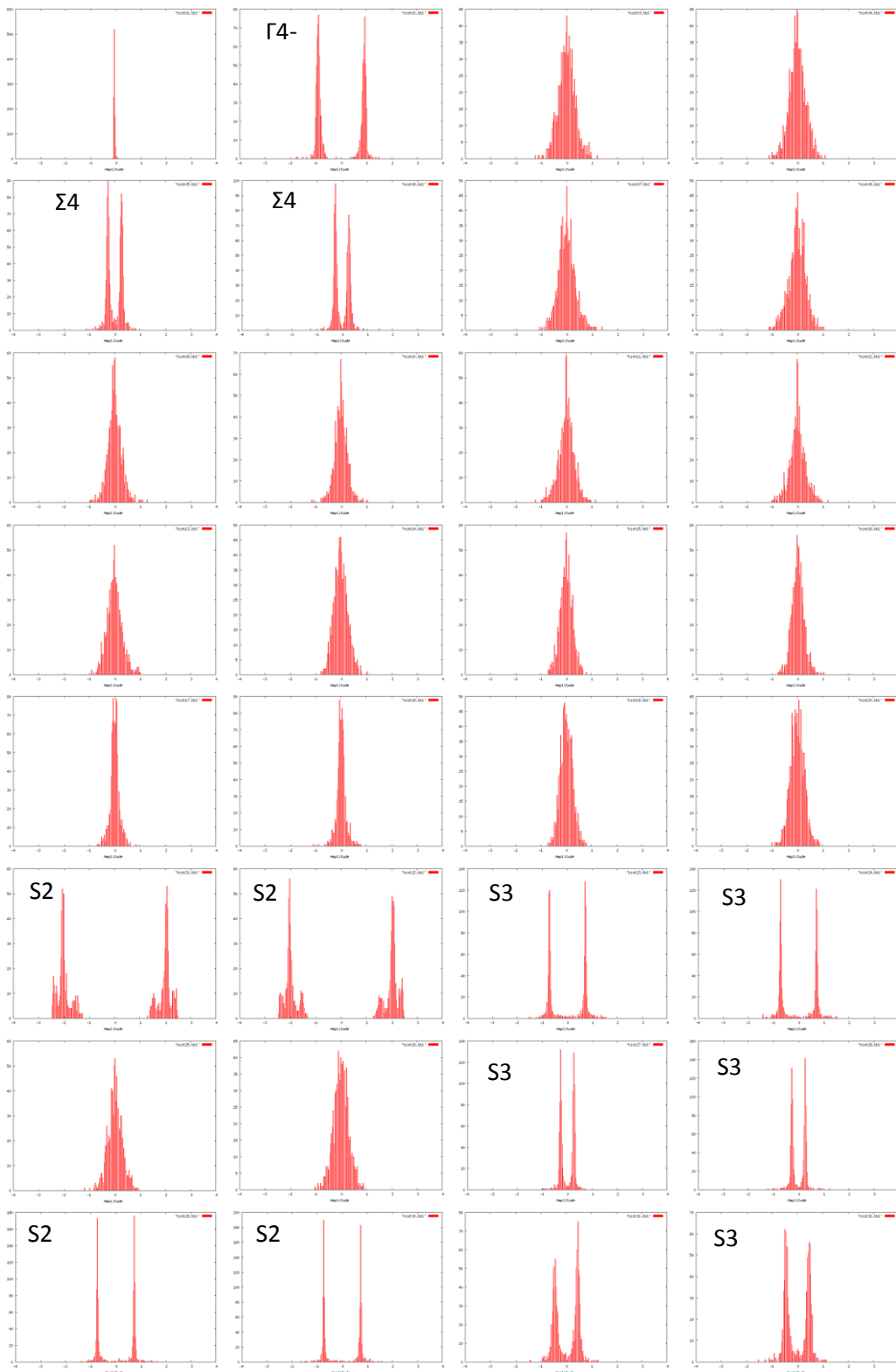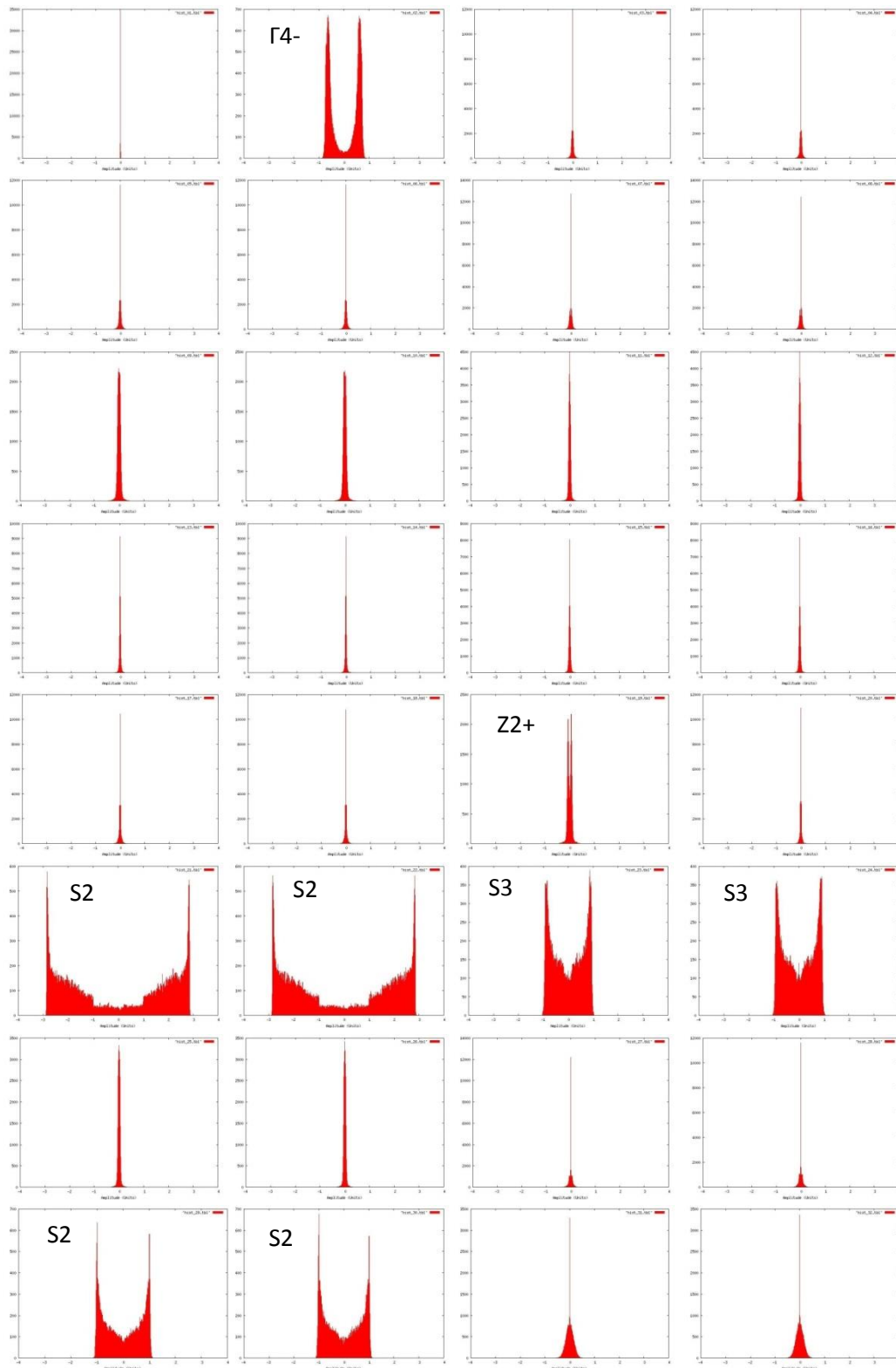
Figure 3.7: *Results from RLM analysis showing multi-convergence histograms for each of the occupancy mode amplitudes in P1 symmetry for a 4√2a$_{subcell}$ × √2a$_{subcell}$ × 2c$_{subcell}$ model of La$_2$O$_2$ZnSe$_2$ based on refinements using XRPD data (d9_06009) with penalties on Zn site occupancies to favour fully occupied or vacant sites.*

The RLM method involves refining all mode amplitudes simultaneously and "phantom modes"[9] can sometimes appear to be active. This can result from a correlated combination of incorrect modes giving a reasonable description of the data, or low/incorrect information content in the experimental data themselves (e.g. X-ray data can be insensitive to O modes, or modes can be artificially activated to described intensity due to impurity phases). To reduce the probability of phantom modes, individual mode inclusion refinements were carried out to assess the influence on the fit of each mode individually. The mode inclusion method involves individually including each relevant mode and carrying out cycles of annealing; the mode amplitude and crystallographic agreement factors for the best solution are then output. The mode amplitude is then set to zero and the next mode included in the refinement.

Rounds of mode inclusion suggest that the two S2 modes at k point (1/8 1/8 1/2) gave a significant improvement in the fit, as shown by a decrease in R_{wp} from 10.024 % to 7.470 % (figure 3.8) when they were included. McCabe showed that an equally good fit can be obtained by refining these two modes individually or simultaneously as these modes are fully correlated with each other.[5] When either of the S2 modes at (1/8 1/8 1/2) was included as an initial mode set, subsequent rounds of mode inclusion analysis suggest that either of the two S2 modes at (3/8 3/8 1/2) give a further improvement in the fit (R_{wp} 7.47 %to 7.32 %). When the four S2 modes were included as the initial mode set and a third round of mode inclusion analysis performed, a slight improvement in the fit was achieved by a correlated pair of S3 modes (modes 23 and 24) or Γ4– (mode 2). The R_{wp} improvement was, however, slight (a decrease of 0.06 % and 0.03 % respectively), and not thought to be significant. The modes identified as important by mode inclusion are consistent with those identified by the RLM method.
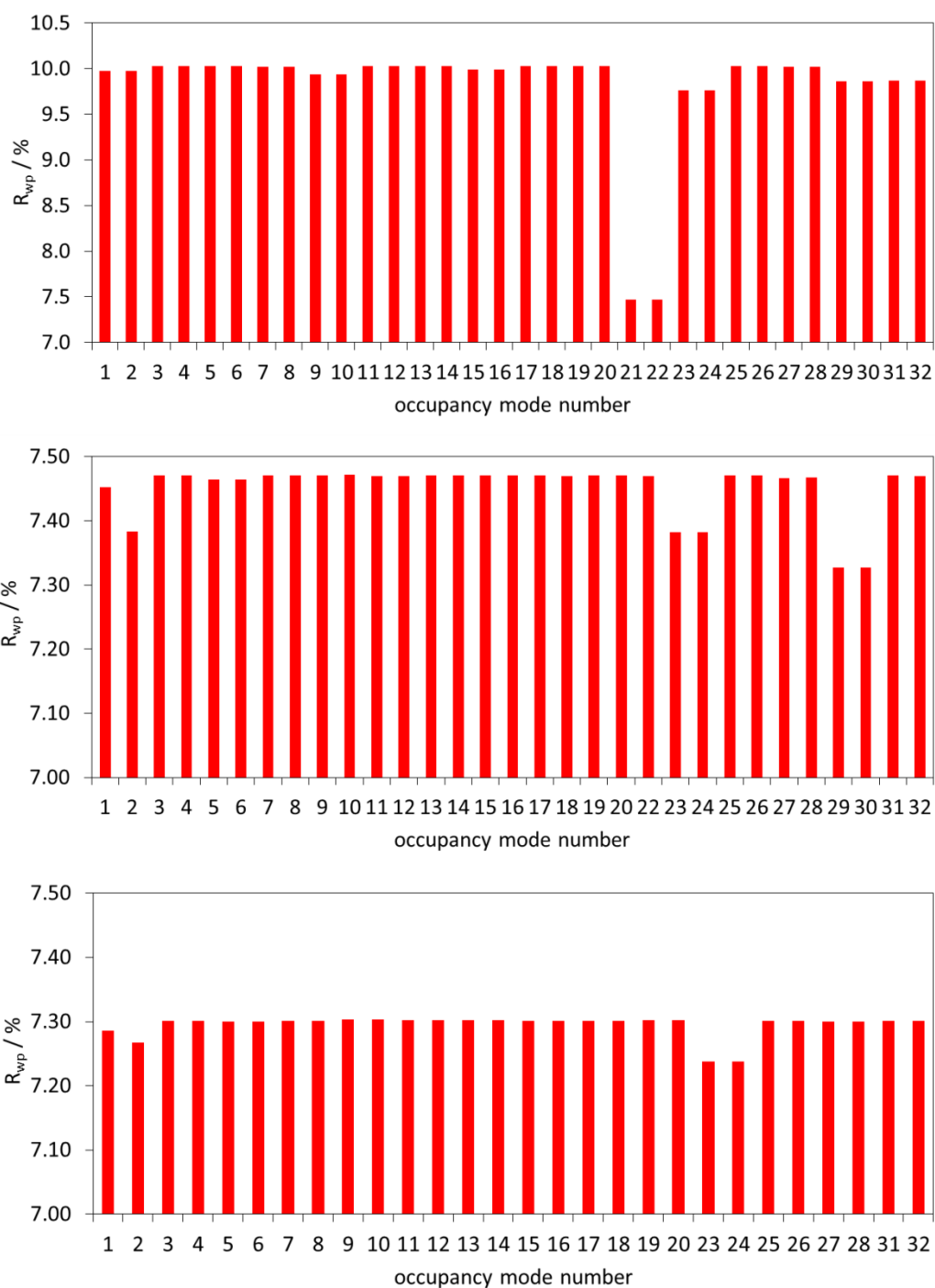
Figure 3.8: *Results from mode inclusion analysis showing (a) initial round of mode inclusion (b) second round of mode inclusion to an initial mode set of S2 mode 21, (c) third round of mode inclusion to an initial mode set of four S2 modes (modes 21, 22, 29 & 30).*

With the four important modes identified from the mode inclusion method, i.e. S2 modes at (1/8 1/8 1/2) and (3/8 3/8 1/2) number 21, 22, 29 and 30 in table 3.1, the RLM method was repeated with just these four modes. Penalties on the zinc site occupancies were again included to favour fully vacant or occupied sites. Multiconvergence histograms for these four

S2 modes show (figure 3.9) that there are four discrete mode amplitudes possible for each mode, giving a total of 16 possible solutions. These 16 solutions are in fact equivalent and correspond to the possible origin choices for the supercell in $P1$ symmetry. All correspond to an identical cation ordered structure.
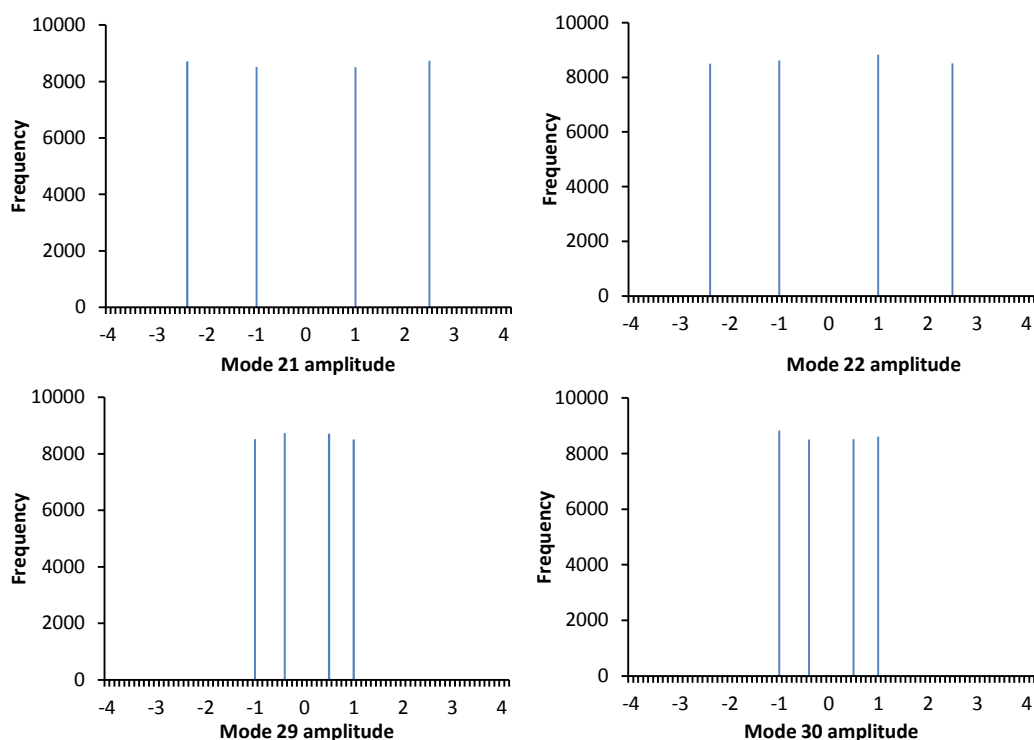
Figure 3.9: *Results from RLM analysis involving only the four S2 occupancy modes at k = (⅛ ⅛ ½) and at k = (⅜ ⅜ ½) with penalties on Zn site occupancies to favour fully occupied or vacant sites. Multi-convergence histograms for these four S2 mode indicate amplitudes of ± 1.00, ± 2.414 for S2 modes at k = (⅛ ⅛ ½) (modes 21, 22) and amplitudes of ± 1.00, ± 0.414 for S2 modes at k = (⅜ ⅜ ½) (modes 29, 30).*

It should be noted that this restrained four mode description gives a fit of equivalent quality to that to when all 32 Zn occupancy modes are freely refined, suggesting that these four modes are sufficient to describe the symmetry lowering from the parent structure. Once the 4 active modes are identified, it is possible to calculate the zinc sites which these distortion modes act upon. We can directly determine the partial reduction in symmetry from the parent $P4/nmm$ that occurs and deduce the material has space group $Cmca$ with basis vectors (4 4 0), (0 0 −2), (−1 1 0) relative to the parent cell.

3.5.2 Displacive modes

The work described in section 3.5.1 identified the likely cation ordering pattern in La$_2$O$_2$ZnSe$_2$ and the resulting lower symmetry space group. It is, of course, highly likely that cation ordering will lead to associated structural distortions. Figure 3.10 shows R-factors from mode inclusion refinements for displacive modes, suggesting that the two most significant structural distortions are both Γ1+ modes acting on La and Se, inclusion of these leads to a reduction in R$_{wp}$ from ~6.85 % to 6.3 % and 6.5 % respectively over the 2θ range of 5-100° analysed. Neither of these two modes lead to a further reduction in symmetry from the *Cmca* space group identified in the cation ordering analysis.
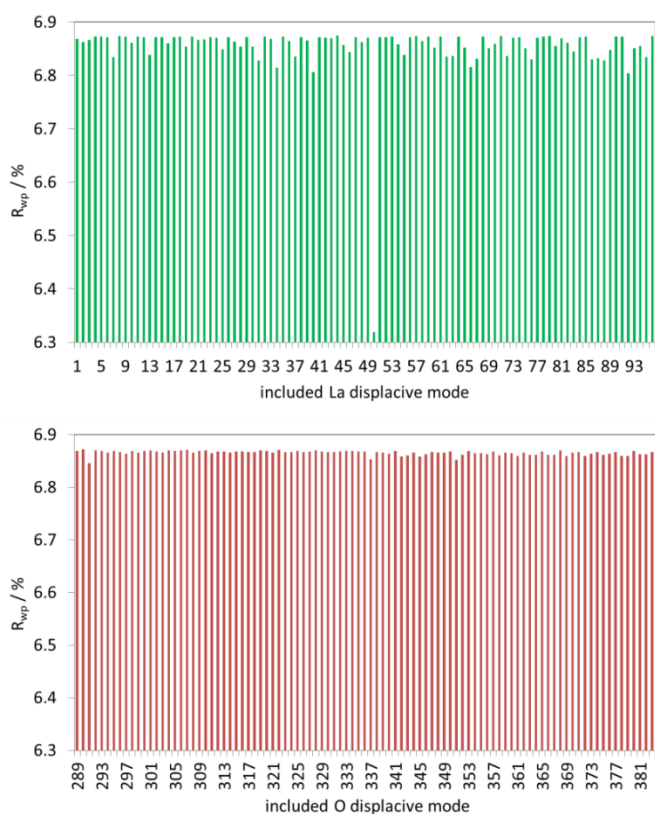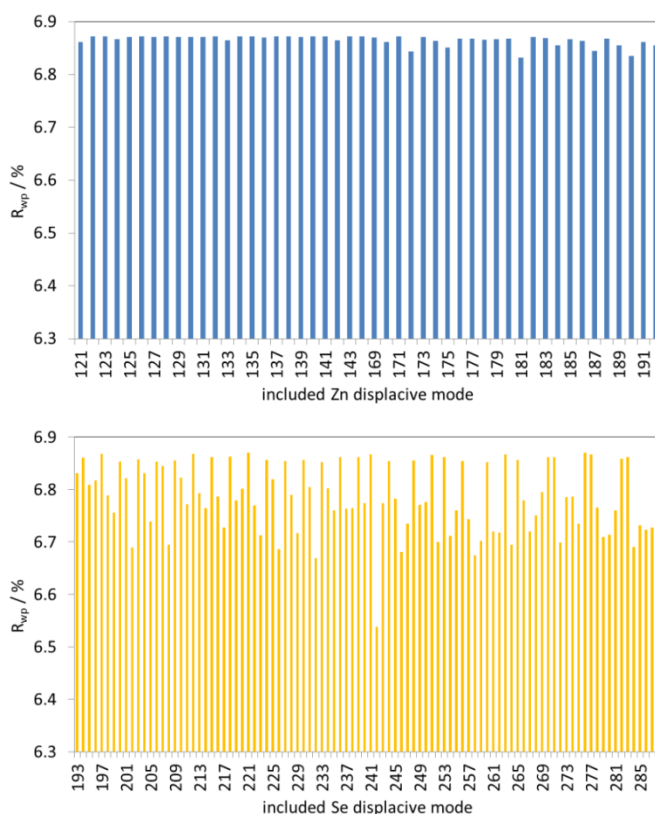
Figure 3.10: *Results from mode inclusion analysis on displacive modes; only a Γ1+ mode acting on La sites, and a Γ1+- mode acting on Se sites (corresponding to displacements along [100]) give a significant improvement in fit, but these do not cause any reduction in symmetry from Cmca.*

3.6 Structure refinement and description

3.6.1 Rietveld refinement

Final refinements were carried out using a cation ordered model with *Cmca* symmetry against combined laboratory X-ray and neutron powder diffraction data collected on GEM; a total of 162 parameters were refined. This structure is illustrated later in figure 3.13 and Rietveld refinement profiles are shown in figure 3.11. Figure 3.11 shows an excellent fit is observed for all neutron data banks giving high confidence in the structural model. When site occupancies were refined with La occupancy fixed at 1, all other site occupancies refined within 3 standard uncertainties of full occupancy, suggesting that the material is stoichiometric within the quality of the current data, and consistent with the EDX data report in section 3.3. Structural parameters are shown in table 3.2. Bond valence sum calculations gave valences of 3.17, 3.02 and 3.11 for La(1), La(2) and La(3), 1.91 and 1.96 for Zn(1) and Zn(2), 1.74, 1.70, 1.77 for Se(1), Se(2) and Se(3), and 2.38 and 2.27 for O(1) and O(2).[11, 12]

While the model proposed here gives an excellent fit to X-ray and neutron powder diffraction data, a couple of very weak reflections are observed in SAED patterns which are inconsistent

with the *Cmca* symmetry proposed, and which can't be explained by double diffraction. These reflections would be allowed in *C*222$_1$ symmetry, where the two S3 modes (modes 23 and 24) and Γ4– (mode 2) in the *P*1 distortion mode analysis would also be active. When this model was tested against the combined diffraction data it only gave a marginal reduction in R$_{wp}$ (by 0.056 %) for equivalent combined refinements, despite a significant increase in the number of structural parameters (28 to 50). The structure was essentially unchanged and we therefore prefer the *Cmca* model within the quality of the current data.

Table 3.2: *Structural parameters of La$_2$O$_2$ZnSe$_2$ from combined refinement using room temperature XRPD and NPD data in space group Cmca; a = 22.9332(2) Å, b = 17.80043(6) Å, c = 5.73241(6) Å; R$_{wp}$ = 5.233 %, R$_p$ = 4.433 % , and χ^2 = 6.538.*

| Site label	Wyckoff site	x	y	z	occupancy	B / Å^2	U$_{iso}$
La(1)	8e	0.25	0.1811(3)	0.25	1	0.27(9)	0.003(1)
La(2)	8f	0	-0.1785(3)	-0.2229(6)	1	0.16(7)	0.0020(9)
La(3)	16g	-0.3745(2)	0.3185(2)	0.2674(5)	1	0.27(6)	0.0034(8)
Zn(1)	8d	-0.4295(3)	0	0	1	0.9(1)	0.011(1)
Zn(2)	8d	-0.1893(5)	0	0	1	0.40(8)	0.005(1)
Se(1)	8e	0.25	0.4174(7)	0.25	1	0.6(1)	0.008(1)
Se(2)	8f	0	-0.4148(4)	-0.2109(9)	1	0.7(1)	0.009(1)
Se(3)	16g	-0.3735(3)	0.0835(4)	0.2600(6)	1	0.45(7)	0.0057(9)
O(1)	16g	-0.3121(5)	0.2469(2)	0.503(2)	1	0.66(8)	0.008(1)
O(2)	16g	0.4376(4)	0.2487(4)	0.5243(9)	1	0.26(6)	0.0029(8)
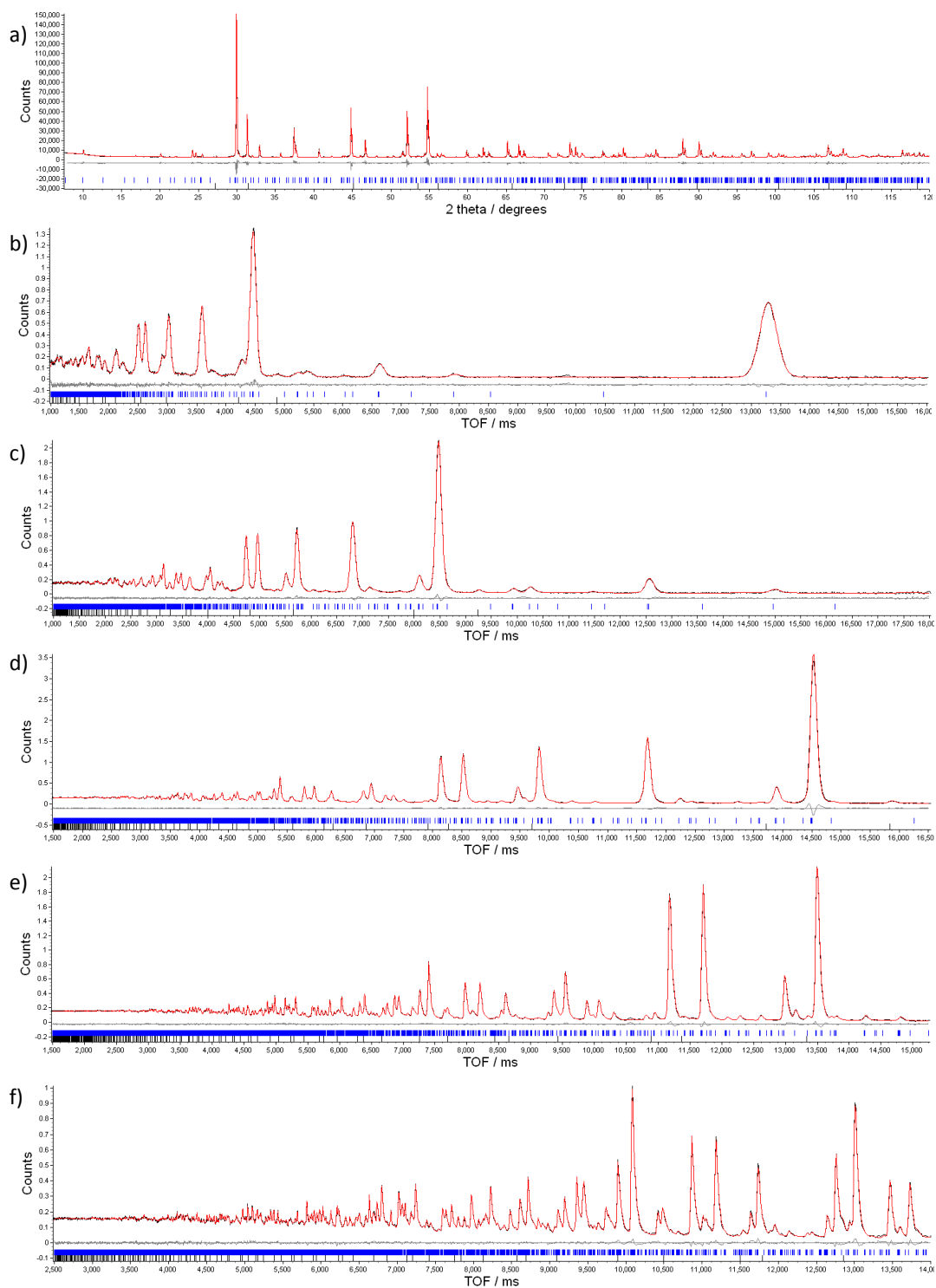
Figure 3.11: *Rietveld refinement profiles from combined refinement of (a) XRPD and (b) Gem 18° (c) 35° (d) 64° (e) 91° (f) 154° data at room temperature for La$_2$O$_2$ZnSe$_2$, space group Cmca. Tick marks show reflection positions for La$_2$O$_2$ZnSe$_2$ (top) and ZnSe (bottom, <1% by weight); AJT039 d9_06009 (XRPD), gem52355 (NPD).*

3.6.2 Single crystal X-ray diffraction

The structural model deduced from symmetry adapted distortion mode analysis and Rietveld analysis of powder diffraction was refined against the major component of the twinned single crystal X-ray diffraction data. 60 parameters were refined in the model: atomic positions, anisotropic displacement parameters for non-oxygen atoms and isotropic for oxygen sites. A good fit was obtained with R = 5.0 % and the structural models obtained from combined refinement of powder X-ray and neutron data and from single crystal X-ray diffraction are consistent. The maximum electron density peaks and holes from Fourier maps are relatively high, but these are located within 0.9 Å of La and Se atoms, and therefore do not suggest further atomic sites. With the La site occupancies fixed at 1 both Se and Zn site occupancies refine to within 3 esds of full occupancy, (the occupancy of oxygen sites were not refined due to the low sensitivity of oxygen in X-ray data), again suggesting that the compound is stoichiometric within the quality of the data. Crystallographic data for La$_2$O$_2$ZnSe$_2$ is listed in table 3.3, and final atomic coordinates and thermal displacement parameters in tables 3.4 and 3.5.

Table 3.3: *Crystallographic data for La$_2$O$_2$ZnSe$_2$.*

Sample code	12AJT013
Formula weight (g mol^{-1})	533.11
Crystal system	Orthorhombic
Space group	*Cmca*
z	16
a (Å)	22.904(5)
b (Å)	17.766(4)
c (Å)	5.7240(11)
Volume (Å^3)	2329.2(8)
Calculated density (g cm^{-1})	6.081
Crystal size (mm^3)	0.08 x 0.08 x 0.008
Temperature (K)	150
Diffractometer	Bruker AXS 6000
Radiation	MoKα
Index ranges (hkl)	0 ≤ h ≤ 32
	-9 ≤ k ≤ 24
	0 ≤ l ≤ 8
R$_{int}$	0.081
Extinction coefficient	11.1(10)
Reflections collected	3234
Independent reflections	1748
Number of refection I / sig I ≥ 3	808
R/wR	0.050/0.133
GOF	0.872
Electron density peak/hole	15.98/–18.10

Table 3.4: *Atomic coordinates and equivalent isotropic thermal displacement parameters for La$_2$O$_2$ZnSe$_2$, isotropic thermal displacement parameters for oxygen sites.*

Site label	Wyckoff site	x	y	z	occupancy	U$_{eq}$ /*U$_{(Iso)}$
La(1)	8e	0.25	0.1792(4)	0.25	1	0.0069
La(2)	8f	0	-0.1788(3)	-0.2234(3)	1	0.0053
La(3)	16g	-0.37499(3)	0.3178(3)	0.2704(2)	1	0.0074
Zn(1)	8d	-0.43053(9)	0	0	1	0.0071
Zn(2)	8d	-0.18950(10)	0	0	1	0.0045
Se(1)	8e	0.25	0.4154(5)	0.25	1	0.0072
Se(2)	8f	0	-0.4159(4)	-0.2136(6)	1	0.0048
Se(3)	16g	-0.37378(6)	0.0818(5)	0.2640(3)	1	0.0103
O(1)	16g	-0.3148(9)	0.2482(4)	0.4916(19)	1	*0.0006(19)
O(2)	16g	0.4347(10)	0.2498(4)	0.5239(14)	1	*0.003(2)

Table 3.5: *Anisotropic thermal displacement parameters for La$_2$O$_2$ZnSe$_2$.*

Site label	U11	U22	U33	U23	U13	U12
La(1)	0.0070(13)	0.0074(14)	0.0062(8)	0	-0.0001(4)	0
La(2)	0.0066(13)	0.0070(12)	0.0022(7)	-0.0032(8)	0	0
La(3)	0.0069(13)	0.0114(12)	0.0039(7)	0.0024(8)	-0.0003(2)	-0.0005(3)
Zn(1)	0.0039(9)	0.0088(11)	0.0087(9)	0.0003(14)	0	0
Zn(2)	0.0048(8)	0.0028(9)	0.0058(9)	0.0008(19)	0	0
Se(1)	0.0062(18)	0.007(2)	0.0082(14)	0	0.0009(6)	0
Se(2)	0.0064(17)	0.0038(18)	0.0041(8)	-0.0022(15)	0	0
Se(3)	0.0084(19)	0.017(3)	0.0051(12)	0.0026(8)	-0.0010(4)	0.0014(6)

3.6.3 Structure description

The structure of La$_2$O$_2$ZnSe$_2$ is closely related to that of LaOCuS, and contains fluorite-like [La$_2$O$_2$]$^{2+}$ layers, constructed of La$_4$O tetrahedra which edge-share forming layers perpendicular to the *b* axis of the material. These lanthanum oxide layers alternate with sheets of [ZnSe$_2$]$^{2-}$, constructed of ZnSe$_4$ tetrahedra. Due to the divalent nature of the transition metal relative to LaOCuS only half of the available tetrahedral sites are occupied within this layer. Selected bond lengths and angles are shown in table 3.6 and table 3.7 respectively.

Three other related divalent transition metal containing compounds have been reported: CeOMn$_{0.5}$Se, Ce$_2$O$_2$FeSe$_2$ and La$_2$O$_2$CdSe$_2$ and it is useful to consider their structures before discussing the Zn material.[2, 6, 13] In CeOMn$_{0.5}$Se the tetrahedral site in the antiflourite-like [MnSe$_2$]$^{2-}$ layers have been reported to be half-occupied in a disordered arrangement. In Ce$_2$O$_2$FeSe$_2$ the Fe^{2+} cations order to produce stripes of edge-shared FeSe$_4$ tetrahedra, figure 3.12b. In La$_2$O$_2$CdSe$_2$ Cd^{2+} ions order in the tetrahedral sites of the antifluorite-like layer such that the CdSe$_4$ tetrahedra corner share producing a checkerboard arrangement, figure 3.12c.

The ordering pattern of Zn^{2+} cations in La$_2$O$_2$ZnSe$_2$, figure 3.13, contains a mixture of edge and corner-sharing ZnSe$_4$ tetrahedra, resulting in alternating "checkerboard" and "stripe" regions along [100]. As a result the structure can be thought of as intermediate between Ce$_2$O$_2$FeSe$_2$ and La$_2$O$_2$CdSe$_2$. This Zn^{2+} ordering leads to corresponding structural distortions of the Zn(1)Se$_4$ edge-shared tetrahedra. As might be expected the Zn(1)–Zn(1) separation within the edge-shared tetrahedra is significantly longer than in an idealized structure, (3.22 Å compared to 2.87 Å), presumably to minimise electrostatic repulsions. The Γ1+ modes acting on Se(2) is responsible for the distortion of the Zn(1)Se$_4$ edge-shared tetrahedra, while the Γ1+ displacive mode acting on the La(2) sites then optimizes the bonding around Se(2). From geometric arguments we would expect a checkerboard arrangement to minimise electrostatic repulsions, compared the striped arrangement found in Ce$_2$O$_2$FeSe$_2$, a more covalent system. The differing cation arrangement between the Zn and Cd systems could be as a result of strain induced by size mismatch between the fluorite-like and antifluorite-like layers.

The zinc-blende of ZnSe structure has similar structural features to La$_2$O$_2$ZnSe$_2$, and consists of corner linked ZnSe$_4$ tetrahedra. The Zn-Se bonds are slightly longer than in ZnSe (~2.49 Å vs ~2.46 Å). While the Zn-Zn distances are shorter (~3.98 Å in corner shared regions and ~3.22 Å in the edge shared regions) than cation-cation distances in ZnSe (~4.023 Å).
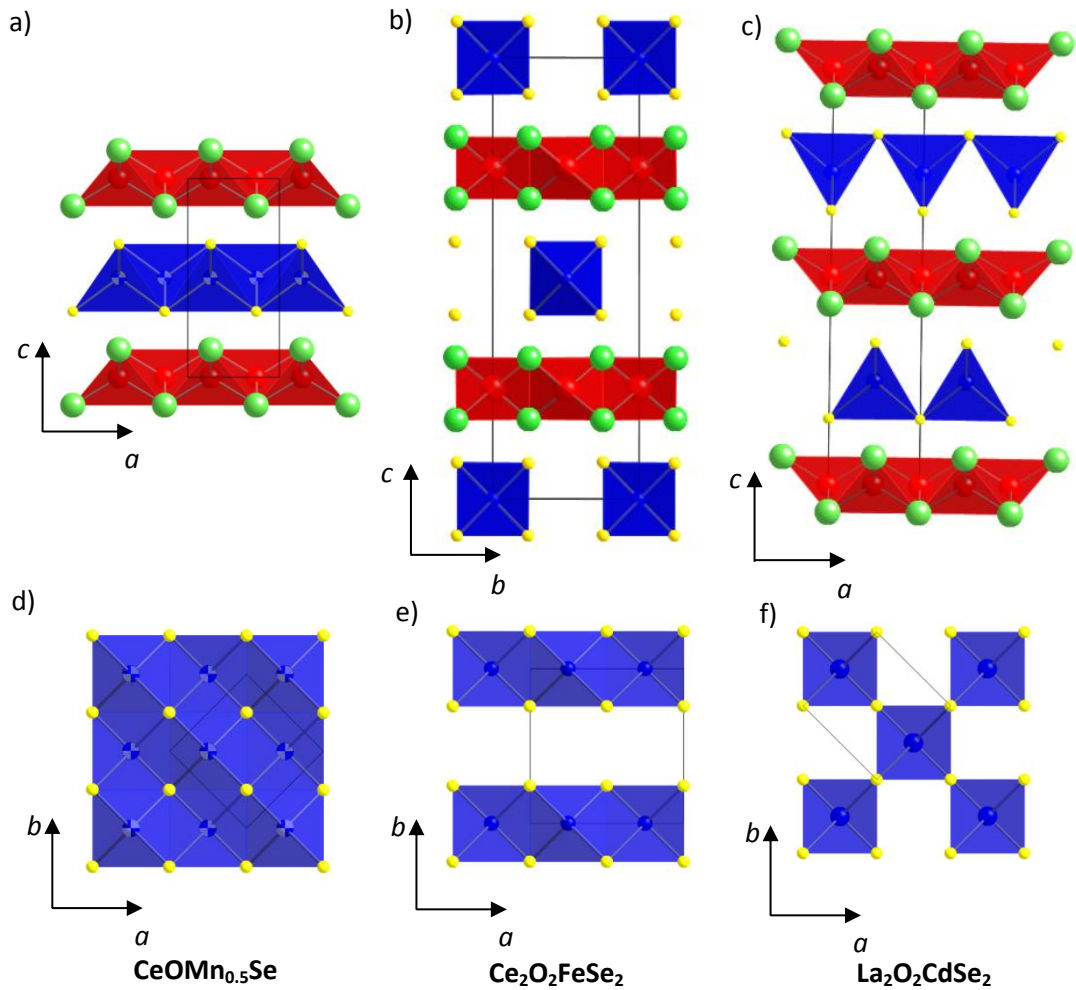
Figure 3.12: *(a) ZrCuSiAs type structure adopted by CeOMn$_{0.5}$Se with fluorite-like sheets of edge-linked Ce$_4$O tetrahedra (red) and antifluorite-like sheets of MnSe$_4$ tetrahedra (blue), Mn sites half occupied in a disordered arrangement, P4/nmm symmetry with a = b =4.0260(7) Å, c = 9.107(2) Å. (b) structure of Ce$_2$O$_2$FeSe$_2$, fluorite-like [Ce$_2$O$_2$]$^{2+}$ sheets (red), chains of FeSe$_4$ edge-sharing tetrahedra (blue), Imcb symmetry, a = 5.70040(3) Å, b = 5.71946(3) Å, c = 17.31342(9) Å. (c) Structure of La$_2$O$_2$CdSe$_2$, fluorite-like [La$_2$O$_2$]$^{2+}$ sheets (red), corner-sharing CdSe$_4$ tetrahedra (blue), P4$_2$/nmc symmetry, a = b = 4.0660(6) Å, c = 18.634(1) Å. (d) View down [001] of CeOMn$_{0.5}$Se showing disordered Mn^{2+} sites. (e) View down [001] in Ce$_2$O$_2$FeSe$_2$ showing chains of edge-shared FeSe$_4$ tetrahedra forming a stripe pattern. (f) View down [001] in La$_2$O$_2$CdSe$_2$ showing corner linked CdSe$_4$ tetrahedra; A^{3+} cations shown in green ,M^{2+} cations shown in blue, Se^{2-} anions shown in yellow, O^{2-} anions shown in red.*
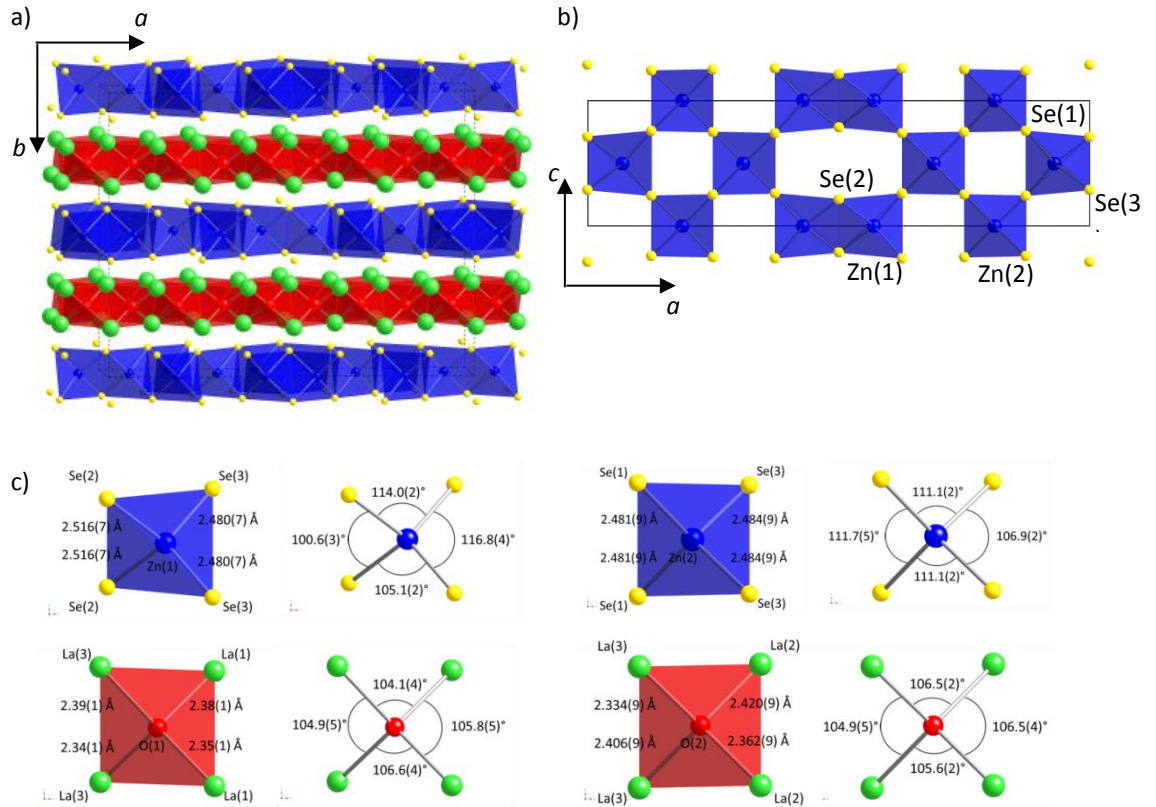
Figure 3.13: Crystal structure of La$_2$O$_2$ZnSe$_2$ showing (a) alternating [La$_2$O$_2$]$^{2+}$ (red) and [ZnSe$_2$]$^{2-}$ (blue) layers along [010] , (b) ordering pattern of Zn^{2+} cations in [ZnSe$_2$]$^{2-}$ layers, and (c) coordination polyhedra for Zn and O site; La = green, Zn = blue, O = red and Se = yellow.

Table 3.6: Selected bond lengths for La$_2$O$_2$ZnSe$_2$ from combined refinement using room temperature XRPD and NPD data in space group Cmca.

La(1)-O(1)	2 × 2.35(1) Å	Zn(1)-Se(2)	2 × 2.521(7) Å
	2 × 2.38(1) Å		
La(2)-O(2)	2 × 2.370(8) Å	Zn(1)-Se(3)	2 × 2.470(7) Å
	2 × 2.414(8) Å		
La(3)-O(1)	1 × 2.35(1) Å	Zn(2)-Se(1)	2 × 2.481(9) Å
	1 × 2.39(1) Å		
La(3)-O(2)	1 × 2.337(8) Å	Zn(2)-Se(3)	2 × 2.484(9) Å
	1 × 2.409(8) Å		

Table 3.7: Selected bond angles for La$_2$O$_2$ZnSe$_2$ from combined refinement using room temperature XRPD and NPD data in space group Cmca.

La(1)-O(1)-La(1)	105.8(5)°	Se(2)-Zn(1)-Se(2)	100.6(3)°
La(1)-O(1)-La(3)	104.1(4), 106.6(4)°	Se(3)-Zn(1)-Se(3)	116.9(3)°
La(2)-O(2)-La(2)	106.5(4)°	Se(2)-Zn(1)-Se(3)	105.1(2)° 114.0(2)°
La(2)-O(2)-La(3)	105.6(2), 106.5(2)°	Se(1)-Zn(2)-Se(1)	111.7(5)°
La(3)-O(1)-La(3)	105.4(5)°	Se(3)-Zn(2)-Se(1)	111.1(2)°
La(3)-O(2)-La(3)	104.9(5)°	Se(3)-Zn(2)-Se(3)	109.2(5)° 106.9(3)°

3.7 Variable temperature structural studies

Variable temperature XRPD data were collecting using the d9 diffractometer, data were Rietveld refined in TOPAS using the local routine multitopas.[14] Figure 3.14 shows the change in unit cell parameters between 12 K and 300 K. A smooth decrease in unit cell parameters on cooling is observed and there is no evidence for any major structural transitions in this temperature range. The volume thermal expansion coefficient from 0 to 300 K is $20.5(1) \times 10^{-6}$ K^{-1}. The thermal expansion of the unit cell parameters for La$_2$O$_2$ZnSe$_2$ can be described using an Einstein-type function, equation 3.1, with two terms, where a_0 is the cell parameter at 0 K, θ is the Einstein temperature and C is a refinable coefficient.[15] Refined parameters for this model are given in table 3.8.

$$ln\left(\frac{a}{a_0}\right) = \sum_i \frac{C_i}{exp\left(\frac{\theta_i}{T}\right) - 1} \qquad \text{eqn 3.1}$$

Table 3.8: *Refined parameters for model of thermal expansion of La$_2$O$_2$ZnSe$_2$.*

	a	b	c
a_0 or b_0 or c_0 (Å)	22.8845(2)	17.7538(1)	5.72036(5)
C_1 (10^{-6})	5.4(4)	7.6(5)	8.0(7)
θ_1 (K)	116(15)	137(11)	213(20)
C_2 (10^{-6})	11(1)	7.8(4)	9.5(9)
θ_2 (K)	866(91)	665(68)	1224(524)
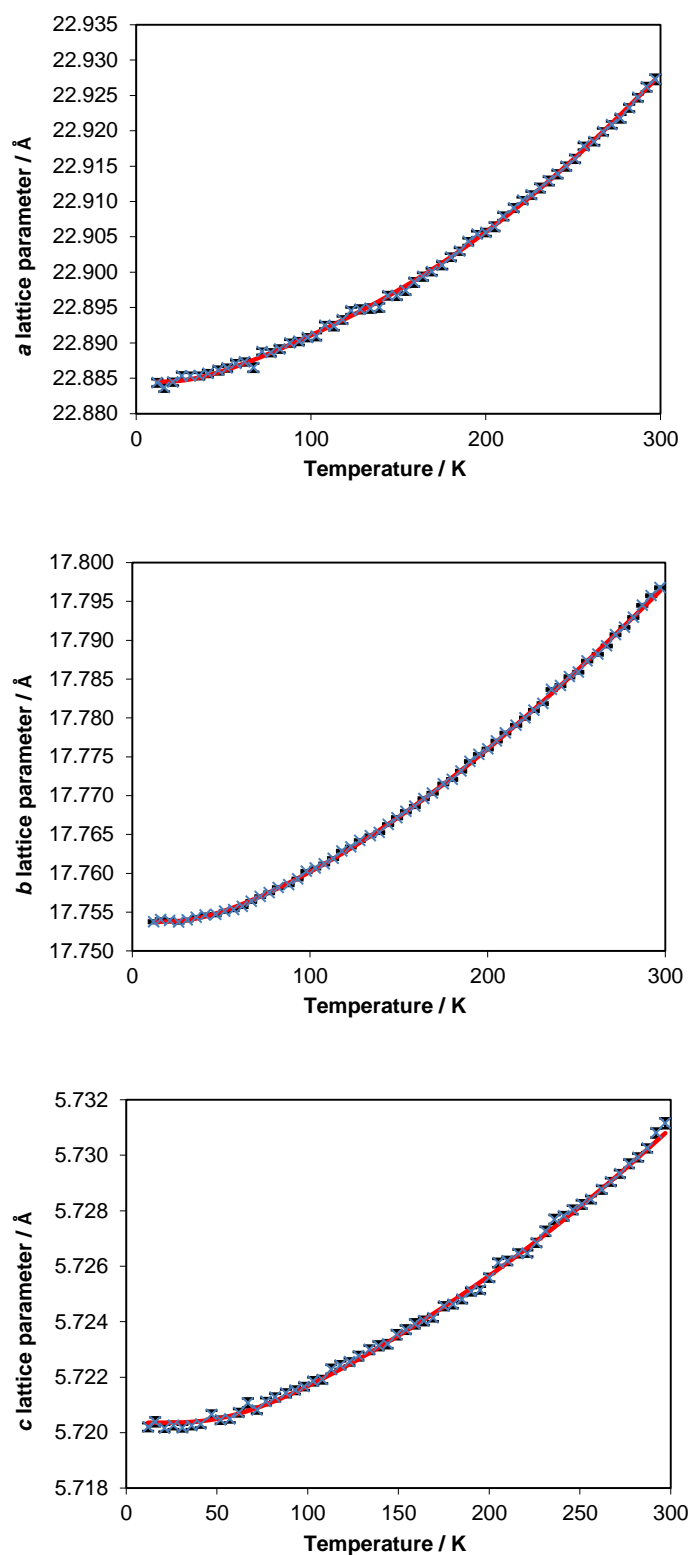
Figures 3.14: *Lattice parameters for La$_2$O$_2$ZnSe$_2$ as a function of temperature (blue), obtained from sequential refinements using XRPD data, red line = Einstein type function.*

3.8 Optical properties

Diffuse reflectance spectroscopy was used to measure the optical band gap of La$_2$O$_2$ZnSe$_2$ diluted in dry NaCl. The spectrum after Kubelka-Munk treatment[16, 17] is shown in figure 3.15. The spectrum shows a slight increase in F(R) with some curvature from low energy (~2 eV), which might indicate the presence of minor Se or ZnSe impurities.[18] A large transition which is attributed to the optical band gap of La$_2$O$_2$ZnSe$_2$ occurs at an energy of 3.4(2) eV. This optical band gap is comparable with the value reported for La$_2$O$_2$CdSe$_2$ (3.3 eV), and consistent with the colour of the two samples (La$_2$O$_2$ZnSe$_2$ is cream, La$_2$O$_2$CdSe$_2$ is pale yellow). This band gap is significantly larger than is reported for binary ZnSe (~2.67 eV).[19, 20] The increase in band gap is likely to be the result of decreased bandwidth and/or band narrowing due to the layered nature of the material.[21]
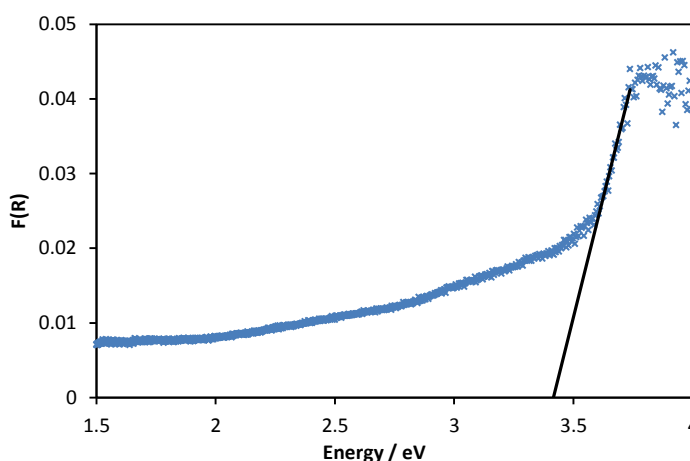
Figure 3.15: *Diffuse reflectance spectrum after Kubelka-Munk treatment for La$_2$O$_2$ZnSe$_2$ diluted in dry NaCl, showing interband transition corresponding to an optical band gap of 3.4(2) eV.*

3.9 Conclusions

In conclusion we have described the synthesis, structural characterisation and optical measurements for the new quaternary oxyselenide La$_2$O$_2$ZnSe$_2$. This material was synthesised via standard solid state methods, and the structure solved via a combination of symmetry adapted distortion mode analysis and Rietveld refinement. The material has been shown to adopt a ZrCuSiAs-related structure based on alternating fluorite-like and antiflourite-like sheets of La$_4$O and ZnSe$_4$ tetrahedra, with ordering of the Zn^{2+} cations over the tetrahedral sites in the [ZnSe$_2$]$^{2-}$ layers. The ordering pattern is unusual and not one we would expect from purely electrostatic arguments and contains both stripe-like and checkerboard-like features. As such it is intermediate between the ordering patterns observed for Ce$_2$O$_2$FeSe$_2$ and

La$_2$O$_2$CdSe$_2$. Diffuse reflectance measurements indicate that La$_2$O$_2$ZnSe$_2$ is a wide band-gap semiconductor with an optical band gap of 3.4(2) eV, comparable with the band gap reported for La$_2$O$_2$CdSe$_2$. The structure and optical properties on La$_2$O$_2$ZnSe$_2$ along with electronic structure calculations have been reported in the joint publication with McCabe.[5]

References

1.	McCabe, E. E., Free, D. G., Mendis, B. G., Higgins, J. S., and Evans, J. S. O., *Chemistry of Materials*, 2010, **22**, 6171-6182
2.	McCabe, E. E., Free, D. G., and Evans, J. S. O., *Chemical Communications*, 2011, **47**, 1261-1263
3.	Hiramatsu, H., Ueda, K., Kamiya, T., Ohta, H., Hirano, M., and Hosono, H., *Journal of Physical Chemistry B*, 2004, **108**, 17344-17351
4.	Baranov, I. Y., Dolgikh, V. A., and Popovkin, B. A., *Zhurnal Neorganicheskoi Khimii*, 1996, **41**, 1916-1919
5.	Tuxworth, A. J., McCabe, E. E., Free, D. G., Clark, S. J., and Evans, J. S. O., *Inorganic Chemistry*, 2013, **52**, 2078-2085
6.	Ijjaali, I., Mitchell, K., Haynes, C. L., McFarland, A. D., Van Duyne, R. P., and Ibers, J. A., *Journal of Solid State Chemistry*, 2003, **176**, 170-174
7.	Free, D., *PhD thesis: Synthesis and Properties of New Oxychalcogenide materials*, Durham University, 2010
8.	*Andrew Tuxworth, M.Chem. project, Durham*, 2010
9.	Kerman, S., Campbell, B. J., Satyavarapu, K. K., Stokes, H. T., Perselli, F., and Evans, J. S. O., *Acta Crystallographica Section A*, 2012, **68**, 222-234
10.	Campbell, B. J., Stokes, H. T., Tanner, D. E., and Hatch, D. M., *Journal of Applied Crystallography*, 2006, **39**, 607-614
11.	Brese, N. E. and Okeeffe, M., *Acta Crystallographica Section B-Structural Science*, 1991, **47**, 192-197
12.	Brown, I. D. and Altermatt, D., *Acta Crystallographica Section B-Structural Science*, 1985, **41**, 244-247
13.	Hiramatsu, H., Ueda, K., Kamiya, T., Ohta, H., Hirano, M., and Hosono, H., *Journal of Materials Chemistry*, 2004, **14**, 2946-2950
14.	Evans, J. S. O., *'Phenixlogfiles', 1999*,
15.	Wang, K. and Reeber, R. R., *Applied Physics Letters*, 2000, **76**, 2203-2204
16.	Kortum, G., Braun, W., and Herzog, G., *Angewandte Chemie-International Edition*, 1963, **75**, 653-404
17.	Tandon, S. P. and Gupta, J. P., *Physica Status Solidi*, 1970, **38**, 363-367
18.	Peng, Q., Dong, Y. J., and Li, Y. D., *Angewandte Chemie-International Edition*, 2003, **42**, 3027-3030
19.	Adachi, S. and Taguchi, T., *Physical Review B*, 1991, **43**, 9569-9577
20.	Aven, M., Marple, D. T. F., and Segall, B., *Journal of Applied Physics*, 1961, **32**, 2261-2265
21.	Zhu, J.-X., Yu, R., Wang, H., Zhao, L. L., Jones, M. D., Dai, J., Abrahams, E., Morosan, E., Fang, M., and Si, Q., *Physical review letters*, 2010, **104**, 216405

Chapter 4: Synthesis, Structure and Properties of the Oxychalcogenide Series $A_4O_4TiSe_4$ (A = Sm, Gd, Tb, Dy, Ho, Er, & Y)

4.1 Introduction

The ZrCuSiAs structure type adopted the by AOFeAs superconductor family can be described as containing alternating layers of fluorite-like edge-shared A_4O tetrahedra and antifluorite-like edge-shared FeAs$_4$ tetrahedra. The A site is in a ASe$_4O_4$ 4+4 distorted square antiprismatic coordination environment and links the two layers together. On changing the anion in the antifluorite layer from group 15 to group 16 (i.e. As^{3-} to Se^{2-}) there are two ways of charge balancing via the transition metal. By moving to a monovalent cation such as Cu$^+$ one creates AOCuSe materials, which we could write as $[A$OSe$]_nM$ with $n = 1$. Alternatively we could retain the 2+ transition metal and charge balance requires 50 % site occupancy, corresponding to a composition AOFe$_{0.5}$Se or A_2O_2FeSe$_2$ ($[A$OSe$]_2M$ or $[A$OSe$]_nM$ where $n = 2$). Two basic structure types have been reported for this composition. α-Ce$_2O_2$FeSe$_2$ adopts a structure directly related to LaOFeAs where half of the tetrahedral sites in the antifluorite layers are occupied in an ordered arrangement, giving stripes of edge-shared tetrahedra of $[$FeSe$_2]^{2-}$ composition,[1] as discussed in Chapter 3; other 2$^+$ metals (Mn, Zn, Cd) adopt different intralayer ordering patterns within the $[M$Se$_2]^{2-}$ layers.[2-4] Alternatively La$_2O_2$FeSe$_2$ can adopt a different structural type, in which the fluorite-like rare earth oxide 2D layers are split into infinite 1D ribbons four tetrahedra in width, known as the β form.[5] Fe is then found in a mixture of FeSe$_4$ tetrahedral and FeSe$_4O_2$ octahedral coordination environments.

This chapter will focus on the $n = 4$ member of the $[A$OSe$]_nM$ series, whose structure has strong similarities to β-La$_2O_2$Se$_2$Fe. The only previously reported member of this family is Gd$_4O_4$TiSe$_4$. Single crystals of this phase, along with its crystal structure and magnetic properties were originally reported by Meerschaut.[6] Like β-La$_2O_2$FeSe$_2$, the structure contains fluorite-like 1D ribbons four tetrahedra in width, linked by chains of edge-shared TiSe$_4O_2$ octahedra, and is shown later in figure 4.3. In terms of the transition metal coordination environment, the α and β-A_2O_2FeSe$_2$ and Gd$_4O_4$TiSe$_4$ structures form a series which ranges from containing exclusively MSe$_4$ tetrahedra (M = transition metal) to mixed MSe$_4O_2$ octahedra and MSe$_4$ tetrahedra to exclusively MSe$_4O_2$ octahedra.

Ti containing oxyselenides are relatively rare. Previously reported examples include $A_{3.67}O_3Ti_2Se_6$ (A = Ce, Nd, Sm), La$_4O_4Ti_2Se_5$, La$_6O_5Ti_3Se_9$ and Gd$_4O_4$TiSe$_4$, all of which contain chains of TiSe$_4O_2$ distorted edge-sharing octahedra connecting rare-earth oxide units.[6-8] $A_3O_8Ti_3Se_2$ (A = Sm, Nd) is a more oxygen rich composition and contains TiO$_6$ and TiO$_5$Se

octahedra.[9, 10] This chapter will discuss the synthesis, structure and magnetic properties of new $A_4O_4TiSe_4$ (A = Sm, Gd, Tb, Dy, Ho, Er and Y) materials. The properties of these materials have been investigated using X-ray powder diffraction, SQUID magnetometry and conductivity measurements. Much of the work has been published.[11]

4.2 Synthesis

Black polycrystalline samples of $A_4O_4TiSe_4$ (A= Sm, Gd, Tb, Dy, Ho, Er and Y) composition were synthesised using the procedures outlined in Section 2.2.4. $Gd_4O_4TiSe_4$ has been prepared as a bulk powder for the first time; the other 6 rare-earth analogues have not been previously prepared. It was not possible to synthesise all samples as single phase products, weight percentage of the target phases achieved are given in table 4.1. For A = Gd to Ho & Y essentially phase pure samples (impurities < 1% by weight) were achived. For Sm, the largest rare earth phase accessible, the highest phase purity obtained was ~90 weight % (Sm_2O_2Se and $SmSe_2$ impurities); for the smallest rare earth, Er, purity was ~75 % (Er_2O_2Se and $TiSe_2$ impurities). A_2O_2Se was the minor impurity phase present in the other syntheses. We could not prepare this phase for larger or smaller rare earths under the synthetic conditions used, nor could we prepare $Eu_4O_4TiSe_4$. The reaction product consisted of a mix of Eu^{2+} and Eu^{3+} compounds: EuSe, $Eu_2Ti_2O_7$ and $Eu_4O_4Se_3$.

Table 4.1: $A_4O_4TiSe_4$ syntheses indicating successful compositions and approximate crystalline phase purity,(±2 %).

A^{3+}	Nd	Pm	Sm	Eu	Gd	Tb	Dy	Ho	Er	Tm	Yb	Y
Prepared	✗	-	✓	✗	✓	✓	✓	✓	✓	-	✗	✓
Weight % purity	-	-	90	-	100	99	100	99	75	-	-	100

4.3 Powder X-ray diffraction and Rietveld refinement of A₄O₄TiSe₄

The room temperature structures of each material were refined from powder X-ray diffraction data collected on a Bruker d8 diffractometer (either d7 or d9). The seven compounds are all isostructural and adopt the C2/*m* monoclinic structure reported by Meerschaut *et al*. for $Gd_4O_4TiSe_4$.[6] Rietveld refinements were performed in TOPAS and included variables to describe both structural and instrumental parameters. Instrumental parameters included 18 Chebychev polynomial coefficients to model the background, a sample height term, a scale parameter for the $A_4O_4TiSe_4$ phase, 4 terms to model a pseudo-Voigt (TCHz) peak-shape, and a term to model the axial divergence. The structural parameters refined included 4 cell parameters (*a*, *b*, *c* and β), 8 atomic positions, 6 isotropic thermal parameters (one for each site other than oxygen,

where a single thermal parameter was refined for both sites). Due to the low sensitivity of X-ray data to oxygen positions, the oxygen site coordinates had to be fixed at the single crystal derived values reported by Meerschaut for the $Gd_4O_4TiSe_4$ analogue. Additional parameters were included to model minor impurity phases or, in the case of $Gd_4O_4TiSe_4$, a silicon internal standard. Specific parameters included in each refinement are given in Appendix 2. XRPD data were also collected at temperatures down to 12 K using a PheniX cryostat. Unit cell parameters derived from Rietveld refinements of data collected at 295 and 12 are listed in table 4.2.

Table 4.2: *Unit cell parameters from Rietveld analysis of XRPD data in space group C2/m for $A_4O_4TiSe_4$ at 295 and 12 K. Numbers in parentheses are Rietveld-derived standard uncertainties.*

		$Sm_4O_4TiSe_4$	$Gd_4O_4TiSe_4$	$Tb_4O_4TiSe_4$	$Dy_4O_4TiSe_4$	$Ho_4O_4TiSe_4$	$Er_4O_4TiSe_4$	$Y_4O_4TiSe_4$
a / Å	295 K	15.8920(2)	15.7901(3)	15.6791(3)	15.5962(2)	15.5577(2)	15.4992(4)	15.5693(2)
	12 K	15.8601(3)	15.7809(3)	15.6581(3)	15.5636(3)	15.5259(2)	-	15.5541(1)
b / Å	295 K	3.79668(4)	3.75792(5)	3.74085(7)	3.71985(4)	3.70315(4)	3.68819(7)	3.71079(4)
	12 K	3.78966(5)	3.74887(5)	3.73413(6)	3.71383(5)	3.69456(4)	-	3.70168(4)
c / Å	295 K	9.7088(1)	9.6641(1)	9.6179(2)	9.5886(1)	9.5686(1)	9.5449(2)	9.5911(1)
	12 K	9.6800(2)	9.6462(2)	9.5883(2)	9.5682(2)	9.5485(1)	-	9.5702(1)
beta / °	295 K	117.5170(9)	117.672(1)	117.544(1)	117.532(1)	117.6000(9)	117.556(2)	117.5407(9)
	12 K	117.493(1)	117.736(1)	117.507(1)	117.491(1)	117.6123(1)	-	117.578(1)
volume / Å³	295 K	519.53(1)	507.86(1)	500.18(2)	493.29(1)	488.54(1)	483.73(2)	491.33(1)
	12 K	516.10(1)	505.10(1)	497.25(2)	490.59(2)	485.33(1)	-	488.41(1)

Rietveld refinement profiles of XRPD data collected at room temperature are shown in figure 4.1 for the seven compositions synthesised. Structural parameters refined for each composition are given in table 4.3, along with crystallographic agreement factors. Full details of each refinement are given in Appendix 2. The Rietveld refinements at 12 K indicate that the structure is unchanged.
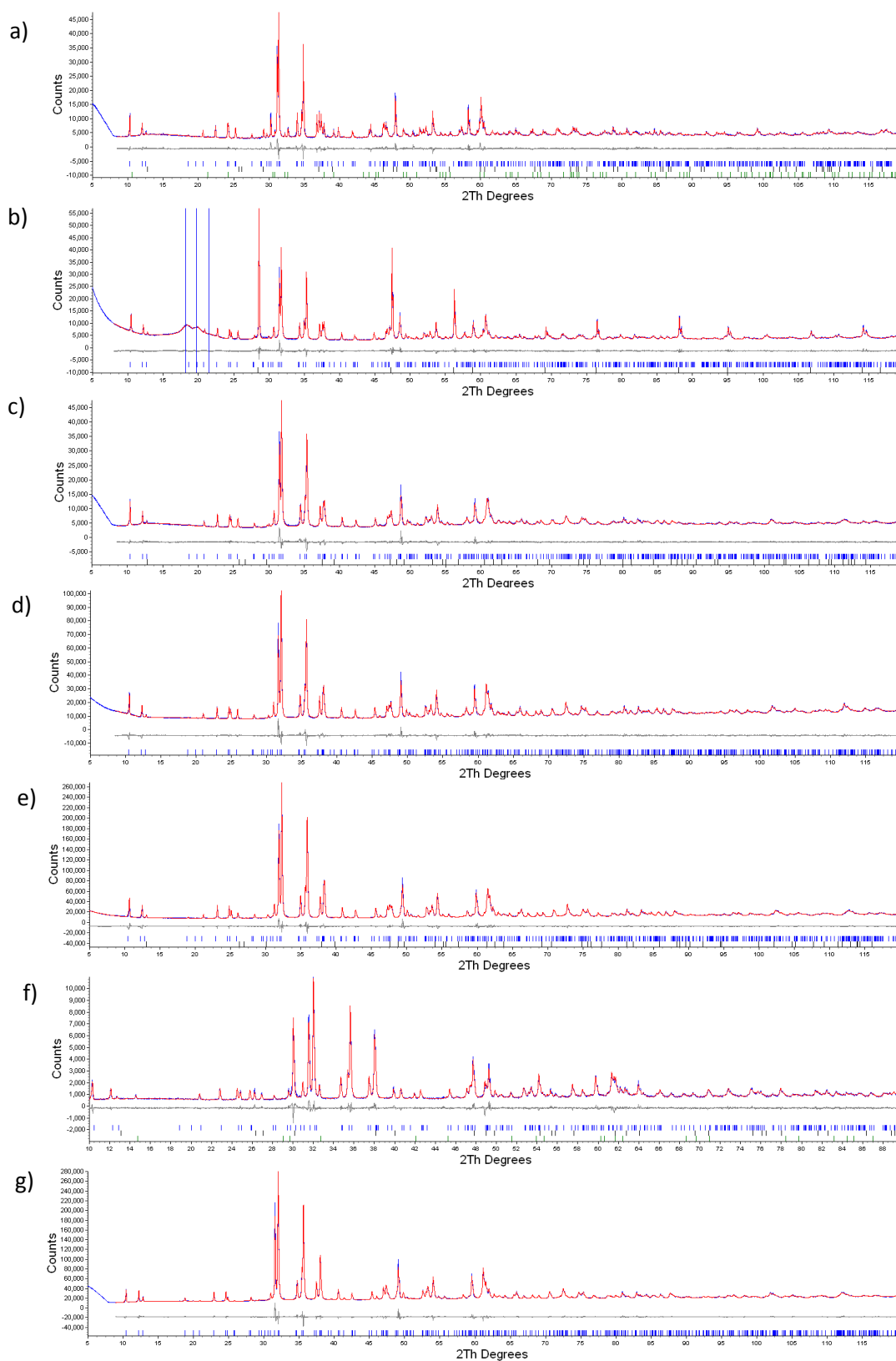
Figure 4.1: *Rietveld refinement profiles of room temperature XRPD data for a) $Sm_4O_4TiSe_4$, b) $Gd_4O_4TiSe_4$, c) $Tb_4O_4TiSe_4$, d) $Dy_4O_4TiSe_4$, e) $Ho_4O_4TiSe_4$, f) $Er_4O_4TiSe_4$, g) $Y_4O_4TiSe_4$; tick marks show reflection positions for $A_4O_4TiSe_4$ (top, blue)), tick marks for impurity phases below.*

Table 4.3: *Results of Rietveld analysis of X-ray data of $A_4O_4TiSe_4$ at room temperature.*

	Sm	Gd	Tb	Dy	Ho	Er	Y
A ionic radii / Å	1.079	1.053	1.04	1.027	1.015	1.004	1.019
Parameters	51	56	46	43	46	59	43
R_{wp} / %	3.710	3.422	3.326	2.861	3.939	5.489	2.986
R_{Bragg} / %	2.226	1.752	2.057	1.710	1.504	1.519	1.545
R_p / %	2.560	2.514	2.271	1.867	2.621	3.995	1.900
gof	2.556	2.407	2.411	3.183	5.007	1.755	4.551
a / Å	15.8920(2)	15.7901(3)	15.6791(3)	15.5962(2)	15.5577(2)	15.4992(4)	15.5693(2)
b / Å	3.79668(4)	3.75792(5)	3.74085(7)	3.71985(4)	3.70315(4)	3.68819(7)	3.71079(4)
c / Å	9.7088(1)	9.6641(1)	9.6179(2)	9.5886(1)	9.5686(1)	9.5449(2)	9.5911(1)
beta / °	117.5170(9)	117.672(1)	117.544(1)	117.532(1)	117.6000(9)	117.556(2)	117.5407(9)
volume / Å^3	519.53(1)	507.86(1)	500.18(2)	493.29(1)	488.54(1)	483.73(2)	491.33(1)
xA_1	0.4782(2)	0.4749(2)	0.4766(2)	0.4758(1)	0.4757(1)	0.4770(3)	0.4756(1)
xA_2	0.2782(2)	0.2753(2)	0.2767(2)	0.2766(2)	0.2771(1)	0.2768(3)	0.2774(2)
zA_2	0.6702(3)	0.6679(3)	0.6687(3)	0.6684(2)	0.6685(2)	0.6699(4)	0.6690(3)
zA_2	0.6768(3)	0.6740(3)	0.6744(3)	0.6743(2)	0.6741(2)	0.6732(4)	0.6727(2)
xSe_1	0.6229(3)	0.6207(3)	0.6239(3)	0.6245(2)	0.6255(2)	0.6255(5)	0.6249(2)
xSe_2	0.6207(4)	0.6149(3)	0.6175(4)	0.6168(3)	0.6170(2)	0.6168(5)	0.6167(2)
zSe_1	0.0156(6)	0.0139(6)	0.0160(5)	0.0159(4)	0.0158(3)	0.0184(9)	0.0152(3)
zSe_2	0.6365(5)	0.6340(5)	0.6360(5)	0.6356(4)	0.6352(3)	0.6352(7)	0.6339(3)
xO_1^*	0.44900	0.44900	0.44900	0.44900	0.44900	0.44900	0.44900
xO_2^*	0.31630	0.31630	0.31630	0.31630	0.31630	0.31630	0.31630
zO_1^*	0.78010	0.78010	0.78010	0.78010	0.78010	0.78010	0.78010
zO_2^*	0.59130	0.59130	0.59130	0.59130	0.59130	0.59130	0.59130
A_1 U_{iso} / 100x$Å^2$	0.62(6)	1.07(6)	1.15(6)	0.26(5)	0.80(4)	1.6(1)	1.22(5)
A_2 U_{iso} / 100x$Å^2$	0.94(6)	0.76(6)	0.92(6)	0.08(5)	0.77(4)	1.6(1)	1.13(5)
Se_1 U_{iso} / 100x$Å^2$	1.2(1)	0.82(9)	0.80(8)	0.17(6)	0.99(5)	2.4(2)	1.59(5)
Se_2 U_{iso} / 100x$Å^2$	1.3(1)	1.43(9)	1.7(1)	0.75(7)	1.16(5)	2.1(2)	1.69(6)
Ti_1 U_{iso} / 100x$Å^2$	0.4(2)	2.5(3)	1.7(3)	1.1(2)	1.4(1)	1.8(5)	1.7(7)
$O_{1,2}$ U_{iso} / 100x$Å^2$	1.8(3)	0.4(2)	1.2(2)	0.5(2)	0.9(1)	2.6(4)	1.6(1)

Atoms on special positions: $yA_1 = 0$, $yA_2 = 0.5$, $ySe_1 = 0$, $ySe_2 = 0.5$, $xTi = 0$, $yTi = 0$, $zTi = 0$, $yO_1 = 0.5$, $yO_2 = 0$.

* Oxygen atom positions fixed

4.4 Structure

The structure of these $A_4O_4TiSe_4$ materials is shown in figure 4.2, it contains some similarities to the LaOFeAs structure, with oxide and chalcogenide ions segregated into layers, which can be thought of a building blocks. Ti sites within the structure disrupt the infinite $[A_2O_2]^{2+}$ fluorite-like layers found in LaOFeAs, hence a zig-zag pattern of $[A_2O_2]^{2+}$ 1D ribbons with finite width is observed. Oxide ions are found within these infinite ribbons of 4 edge-sharing tetrahedra which run parallel to the b-axis and contain both A_4O and A_3TiO oxygen coordination environments. There are two crystallographically independent A^{3+} ions which have either ASe_4O_4 or ASe_5O_3 4+4 square antiprismatic coordination environments, figure 4.2. The ASe_4O_4 square antiprism of $A2$ is similar to that found in LaOFeAs phases, though with a small distortion due to the loss of 4-fold symmetry in this system; this is shown in figure 4.3. Due to the finite width of the tetrahedral ribbons, one oxygen atom is replaced by selenium in the $A1$ site coordination sphere forming ASe_5O_3 units.

The tetrahedral (A_4O and A_3TiO containing) ribbons are interconnected by $TiSe_4O_2$ octahedra which themselves form edge-shared chains parallel to the b-axis. Se sites in the $TiSe_4O_2$ octahedra form part of the $A1$ ASe_5O_3 coordination polyhedra, whilst the O sites are those (O1) at the edge of the tetrahedral ribbons with A_3TiO pseudo-tetrahedral coordination, figure 4.2. Work by Meerschaut at al. on the only phase previously reported, $Gd_4O_4TiSe_4$, shows the U_{22} parameter for Ti is much larger than for other atoms while the U_{33} parameter is particularly small, as shown in figure 4.2b.[6] Figure 4.4 shows that there is an essentially smooth increase in cell parameters and unit cell volume with A site ionic radius, providing evidence of a smooth change of the structural building blocks across the series.
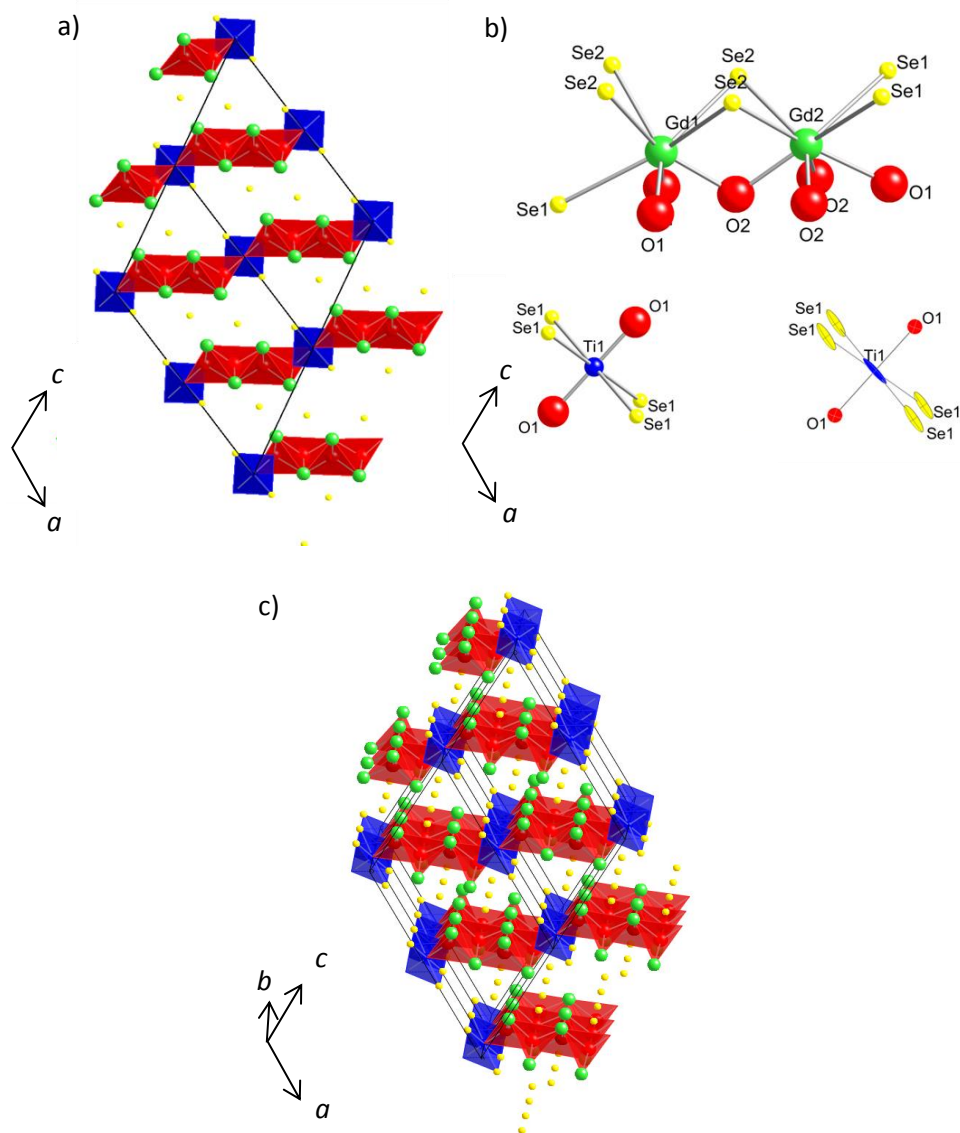
Figure 4.2: *a) Illustration of the $A_4O_4TiSe_4$ crystal structure (C2/m symmetry), A_4O & A_3TiO edge sharing tetrahedral ribbons in red, chains of edge-sharing $TiSe_4O_2$ in blue. b) Polyhedral environments of selected atoms, including anisotropic thermal parameters for $TiSe_4O_2$ octahedra as reported for $Gd_4O_4TiSe_4$ by Meerschaut et al..[6] c) Illustration of the $A_4O_4TiSe_4$ crystal structure A_4O & A_3TiO edge sharing tetrahedral ribbons in red along [010], chains of edge-sharing $TiSe_4O_2$ in blue along [010]. Rare earth = green, titanium = blue, selenium = yellow, and oxygen = red.*
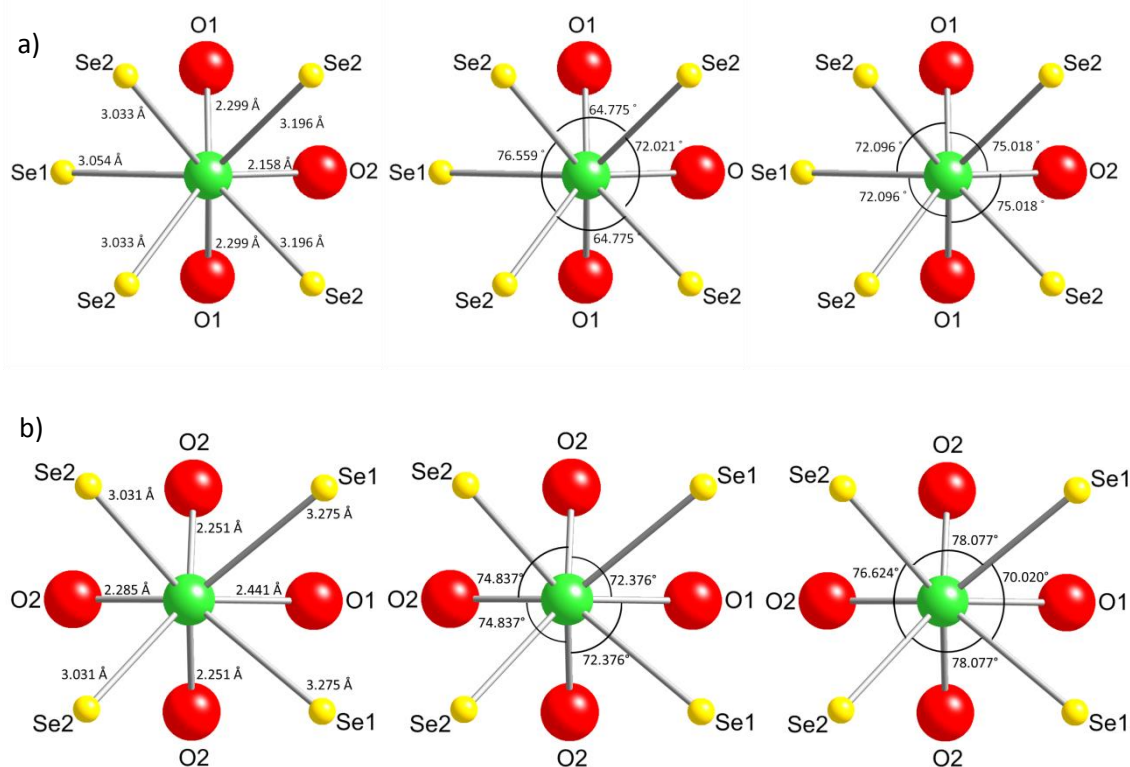
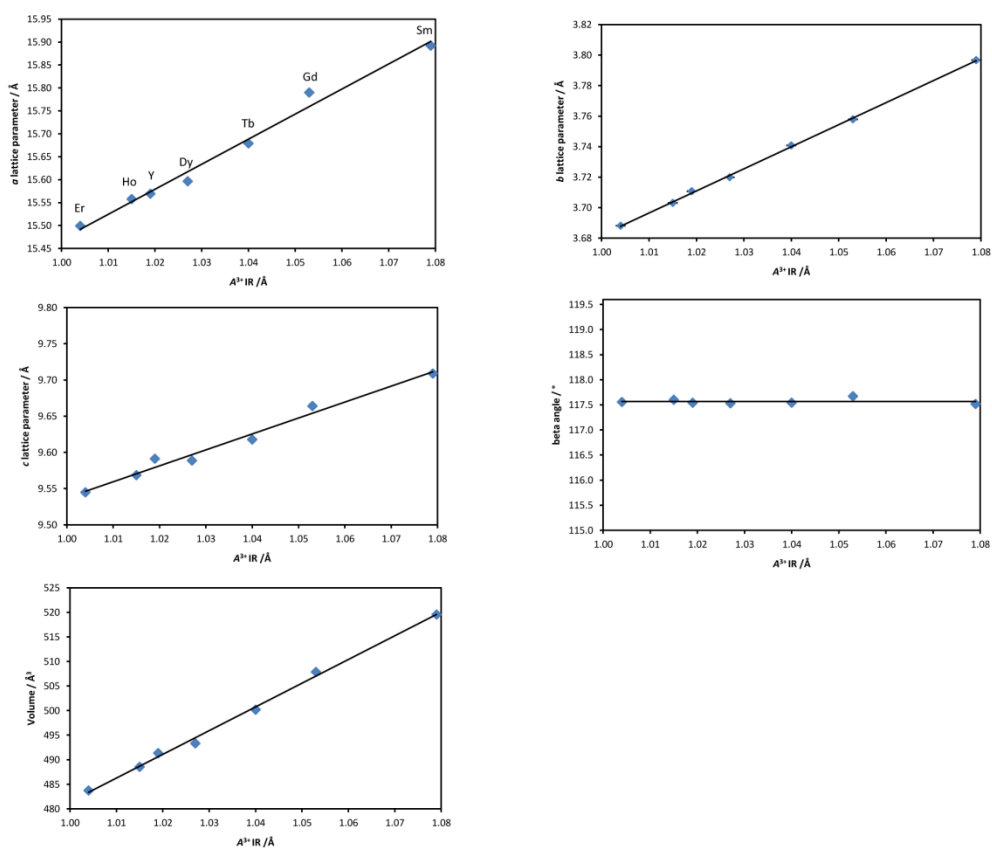**Figure 4.3:** *Local environment around a) A1 and b) A2 sites.*

Figure 4.4: *The effect of increasing rare-earth radius on the unit cell parameters of $A_4O_4TiSe_4$, error bars contained within the data points. Ionic radii are the values reported by Shannon.*[12]

101

In addition to the relationship to LaOFeAs it is useful to compare this structure to β-$La_2O_2MSe_2$ (M = Fe, Mn) i.e. $A_4O_4M_2Se_4$. This structure contains similar infinite ribbons of 4 edge-shared tetrahedra with A_4O and A_3MO coordination.[5] These ribbons are again connected by octahedral MO_2Se_4 units, which edge share to produce 1 dimension chains (figure 4.5). The major difference between the two structures is that in $A_4O_4TiSe_4$ materials the rare-earth oxide ribbons are parallel to each other on either side of the joining octahedra, while in $La_2O_2MnSe_2$ they are at ~128° to each other. The difference presumably arises from the requirement to provide a second transition metal coordination site in the $La_2O_2MSe_2$ composition. The volume per A^{3+} ion in the unit cell is smaller for $A_4O_4TiSe_4$ (~65 Å^3 to ~60 Å^3) compared with $La_2O_2MnSe_2$ (~72 Å^3), and therefore represents a more dense packing arrangement.
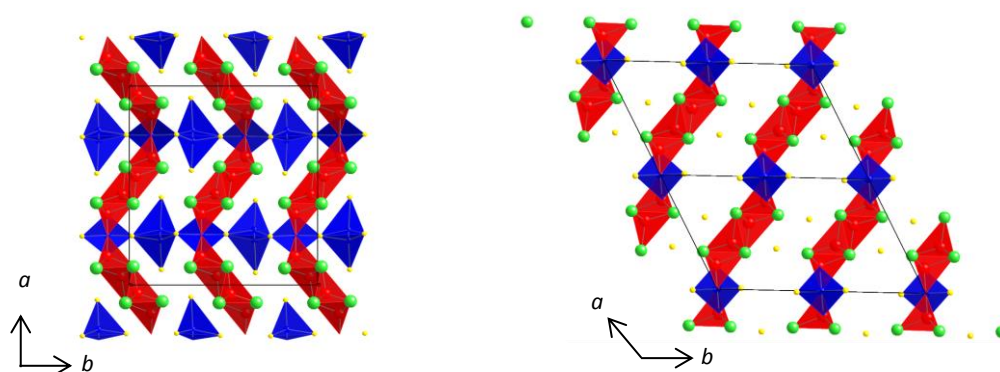

Figure 4.5: *Crystal structures of β-$La_2O_2MSe_2$ (M = Fe, Mn) Pna2$_1$ symmetry and $A_4O_4TiSe_4$ C2/m symmetry, orientated parallel to the MSe$_2$O$_4$ chains.*

It is also possible to consider the structure of $A_4O_4TiSe_4$ as arising from the need to segregate $[A_2O_2]^{2+}$ ribbons (connected by octahedrally coordinated Ti atoms) and Se ions. This is then conceptually similar to the structure of α-$A_4O_4Se_3$ (A=La-Nd, Sm) [these material will be discussed further in chapter 5], which contain infinite layers of fluorite-like $[A_2O_2]^{2+}$ separated by layers of Se ions, figure 4.6. Both series of materials contain either infinite layers or ribbons (with discrete width) constructed of distorted A_4O (or A_3MO) tetrahedra which share 4 edges. The A site cations in $A_4O_4TiSe_4$ adopt a square antiprism environments of either AO_4Se_4 or AO_3Se_5 coordination. By comparison A sites in α-$A_4O_4Se_3$ are coordinated in AO_4Se_4 square antiprism or AO_4Se_2 environments.
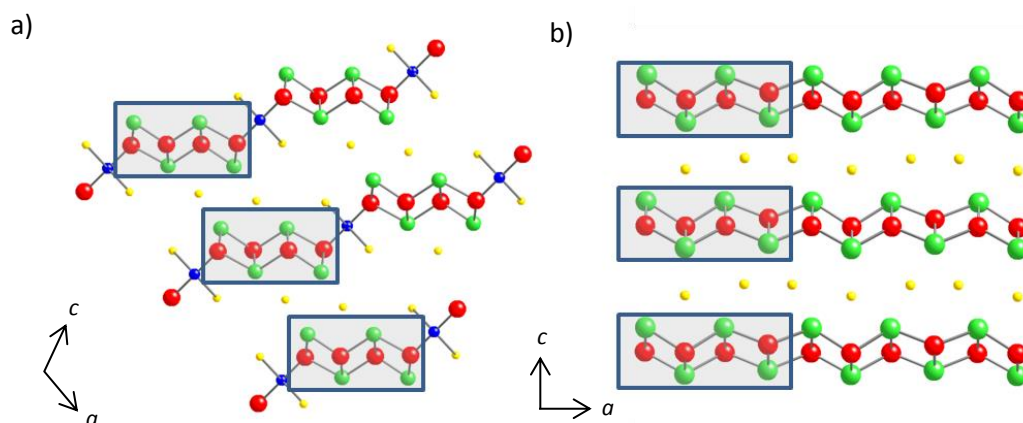
Figure 4.6: *Comparison a) $A_4O_4TiSe_4$ C2/m symmetry and b) $A_4O_4Se_3$ (A=La-Nd, Sm) Amm2 symmetry crystal structures.*

4.5 Variable temperature structural studies

X-ray powder diffraction patterns of six of the synthesised compositions (*A* = Sm, Gd–Ho, & Y) were recorded as a function of temperature between 300 and 12 K. No additional reflections or peak splittings were observed on cooling to indicate any major structural phase changes. Figure 4.6 shows the evolution of the unit cell volume obtained from Rietveld analysis of the XRPD data. For the smaller *A* site elements (Tb–Ho and Y) a smooth variation in unit cell volume was observed across the entire temperature range investigated.

The overall volume expansion of each phase was similar, with a volume of coefficient of thermal expansion $\alpha_V = \frac{V_{T1}-V_{T2}}{V_{T1}(T2-T1)}$ ranging from +2.01(4)x10^{-5} K^{-1} to 2.32(3)x10^{-5} K^{-1} over the temperature range 12 to 300 K; values for each composition are given in table 4.4. The temperature behaviour for the individual cell parameters is shown in figure 4.7 and show slight differences in thermal expansion, this being most notable in the cell angle β which forms two groups with positive and negative temperature gradient. The 3 materials (Gd, Ho, Y) for which β decreases with temperature have a larger linear expansion in the *b* cell parameter than other phases.
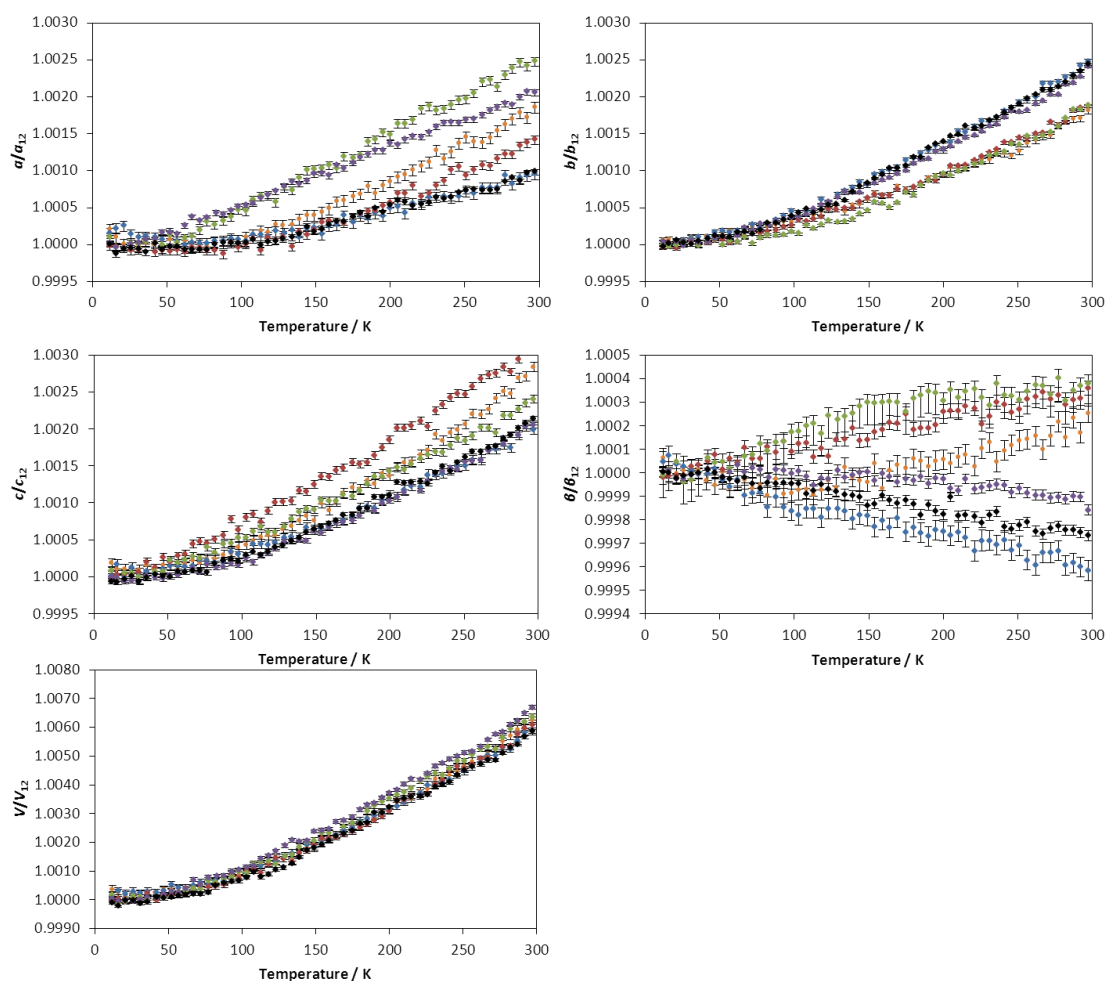
Figure 4.7: Unit cell parameters of $A_4O_4TiSe_4$ (A= Sm, Gd–Ho, Y) as a function of temperature between 300 and 12 K, obtained from refinement of XRPD data. $Sm_4O_4TiSe_4$ = orange, $Gd_4O_4TiSe_4$ = blue, $Tb_4O_4TiSe_4$ = red, $Dy_4O_4TiSe_4$ = green, $Ho_4O_4TiSe_4$ = purple, $Y_4O_4TiSe_4$ = black.

Table 4.4: Coefficients of volume expansion over the temperature range 12 to 300 K for $A_4O_4TiSe_4$ (A = Sm, Gd, Tb, Dy, Ho, Y) compositions.

A^{3+}	Volume expansion coefficient, α_V / K^{-1}
Sm	$+2.06(4) \times 10^{-5}$
Gd	$+2.01(4) \times 10^{-5}$
Tb	$+2.15(4) \times 10^{-5}$
Dy	$+2.17(5) \times 10^{-5}$
Ho	$+2.32(3) \times 10^{-5}$
Y	$+2.09(3) \times 10^{-5}$

The observation that some samples showed an increase in β with temperature was somewhat puzzling, though figure 4.7 suggested that β might change from positive to negative slope for same composition. For the *A* = Tb material we therefore investigated the thermal expansion over a wider temperature 100 K and 500 K using the setup described in Chapter 8. A 0.1 mm diameter borosilicate capillary was filled with $Tb_4O_4TiSe_4$, measured in 30 minute slices the

sample was warmed from 100 K to 500 K at 20 K hr^{-1} on a laboratory powder diffractometer (d7) with the temperature controlled using an Oxford Cryosystems Cryostream 700 compact. Due to the sample composition and the CuK$\alpha_{1,2}$ source used absorption was a major problem, therefore the signal to noise of the diffraction patterns collected was relatively poor using a reasonable time per step. Sequential Rietveld analysis was carried out using Topas to determine the temperature dependence of the unit cell parameters. Accurate sample temperatures were determined using equation 8.3 of Chapter 8. Unit cell parameters between 100 K and 300 K are in good agreement with the unit cell parameters collected in flat plate geometry using an Oxford Cryosystems PheniX to control the environment, figure 4.8. Between 300 K and 500 K a smooth increase in lattice parameters is observed consistent with low temperature data. The monoclinic angle β was found to increase to a maximum at ~350 K before decreasing at higher temperatures. The temperature coefficient of β therefore varies subtly with temperature and we do not ascribe any structural significance to the two 'families' of behaviour suggested by figure 4.7.

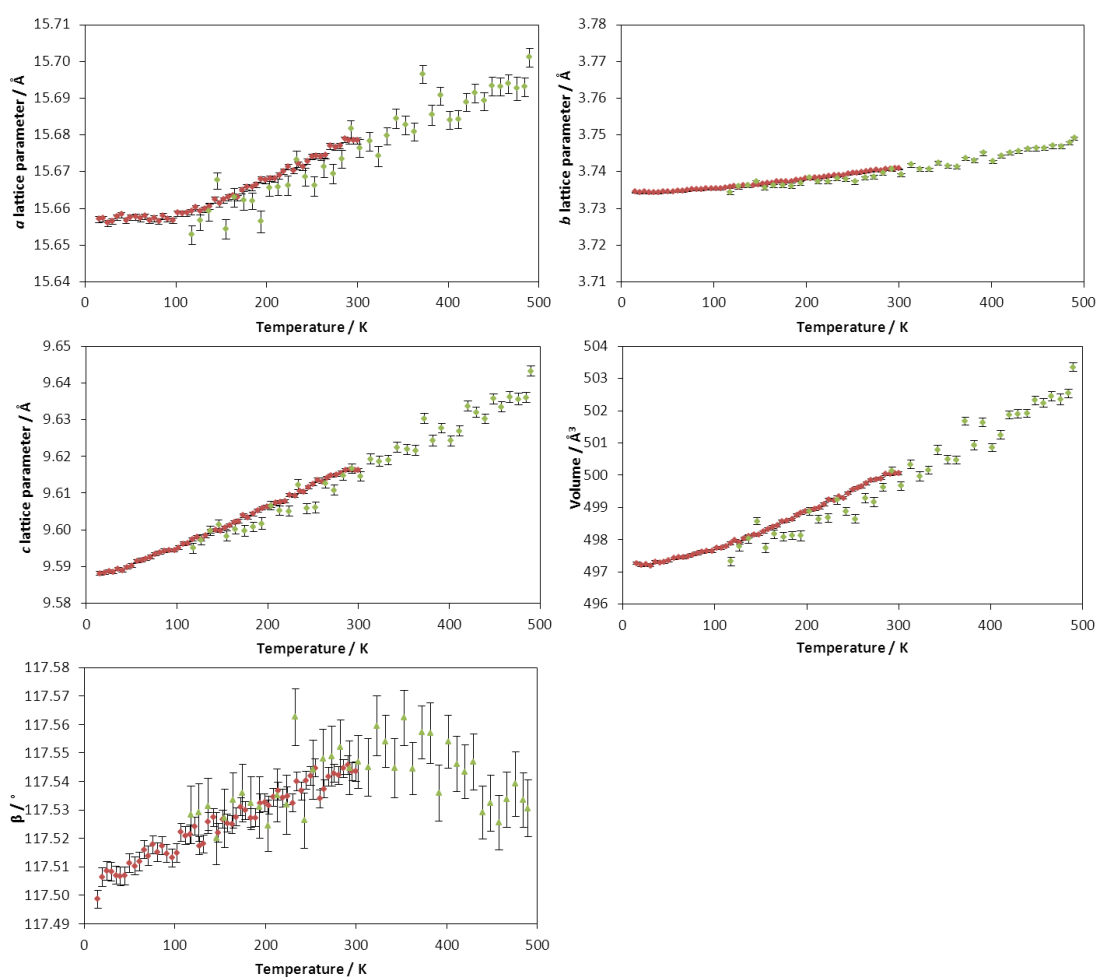

Figure 4.8: *Unit cell parameters from Rietveld analysis for Tb$_4$O$_4$TiSe$_4$ between 12 K and 500 K. Red = d9_06546 AJT079 temperature controlled using PheniX, green = d7_00875 AJT079 temperature controlled using Cryostream 700 compact.*

4.6 $Gd_4O_4TiSe_4$ and $Sm_4O_4TiSe_4$ low temperature behaviour

The behaviour of $Gd_4O_4TiSe_4$ and $Sm_4O_4TiSe_4$ below ~100 K differs from that of the other members of the $A_4O_4TiSe_4$ series in that a significant increase in the a cell parameter is observed on cooling at 15 K hr^{-1} below this temperature. The a cell parameter for $Gd_4O_4TiSe_4$ also shows hysteretic behaviour, with values on warming differing from values on cooling, figure 4.9; a similar behaviour is observed for the β angle. The b and c cell parameters decrease smoothly upon cooling in agreement with the other $A_4O_4TiSe_4$ materials and did not appear to show any hysteresis. In order to investigate this unusual behaviour a sample of $Gd_4O_4TiSe_4$ was mixed with a Si internal standard in order to extract accurate lattice parameters; 1 hour data sets were collected as the sample temperature was slowly ramped from 5 to 120 ° 2θ. Figure 4.10 shows cell parameters extracted from Rietveld analysis from data collected from a sample cooled from 300 K to 12 K at 5 K hr^{-1}, (5 K range per pattern), then left at 12 K for 12 hours to equilibrate, before warming at 5 K hr^{-1}. As with the data collected at 15 K hr^{-1}, a smooth decrease in b and c lattice parameters is observed. However the a lattice parameter and β angle both show significant differences below ~100 K between cooling and warming experiments, decreasing from ~300 K to ~100 K before increasing from ~100 K to 12 K. Beta increases upon cooling from 300 to 12 K with evidence for a discontinuity at ~50 K. Figure 4.10 also contains the unit cell parameters of $Gd_4O_4TiSe_4$ when quenched-cooled from 300 K to 12 K in 48 minutes (the maximum cooling rate of the cryostat) and then held at this temperature for ~22 hours, again an Si internal standard was incorporated so accurate cell parameters could be extracted. These data show that a and β change with time while the other unit cell parameters remain effectively unchanged. For $Gd_4O_4TiSe_4$ the a cell parameter increases from 15.7742(4) Å to 15.7802(5) Å, and β from 117.716(2) to 117.737(2)°. A similar but less pronounced behaviour was observed for a sample with $Sm_4O_4TiSe_4$ composition, cell parameter plots for $Sm_4O_4TiSe_4$ are given in figure 4.11. No major change in either peak intensity or any splitting of peaks was seen in this temperature range for either $Gd_4O_4TiSe_4$ or $Sm_4O_4TiSe_4$.
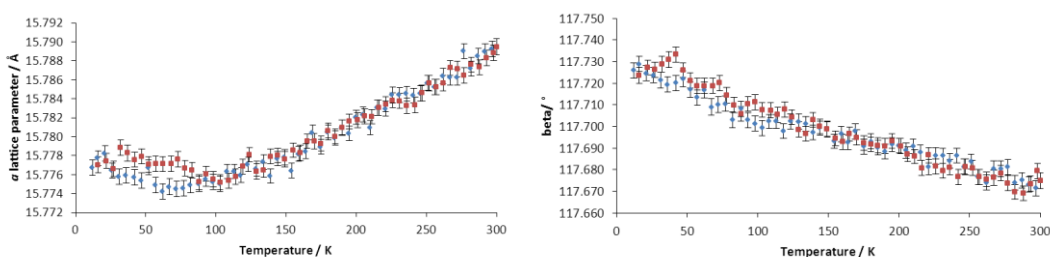

Figure 4.9: *a & β cell parameters of $Gd_4O_4TiSe_4$ between 12 and 300 K, cooling/heating at 15 K hr^{-1}. Blue d9_06697 (cooling) & red d9_06700 (warming), AjT078b.*
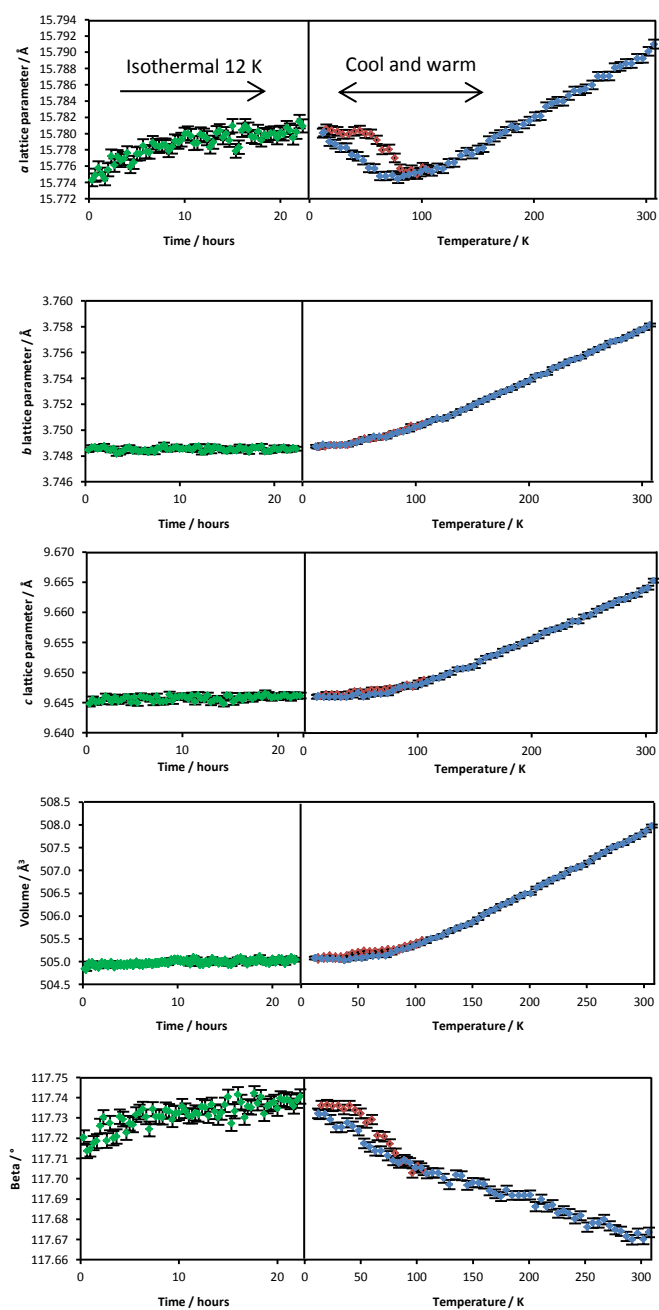
Figure 4.10: *Unit cell parameters of $Gd_4O_4TiSe_4$ extracted from XRPD data at 12 K following rapid cooling (green, left), and cooling (blue, filled) and warming (red, open) at 5 K hr^{-1}.*
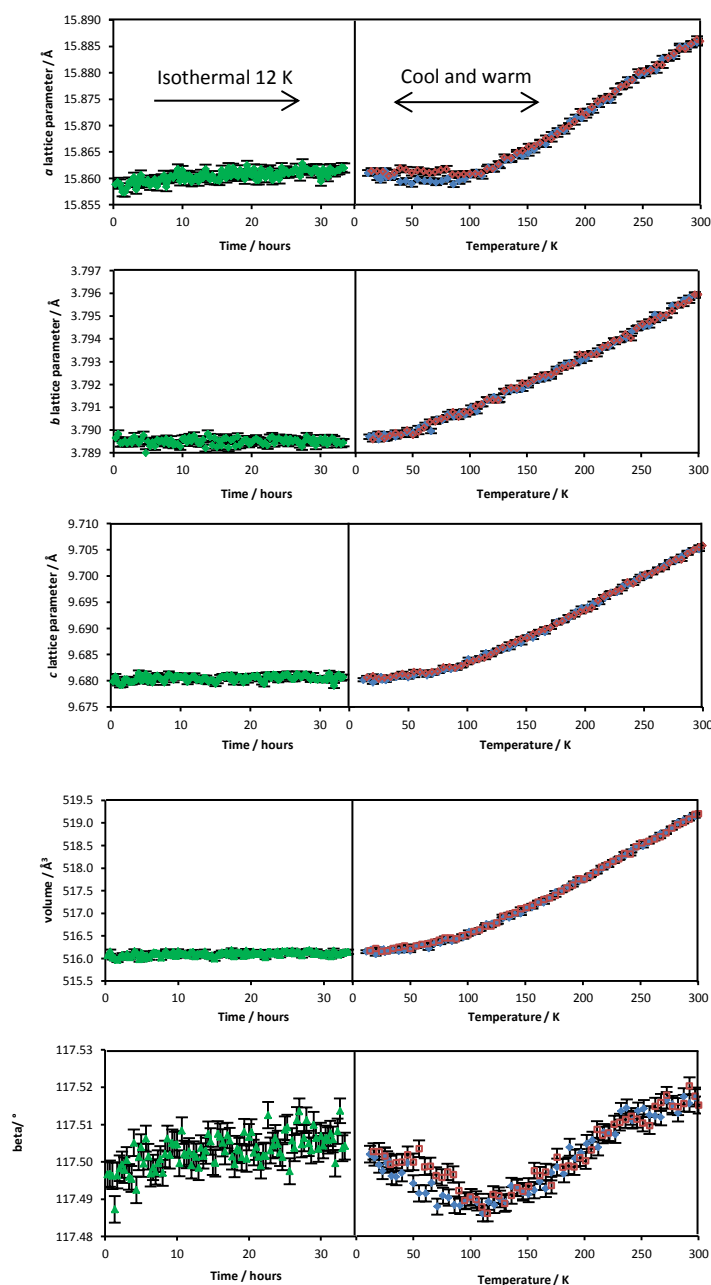
Figure 4.11: *Unit cell parameters of $Gd_4O_4TiSe_4$ extracted from XRPD data at 12 K following rapid cooling (green, left), and cooling (blue, filled) and warming (red, open) at 5 K hr^{-1}.*

The origins of this unusual behaviour aren't clear, however Meerschaut *et al.* report a large thermal parameter for the Ti site from single crystal studies of $Gd_4O_4TiSe_4$ at 293 K.[6] Meerschaut observed that the Ti U_{22} anisotropic thermal parameter is much larger than those of the other atoms, while the U_{33} is too small to be physically reasonable, suggesting that the Ti position could be displaced from (0,0,0). The ellipsoid shape suggests displacement in the *ab* plane (approximately the TiSe$_4$ plane) to an (0,*y*,0) or (*x*,*y*,0) position with *x* & *y* close to zero. It therefore seems likely that the discontinuities in unit cell parameters at low temperature could be caused by ordering (either short or long range) across a displaced site at the centre of the

$TiSe_4O_2$ octahedron. Off centre Ti displacements have been observed in other $TiSe_4O_2$ octahedra such as $La_6O_5Ti_3Se_9$ and $La_4O_4Ti_2Se_5$, figure 4.12.[8] The X-ray powder diffraction data collected in this work gives strong evidence from peak positions of a low temperature phase transition, however changes in peak intensity have not been sufficient to determine its origin. It should be noted that calculated X-ray diffraction patterns for Ti ordering at $(0,y,0)$ with $y = 0.05$ would lead to a maximum intensity of superstructure reflections of ~0.1 % of the most intense reflection.
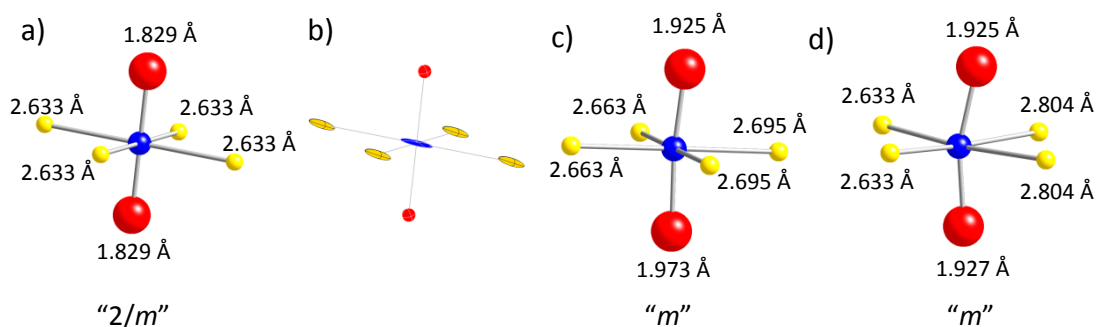

Figure 4.12: *$TiSe_4O_2$ octahedra in a) $Gd_4O_4TiSe_4$, b) thermal ellipsoids (at 90 %) reported by Meerschaut for $Gd_4O_4TiSe_4$, c) $La_6O_5Ti_3Se_9$ and d) $La_4O_4Ti_2Se_5$.[6, 8] Ti = blue, O = red, Se = yellow.*

4.7 Conductivity measurements

The conductivity of pelletised samples of five samples of $A_4O_4TiSe_4$ (A = Gd, Tb, Dy, Ho & Y) was measured on cooling and warming between 300 K and 130–70 K (depending on where the sample resistance became too high to measure), using the 4 point probe method outlined in section 2.8.5, pellet dimensions are given in table 4.5. Room temperature conductivities, given in table 4.6, show an increase in conductivity with decreasing rare earth radius. Plots of ln(conductivity) vs reciprocal temperature show linear behaviour for all samples (figure 4.13), indicating semiconducting behaviour with activation energies of between ~0.19 and ~0.13 eV, suggesting electronic band gaps between 0.378(2) and 0.254(3) eV (table 4.2). Figure 4.14 shows a smooth decrease in band gap with rare earth radius is observed for this series of compounds. For A = Gd to Ho. Preliminary DFT calculations by Dr Chun-Hai Wang, suggest the top of the valence band has predominantly Se p character and the bottom of the conduction band predominantly Ti d character, appendix 2. The smooth decrease in band gap presumably arises from band broadening as the rare earth radius and unit cell volume decreases.

Table 4.5: Pellet dimensions for conductivity measurements.

Composition	Sample code	Length / mm	Width / mm	Depth / mm
$Gd_4O_4TiSe_4$	AJT089	3.9	4.1	3.4
$Tb_4O_4TiSe_4$	AJT101	4.2	4.1	4.0
$Dy_4O_4TiSe_4$	AJT090	4.3	3.7	4.3
$Ho_4O_4TiSe_4$	AJT104	4.3	3.8	3.2
$Y_4O_4TiSe_4$	AJT091	4.3	3.6	3.1

Table 4.6: Room temperature conductivities(±0.01 S m^{-1}) and electronic band gaps for $A_4O_4TiSe_4$ (A = Gd, Tb, Dy, Ho & Y) series.

Composition	Room temperature conductivity / S m^{-1}	Band gap / eV
$Gd_4O_4TiSe_4$	1.04	0.378(2)
$Tb_4O_4TiSe_4$	1.02	0.331(2)
$Dy_4O_4TiSe_4$	1.85	0.307(3)
$Ho_4O_4TiSe_4$	2.90	0.254(3)
$Y_4O_4TiSe_4$	1.68	0.317(3)
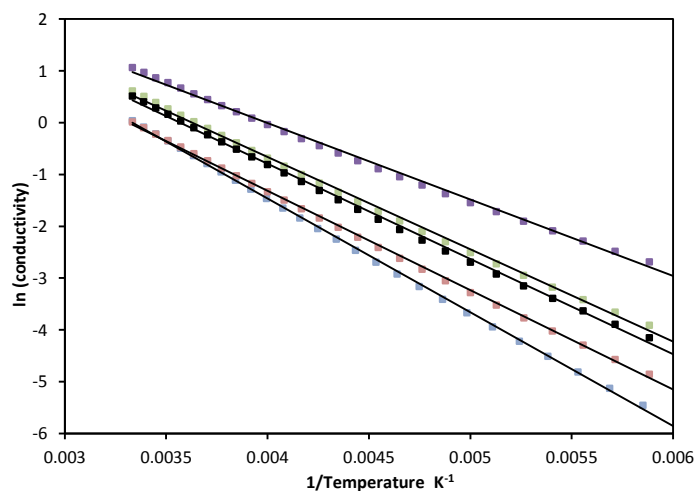
Figure 4.13: Temperature dependence of conductivity for $Gd_4O_4TiSe_4$ (blue), $Tb_4O_4TiSe_4$ (red), $Dy_4O_4TiSe_4$ (green), $Ho_4O_4TiSe_4$ (purple) & $Y_4O_4TiSe_4$ (black).
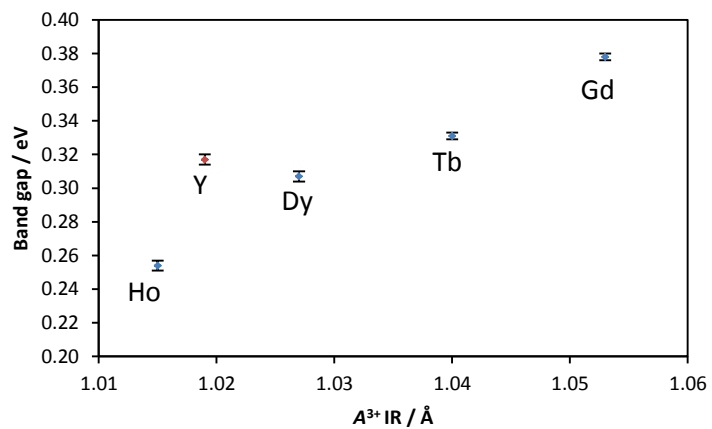
Figure 4.14: *Estimated electronic band gap plotted versus ionic radii of A^{3+} ions.*

4.8 Magnetic properties

Magnetic properties of $A_4O_4TiSe_4$ (A = Gd, Tb, Dy & Ho) were measured in the temperature range 2–292 K with magnetic fields of 100 and 10 Oe using SQUID magnetometry. Magnetization versus applied field plots at 292 K were linear for all four samples between 0 and 5 T (shown in appendix 2), with an essentially zero intercept indicating paramagnetic behaviour at this temperature with no significant ferromagnetic impurities. All samples showed linear $1/\chi$ vs T behaviour at high temperature, which was fitted using the Curie-Weiss law between 32 and 292 K. Negative values of the Weiss constant indicate weak antiferromagnetic interactions in all four compounds. All samples showed effective magnetic moments deduced from the Curie constants close to the expected Landé values for A^{3+} ions, which is consistent with the presence of Ti^{4+} within the materials (table 4.7).

Table 4.7: *Experimental magnetic moments μ_{exp} & Weiss constants (θ) obtained from fitting 100 Oe FC data in the range 32–292 K.*

	Sample code	μ_{exp} / μ_B/A	μ_{eff} / μ_B/A	θ / K
$Gd_4O_4TiSe_4$	AJT078b	7.82(1)	7.94	−5.6(5)
$Tb_4O_4TiSe_4$	AJT079	9.26(2)	9.72	−9.6(8)
$Dy_4O_4TiSe_4$	AJT082	10.28(1)	10.65	−5.3(4)
$Ho_4O_4TiSe_4$	AJT093c	10.36(1)	10.60	−4.6(3)

Figure 4.15a shows $Gd_4O_4TiSe_4$ field cooled (FC) and zero field cooled (ZFC) data collected in 5 K intervals with more closely spaced FC measurements taken between 2 and 10 K. No difference in FC and ZFC measurements was observed. Magnetic properties of $Gd_4O_4TiSe_4$ have previously been reported by Meerschaut, magnetic moments and Weiss constants (μ_{exp} 7.94 μ_B/Gd and θ −12.8(2) K) are broadly consistent with this work.[6] A sharp increase in susceptibility is observed between 2.5 and 4 K; figure 4.15b shows the field dependence of this feature. We observe a ~1.5 fold increase in peak susceptibility between 100 and 10 Oe compared to the ~4 fold increase reported by Meerschaut.[6] The overall behaviour has been attributed to a transition to an antiferromagnetically ordered state below ~1.5 K.[6] Between ~4 and 2.5 K a small canting of the Gd spins (approximately 3°) is proposed to give a ferromagnetic component to the susceptibility which disappears at low temperature. This canting saturates at relatively low field (a few hundred Oe) giving rise to the observed field-dependent susceptibility below the saturation field.
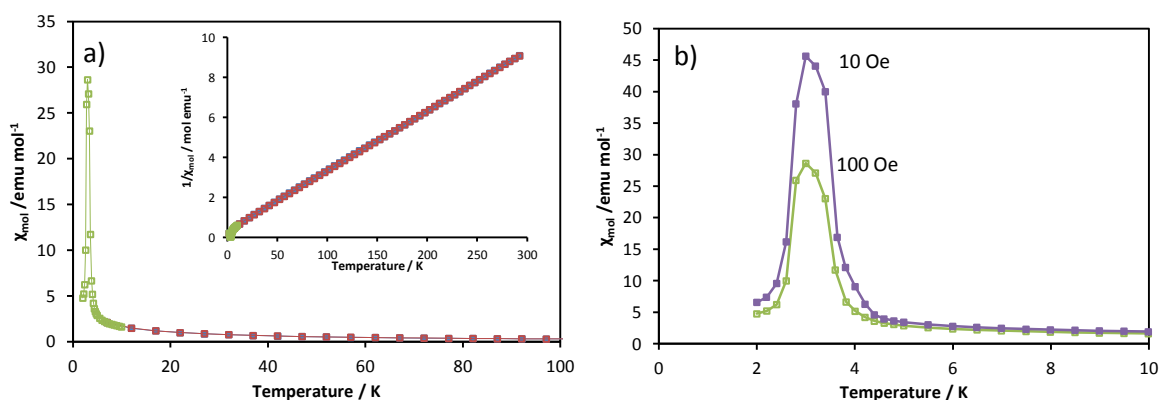
Figure 4.15: *a) Magnetic susceptibility and inverse susceptibility (inset) of $Gd_4O_4TiSe_4$ at 100 Oe, a sharp increase in susceptibility is observed between 4 and 2.5 K. b) Field dependence of susceptibility. FC = red (open), ZFC = blue (closed), additional FC data points = green (open), 10 Oe FC = purple (closed).*

Figure 4.16a shows FC and ZFC susceptibility data for $Tb_4O_4TiSe_4$ between 2 and 300 K measured in a 100 Oe field. Figure 4.16b shows the magnetic susceptibility measured in fields of 10 and 100 Oe. In contrast to $Gd_4O_4TiSe_4$ there is no marked increase in susceptibility on cooling. Both FC and ZFC data recorded at 100 Oe show a decrease in susceptibility below 4 K suggesting antiferromagnetic ordering. The upturn in susceptibility at ~5 K and the field dependence of susceptibility could indicate a small ferromagnetic component due to canting as in $Gd_4O_4TiSe_4$. The magnitude of any canting is, however, significantly lower than in $Gd_4O_4TiSe_4$.
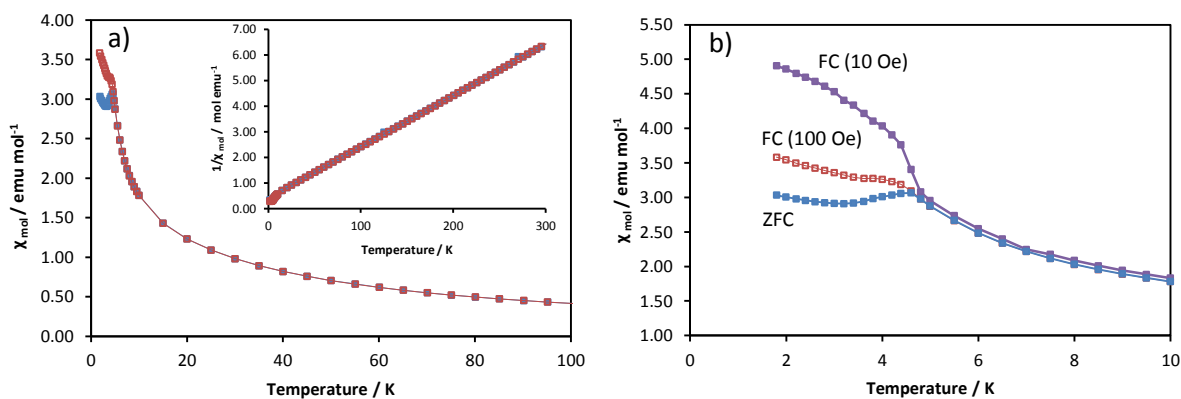
Figure 4.16: *a) Magnetic susceptibility and inverse susceptibility (inset) of $Tb_4O_4TiSe_4$ versus temperature under an applied field of 100 Oe. b) Susceptibility between 0 and 10 K. 100 Oe FC= red (open), ZFC = blue (closed); 10 Oe FC = purple (closed).*

Figures 4.17 shows magnetic susceptibility data for $Dy_4O_4TiSe_4$ and $Ho_4O_4TiSe_4$. These data suggest antiferromagnetic ordering with $T_N \approx 4$ K; no marked increase in susceptibility is observed prior to antiferromagnetic order.

The rare earth ordering temperatures measured for these phases are comparable to those of, for example $AFeO_3$ materials. In $GdFeO_3$ a maximum is susceptibility at 2.5 K is attributed to

antiferromagnetic ordering of the Gd moments, while in $TbFeO_3$ system there is some interaction between the Fe and Tb spin below 10 K, with Tb moments ordering antiferromagnetically below 3.1 K.[13-15] In $DyFeO_3$ ordering occurs below 4.5 K and $HoFeO_3$ is reported to have a T_N of 4.1 K.[16] In each of these $AFeO_3$ systems the Fe sites order antiferromagnetically with Néel temperatures in excess of 600 K.[17, 18]
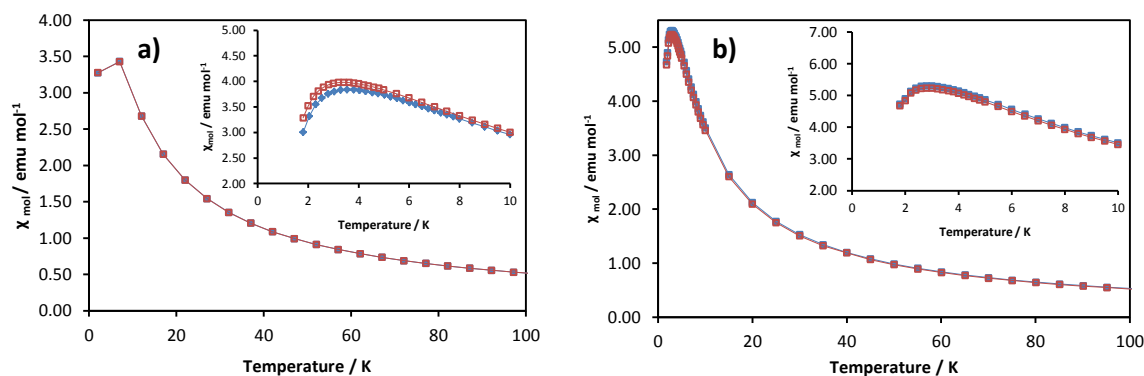

Figure 4.17: *FC and ZFC Magnetic susceptibility of a) $Dy_4O_4TiSe_4$ and b) $Ho_4O_4TiSe_4$ at 100 Oe, insets low temperature regions. FC =red (open), ZFC =blue (closed).*

4.9 Conclusions

Six new members of the $A_4O_4TiSe_4$ family of materials have been synthesised and $Gd_4O_4TiSe_4$ has been prepared as a bulk polycrystalline sample for the first time. Synthesis of other rare-earth containing materials was unsuccessful, suggesting that the structure is only accessible using the synthetic route described in section 2.2.4 for rare earths with resulting cell volumes ranging from ~483 to 520 Å^3. Variable temperature X-ray diffraction experiments show the Sm and Gd analogues undergo a structural distortion on cooling, revealed most clearly in the *a* lattice parameter and monoclinic angle β. No appreciable change in diffraction intensity was observed, so the exact nature of the distortion has yet to be determined. We presume however that this is an order disorder transition associated with off-centre distortion of Ti in the $TiSe_4O_2$ octahedra. Conductivity measurements show the series to be semi-conductors, with electronic band gaps of between 0.378(2) and 0.254(3) eV, with the size of the band gap proportional to the ionic radius of the A^{3+} cation. SQUID magnetometry shows that $Gd_4O_4TiSe_4$ has a significant increase in susceptibility between 2.5 and 4 K consistent with previous measurements. This is thought to be due to spin canting prior to the onset of full antiferromagnetic order. $Tb_4O_4TiSe_4$ shows similar but less pronounced effects. $Dy_4O_4TiSe_4$ and $Ho_4O_4TiSe_4$ order antiferromagnetically below 4 K.

References

1.   McCabe, E. E., Free, D. G., and Evans, J. S. O., *Chemical Communications*, 2011, **47**, 1261-1263

2.   Ijjaali, I., Mitchell, K., Haynes, C. L., McFarland, A. D., Van Duyne, R. P., and Ibers, J. A., *Journal of Solid State Chemistry*, 2003, **176**, 170-174

3.   Tuxworth, A. J., McCabe, E. E., Free, D. G., Clark, S. J., and Evans, J. S. O., *Inorganic Chemistry*, 2013, **52**, 2078-2085

4.   Hiramatsu, H., Ueda, K., Kamiya, T., Ohta, H., Hirano, M., and Hosono, H., *Journal of Physical Chemistry B*, 2004, **108**, 17344-17351

5.   McCabe, E. E., Free, D. G., Mendis, B. G., Higgins, J. S., and Evans, J. S. O., *Chemistry of Materials*, 2010, **22**, 6171-6182

6.   Meerschaut, A., Lafond, A., Meignen, V., and Deudon, C., *Journal of Solid State Chemistry*, 2001, **162**, 182-187

7.   Tougait, O. and Ibers, J. A., *Chemistry of Materials*, 2000, **12**, 2653-2658

8.   Tougait, O. and Ibers, J. A., *Journal of Solid State Chemistry*, 2001, **157**, 289-295

9.   Meignen, V., Deudon, C., Lafond, A., Boyer-Candalen, C., and Meerschaut, A., *Solid State Sciences*, 2001, **3**, 189-194

10.   Person, H. and Urland, W., *Journal of Alloys and Compounds*, 2001, **323**, 57-60

11.   Tuxworth A. J. and Evans J.S.O., *Journal of Solid State Chemistry*, 2013, http://dx.doi.org/10.1016/j.jssc.2013.11.006

12.   Shannon, R. D., *Acta Crystallographica Section A*, 1976, **32**, 751-767

13.   Tokunaga, Y., Furukawa, N., Sakai, H., Taguchi, Y., Arima, T.-h., and Tokura, Y., *Nature Materials*, 2009, **8**, 558-562

14.   Tejada, J., Zhang, X. X., Roig, A., Nikolov, O., and Molins, E., *Europhysics Letters*, 1995, **30**, 227-232

15.   Cashion, J. D., Cooke, A. H., Martin, D. M., and Wells, M. R., *Journal of Applied Physics*, 1970, **41**, 1193-1194

16.   Nowik, I. and Williams, H. J., *Physics Letters*, 1966, **20**, 154-156

17.   Shao, M., Cao, S., Wang, Y., Yuan, S., Kang, B., and Zhang, J., *Solid State Communications*, 2012, **152**, 947-950

18.   Bhattacharjee, A., Saito, K., and Sorai, M., *Journal of Physics and Chemistry of Solids*, 2002, **63**, 569-574

Chapter 5: Synthesis and Characterisation of $A_4O_4Se_3$ Materials (A = Eu-Er, Yb & Y)

5.1 Introduction

Ternary rare-earth oxyselenides are known with a variety of A:O:Se ratios. Four compositions have been reported in the literature: $A_{10}OSe_{14}$ (A = La-Nd),[1-3] A_2OSe_2 (A = Pr & Gd),[1, 4] A_2O_2Se (A= La, Pr, Nd, Sm, Gd, Er, Ho, Yb, Lu)[1, 5] and $A_4O_4Se_3$ (A = La-Nd, Sm).[1, 6, 7] All these materials contain distorted A_4O tetrahedra with differing connectivity. The Se-rich system $A_{10}OSe_{14}$ contains discrete A_4O tetrahedra, while the other 3 compositions form 4 structure types with differing chains and layers constructed of edge and corner sharing A_4O tetrahedra; each structure is shown in figure 5.1. In this chapter we describe seven new materials with $A_4O_4Se_3$ composition with smaller A^{3+} cations than have been reported previously, which adopt one of 3 new structure types. The chapter will discuss: structure solution of $Eu_4O_4Se_3$ from laboratory single crystal data (the β structure), structure solution of $Gd_4O_4Se_3$ (γ structure) and $Y_4O_4Se_3$ (δ structure) from X-ray powder diffraction, and the assignment of other rare earth compositions to one of these structure types. The structures of these new (but closely related) oxychalcogenides will be discussed. All the new $A_4O_4Se_3$ materials contain fluorite-like $[A_2O_2]^{2+}$ layers constructed from distorted edge sharing A_4O tetrahedra, separated by layers of selenium containing different arrangements of Se^{2-} and Se_2^{2-}.
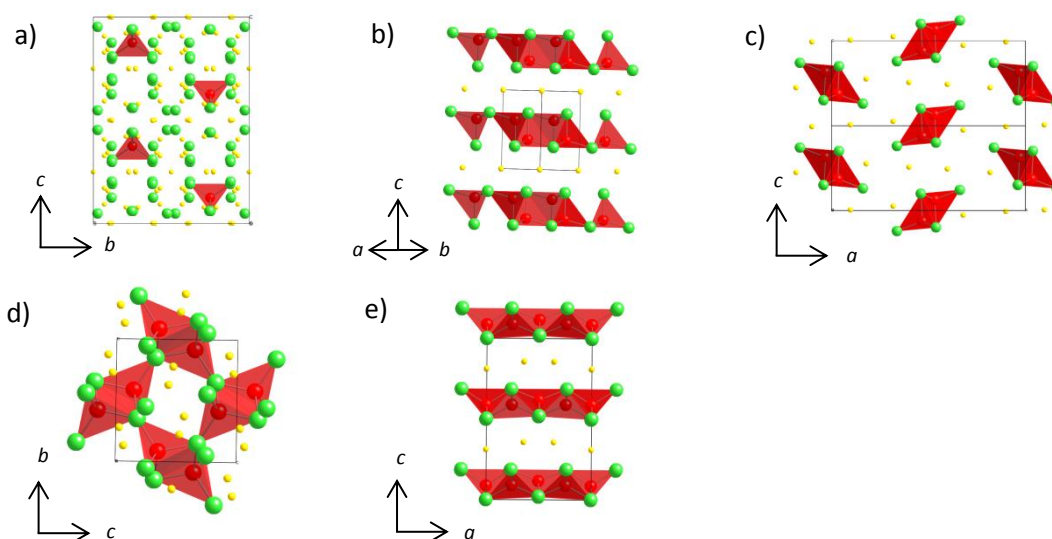

Figure 5.1: *Materials with $A_xO_ySe_z$ composition a) $A_{10}OSe_{14}$ $I4_1/acd$ symmetry , b) A_2O_2Se P-3m symmetry, c) A_2OSe_2 type 1 Pnma symmetry, d) A_2OSe_2 type 2 $P2_1/c$ symmetry, e) α-$A_4O_4Se_3$ Amm2 symmetry. A = green, O = red, Se = yellow, A_4O tetrahedra highlighted in red.*

The materials reported in the literature $A_4O_4Se_3$ (A = La, Ce, Pr, Nd, Sm) adopt an orthorhombic structure with an ~8.6 Å x ~4.1 Å x ~13.1 Å cell and $Amm2$ symmetry which we define as the α-$A_4O_4Se_3$ structure type.[1, 6, 7] In this structure A_4O distorted tetrahedra edge-share to form infinite layers which stack parallel to [001]. These $[A_2O_2]^{2+}$ layers are interleaved by Se^{2-} and Se_2^{2-} anions. The infinite edge-shared tetrahedra are similar to those found in A_2O_2Te or AOCuSe, and share 4 common edges. The $[A_2O_2]^{2+}$ layers common to $A_4O_4Se_3$, A_2O_2Te and AOCuSe differ significantly from those in A_2O_2S and A_2O_2Se systems. In the latter tetrahedra share 3 edges leading to trigonal symmetry and a less dense AO packing. The pseudo-tetragonal 4-edge sharing arrangement allows accommodation of the larger Te^{2-} anion in A_2O_2Te or excess Se in $A_4O_4Se_3$ ($A_2O_2Se_{1.5}$). A significant difference between $A_4O_4Se_3$ and A_2O_2Te/LaOCuSe structures is that every second $[A_2O_2]^{2+}$ layers is shifted ½ the length of the b axis, thus A^{3+} cations are located above O^{2-} anions within the $A_4O_4Se_3$ structure and vice versa, figure 5.2. The layer shift means that Se^{2-} and Se_2^{2-} no longer sit midway between $[A_2O_2]^{2+}$ layers but are displaced either towards or away from a given layer to satisfy local bonding requirements.
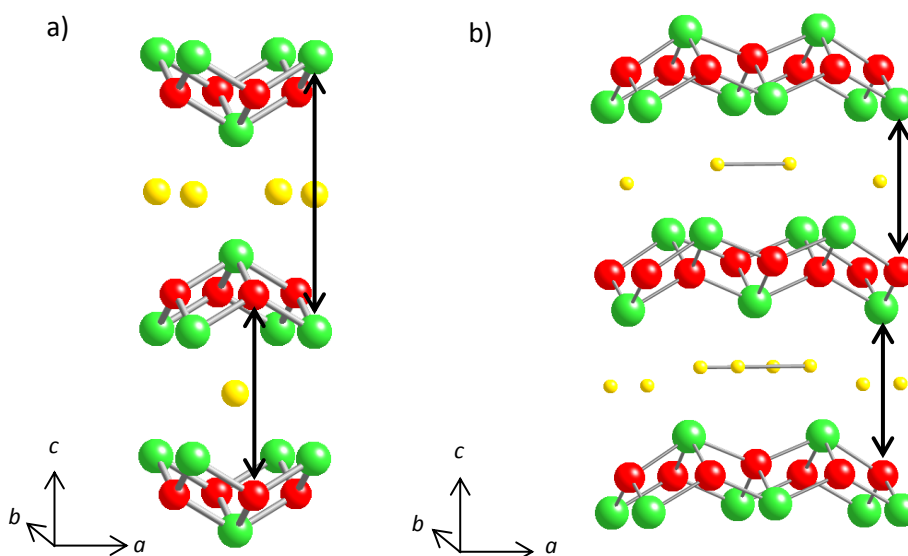
Figure 5.2: *Stacking arrangement $[A_2O_2]^{2+}$ layers in a) La_2O_2Te and b) α-$A_4O_4Se_3$. A = green, O = red, Se/Te = yellow.*

Three crystallographically independent A^{3+} cations are found within the α-$A_4O_4Se_3$ structure with coordination numbers of either 6 or 8 by selenium and oxygen, figure 5.3. All 3 A^{3+} cations are coordinated with a square-like arrangement of O^{2-} anions from the $[A_2O_2]^{2+}$ layers. $A2$ is also coordinated by two η^2 (side on) Se_2^{2-} units, forming a 4+4 square antiprism type coordination environment. The $A3$ site is coordinated by two Se^{2-} and two η^1 (end-on) Se_2^{2-} units making up a similar geometry. The $A1$ site is 6 coordinated by the square arrangement of

O^{2-} ions and two Se^{2-} anions; the coordination of $A1$ resembles a square prism with two vertices removed.
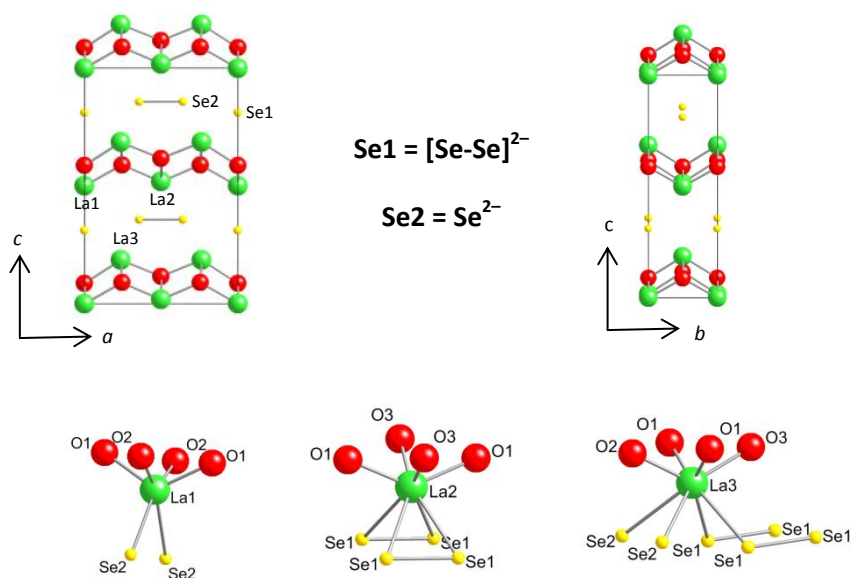

Figure 5.3: *Structure of α-$A_4O_4Se_3$ (A = La, Ce, Pr, Nd and Eu) Amm2 symmetry ~8.6 Å x ~4.1 Å x ~13.1 Å.*

5.2 Synthesis of $A_4O_4Se_3$ (A = Eu-Er, Yb, Y)

In an attempt to synthesise a material with hypothetical composition "$Dy_4O_4VSe_4$", Dy_2O_3, V and Se powders were ground together in a 2:1:4 ratio, and sealed in an evacuated quartz tube along with Al powder to act as a getter (forming Al_2O_3 during the reaction), before heating to 900 °C for 12 hours. The resulting powder was analysed by XRPD. Search-match suggested some reflections consistent with VSe_2 (and having strong preferred orientation), and another(s) additional phase with several high d spacing reflections, but no match in the 2012 PDF4+ database.[8] In order explore this additional phase, quantitative EDX analysis was carried out on pelletised samples of the reaction product using a scanning electron microscope. Figure 5.4 shows a representative backscattered electron image showing that at least 2 phases are present, one consisting of small crystallites and the other larger crystallites with a plate-like morphology. These plates were shown to have a V:Se ratio of 1:2, and therefore correspond to the VSe_2 inferred from powder diffraction. The "polycrystalline" region contained no vanadium and Dy:O:Se in an approximately 4:4:3 ratio, but is presumably not a single phase in this sample to account for the overall stoichiometry of the synthesis.
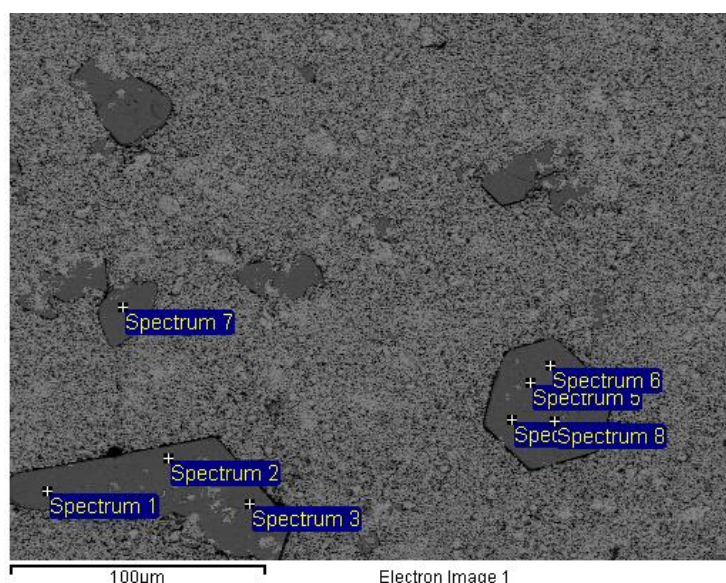
Figure 5.4: *Backscattered electron diffraction image of "Dy$_4$O$_4$VSe$_4$" collected at 15 keV. Large crystals are VSe$_2$; remainder of sample is Dy$_4$O$_4$Se$_3$.*

Following this discovery, materials with $A_4O_4Se_3$ composition (A = Eu-Er, Yb & Y) were synthesised according to the method outlined in section 2.2.5. These compounds adopt 3 new phases which we define as β, γ and δ-$A_4O_4Se_3$. Not all of the compositions could be synthesised as pure phase products, table 5.1, with decreased phase purity for smaller A^{3+} ionic radii. Additional phases observed include A_2O_2Se (A = Dy, Ho & Yb), and A_2O_3 (A = Ho, Er & Yb).

Table 5.1: *Purity of β, γ and δ-$A_4O_4Se_3$ phases (±2 %) achieved.*

A^{3+}	Eu	Gd	Tb	Dy	Ho	Er	Yb	Y
Weight % purity	>99	>99	>99	>99	~94	~72	~81	>99
Structure type	β	γ	γ	δ	δ	δ	δ	δ
Major impurities	–	–	–	–	Ho$_2$O$_2$Se Ho$_2$O$_3$	Er$_2$O$_3$	Yb$_2$O$_2$Se Yb$_2$O$_3$	–

The effect of reaction temperature was investigated for the Y$_4$O$_4$Se$_3$ composition, with the reactant mixtures heated to temperatures of 700 °C, 900 °C, 950 °C and 1100 °C for 12 hours. This suggested the target phase could only be formed over a relatively small temperature range, with good yields at either 900 °C or 950 °C. Heating the sample to higher temperatures such as 1100 °C resulted in the formation of predominantly the Y$_2$O$_2$Se phase, whereas 700 °C was insufficient for reaction to occur between Y$_2$O$_3$ and Se.

5.3 β-Eu₄O₄Se₃

After synthesising a phase-pure polycrystalline sample of $Eu_4O_4Se_3$ a high quality XRPD pattern was collected using Cu K$\alpha_{1,2}$ radiation. Rietveld analysis showed this material was not isostructural with α-$A_4O_4Se_3$ materials, and we define it as adopting the β-$A_4O_4Se_3$ structure. The powder diffraction pattern showed some similarities to that of orthorhombic α-$A_4O_4Se_3$ with several reflections appearing to be split, suggesting a change in Bravais lattice. Analysis of the *hkl* indices of these reflections showed that a good fit to the observed data could be obtained if a distorted monoclinic cell were adopted with β ~91.3°.

Pawley refinement in *P*1 symmetry carried out using this cell showed that the majority of observed reflections could be well accounted for using a cell of *a* = 8.40408(7) Å, *b* = 3.90452(2) Å, *c* = 12.63857(7) Å and β = 91.3587(7)° (α and γ were fixed at 90°), figure 5.5. However several weak un-indexed reflections were present which could only be accounted for by doubling the *b* axis. A Pawley refinement using this larger cell accounted for all the observed reflections, *a* = 8.40437(8) Å, *b* = 7.80923(5) Å, *c* = 12.63876(7) Å and β = 91.3601(7)° (figure 5.6).
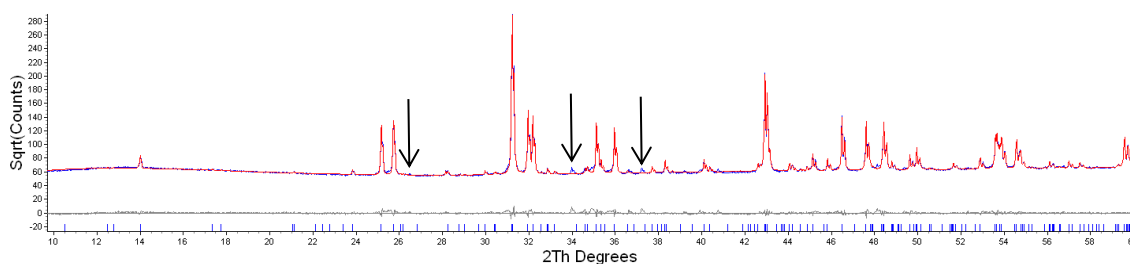
Figure 5.5: *Pawley refinement of Eu₄O₄Se₃ in P1 with, a = 8.40408(7) Å, b = 3.90452(2) Å, c = 12.63857(7) Å, β = 91.3587(7)° (α = γ = 90°), R$_{wp}$ = 2.939 %, AJT143 d7_02547. Unindexed reflections marked by black arrows. Note square root counts scale to emphasise weak reflections.*
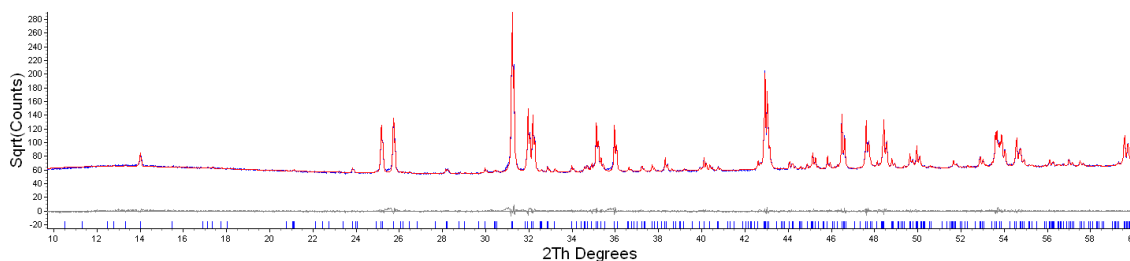
Figure 5.6: *Pawley refinement in P1 Eu₄O₄Se₃ a = 8.40437(8) Å, b = 7.80923(5) Å, c = 12.63876(7) Å, beta = 91.3601(7)° (α = γ = 90°), R$_{wp}$ = 2.362 % AJT143 d7_02547. Note square root counts scale.*

It was also possible to obtain single crystals of $Eu_4O_4Se_3$ via the method described in section 2.2.5. Single-crystal X-ray diffraction data were collected at 120 K with Mo Kα_1 radiation using a

laboratory 3 circle diffractometer. A total of 2070 frames were collected in ω steps of 0.3° using a frame collection time of 35 seconds. Analysis of multiple crystals from the batch indicated that all crystals obtained were twinned. The software package Gemini was used to index the harvested diffraction spots of the best crystal and determine a rotation matrix between the two twin components present. This confirmed the monoclinic cell determined from powder diffraction: 8.393(3) Å x 7.795(2) Å x 12.618(3) Å and β = 91.35(3)°. Analysis of systemic absences using XPREP software identified $P2_1/c$ symmetry.

Selected area election diffraction (SAED) images taken down the [001] zone axes confirmed the presence of a 2_1 screw axis parallel to b, with the reflection condition: 0k0 k=2n and that only reflections predicted by the X-ray derived cell were observed (Figure 5.7).
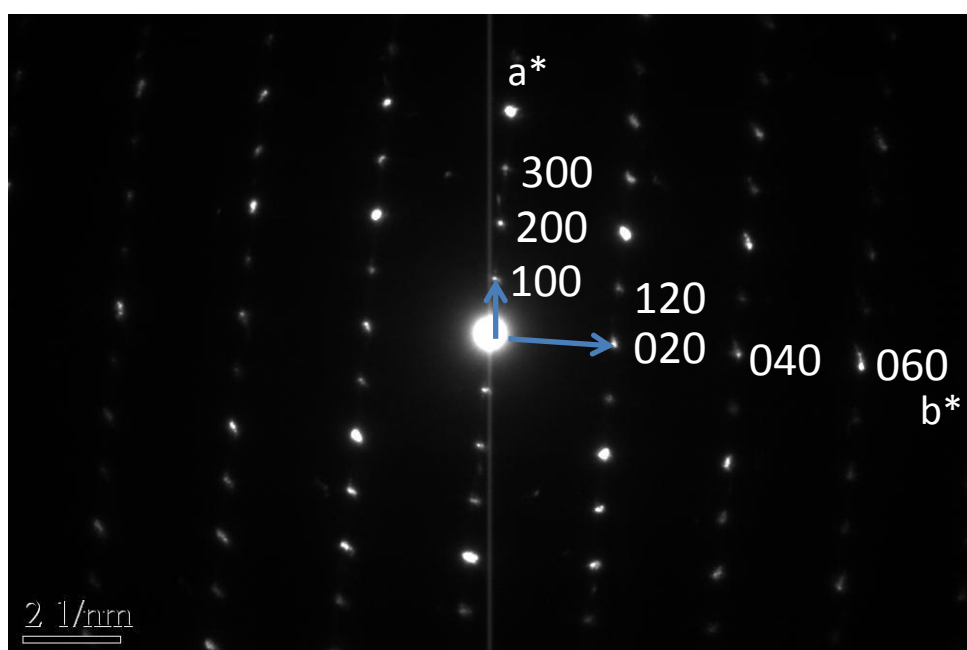
Figure 5.7: Selected area election diffraction of $Eu_4O_4Se_3$, AJT143d, down [001].

Ab initio structure solution was carried out using the charge flipping algorithm implemented in Superflip against the larger of the two domains of the single crystal data.[9] Whilst prior knowledge of symmetry is not required within the charge flipping algorithm, it can be included to increase the speed of the structure solution by increasing the number of constraints on the electron density. Charge flipping with $P2_1/c$ symmetry and the expected cell contents was successful at identifying Eu and Se sites. Due to the relatively small electron count of oxygen, O sites were identified by least squares refinements and Fourier difference mapping carried out using the Crystals software suite.[10] Final rounds of refinement were carried out using both twin components and a corresponding twin law. A total of 46 independent parameters were refined including 33 atomic positions, 11 isotropic thermal parameters, an overall scale factor and a

scale factor between the two twin components. It was not possible to include anisotropic thermal displacement parameters (ADPs) in the refinement without several sites going non-positive definite, therefore thermal displacement parameters were modelled isotropically. Crystallographic data are given in table 5.2, atomic coordinates and isotropic thermal displacement parameters in table 5.3 and selected bond lengths in table 5.4.

Table 5.2: *Crystallographic information for $Eu_4O_4Se_3$ from single crystal refinement.*

Formula	$Eu_4O_4Se_3$
Radiation	0.71973 Å
Temperature / K	120
Instrument	6K
Data collection	13ajt018
a / Å	8.3925(17)
b / Å	7.7949(16)
c / Å	12.618(3)
Beta / °	91.35(3)
Space group	$P2_1/c$
Z	4
Measured reflections	3945
Independent reflections	1681
$R_{int}(1)$	0.036
$R_{int}(2)$	0.033
h	$-10 \leq h \leq 10$
k	$-9 \leq k \leq 9$
l	$-15 \leq l \leq 15$
R	0.063
wR	0.172
gof	1.27
Δρ max	5.01
Δρ min	-6.06
Number of variables	46
Twin scale factors	0.585(3) 0.415(3)

Table 5.3: *Atomic coordinates and isotropic thermal displacement parameters for $Eu_4O_4Se_3$ at 120 K.*

	x	y	z	U_{iso}
Eu1	0.1141(3)	0.3660(6)	0.40797(15)	0.0034(5)
Eu2	0.3710(3)	0.1182(7)	0.58242(14)	0.0036(6)
Eu3	0.1141(3)	-0.1306(7)	0.40870(15)	0.0035(5)
Eu4	0.3713(3)	-0.3782(7)	0.57970(14)	0.0041(5)
Se5	0.2331(4)	-0.6233(12)	0.7402(3)	0.0057(8)
Se6	0.5252(4)	-0.6226(14)	0.7423(3)	0.0048(8)
Se7	0.1230(5)	-0.1287(11)	0.7214(3)	0.0045(8)
O8	0.372(3)	-0.101(4)	0.4833(19)	0.000(7)
O9	0.120(3)	-0.391(6)	0.4981(19)	0.005(7)
O10	0.375(3)	-0.612(6)	0.4842(18)	0.002(6)
O11	0.120(3)	0.116(7)	0.5046(19)	0.004(6)

Table 5.4: *Selected bond lengths (Å) for $Eu_4O_4Se_3$ in $P2_1/c$ symmetry at 120 K.*

Eu(1) - Se(5)	3.027(7)	Eu(2) - Se(5)	3.077(7)	Eu(3) - Se(5)	3.088(7)	Eu(4) - Se(5)	3.034(7)
Eu(1) - Se(7)	3.146(7)	Eu(2) - Se(6)	3.115(9)	Eu(3) - Se(7)	3.254(7)	Eu(4) - Se(6)	3.063(9)
Eu(1) - Se(7)	3.122(7)	Eu(2) - Se(6)	3.014(9)	Eu(3) - Se(7)	3.020(7)	Eu(4) - Se(6)	3.111(9)
Eu(1) - O(9)	2.21(4)	Eu(2) - Se(7)	3.359(7)	Eu(3) - O(8)	2.35(3)	Eu(4) - Se(7)	3.391(7)
Eu(1) - O(9)	2.33(3)	Eu(2) - O(8)	2.11(3)	Eu(3) - O(9)	2.32(4)	Eu(4) - O(8)	2.48(3)
Eu(1) - O(10)	2.38(3)	Eu(2) - O(8)	2.33(3)	Eu(3) - O(11)	2.27(5)	Eu(4) - O(9)	2.33(3)
Eu(1) - O(11)	2.30(5)	Eu(2) - O(10)	2.44(4)	Eu(3) - O(11)	2.27(3)	Eu(4) - O(10)	2.18(4)
		Eu(2) - O(11)	2.30(3)			Eu(4) - O(10)	2.29(3)
						Se(5) - Se(6)	2.451(5)

β-$Eu_4O_4Se_3$ adopts a monoclinic unit cell with a structure closely related to α-$A_4O_4Se_3$ and can be described as having layers of A_4O distorted tetrahedra which edge-share to form infinite sheets which stack parallel to [001]. These $[A_2O_2]^{2+}$ layers are interleaved by Se^{2-} and Se_2^{2-} anions, figure 5.8. Every second $[A_2O_2]^{2+}$ is layer shifted by ½ along [010], such that A^{3+} cations are located above O^{2-} anions, as is found in α-$A_4O_4Se_3$ materials. The Eu_4O tetrahedra share 4 common edges to form layers and are found in relatively distorted geometries, bond angles are given in figure 5.9. Four crystallographically independent A^{3+} cations are found within the structure with coordination numbers of either 7 or 8. All A^{3+} sites are coordinated to a square-like arrangement of O^{2-} anions. $A1$ and $A3$ have their 7-coordinate environment completed by one η^1 (end on) Se_2^{2-} unit and two Se^{2-} anions. $A2$ and $A4$ site environments are completed by one η^2 Se_2^{2-} unit, one η^1 Se_2^{2-} unit, and a Se^{2-} anion, forming a 4+4 square antiprism type coordination environment. Bond valence sums are 2.959, 3.146, 2.807 and 2.953 for Eu(1), Eu(2), Eu(3) and Eu(4) respectively suggesting that the compound contains Eu^{3+} ions.
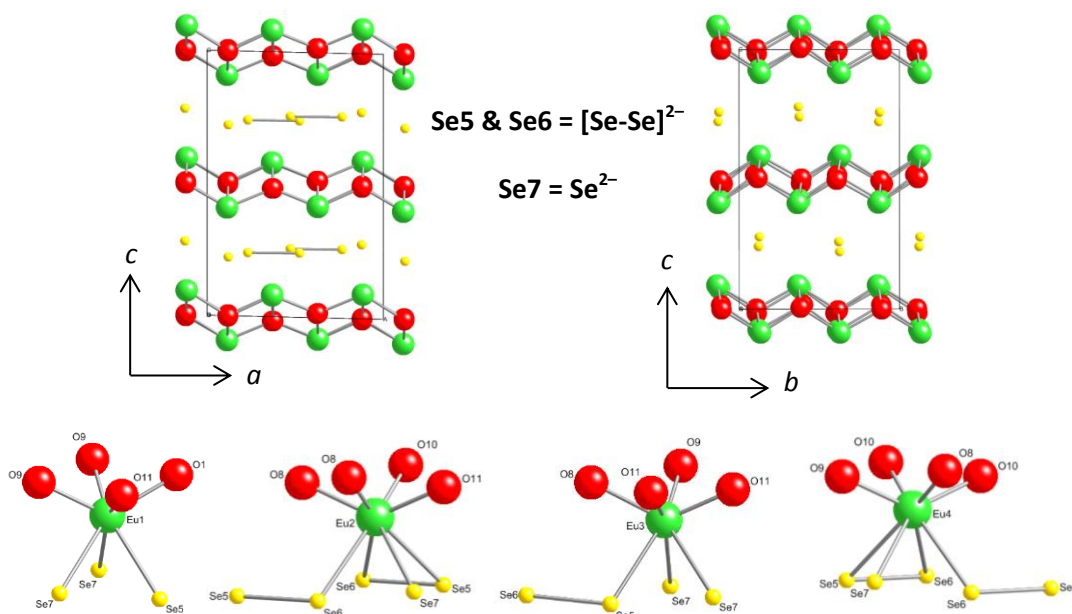
Se5 & Se6 = [Se-Se]$^{2-}$

Se7 = Se^{2-}

Figure 5.8: *Crystal structure of Eu$_4$O$_4$Se$_3$, P2$_1$/c symmetry, including views in [010] and [100] directions, and local coordination environments of Eu^{3+} sites.*
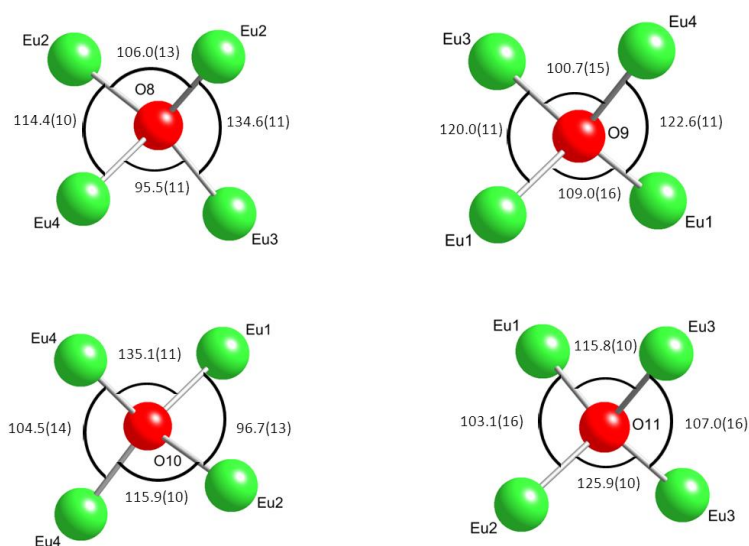

Figure 5.9: *Selected bond angles of Eu$_4$O polyhedra in Eu$_4$O$_4$Se$_3$ composition.*

It is clear from this discussion that, despite their similarities, the α (A = La-Nd, Sm) and β (A = Eu) structures contain subtly different A^{3+} coordination geometries. The α structure has 1 x (4+2) and 2 x (4+4) (O+Se) coordination and β structure has 2 x (4+3) and 2 x (4+4). The selenium arrangement between the $[A_2O_2]^{2+}$ oxide layers in the two structures are shown viewed down the [001] direction in figure 5.10. Each structure contains alternating Se^{2-} and Se$_2^{2-}$ ions in rows parallel to the a axis. The key difference between them is that in the β structure adjacent rows are offset along a. This leads to the b-axis doubling and reduction to monoclinic symmetry found for β-$A_4O_4Se_3$. The offsets also lead to the different AO$_4$Se$_x$

coordination environments observed. This is shown schematically in figures 5.10 and 5.11 where an individual Se layer in each structure is shown along with the A layers above and below. The Se^{2-}/Se_2^{2-} anion chains are highlighted in blue. In α-$A_4O_4Se_3$ each row has the same origin along x, whilst in β-$A_4O_4Se_3$ it is shifted by half a unit cell. The off set of along [100] results in either 4 or 3 bonds from each A site to selenium.
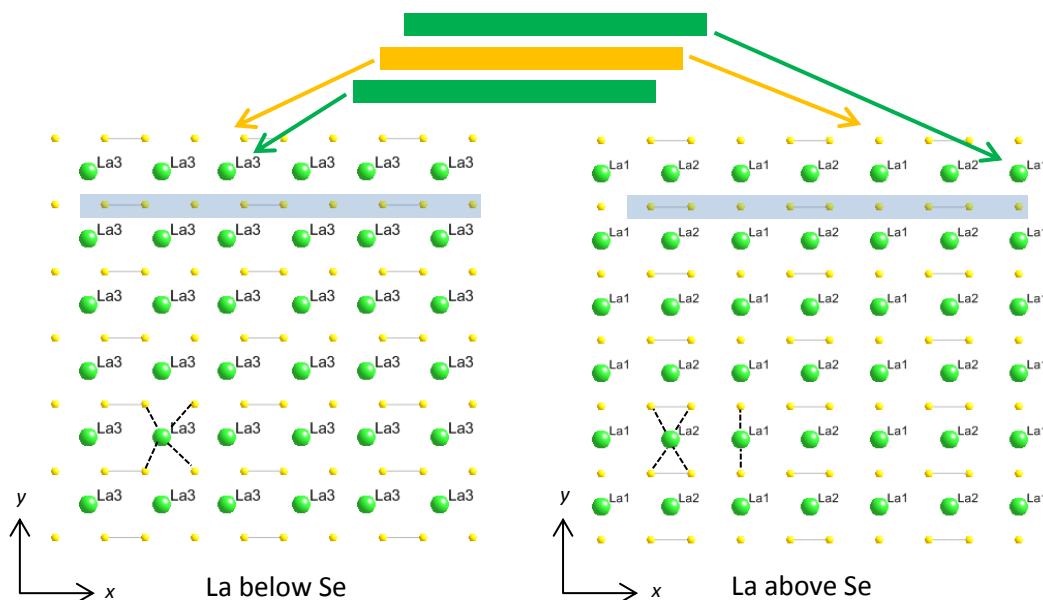

Figure 5.10: *Single layer of Se viewed down [001] direction for α-$La_4O_4Se_3$, La = green, Se = yellow. La sites on the left & right pictures are below & above the Se layers respectively. Blue shows an Se^{2-}/Se_2^{2-} anion chain.*
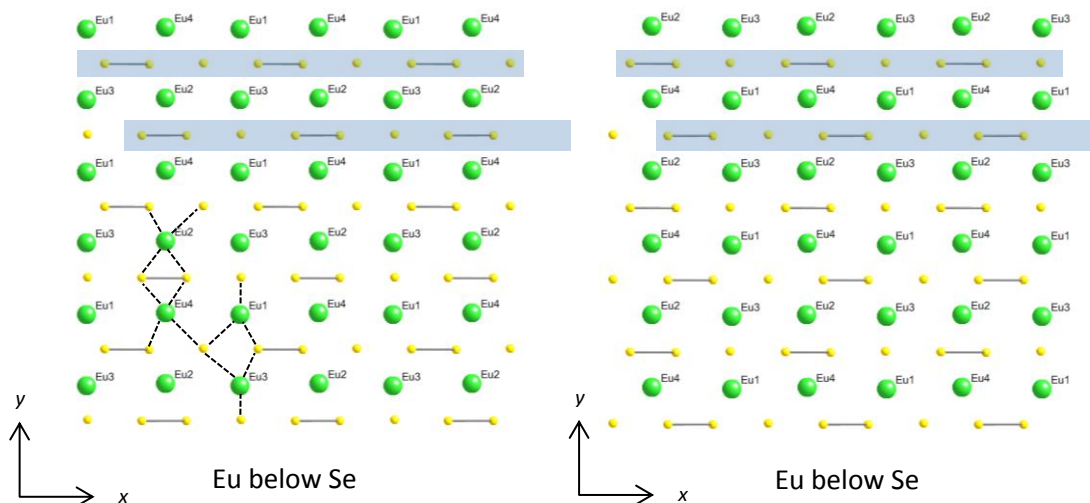

Figure 5.11: *Single layer of Se and A viewed down [001] direction for β-$Eu_4O_4Se_3$, Eu = green, Se = yellow. Two different rows of Se environments are highlighted in blue and red. Eu sites on the left & right pictures are below & above the Se layers respectively.*

A high resolution X-ray powder diffraction pattern of $Eu_4O_4Se_3$ was collected in transmission geometry on the 11-BM beamline at the Argonne national laboratory using a wavelength of 0.413850 Å. The sample was loaded in a 0.8 mm diameter Kapton capillary; in order to reduce absorption $Eu_4O_4Se_3$ was diluted with amorphous SiO_2 in a 1:10 molar ratio. An identical sample preparation and instrumental configuration was used for all synchrotron XRPD data collected in this chapter. Rietveld refinement was carried out using Topas with the structure determined from single crystal data as the starting model. 92 independent parameters were refined: 30 background parameters of a Chebyshev polynomial, 4 unit cell parameters, a sample scale factor, a zero point correction, 8 isotropic thermal parameters (one for each site, excluding oxygen where a single thermal parameter for all sites was refined), 33 atomic coordinates, 4 refining parameters of a full Voigt peak shape, an absorption correction, and 10 terms of a *hkl* dependence of the peak shape as parameterised by Stephens.[11] As can be seen in figure 5.12 an excellent fit to the diffraction data was obtained giving high confidence in the structural model, and proving sample purity. Atomic coordinates do not change significantly from the single crystal derived values, and are listed in appendix 3.

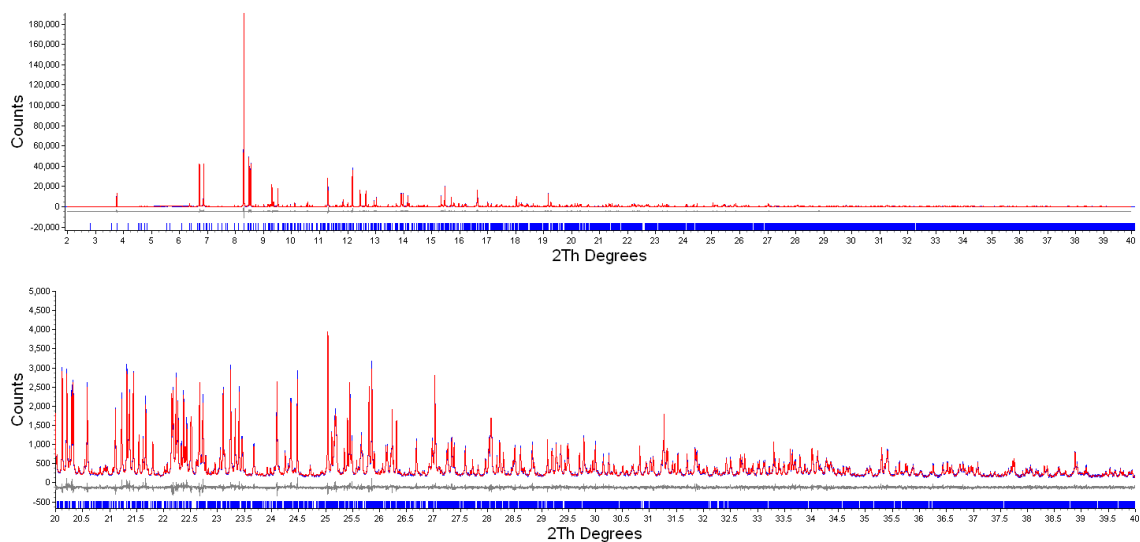
Figure 5.12: *Rietveld refinement profile for $Eu_4O_4Se_3$, monoclinic $P2_1/c$ symmetry, a = 8.403986(7) Å, b = 7.808815(6) Å, c = 12.63788(1) Å and β = 91.36046(7)°. R_{wp} = 7.206 %, R_p = 5.197 %, R_{Bragg} = 2.365 %, gof = 1.896.*

5.4 $A_4O_4Se_3$ materials (A = Gd, Tb, Dy, Ho, Er, Yb & Y)

Synthesis of $A_4O_4Se_3$ materials with smaller A^{3+} cations than Eu^{3+} resulted in a series of compounds with X-ray powder diffraction patterns containing many features similar to the α and β structures. These are highlighted in figure 5.13 which shows powder patterns for samples with nominal compositions of $Nd_4O_4Se_3$, $Eu_4O_4Se_3$, $Gd_4O_4Se_3$, $Dy_4O_4Se_3$ and $Y_4O_4Se_3$. Three regions in the two theta range 10-60° have been highlighted. The changes observed indicate that there are 4 different structure types across this series which we label α, β, γ and δ. The regions highlighted in pink identify 3 reflections, (202) and (204)/(302) in the α-phase, which split in the β-phase due to the change in crystal system from orthorhombic to monoclinic (β ≈ 91.3°). In the γ-phase this splitting is retained suggesting retention of a monoclinic cell. In the δ phase these reflections are not split, suggesting a change back to orthorhombic symmetry. The reflections highlighted in yellow have a major contribution from long range selenium site order, and are present in the α and β-phases, but absent from both the γ and δ-phases.
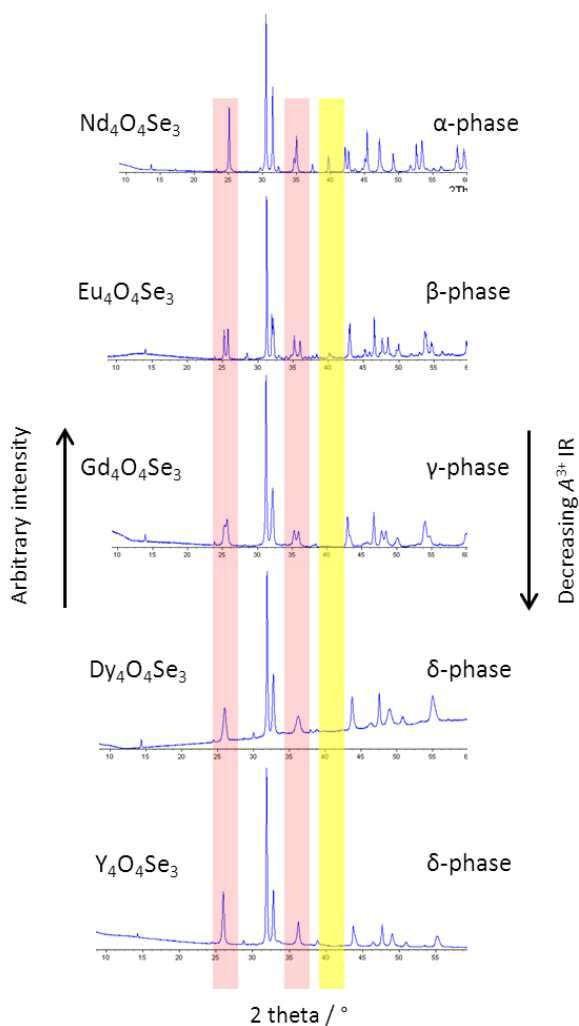

Figure 5.13: X-ray powder diffraction patterns as a function of ionic radii (IR) of the A^{3+} cation, obtained in Bragg-Brentano geometry using Cu Kα$_{1,2}$ radiation.

5.5 γ-$A_4O_4Se_3$ materials (A = Gd & Tb)

X-ray powder diffraction patterns for $Gd_4O_4Se_3$ and $Tb_4O_4Se_3$ show many similarities to β-$Eu_4O_4Se_3$. A powder diffraction pattern collected on a laboratory instrument (d9) for $Gd_4O_4Se_3$ was indexed using Topas to a a = 12.6021 Å, b = 3.8819 Å, c = 4.1777 Å, β = 91.0° monoclinic cell, i.e. (c b a/2) relative to α-$A_4O_4Se_3$. Analysis of systematic absences indicated C2 symmetry. Structure solution was carried out using the charge flipping algorithm implemented in Topas, this resulted in positions of Gd and Se similar to the other members of the series. The oxygen positions were located by Fourier maps. Using the atomic positions of Gd and O for phasing, Fourier maps of the interlayer region suggest a "wave" of electron density for Se (figure 5.14) within the material which we assign to a disordered Se layer.
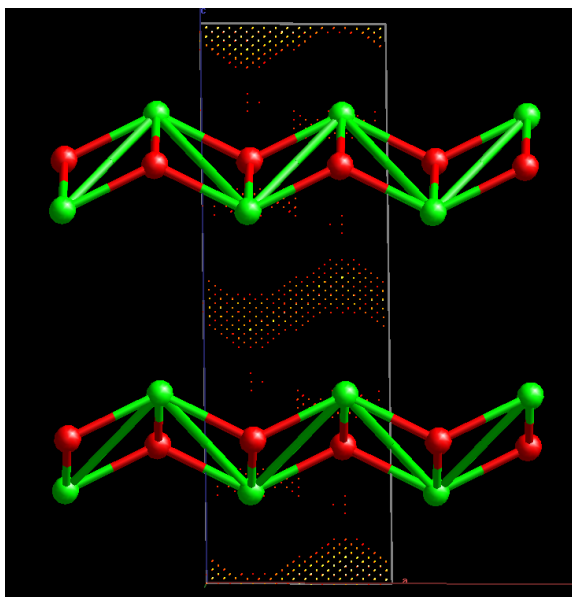

Figure 5.14: *Fourier difference map (Fobs – Fcalc) of $Gd_4O_4Se_3$ with Se sites removed. Dots represent difference electron density.*

Three Se sites were included in the structural model to account for this electron density. The axis setting chosen was a = 4.1777 Å, b = 3.8819 Å, c = 12.6021 Å and β = 91.0° with symmetry A2, i.e. (a/2 b c) relative to α-$A_4O_4Se_3$. Initial Rietveld refinement was carried out on $Gd_4O_4Se_3$, and analysis of the atomic positions indicted the structure to have higher A2/m symmetry. Final Rietveld refinements for $Gd_4O_4Se_3$ and $Tb_4O_4Se_3$ (which appears to be isostructural) are shown in table 5.5 and table 5.6 respectively. 47 independent parameters were used during these refinements: 4 unit cell parameters, 12 parameters of a Chebyshev polynomial to model the background, 4 refining parameters of a pseudo Voigt peak shape (TCHz), 10 parameters to model a *hkl* dependence of peak shape as parameterised by Stephens[11], 5 isotropic temperature factors (one for each site), 6 refining atomic positions, 1 scale parameter, 3

refining occupancies of Se sites, a parameter to model the axial divergence and a sample height correction. Rietveld refinement profiles for these two systems are shown in figure 5.15.

Table 5.5: *Crystallographic parameters obtained from Rietveld refinement, $Gd_4O_4Se_3$, A2/m symmetry, a = 4.1738(2) Å, b = 3.8808(1) Å, c = 12.6051(4) Å, β = 90.984(4)°, AJT180a d9_07160, R_{wp} = 2.457, R_p = 1.781, R_{Bragg} = 0.958 %, gof = 2.321.*

Site label	Wyckoff symbol	x	y	z	Occupancy	B / Å^2
Gd1	4i	0.2439(3)	0	0.66390(9)	1	0.44(2)
Se1	2d	0.5	0	0	0.475(8)	0.9(2)
Se2	2a	0	0	0	0.33(1)	0.01(28)
Se3	4i	0.209(2)	0	-0.0226(3)	0.364(7)	0.8(2)
O1	4i	0.257(2)	0	0.2547(6)	1	0.6(2)

Table 5.6: *Crystallographic parameters obtained from Rietveld refinement, $Tb_4O_4Se_3$, A2/m symmetry, a = 4.1562(2) Å, b = 3.8582(1) Å, c = 12.5028(4) Å, β = 91.017(3)°, AJT190a d7_03533, R_{wp} = 3.058, R_p = 2.206, R_{Bragg} = 1.110 %, gof = 2.256.*

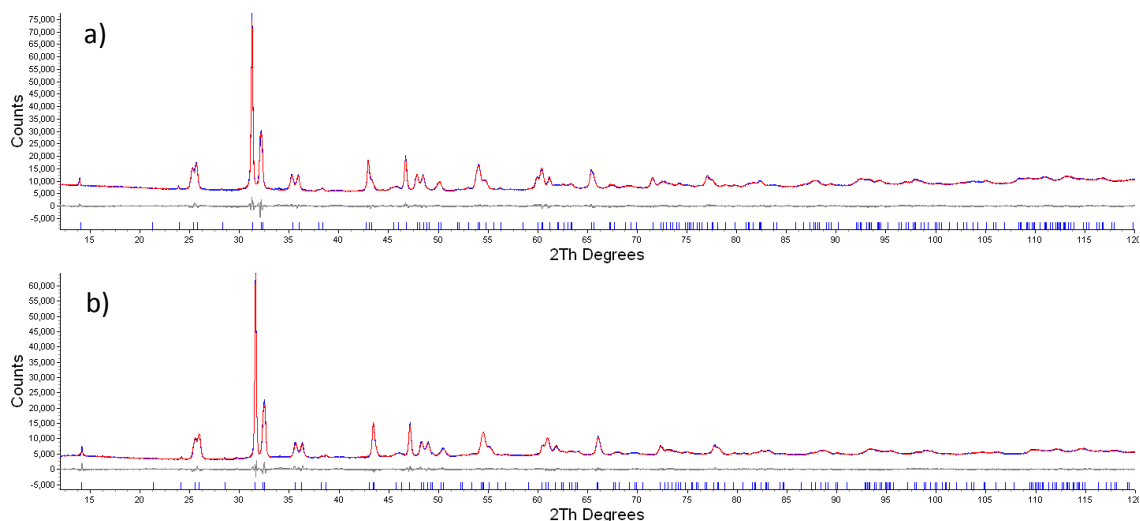| Site label	Wyckoff symbol	x	y	z	Occupancy	B / Å^2
Tb1	4i	0.2450(4)	0	0.6644(1)	1	1.02(2)
Se1	2d	0.5	0	0	0.478(9)	2.8(2)
Se2	2a	0	0	0	0.31(1)	0.2(3)
Se3	4i	0.212(3)	0	-0.0270(4)	0.360(8)	2.8(2)
O1	4i	0.251(3)	0	0.2543(7)	1	2.1(2)

Figure 5.15: *Rietveld refinement profiles of X-ray powder diffraction data of a) $Gd_4O_4Se_3$ and b) $Tb_4O_4Se_3$ at room temperature, A2/m symmetry.*

The structure of γ-$A_4O_4Se_3$ contains the same basic stacking arrangement of $[A_2O_2]^{2+}$ layers as the α and β-$A_4O_4Se_3$ materials, figure 5.16. The fluorite-like layers are separated by selenium

129

containing layers. Selenium site occupancies were refined giving compositions of $Gd_4O_4Se_{3.07(4)}$ and $Tb_4O_4Se_{3.15(5)}$ consistent with the target phase composition. The model of Se sites used is only approximate as the layers are thought to consist of Se_2^{2-} and Se^{2-} chains as found in the α and β-phases, but with a high degree of intrachain disorder. This disorder is discussed in detail in Section 5.7.
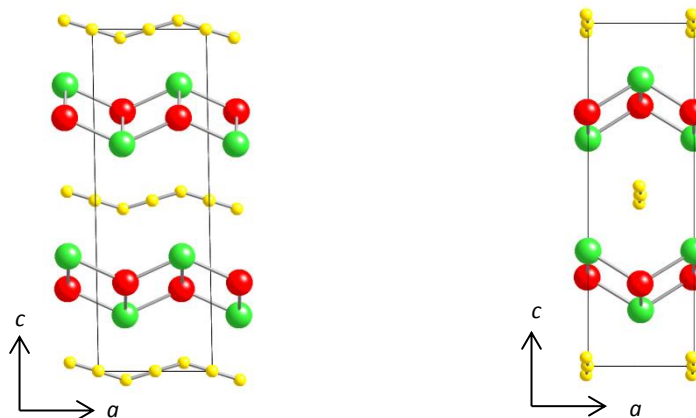

Figure 5.16: *Crystal structure of γ-$A_4O_4Se_3$ materials, A2/m symmetry, monoclinic unit cell a ~ 4.2 Å, b ~ 3.9 Å, and c ~ 12.6 Å with β ~ 91°. A = green, O = red, Se = yellow.*

5.6 δ-$A_4O_4Se_3$ materials (A = Dy, Ho, Er, Yb & Y)

Pawley refinements against laboratory X-ray powder diffraction for $Y_4O_4Se_3$ suggested the α-phase orthorhombic cell with *Amm*2 symmetry could account for all of the observed reflections. No peak splitting as found for the β and γ-phases was observed. Structure solution was attempted using a high resolution RT powder diffraction pattern collected on the 11-BM beamline at the Argonne national laboratory. Comparison of the observed diffraction pattern with the diffraction pattern calculated for the α-$A_4O_4Se_3$ structure revealed that several reflections predicted by the α structure were missing. The *hkl* indices of the missing reflections suggested a higher symmetry of $A2_122$, in an orthorhombic unit cell with dimensions a = ~4.12 Å, b = ~3.81 Å, c = ~12.42 Å, i.e.(a/2, b, c,) relative to α-$A_4O_4Se_3$. Charge flipping using Topas gave Y and Se sites located in a similar geometric arrangement to those in α-$A_4O_4Se_3$, O sites were added to chemically sensible positions using Fourier maps. Rietveld analysis using the structural model shown in table 5.7 resulted in the Se2 site refining close to the (0 $^1/_2$ 0) special position. The space group was therefore modified to *Amma* with a = 4.12056(6) Å, b = 3.81484(4) Å and c =12.4212(1) Å, to account for the higher symmetry and give a consistent axis set to the α, β and γ-structures, i.e. (a/2, b , c) relative to α-$A_4O_4Se_3$. The Se site occupancies were initially fixed at 0.375 to give the overall composition expected. This structural model gave a good fit to the synchrotron X-ray powder diffraction pattern.

Table 5.7: *Atomic positions for δ-$A_4O_4Se_3$ in $A2_122$ symmetry.*

Site	x	y	z	Occ
Y1	0.25	0	~0.16	1
Se1	0.25	0	~0.48	0.375
Se2	0	~0.50	0	0.375
O1	0.25	0	~0.76	1

The experimental peak shape of $Y_4O_4Se_3$ was significantly broader than $Eu_4O_4Se_3$, with a noticeable *hkl* dependence to peak widths (the intrinsic high instrumental resolution of 11-BM makes this clearly observable). A Stephens model of anisotropic strain broadening was introduced.[11] The Rietveld refinement profile and refined parameters of the Stephens model are given in figure 5.17 and table 5.8 respectively.
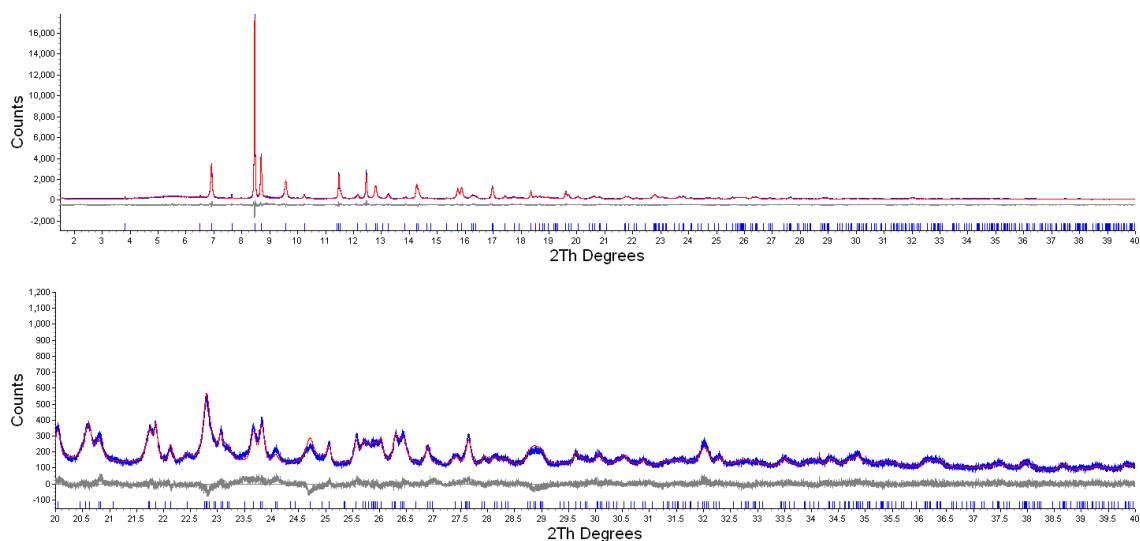
Figure 5.17: *Rietveld refinement profile of $Y_4O_4Se_3$, 11bmb_8961 AJT195, Amma symmetry, a = 4.12056(6) Å, b = 3.81484(4) Å and c =12.4212(1) Å. R_{wp} = 8.629 %, R_p = 6.663, R_{Bragg} =2.866 %, gof = 1.488.*

Table 5.8 *Refined parameters for the Stephens model of anisotropic peak broadening for $Y_4O_4Se_3$ at room temperature.*

Parameter	Value
s400	3455(1214)
s040	37(14)
s004	-5(1)
s220	-1923(667)
s202	1859(657)
s022	-33(14)
eta	0.9(2)

The structural model proposed for $Y_4O_4Se_3$ is given in table 5.9. 51 independent parameters were used during this refinement: 3 unit cell parameters, 26 parameters of a Chebyshev polynomial to model the background, 4 refining parameters of a full Voigt peak shape, 7 parameters to model the *hkl* dependence of peak shape, 4 isotropic temperature factors (one for each site), 3 refining atomic positions, 1 scale parameter, 2 site occupancies of Se sites, a zero point correction.

Table 5.9: *Structural model for $Y_4O_4Se_3$, a = 4.12056(6)Å, b = 3.81484(4) Å and c =12.4212(1) Å, Amma symmetry, R_{wp} = 8.629 %, R_p = 6.663, R_{Bragg} =2.866 %, gof = 1.488.*

Site label	Wyckoff site	x	y	z	occupancy	B
Y(1)	4c	0.25	0	0.83422(4)	1	0.680(9)
Se(1)	4c	0.25	0	0.5221(1)	0.335(2)	2.18(6)
Se(2)	4b	0	0	0.5	0.372(2)	1.64(5)
O(1)	4c	0.25	0	0.2433(2)	1	0.18(5)

Rietveld refinement was also carried out against laboratory X-ray powder diffraction data collected at room temperature for A = Dy, Ho, Er and Yb compositions using the structural model determined for $Y_4O_4Se_3$. Figure 5.18 shows good Rietveld fits could be obtained using this structural model. Minor impurities were included as additional phases in the refinements. Crystallographic parameters for these refinements, along with A = Y, are listed in table 5.10. Refinement details are given in Appendix 2.
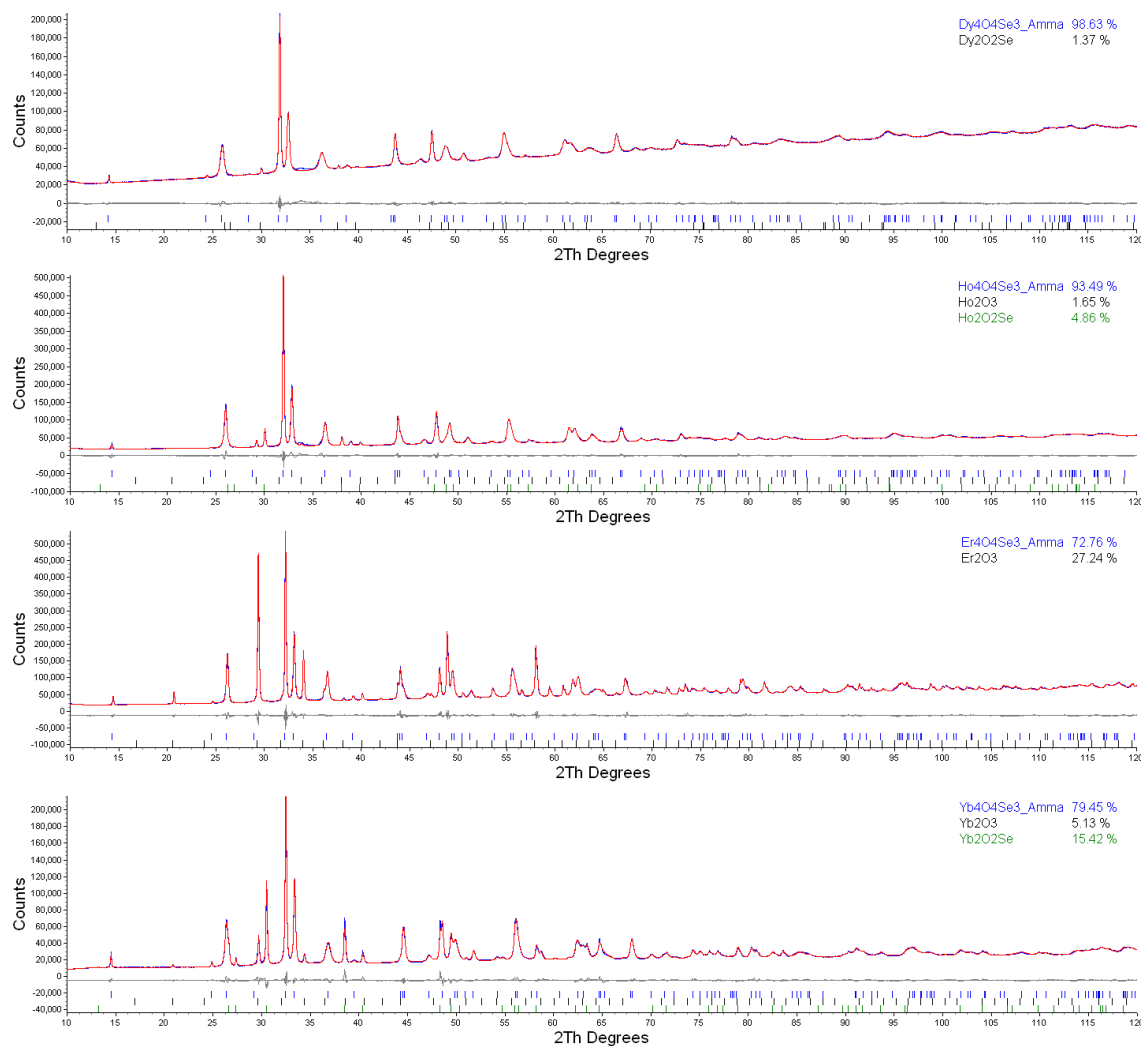
Figure 5.18: *Rietveld refinement profiles of δ-$A_4O_4Se_3$ powder X-ray diffraction data at room temperature, a) $Dy_4O_4Se_3$, b) $Ho_4O_4Se_3$, c) $Er_4O_4Se_3$ and d) $Yb_4O_4Se_3$. Blue vertical tick marks correspond to the calculated peak positions of $A_4O_4Se_3$ phase.*

δ-$A_4O_4Se_3$ adopts an orthorhombic structure closely related to α-$A_4O_4Se_3$ with the same stacking arrangement of $[A_2O_2]^{2+}$ layers interleaved by layers containing selenium, figure 5.19. Refinement of Se occupancies for the various phases gave Rietveld compositions of $Dy_4O_4Se_{3.01(4)}$, $Ho_4O_4Se_{2.93(4)}$, $Er_4O_4Se_{3.02(4)}$, $Yb_4O_4Se_{2.82(5)}$ and $Y_4O_4Se_{2.83(1)}$. There is some indication of a Se composition below 3 for the Y and Yb materials. The way this may occur is discussed later. To investigate possibility of a fixed substoichiometric composition < 3.0, attempts were made to synthesise δ-$A_4O_4Se_3$ phases with 7 % and 14 % molar per cent Se deficiency (i.e. $A_4O_4Se_{2.8}$ and $A_4O_4Se_{2.6}$). These resulted in only the A_2O_2Se phase being formed. No selenium rich impurity phases were found with δ-$A_4O_4Se_3$ samples, but we could see evidence of small amounts of selenium vapour condensing on the insides of the sealed tubes after synthesis.

Table 5.10: *Crystallographic parameters for $A_4O_4Se_3$ extracted from Rietveld analysis in space group Amma.*

|	$Dy_4O_4Se_3$	$Ho_4O_4Se_3$	$Er_4O_4Se_3$	$Yb_4O_4Se_3$	$Y_4O_4Se_3$
Sample	AJT181a	AJT154a	AJT148c	AJT197b	AJT195
Scan	d9_07182	d9_07219	d9_07192	d7_03733	11bmb_8961
R_{wp}	1.104	2.790	2.640	2.935	8.629
R_p	0.735	1.904	1.821	2.032	6.663
R_{Bragg}	0.334	1.020	0.828	0.660	2.866
gof	2.630	5.910	6.282	4.628	1.488
Parameters	42	45	41	45	51
a / Å	4.1352(2)	4.1126(1)	4.0919(1)	4.0565(1)	4.12056(6)
b / Å	3.8319(1)	3.8073(1)	3.78584(6)	3.74734(9)	3.81474(4)
c / Å	12.4455(5)	12.4021(4)	12.3468(2)	12.2102(4)	12.4212(1)
Volume / Å^3	197.11(1)	194.19(1)	191.205(7)	185.610(9)	195.247(4)
Se1 Occupancy	0.331(7)	0.378(7)	0.384(7)	0.345(8)	0.335(2)
Se2 Occupancy	0.420(8)	0.355(6)	0.372(7)	0.359(8)	0.372(2)
$zA1$	0.8352(1)	0.8354(1)	0.83560(9)	0.8358(1)	0.83422(4)
$zSe1$	0.5261(5)	0.5240(4)	0.5240(4)	0.5220(5)	0.5221(1)
$zO1$	0.2509(7)	0.2486(6)	0.2423(5)	0.2418(8)	0.2433(2)
$A1$ B / Å^2	0.47(3)	1.02(3)	0.24(3)	1.14(3)	0.680(9)
Se1 B / Å^2	2.2(2)	3.8(2)	2.7(2)	2.3(3)	2.18(6)
Se2 B / Å^2	3.0(3)	1.7(2)	1.7(2)	2.3(3)	1.64(5)
O1 B / Å^2	1.0(2)	3.0(2)	0.07(18)	2.0(3)	0.18(5)
Refined Se composition	3.01(4)	2.93(4)	3.02(4)	3.82(5)	2.83(1)
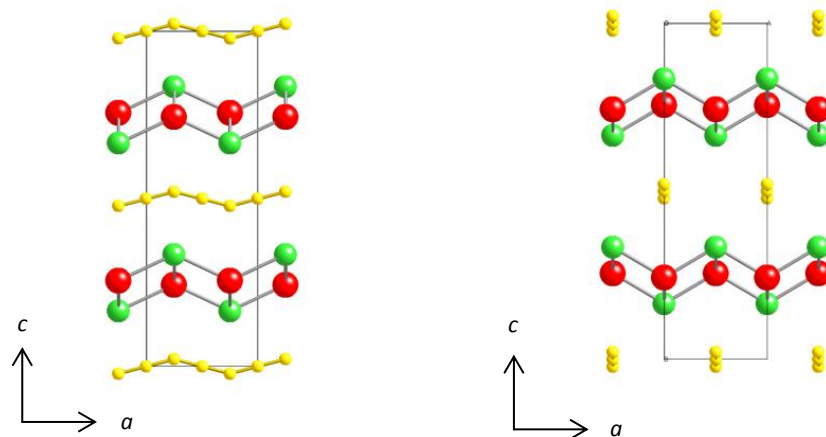
Figure 5.19: *Crystal structure of δ-$A_4O_4Se_3$ in Amma symmetry, A = green, O = red, Se = yellow.*

A degree of *hkl*-dependent sample peak broadening is present for all members of this δ-$A_4O_4Se_3$ series, this is especially evident for the Dy containing analogue, figure 5.18. This is likely due both to strain induced from selenium site disorder, and that the system is only ordered on a small length scale due to the disorder (see below), thus scattering occurs from small domains within the material.

5.7 comparison of α, β, γ and δ structures

There is clearly a close structural relationship between the α, β, γ and δ-$A_4O_4Se_3$ structures. Figure 5.20 shows how the Rietveld derived cell parameters vary across the series, the unit cell parameters have been normalised to a ~4.1 Å x 3.9 Å x 12 Å cell (δ phase). The unit cell parameters for α-$A_4O_4Se_3$ (A = La, Pr, Ce) are those reported by Srobel.[7] There is a relatively smooth decrease in cell volume with decreasing ionic radii of the A^{3+} cation across all 4 phases. The normalised a/b ratio for the β phase is slightly larger than expected due to a larger a axis. This is not un-expected given the different Se^{2-}/Se_2^{2-} packing arrangements present. There is also a clear break in the a/b ratio between the α/β and the γ/δ phases which contain disordered Se layers. The c cell parameter shows a general decrease for smaller A^{3+} cations, with a small break between α/β and the γ/δ structure types.
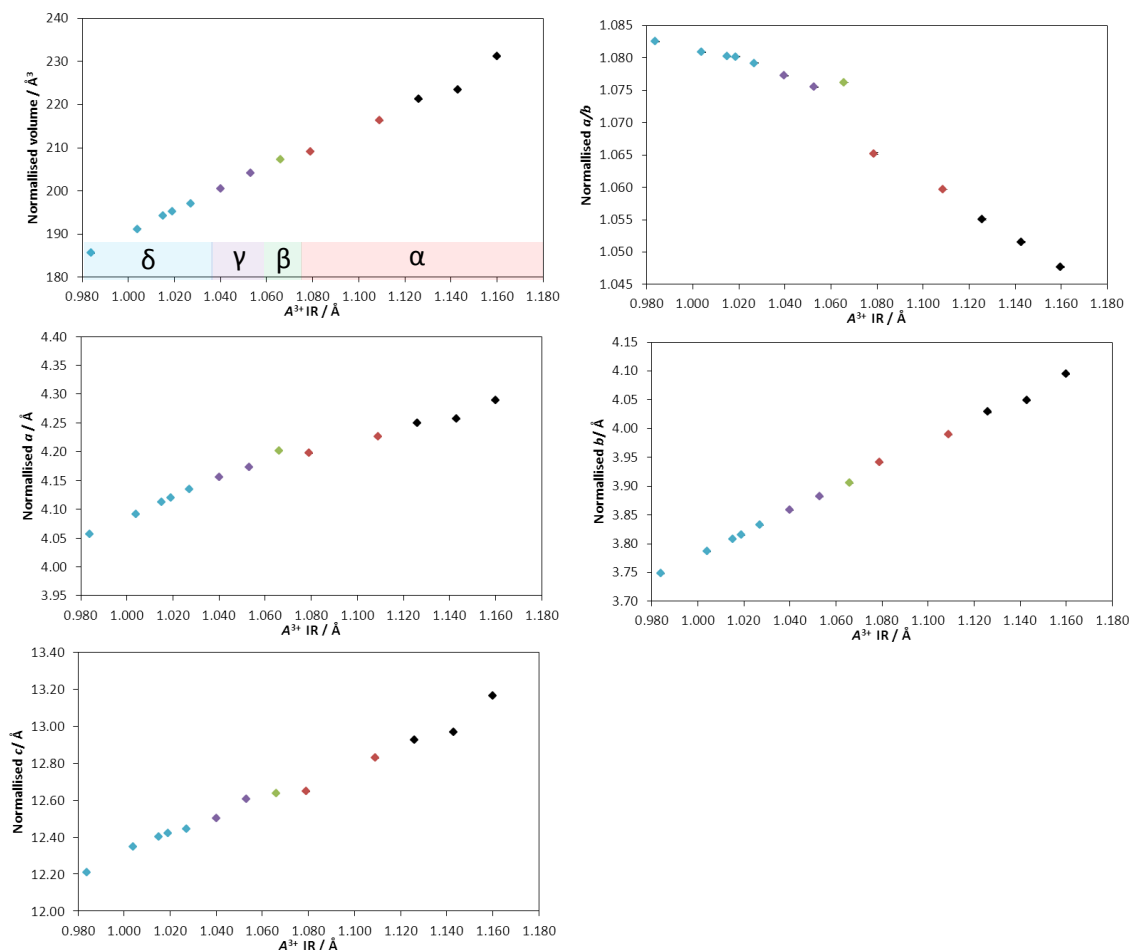

Figure 5.20: Unit cell parameters for $A_4O_4Se_3$ normalised to δ-$A_4O_4Se_3$ cell, α = red & black (literature values[7]), β = green, γ = purple, δ = blue. A site from left to right, Yb, Er, Ho, Y, Dy, Tb, Gd, Eu, Sm, Nd, Pr, Ce and La.

Each structure type contains essentially identical $[A_2O_2]^{2+}$ layers and differ only in the arrangements of interlayer Se^{2-} and Se_2^{2-} anions. As already discussed for the α and β structures, the Se-ordered materials contain chains of alternating Se^{2-} and Se_2^{2-} anions along

136

the larger of the pseudo-tetragonal axes (a). In both the γ and δ disordered structures we observed a wave-like smear of Se electron density in this direction. It seems likely that this 'smear' is mimicking the ordered arrangement in the α and β structures. One possible mechanism for the disorder is via the disordered anion chain origins shown in figure 5.21. In β-$Eu_4O_4Se_3$ there are two positions which the Se/Se$_2$ anion chain adopts with a different origin shift along a. This results in Se_2^{2-} units bonding through a η^2 type interaction to a A^{3+} cation in either the $[A_2O_2]^{2+}$ layer above or below the chain, figure 5.21. These two anion chain origins alternate along [010], resulting in the doubled b cell parameter of the β structure relative to the α structure. We can imagine merging both anion chain positions onto one row, figure 5.21. Here it is clear that only two from every four A^{3+} sites is bonded through a η^2 interaction to a Se_2^{2-} anion. Thus there are two other anion chain shifts along a which could possibly be adopted, which can be generated by shifting the Se^{2-} and Se_2^{2-} positions half a unit cell along [100] of the β-$Eu_4O_4Se_3$ structure (a = 8.40437(8) Å). The presence of all four anion chain displacements rather than two in β-$Eu_4O_4Se_3$ introduces extra symmetry and results in the halved a cell parameter in the γ and δ structures.

Figure 5.22a show the anions found in a single β-$Eu_4O_4Se_3$ chain in yellow and the anion positions which would be occupied from the described shift along [100] in pink, for each of the origin choices of figure 5.21. If we then merge these 4 anion chain positions onto a single row, figure 5.22b, we see that the selenium sites would adopt on average a wavelike pattern in excellent agreement with the γ and δ structures presented above. The agreement between the two models gives us confidence in the disordered anion structure proposed for the γ and δ structures. Attempts to model stacking faults and peak broadening due to these disordered chain positions are ongoing. It is also worth noting that the single anion chain in α-$A_4O_4Se_3$ leads to a polar structure the "$_{Se}/^{Se-Se}\backslash_{Se}$" mean Se^{2-} in the anion chain always points along c. in the other structures the presence of "$_{Se}/^{Se-Se}\backslash_{Se}$" and "$^{Se}\backslash_{Se-Se}/^{Se}$" chains destroys the polarity. Figure 5.22b also suggests one model for allowing Se deficiency in these structures. We can imagine Se deficiency as occurring via $Se_2^{2-}{}_{(s)} \rightarrow Se_{(g)} + Se^{2-}{}_{(s)}$. There is a potential Se^{2-} site close to each Se_2^{2-} site in a chain, such that a defect of the type $(Se^{2-} Se_2^{2-})_n Se^{2-} Se^{2-} (Se_2^{2-} Se^{2-})_n$ would be of relatively low energy.
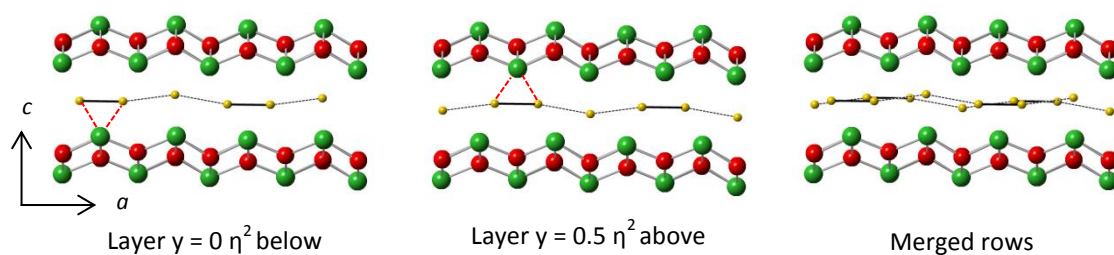
Figure 5.21: *Ordered anion chain displacements along [100] adopted in β-$Eu_4O_4Se_3$ viewed down [010]. A = green, O = red, Se = yellow. Se_2^{2-} units identified by solid black lines, connections between Se^{2-} and Se_2^{2-} anions marked by dashed lines. $η^2$ interaction marked in red.*
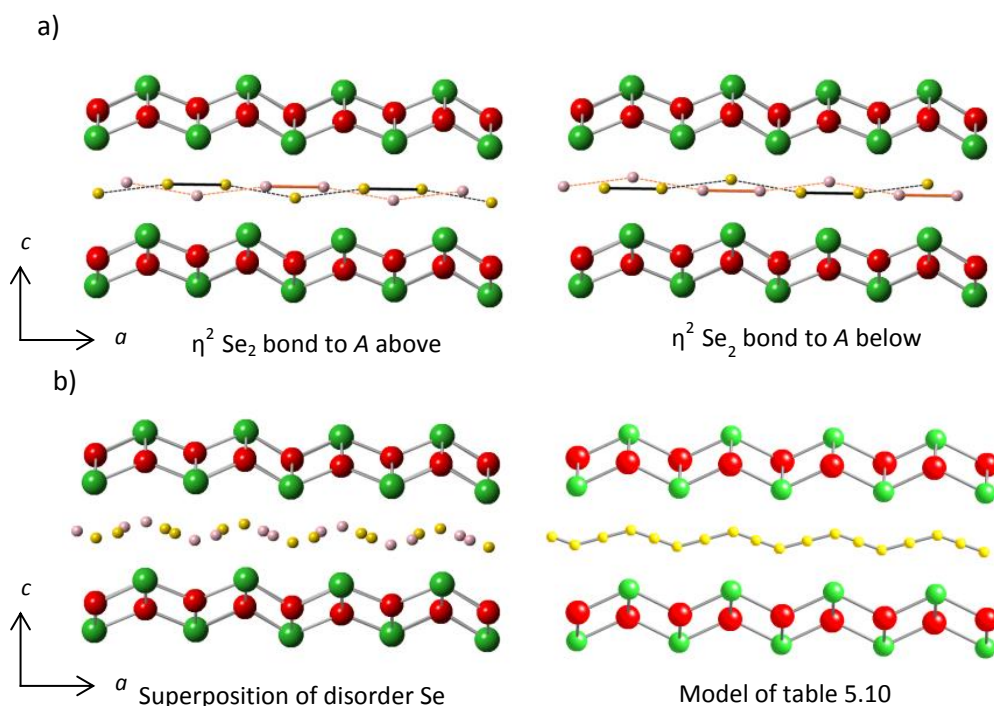

Figure 5.22: *a) Possible ordered anion chain displacements along [100] adopted in γ & δ-$A_4O_4Se_3$ with 4 chain positions, b) comparison of ordered anion chains with 4 chain positions and disordered model of γ and δ-$A_4O_4Se_3$.*

While this work was being carried out synthesis of nanoparticles with a plate like morphology with $A_4O_4Se_{3-x}$ (A = Gd-Ho) composition were reported by Gu *et al*., via a solution state method.[12] Gu showed a gradual decrease of A:Se ratio of these nanoparticles from EDX analysis, table 5.11, suggesting an increasing number of Se vacancies within the structure.[12] Since we were unable to prepare phase pure samples of δ-$A_4O_4Se_3$ materials via our solid state route EDX analysis was not attempted. Such a large selenium deficiency was not observed in the crystallographically derived compositions in this work. The XRPD patterns reported by Gu are of very low quality, but consistent with those reported in this work. Gu reported the

disappearance of some weak diffraction peaks for small, possibly due to the thickness of the samples.[12] In light of our work, where we also see the disappearance of Bragg peaks, we ascribe this observation to the loss of long range order due to disorder of the selenium layer.

Table 5.11: *A:Se ratio from EDX measurements on nanoparticles by Gu.*[12]

Elements	Ratio
Gd:Se	4:3.27
Tb:Se	4:2.78
Dy:Se	4:2.67
Ho:Se	4:2.25

5.8 Thermal expansion behaviour of $A_4O_4Se_3$ systems

The thermal expansion behaviour of each $A_4O_4Se_3$ (*A* = Nd, Sm, Eu, Gd, Tb, Dy, Ho, Er and Y) composition was measured by powder X-ray diffraction between 300 K and 12 K. 20 minute diffraction patterns were recorded while ramping the temperature of the cryostat at 15 K hr^{-1} such that each diffraction pattern was obtained over a ~5 K range, and the average temperature of each scan was recorded. Rietveld analysis was carried out on each of the diffraction patterns to determine the temperature dependence of the unit cell parameters. Unit cell parameters, a single isotropic temperature factor for all sites, a scale factor, 4 refining parameter of a pseudo Voigt peak shape (TCHz) and a sample height were typically refined, along with parameters to model any impurity phases present. Anisotropic peak broadening was described using fixed values extracted from a Stephens model at room temperature. No structural phase transitions were observed over this temperature range for any of the materials, with a smooth decrease in unit cell volume observed for all compositions. The overall volume expansion of each phase was similar, with a volume coefficient of thermal expansion $\alpha_V = \frac{V_{T1}-V_{T2}}{V_{T1}(T2-T1)}$ ranging from 1.746(9) x 10^{-5} K^{-1} to 2.237(3) x 10^{-5} K^{-1} over the temperature range 12 to 300 K; coefficients for each composition are given in table 5.11, with no clear trend between the structure type adopted and the magnitude of thermal expansion. Thermal expansion plots of unit cell parameters for these materials are included in Appendix 3.

Table 5.11: Volume coefficient of thermal expansion for samples with $A_4O_4Se_3$ composition determined from X-ray powder diffraction.

Composition	α_V / K^{-1}
$Nd_4O_4Se_3$	$2.237(3) \times 10^{-5}$
$Sm_4O_4Se_3$	$2.076(5) \times 10^{-5}$
$Eu_4O_4Se_3$	$1.789(3) \times 10^{-5}$
$Gd_4O_4Se_3$	$1.85(1) \times 10^{-5}$
$Tb_4O_4Se_3$	$1.746(9) \times 10^{-5}$
$Dy_4O_4Se_3$	$2.19(1) \times 10^{-5}$
$Ho_4O_4Se_3$	$1.948(4) \times 10^{-5}$
$Er_4O_4Se_3$	$2.063(4) \times 10^{-5}$
$Y_4O_4Se_3$	$1.798(3) \times 10^{-5}$

5.9 Conclusions

Eight new compositions have been prepared via a solid state route, with an atomic ratio A:O:Se of 4:4:3. These new materials adopt 3 new structure types and are closely related to the previously reported α-$A_4O_4Se_3$ (A = La-Nd, Sm) series. The β, γ and δ phases all have the same $[A_2O_2]^{2+}$ fluorite-like layers as found in α-$A_4O_4Se_3$, and in all 4 polymorphs these fluorite-like layers are separated by selenium layers containing Se^{2-} and Se_2^{2-} units. α-$A_4O_4Se_3$ contains an ordered arrangement of Se_2^{2-} and Se^{2-} ions, resulting in 3 different A^{3+} coordination environments. β-$A_4O_4Se_3$ contains similar rows of ordered anions which adopt two positions along [100] resulting in a doubling of the b axis, and a change to monoclinic symmetry. Four A^{3+} coordination environments are found with either AO_4Se_3 or AO_4Se_4 coordination. γ-$A_4O_4Se_3$ and δ-$A_4O_4Se_3$ adopt related monoclinic and orthorhombic unit cells but contain disordered selenium layers separating the fluorite-like layers. We believe that locally the structures contain similar Se anion chains between each layer, but with the chain positions disordered along either the stacking c-axis or along the b-axis, leading to an averaged long-range structure. Both γ and δ phases contain significant anisotropic peak broadening as a result of these stacking faults.

References

1. Weber, F. A. and Schleid, T., *Zeitschrift Fur Anorganische Und Allgemeine Chemie*, 2001, **627**, 1383-1388
2. Wu, L.-B. and Huang, F.-Q., *Zeitschrift Fur Kristallographie-New Crystal Structures*, 2007, **222**, 175-176
3. Weber, F. A., Schurz, M. C., Frunder, S., Kuhn, C. F., and Schleid, T., *Crystals*, 2012, **2**, 1136-1145
4. Tougait, O. and Ibers, J. A., *Acta Crystallographica Section C-Crystal Structure Communications*, 2000, **56**, 623-624
5. Eick, H. A., *Acta Crystallographica*, 1960, **13**, 161-161
6. Dugue, J., Adolphe, C., and Khodadad, P., *Acta Crystallographica Section B-Structural Crystallography and Crystal Chemistry*, 1970, **B 26**, 1627-1628
7. Strobel, S., Choudhury, A., Dorhout, P. K., Lipp, C., and Schleid, T., *Inorganic Chemistry*, 2008, **47**, 4936-4944
8. ICDD, *PDF4+*, 2012
9. Palatinus, L. and Chapuis, G., *Journal of Applied Crystallography*, 2007, **40**, 786-790
10. CRYSTALS, Betteridge, P. W., Carruthers, J. R., Cooper, R. I., Prout, K., Watkin, D. J. (2003). J. Appl. Cryst. 36, 1487-1487
11. Stephens, P. W., *Journal of Applied Crystallography*, 1999, **32**, 281-289
12. Gu, J., Zhao, Z.-Q., Ding, Y., Chen, H.-L., Zhang, Y.-W., and Yan, C.-H., *Journal of the American Chemical Society*, 2013, **135**, 8363-8371

Chapter 6: Synthesis and Structural Characterisation of $A_2O_2Se_2M_2O$ Materials

6.1 Introduction

The syntheses of $La_2O_2Se_2Fe_2O$ and $La_2O_2S_2Fe_2O$ ($A_2O_2Q_2M_2O$) were originally reported by Mayer *et al.* and their structures determined from single crystal X-ray diffraction studies at room temperature.[1] Both phases are tetragonal, with $a = b$ ~4.0 Å, c ~17.9 Å and $a = b$ ~4.1 Å, c ~18.6 Å for the S and Se analogues respectively, and have $I4/mmm$ symmetry. Their structure can be described as containing fluorite-like $[A_2O_2]^{2+}$ layers separated from anti-CuO_2-type $[Fe_2O]^{2+}$ layers by Se^{2-} ions (Figure 6.1). The Se^{2-} ions complete a square 4+4 antiprismatic coordination of La (LaO_4Se_4), and also coordinate to the Fe atoms such that the Fe-containing layer can also be described as an unusual network of face-sharing FeO_2Se_4 octahedra with two axial oxide ions and four equatorial selenide ions, see figure 6.1. This arrangement leads to a square array of Fe sites with a Fe-Fe edge of ~2.8 Å. Powder neutron diffraction studies reported by Free suggested that both materials order antiferromagnetically on cooling (T_N = 110 and 90 K, for $La_2O_2Fe_2OS_2$ and $La_2O_2Fe_2OSe_2$). There has been significant recent interest in these materials due to the similarity between their Fe arrangements and that of the LaOFeAs superconductors, and it has been proposed that they can be viewed as the Mott-insulator parents of the superconductors. As discussed in Chapter 1, in recent years this family has been expanded to include a wide range of rare earths and a number of different divalent transition metals. Table 6.1 shows reported compositions of the $A_2O_2Se_2M_2O$ series and crystal structure details are given in table 6.2.[2-5]
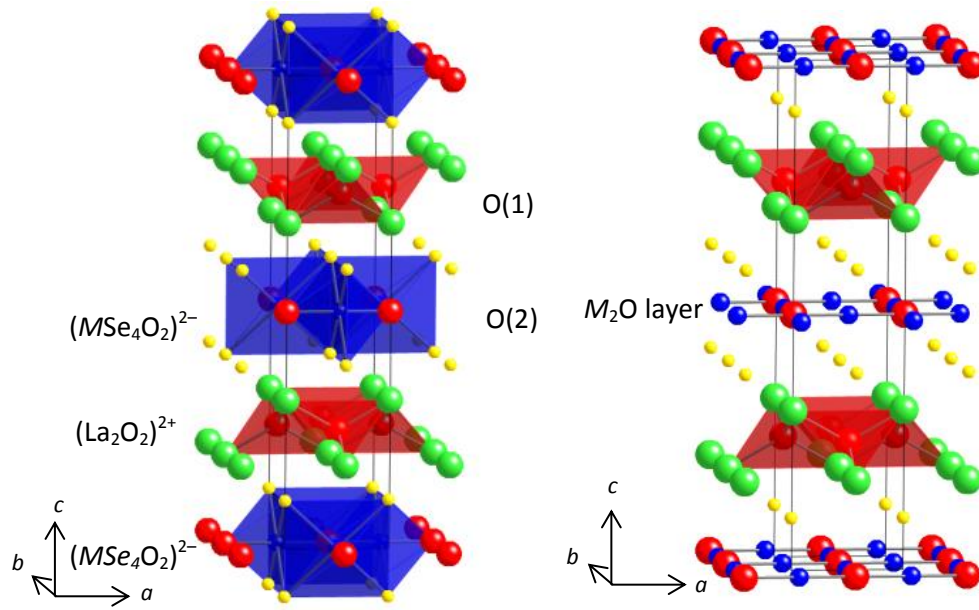
Figure 6.1: *Nuclear structure of $A_2O_2Se_2M_2O$, La = green, O = red, Se = yellow, M = blue, we define O(1) as the oxygen within the La_4O tetrahedra, and O(2) as within the transition metal octahedra.*

Table 6.1: *Reported compositions for $A_2O_2Se_2M_2O$ series.*

M^{2+}	A^{3+}	Ref
Mn	La Ce Pr	[4, 5]
Fe	La Ce Pr Nd Sm	[5, 6 7]
Co	La	[8]

Table 6.2: *Crystal structure of $A_2O_2Se_2M_2O$ with I4/mmm symmetry, a = b ~4.1 Å, c ~18.6 Å.*

Site label	Wyckoff site	x	y	z
A(1)	4e	0.5	0.5	zA
Se(1)	4e	0	0	zSe
M(1)	4c	0.5	0	0
O(1)	2b	0.5	0	0.25
O(2)	4d	0.5	0.5	0

It has been shown by Free (a previous member of the group) that some of the manganese and iron containing compositions undergo subtle structural phase transitions upon cooling resulting in discontinuities in unit cell parameters and in some cases weak superstructure reflections in their diffraction patterns.[5] To date the details of these transitions and their impact for magnetic ordering have not been explored. In this work low temperature single

crystal X-ray diffraction has been carried out to investigate this. Data collections were carried out using both laboratory-based sealed tube molybdenum 3 circle area diffractometers and synchrotron beamlines fitted with nitrogen and helium open flow cooling devices to reach ~80 K and ~20 K respectively.

6.2 Synthesis

Materials with $A_2O_2Se_2M_2O$ composition were synthesised using the procedure outlined in section 2.2.6. Single crystals of $La_2O_2Se_2Fe_2O$, $La_2O_2Se_2Mn_2O$ and $Pr_2O_2Se_2Mn_2O$ of suitable size and quality for diffraction studies were obtained by slow cooling polycrystalline samples from ~1300 °C to ~ 1000°C. Attempts to synthesise single crystals from bulk polycrystalline samples of $Pr_2O_2Se_2Fe_2O$ and $La_2O_2Se_2Co_2O$ using this synthetic method were not successful.

6.3 Investigation of the low temperature structure of $La_2O_2Se_2Fe_2O$

Free reported the cell parameters for $La_2O_2Se_2Fe_2O$ from Rietveld analysis of powder X-ray and neutron data; his data are reproduced in figure 6.2. There is a small discontinuity in the *c* lattice parameter at ~90 K, indicating the possibility of a structural phase transition at low temperature.
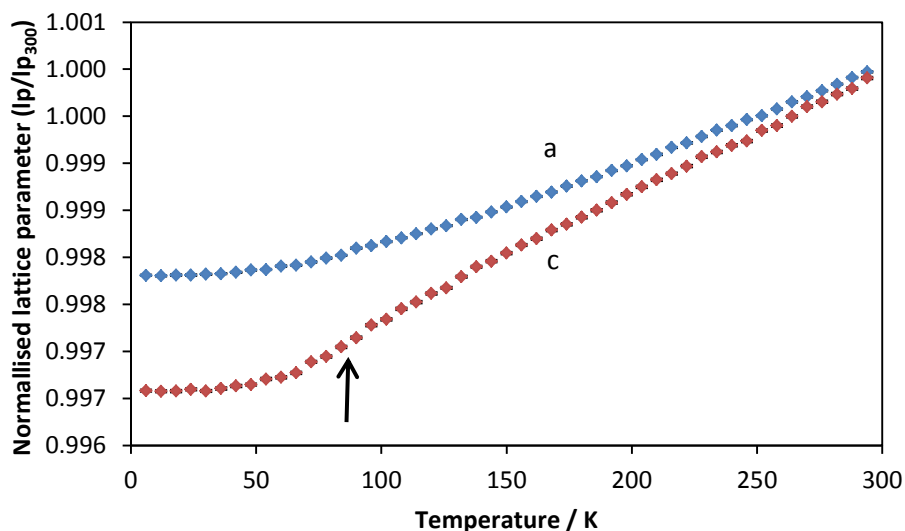

Figure 6.2: *Normalised lattice parameters for $La_2O_2Se_2Fe_2O$ from 6 to 300 K, adapted from Free.[9] Blue = a lattice parameter, red = c lattice parameter.*

Black single crystals of $La_2O_2Se_2Fe_2O$ with a plate like morphology were obtained. Single crystal X-ray diffraction data were collected at 200 K and 85 K, using a Bruker SMART-6000 (6K) equipped with a nitrogen flow cooling device to control temperature. A full sphere of data was collected at each temperature and an empirical absorption (SADABS) correction was applied to both data sets. The diffraction data were consistent with the *I*4/*mmm* symmetry reported.

Least squares refinement against F^2 was carried out using the Crystals software package.[10] A total of 15 parameters were refined including: z atomic coordinates of the lanthanum and selenium sites, anisotropic thermal parameters on all sites, scale and extinction parameters. The results of these refinements are shown in table 6.3. A second crystal from the same batch was mounted onto a glass fibre using epoxy resin and further diffraction data collected at 293 K and 35 K using a Bruker SMART-CCD 1000 (1K), equipped with an Oxford Cryosystems HELIX helium flow cooling device to control temperature. A full sphere of data was collected at each temperature and an identical data processing and refinement protocol adopted; the results of these refinements are also given in table 6.3. Analysis of the raw images indicated that no additional reflections or peak splittings were present in the 35 K images, well below the observed discontinuity in the c lattice parameter (~90 K), suggesting that the symmetry of the system remains $I4/mmm$.

Table 6.3: Results from single crystal refinement of $La_2O_2Se_2Fe_2O$.

Formula	$La_2O_2Se_2Fe_2O$			
Radiation	0.71973 Å	0.71973 Å	0.71973 Å	0.71973 Å
Temperature / K	35	85	200	293
Instrument	1K	6K	6K	1K
Data collection	11ajt006	11ire002	11ire002	11ajt006
a / Å	4.0577(9)	4.0658(3)	4.0704(3)	4.0788(3)
b / Å	4.0577(9)	4.0658(3)	4.0704(3)	4.0788(3)
c / Å	18.610(8)	18.6118(15)	18.625(6)	18.648(3)
Space group	$I4/mmm$	$I4/mmm$	$I4/mmm$	$I4/mmm$
z	2	2	2	2
Measured reflections	1421	2696	2287	1448
Independent reflections	143	207	170	141
Rint	0.03	0.03	0.04	0.03
h	-4≤h≤5	-6≤h≤6	-5≤h≤5	-5≤h≤5
k	-5≤k≤5	-6≤k≤6	-5≤k≤5	-5≤k≤4
l	-23≤l≤23	-28≤l≤28	-26≤l≤26	-23≤l≤23
R	0.026	0.021	0.021	0.023
wR	0.045	0.038	0.047	0.043
gof	1.201	1.052	1.087	1.115
Δρ max	2.44	1.54	0.91	1.37
Δρ min	-3.03	-1.97	-1.47	-1.54
Number of variables	15	15	15	15
Extinction	2.0(3)	0.76(13)	1.7(2)	1.6(2)
Se Z	0.09656(10)	0.09654(6)	0.09657(7)	0.09664(9)
La Z	0.18404(6)	0.18409(3)	0.18418(4)	0.18430(5)
Fe u_{11} / Å^2	0.035(2)	0.0241(11)	0.0289(16)	0.038(2)
Fe u_{22} / Å^2	0.021(2)	0.0153(10)	0.0195(14)	0.0249(19)
Fe u_{33} / Å^2	0.0095(14)	0.0100(7)	0.0148(9)	0.0194(14)
Se u_{11}/u_{22} / Å^2	0.0058(7)	0.0057(3)	0.0083(4)	0.0116(6)
Se u_{33} / Å^2	0.0068(9)	0.0063(5)	0.0095(6)	0.0094(8)
La u_{11}/u_{22} / Å^2	0.0048(4)	0.0038(2)	0.0057(3)	0.0071(4)
La u_{33} / Å^2	0.0037(5)	0.0049(3)	0.0084(4)	0.0080(5)
O(1) u_{11}/u_{22} / Å^2	0.007(4)	0.007(2)	0.005(2)	0.007(3)
O(1) u_{33} / Å^2	0.006(5)	0.007(3)	0.012(4)	0.013(5)
O(2) u_{11}/u_{22} / Å^2	0.012(7)	0.010(4)	0.007(4)	0.020(7)
O(2) u_{33} / Å^2	0.010(10)	0.015(6)	0.030(8)	0.029(11)

Figure 6.3 shows a decrease in a and c lattice parameters from 293 to 35 K consistent with previously reported data from powder diffraction by Free. Anisotropic thermal parameters show no anomalous behaviour with decreasing temperature. Free reported a large thermal displacement of the O(2) anion site at 295 K, from combined X-ray and neutron powder data,

which was not observed in this work, figure 6.4. There is weak evidence that Fe ADPs are slightly elongated in the *ab* plane at low temperature which could suggest minor disorder in the Fe$_2$O layer.
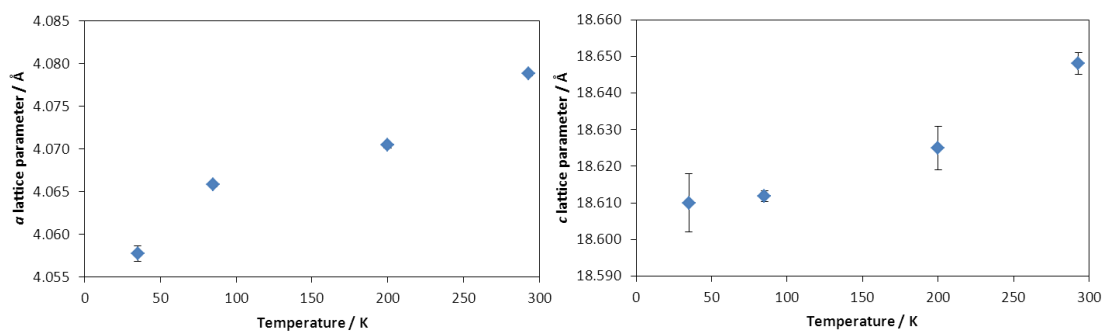

Figure 6.3: *Lattice parameters as a function of temperature for La$_2$O$_2$Se$_2$Fe$_2$O.*
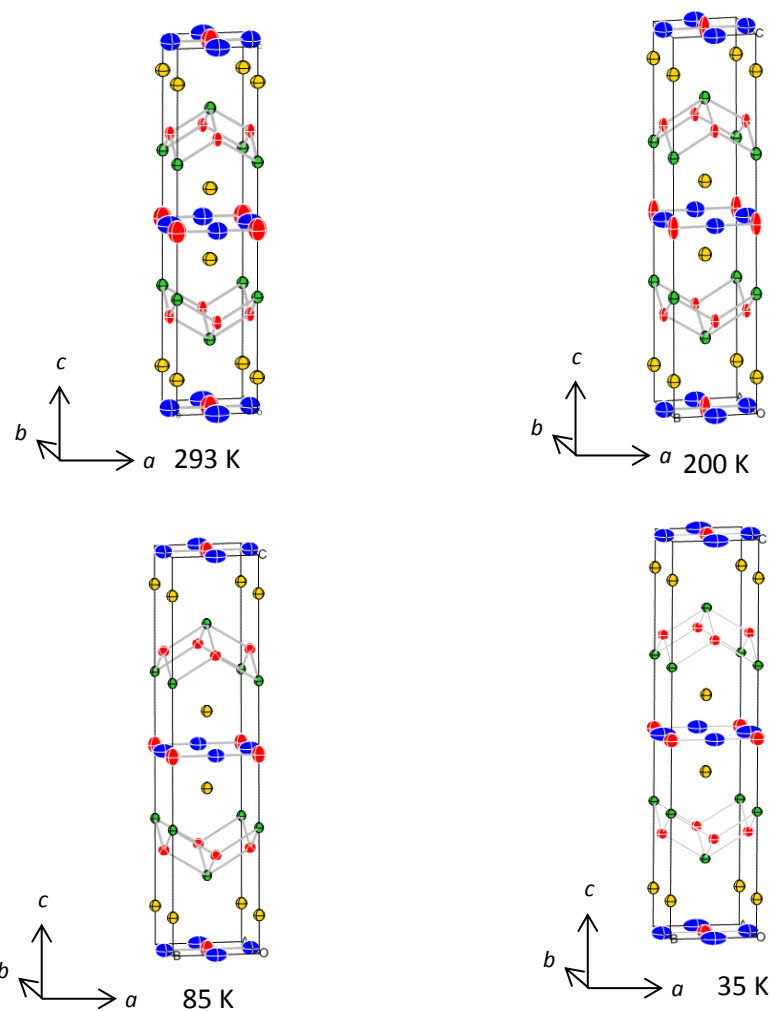

Figure 6.4: *Thermal ellipsoid plots for La$_2$O$_2$Se$_2$Fe$_2$O, shown at 99 % probability, at 293 K, 200 K, 85 K and 35 K, La = red, Se = yellow, O = red, Fe = blue.*

6.4 Investigation of the low temperature structure of $La_2O_2Se_2Mn_2O$

Powder neutron diffraction data of $La_2O_2Se_2Mn_2O$ were reported by Free between 282 K and 12 K. Close inspection of 12 K data showed the presence of two weak additional peaks at d = 1.68 and 1.70 Å, which do not appear in the room temperature pattern, figure 6.5.[5] The intensity of these peaks is only around 0.4 % of the most intense reflection (015) in the pattern (at 2.78 Å). These additional peaks are also observed in laboratory X-ray powder diffraction data, suggesting that they are structural and not magnetic in origin.[9]
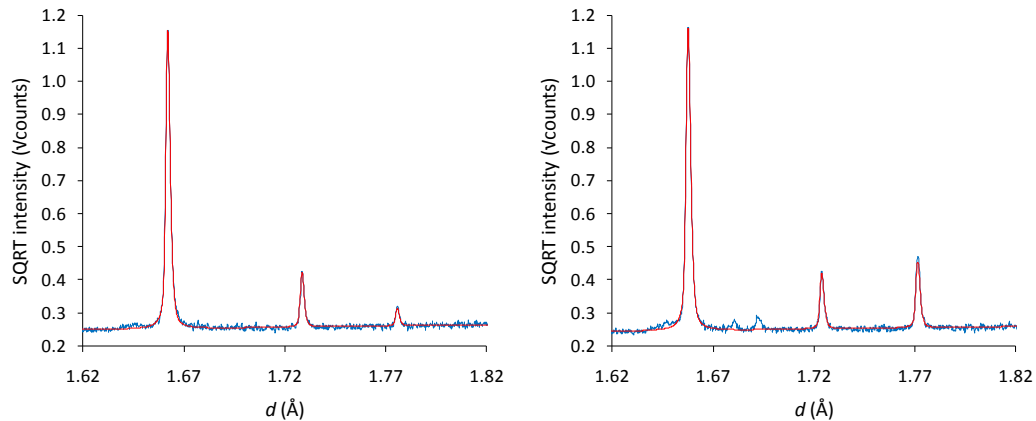
Figure 6.5: *Rietveld plots produced by Free from neutron powder diffraction data for $La_2O_2Se_2Mn_2O$ at 295 (left) and 12 K (right), highlighting the appearance of two extra peaks at 1.68 and 1.70Å. Note the square root intensity scale to emphasise these weak features.*[9]

The intensity of these peaks was modelled from variable temperature X-ray data collected over a very narrow two theta range, and fitted to an equation of the form:

$$I(T) = I_0 \times (1 - \frac{T}{T_c})^\beta \qquad \text{eqn 3.1}$$

Where $I(T)$ is the calculated intensity at any temperature, I_0 is the intensity at 0 K, β is the critical exponent, and T_c is the temperature below which the peaks appear. It was been reported that T_c = 106(1) K, which is approximately the temperature where a discontinuity in the c cell parameter (T_c = 115 K) occurs, figure 6.6. It was also reported from powder data that the O(2) site (in the Mn_2O layer) has a highly anisotropic thermal parameter elongated along the c axis (U_{33}). Free *et al.* suggested that the extra peaks arose due to ordering of the O(2) ions but were unable to index the extra peaks to a commensurate supercell.[5] Similar diffraction peaks were also observed in $Pr_2O_2Se_2Mn_2O$, below T_c = 170 K. However only a single broad additional peak was observed at 12 K[5]. $Pr_2O_2Se_2Mn_2O$ will be discussed in section 6.5. These observations are all consistent with a structural phase transition at low temperature.
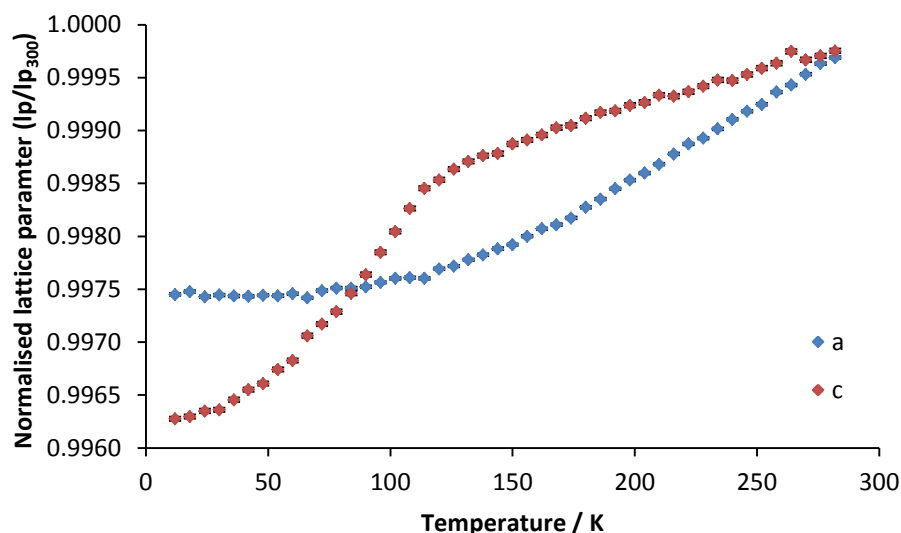
Figure 6.6: *Normalised lattice parameters for La$_2$O$_2$Se$_2$Mn$_2$O plotted as a function of temperature from 12 to 282K, adapted from Free.*[9]

Pale green single crystals of La$_2$O$_2$Se$_2$Mn$_2$O with a plate like morphology were obtained and a single crystal mounted onto a glass fibre using epoxy resin. A full sphere of data was collected at 293 K and 35 K using a Bruker SMART-CCD 1000 (1K) diffractometer. A second crystal was mounted in oil on a Bruker SMART-6000 (6K) diffractometer with the temperature controlled using a nitrogen flow cooling device, and a full sphere of data collected at 90 K. Equivalent data processing and refinement protocols were applied as for La$_2$O$_2$Se$_2$Fe$_2$O. A total of 14 parameters were refined for all analysis in this section including: z atomic coordinates of lanthanum and selenium atoms, anisotropic thermal parameters on all sites and a scale factor.

The structure adopts the same $I4/mmm$ symmetry and structure as La$_2$O$_2$Se$_2$Fe$_2$O.[6] At 90 K no additional diffraction spots were observed in the raw images, in contrast to the reported data from X-ray powder diffraction where additional weak reflections were observed below 106 K. As this data set was recorded only just below T_C, any additional reflections may have been below the detection limit of the CCD.

When the crystal was cooled to 35 K using an Oxford Cryosystems Helix, additional reflections which were not present at room temperature were observed, figure 6.7. These reflections could not be indexed to a commensurate unit cell, reciprocal space images indicate that these weak reflections could be indexed in an incommensuratly modulated structure with $q = (0 \approx 1/3$ $0)$. The observed superstructure reflections were too low in number and intensity to allow refinement of the modulation vector. Structure refinements were therefore carried out using the high temperature cell. Crystallographic parameters are reported in table 6.4 and figure 6.8 and derived bond distances will be discussed later in Section 6.6. It is noticeable that the O(2)

U_{33} parameter is significantly elongated along the *c* axis of the material, especially in the room temperature and 90 K data. This is consistent with the observations made by Free.
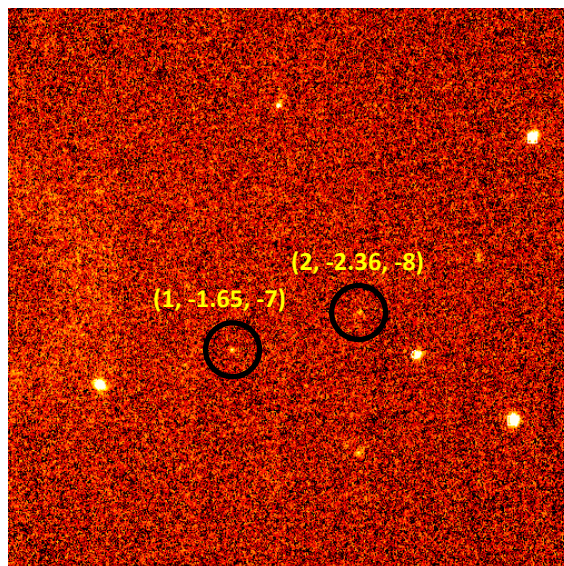

Figure 6.7: *Addition spots observed in some frames of $La_2O_2Se_2Mn_2O$ at 35 K, hkl indices given relative to the parent a ~4.1 Å, b ~ 4.1 Å, c ~18.8 Å cell.*
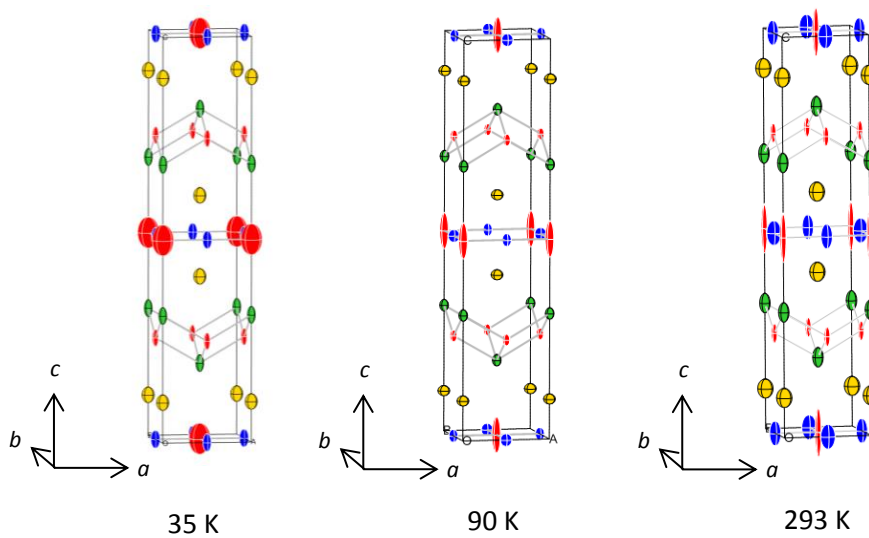
Figure 6.8: *Thermal ellipsoid plots from $La_2O_2Se_2Mn_2O$ shown at 99 % probability.*

Table 6.4: *Crystallographic data for $La_2O_2Se_2Mn_2O$ at 293 K, 90 K and 35 K.*

Formula	$La_2O_2Se_2Mn_2O$		
Radiation	0.71973 Å	0.71973 Å	0.71973 Å
Temperature / K	35	90	293
Instrument	1K	6K	1K
Data collection	11ajt006	ajt041e	11ajt006
a / Å	4.1251(11)	4.1335(9)	4.1562(6)
b / Å	4.1251(11)	4.1335(9)	4.1562(6)
c / Å	18.762(7)	18.825(6)	18.931(5)
Space group	*I4/mmm*	*I4/mmm*	*I4/mmm*
z	2	2	2
Measured reflections	1408	2834	2834
Independent reflections	144	146	146
Rint	0.04	0.04	0.04
h	-5≤h≤5	-5≤h≤5	-5≤h≤5
k	-5≤k≤5	-5≤k≤5	-5≤k≤5
l	-23≤l≤23	-24≤l≤24	-24≤l≤24
R	0.022	0.017	0.027
wR	0.063	0.033	0.045
gof	0.935	1.004	1.046
Δρ max	2.22	1.93	2.79
Δρ min	-1.55	-0.96	-1.70
Number of variables	14	14	14
Se Z	0.09987(8)	0.09996(7)	0.10003(12)
La Z	0.18632(5)	0.18634(4)	0.18653(7)
Mn u_{11} / Å^2	0.0030(12)	0.0068(11)	0.0106(18)
Mn u_{22} / Å^2	0.0039(12)	0.0041(10)	0.0063(17)
Mn u_{33} / Å^2	0.0150(12)	0.0084(9)	0.0305(17)
Se u_{11}/u_{22} / Å^2	0.0069(7)	0.0069(5)	0.0115(9)
Se u_{33} / Å^2	0.0115(8)	0.0051(6)	0.0181(11)
La u_{11}/u_{22} / Å^2	0.0028(4)	0.0037(3)	0.0053(4)
La u_{33} / Å^2	0.0136(5)	0.0066(4)	0.0188(6)
O(1) u_{11}/u_{22} / Å^2	0.002(3)	0.003(3)	0.002(4)
O(1) u_{33} / Å^2	0.014(5)	0.007(4)	0.019(6)
O(2) u_{11}/u_{22} / Å^2	0.021(8)	0.004(6)	0.002(8)
O(2) u_{33} / Å^2	0.046(13)	0.064(13)	0.12(3)

Single crystal data collections on $La_2O_2Se_2Mn_2O$ were also recorded using the i19 beam line at the Diamond light source, where it was hoped that the brightness of the incident X-ray incident beam would enable observation of a larger number of superstructure reflections, thus allowing refinement of the modulated structure. A hemisphere of data were collected at room temperature with the frame acquisition and beam attenuation varied to optimise the diffracted intensity. Data collected at room temperature were consistent with the refinement reported above from laboratory data. Upon cooling the crystal to 30 K a number of additional reflections were observed in the raw images. The reflections in these images were indexed using the Bruker ApexII software package.[11] Reciprocal lattice images were used to index the reflections to a a = 4.1868(2) Å, b = 4.1868(2) Å and c = 19.071(1) Å tetragonal unit cell, with two modulation vectors, q_1 = (0.367 0 0) and q_2 = (0 0.367 0).

Attempts to refine a modulated structural model using JANA2006 proved problematic as the high dynamic range required to measure both the very weak satellites and the strong main reflections on the same image resulted in poorly determined intensities for the relatively few weak supercell reflections.[12] Figure 6.9 shows a Pawley refinement carried out using JANA2006, of the powder neutron data shown in figure 6.5. This was performed using the $I4/mmm(a,0,0)0000(0,a,0)0000$ superspace group (i.e. the high temperature cell with modulation vectors along a and b), as formalized by van Smaalen[13], with intensities of the main and 1st order satellites refined. The two additional reflections observed at 1.68 Å and 1.70 Å could be indexed with the modulation vectors determined from single crystal studies as the (2 1 7 -1 0) and (1 1 8 1 0) reflections.
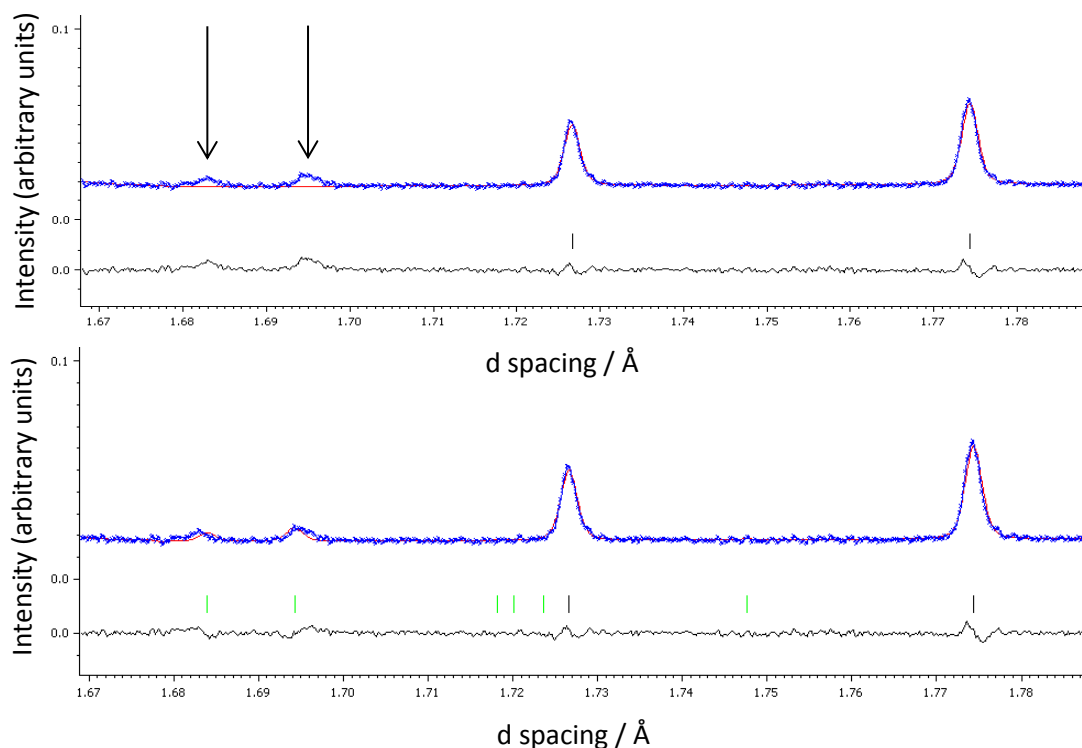
Figure 6.9: *Pawley refinement against neutron powder diffraction data for $La_2O_2Se_2Mn_2O$ 12 K, using commensurate (top) and incommensurate (bottom) cells. The two extra peaks at 1.68 and 1.70Å can be assigned intensity using the incommensurate cell described in the text. Vertical tick marks indicate the predicted position of reflections, black ticks = main reflections, green ticks = 1st order satellite reflections, observed data = blue, calculated fit = red, difference line = grey.*

Further single crystals from the same batch were studied on the BL02B1 beamline at the Spring 8 synchrotron. Data were collected and processed on the beamline by Dr Claire Wilson. It was hoped the high dynamic range of the image plate detector would allow the reliable measurement of intensities of both strong and weak superstructure reflections simultaneously. The shorter operational wavelength (0.34958 Å) relative to the i19 beamline, also minimised absorption. Data collected at 20 K using an open flow helium system to control the sample temperature confirmed the cell and modulation vectors determined previously. Diffraction data were collected at 20 K using an image plate detector scanning at 2 minutes per degree, with 22 5° wide images. Indexing and integration of the measured intensities were carried out using Twinsolve v1.92 up to 0.35 Å resolution.[14] Data were also collected at 55 K, 90 K and 125 K with a reduced exposure time of 1.5 minutes per degree. A face-indexed absorption correction was applied each dataset within Twinsolve.

Analysis of the raw images confirmed the presence of satellite reflections in the 20 K, 55 K, & 90 K data collections, which disappeared in the 125 K data, in agreement with the powder

diffraction conclusions reported by Free, figure 6.10. The reflections gave the tetragonal unit cells reported in table 6.5, with a significantly larger contraction of the *c* lattice parameter than *a* and *b* over the temperature range studied, figure 6.11, again consistent with powder diffraction data.
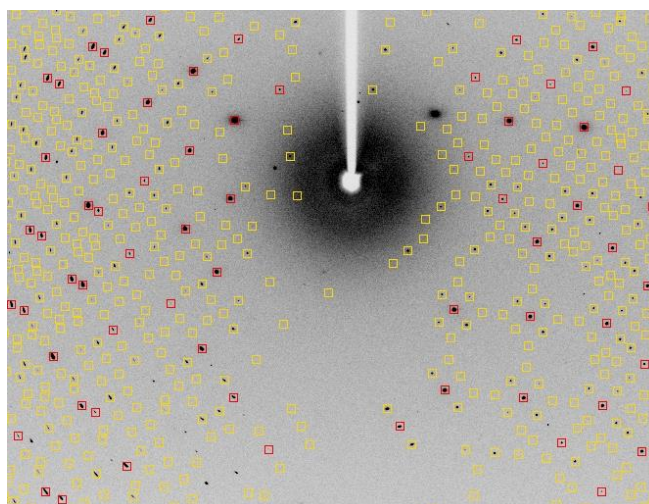

Figure 5.10: *Close up of image plate*, at 20 K overlay shows the main peaks in red, the satellites in yellow.

Table 6.5: *Unit cell parameters for La$_2$O$_2$Se$_2$Mn$_2$O determined from BL02B1.*

Temperature / K	$a = b$ / Å	c / Å
20	4.1285(1)	18.7760(21)
55	4.1282(4)	18.7902(17)
90	4.1287(2)	18.8108(10)
125	4.1293(3)	18.8296(17)
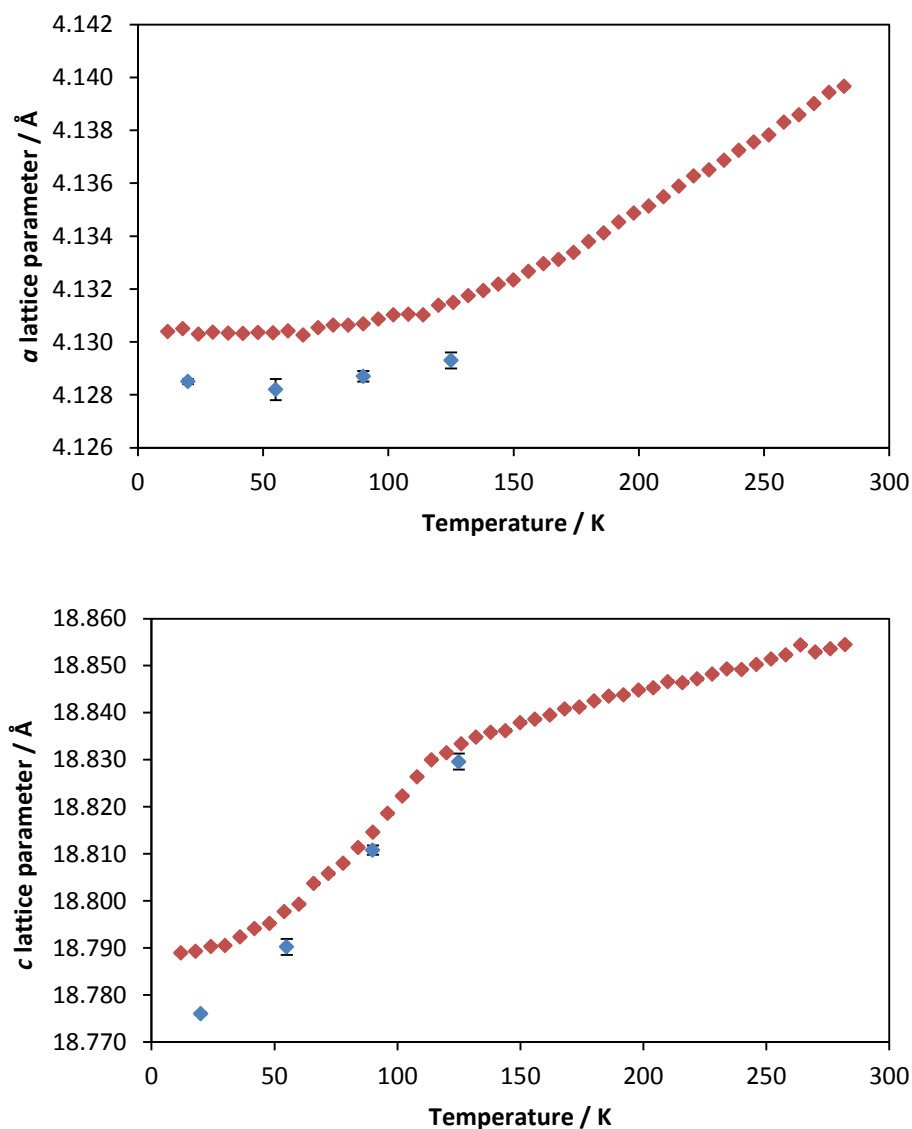
Figure 6.11: *Comparison of lattice parameters derived from Spring 8 single crystal X-ray diffraction (blue) and powder diffraction (red) reproduced from Free.[9]*

At 20 K weak satellite reflections were clearly observed along both the crystallographic *a* and *b* axes, consistent with the data from i19 and laboratory experiments. These could be indexed by two modulation waves based on a tetragonal unit cell with q_1 = (−0.3653 0 0) and q_2 = (0 − 0.3653 0). We note that it would be possible to index the strongest incommensurate reflections with a single modulation vector and an orthorhombic cell (*a*, *b*≈*a*, *c*) with twinning along [110]. However several cross terms were observed with intensities just above the detection threshold of 3σ(I) corresponding to diffraction vectors ±(q_1 + q_2) and ±(q_1 − q_2). Although weak and low in number these prove a (3+2)-dimensional model is required and all reflections were indexed using five integers (*h,k,l,m,n*). Only approximately 8 % of first order

(m, n = ±1) satellites were observed above the detection threshold $3\sigma(I)$. No reflections corresponding to m = ±2 or n = ±2 were observed, which is not unsurprising as satellite intensities in X-ray experiments are generally quite weak and decrease rapidly with satellite order. Due to the low number of satellites observed unequivocal determination of the superspace group has not been possible. Refinements in the $I4/mmm(a,0,0)0000(0,a,0)0000$ superspace group using the high temperature structure as an initial model, with arbitrary but small modulation amplitudes were not satisfactory. To date an incommensurate structural model for $La_2O_2Se_2Mn_2O$ at low temperature has not been determined.

To gain some insight into the changes that occur in the incommensurate structure, refinements were carried using the data sets collected at 20 K, 55 K, 90 K and 125 K with the high temperature model ($I4/mmm$ symmetry) using JANA2006. The 20 K and 55 K data sets images were integrated for both the main and 1st order satellite reflections, while in the 90 and 125K K data only the main reflections were integrated. The results of these refinements are shown in table 6.6 and selected bond lengths and angles in table 6.7 key structural changes will be discussed alongside the Pr analogue in Section 6.6. Thermal ellipsoid plots at 99 % probability are shown in figure 6.12. Abnormally large thermal parameters are found for the O(2) site at these temperature with an elongated U_{33} parameter along the c axis, consistent with previous data. It seems likely that the large thermal parameter for O(2) site is masking disorder within the structure. However the quality of oxygen ADPs from these data is somewhat questionable as the trends in O2 U_{ij} with temperature aren't smooth and O1 shows unexpectedly large U_{33} at 20 K.

Table 6.6: *Crystallographic data for La$_2$O$_2$Se$_2$Mn$_2$O at 125 K, 90 K, 55 K and 20 K collect at Spring 8.*

Radiation / Å	0.34958	0.34958	0.34958	0.34958
Temperature / K	20	55	90	125
Instrument	BL02B1	BL02B1	BL02B1	BL02B1
a / Å	4.1285(1)	4.1282(4)	4.1287(2)	4.1293(3)
b / Å	4.1285(1)	4.1282(4)	4.1287(2)	4.1293(3)
c / Å	18.776(21)	18.7902(17)	18.8108(10)	18.8296(17)
Space group	$I4/mmm$	$I4/mmm$	$I4/mmm$	$I4/mmm$
Z	2	2	2	2
Measured reflections	1221	1222	1223	1224
Independent reflections	838	826	852	766
Rint	0.08	0.07	0.04	0.06
h	-12≤h≤11	-12≤h≤10	-11≤h≤10	-11≤h≤10
k	-12≤k≤11	-12≤k≤11	-11≤k≤11	-11≤k≤11
l	-53≤l≤47	-53≤l≤47	-46≤l≤53	-53≤l≤46
R	0.046	0.044	0.020	0.044
wR	0.0567	0.046	0.024	0.050
gof	2.9	2.37	1.23	2.55
Number of variables	14	14	14	14
Se z	0.09977(5)	0.10003(3)	0.10001(2)	0.10003(3)
La z	0.18623(3)	0.18624(2)	0.18636(1)	0.18641(2)
Mn u_{11} / Å^2	0.0027(2)	0.0030(2)	0.0039(1)	0.0058(3)
Mn u_{22} / Å^2	0.0015(2)	0.0016(2)	0.00196(9)	0.0032(2)
Mn u_{33} / Å^2	0.0088(3)	0.0106(3)	0.0084(1)	0.0010(3)
Se u_{11}/u_{22} / Å^2	0.005(1)	0.0051(1)	0.00491(5)	0.0057(1)
Se u_{33} / Å^2	0.0055(2)	0.0054(2)	0.0035(1)	0.0045(2)
La u_{11}/u_{22} / Å^2	0.00146(6)	0.00162(5)	0.00188(3)	0.00309(6)
La u_{33} / Å^2	0.0083(1)	0.0079(1)	0.00536(5)	0.0054(1)
O(1) u_{11}/u_{22} / Å^2	0.0021(6)	0.0030(5)	0.0033(3)	0.0055(7)
O(1) u_{33} / Å^2	0.017(2)	0.008(1)	0.0063(3)	0.006(1)
O(2) u_{11}/u_{22} / Å^2	0.002(1)	0.011(1)	0.0044(6)	0.009(7)
O(2) u_{33} / Å^2	0.08(1)	0.16(1)	0.049(4)	0.048(9)

Table 6.7: *Selected bond lengths and angles for $La_2O_2Se_2Mn_2O$ calculated using cells given in text.*

Bond length (Å)	20 K	55 K	90 K	125 K	293 K	90 K
Instrument	BL02B1	BL02B1	BL02B1	BL02B1	1 K	6 K
d_{M-M}	2.9193(1)	2.9191(1)	2.9194(2)	2.9199(2)	2.9389(1)	2.9228(6)
d_{M-O}	2.06425(8)	2.06410(8)	2.06435(9)	2.0647(22)	2.07810(9)	2.0668(5)
d_{M-Se}	2.7876(5)	2.7916(4)	2.7929(2)	2.7947(5)	2.8116(15)	2.7951(9)
d_{A-O}	2.3864(2)	2.38656(19)	2.38634(9)	2.3867(2)	2.4004(6)	2.3891(4)
d_{A-Se}	3.3403(4)	3.3385(3)	3.34090(17)	3.3424(4)	3.3643(13)	3.3447(8)
Bond angles (°)						
M-Se-M	63.152(13)	63.044(10)	63.019(5)	62.987(11)	63.02(4)	63.05(2)
Se-M-Se (θ_1)	95.55(2)	95.358(17)	95.315(9)	95.26(2)	95.31(7)	95.36(4)
Se-M-Se (θ_2)	84.448(16)	84.642(12)	84.685(6)	84.744(15)	84.69(7)	84.64(4)
A-O-A (δ_1)	104.580(6)	104.594(5)	104.576(2)	104.577(6)	104.51(2)	104.575(15)
A-O-A (δ_2)	119.771(14)	119.739(11)	119.781(6)	119.778(13)	119.93(5)	119.78(3)
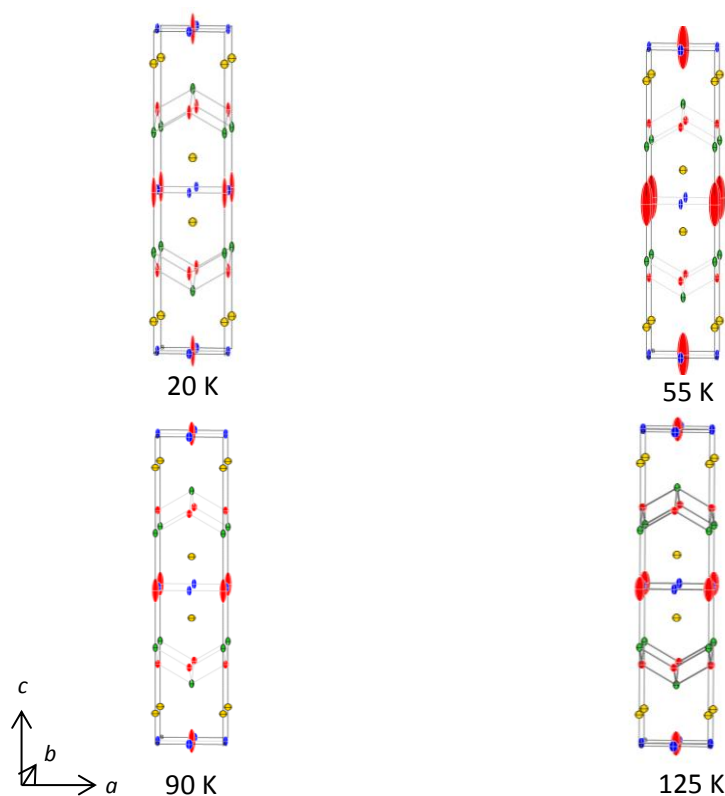
Figure 6.12: *Thermal ellipsoid plots from $La_2O_2Se_2Mn_2O$ shown at 99 % probability.*

6.5 Investigation of the low temperature structure of $Pr_2O_2Se_2Mn_2O$

Additional diffraction peaks similar to those observed in $La_2O_2Se_2Mn_2O$ are observed in both powder X-ray and neutron diffraction data of the Pr analogue upon cooling, below T_c = 170 K. Pale green single crystals of $Pr_2O_2Se_2Mn_2O$ with a plate-like morphology were prepared and studied using a laboratory based Bruker SMART-6000 (6K) diffractometer. Hemispheres of data were collected as the sample was cooled to the following temperatures: 300 K, 265 K, 230 K, 180 K, 130 K, and 90 K. An empirical absorption correction (SADABS) was applied to each data set, and refinements were carried out against F^2 using the Crystals software package using. Results of structure refinements are shown in table 6.8. A selection of bond lengths and angles for this material as temperature is varied is given in table 6.9 and will be discussed in Section 6.6; the O(2) site was refined isotropically for these refinements as use of ADPs resulted in the site going no-positive definite. Values of O(2) ADPs (and corresponding R-factors) from an anisotropic refinement have been appended to the table for completeness. A plot of ADPs at 99 % probability is included in figure 6.13. A large U_{iso} for O2 at all temperatures is clear, U_{ij} values in table 6.8 and plotted in figure 6.13 show that this again appears to be associated with disorder along the c-axis. The same trend in cell parameters was observed in these data as previously reported from powder diffraction, with a significant discontinuity in the thermal expansion of the c lattice parameter at ~170 K, figure 6.14. A small offset between the powder and single crystal data is observed most likely due to a slight error in the assigned single crystal to detector distance. No additional reflections or change in symmetry were observed upon cooling. This is inconsistent with powder diffraction studies which suggest that additional reflections should have been observed in the 90 K and 130 K datasets. This this may be due to the weak nature (0.6 %) of the expected superstructure peaks.

Table 6.8: Results of single crystal refinement of $Pr_2O_2Se_2Mn_2O$. R-factors and values of ADPs for refinements with anisotropic temperature factors for O(2) sites given at bottom.

| Formula	$Pr_2O_2Se_2Mn_2O$					
Radiation	0.71973 Å	0.71973 Å	0.71973 Å	0.71973 Å	0.71973 Å	0.71973 Å
Temperature / K	90	130	180	230	265	300
Instrument	6K	6K	6K	6K	6K	6K
Data collection	12AJT012	12AJT012	12AJT012	12AJT012	12AJT012	12AJT012
a / Å	4.0873(2)	4.0888(2)	4.0894(3)	4.0920(17)	4.0933(17)	4.0952(2)
b / Å	4.0873(2)	4.0888(2)	4.0894(3)	4.0920(17)	4.0933(17)	4.0952(2)
c / Å	18.5739(18)	18.6098(16)	18.6591(13)	18.673(15)	18.676(15)	18.679(2)
Space group	$I4/mmm$	$I4/mmm$	$I4/mmm$	$I4/mmm$	$I4/mmm$	$I4/mmm$
z	2	2	2	2	2	2
Measured reflections	1306	1315	1781	1781	1781	1353
Independent reflections	170	172	174	174	174	174
Rint	0.03	0.03	0.05	0.05	0.05	0.03
h	-5≤h≤5	-5≤h≤5	-5≤h≤5	-5≤h≤5	-5≤h≤5	-5≤h≤5
k	-5≤k≤5	-5≤k≤5	-5≤k≤5	-5≤k≤5	-5≤k≤5	-5≤k≤5
l	-26≤l≤25	-26≤l≤25	-26≤l≤25	-26≤l≤25	-26≤l≤25	-26≤l≤25
R	0.024	0.024	0.025	0.024	0.024	0.025
wR	0.064	0.061	0.060	0.062	0.061	0.072
GOF	1.132	1.11	0.858	0.867	0.83	0.921
Δρ max	4.34	4.01	4.11	4.49	3.41	3.72
Δρ min	-1.78	-1.96	-2.08	-1.98	-2.01	-1.81
Number of variables	13	13	13	13	13	13
Se z	0.10167(8)	0.10169(7)	0.10186(6)	0.10188(5)	0.10183(6)	0.10183(6)
Pr z	0.18777(5)	0.18783(4)	0.18798(4)	0.18801(4)	0.18807(4)	0.18808(4)
Mn u_{11} / Å^2	0.0047(9)	0.0048(9)	0.0071(10)	0.0091(9)	0.0090(10)	0.0123(11)
Mn u_{22} / Å^2	0.0066(9)	0.0055(9)	0.0058(9)	0.0072(8)	0.0072(9)	0.0090(10)
Mn u_{33} / Å^2	0.0177(9)	0.0181(9)	0.0193(9)	0.0234(8)	0.0268(9)	0.0269(10)
Se u_{11}/u_{22} / Å^2	0.0075(6)	0.0090(6)	0.0081(5)	0.0102(5)	0.0103(5)	0.0112(6)
Se u_{33} / Å^2	0.0085(7)	0.0088(7)	0.0095(6)	0.0109(6)	0.0118(6)	0.0130(7)
Pr u_{11}/u_{22} / Å^2	0.0049(3)	0.0054(3)	0.0057(3)	0.0069(3)	0.0073(3)	0.0082(3)
Pr u_{33} / Å^2	0.0142(4)	0.0136(4)	0.0128(4)	0.0143(4)	0.0144(3)	0.0148(4)
O(1) u_{11}/u_{22} / Å^2	0.017(3)	0.017(3)	0.014(3)	0.016(3)	0.014(3)	0.020(3)
O(1) u_{33} / Å^2	0.012(4)	0.005(3)	0.020(4)	0.012(3)	0.016(3)	0.010(3)
O(2) u_{iso} / Å^2	0.046(7)	0.048(7)	0.027(4)	0.033(4)	0.033(4)	0.041(6)
R	0.019	0.019	0.021	0.019	0.020	0.020
wR	0.041	0.039	0.043	0.039	0.040	0.043
O(2) u_{11}/u_{22} / Å^2	−0.005(3)	−0.006(3)	−0.008(5)	−0.008(4)	−0.008(4)	−0.003(5)
O(2) u_{33} / Å^2	0.15(2)	0.13(2)	0.096(16)	0.103(15)	0.105(16)	0.105(16)
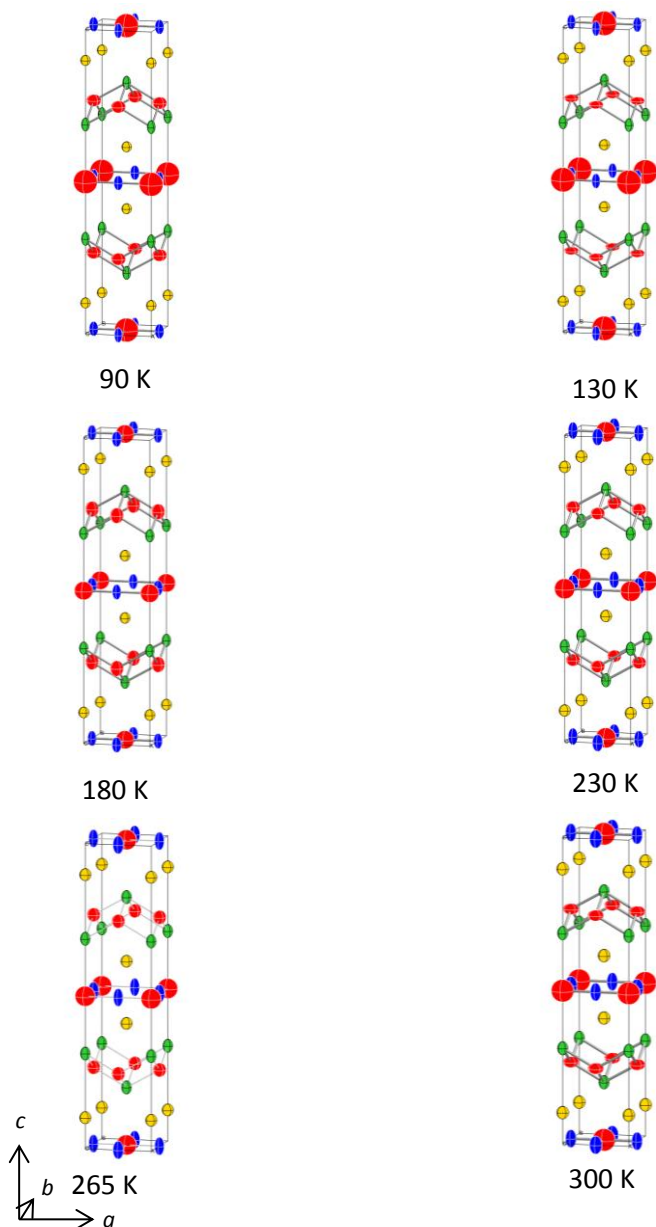
Figure 6.13: *Thermal ellipsoid plots for $Pr_2O_2Se_2Mn_2O$, shown at 99 % probability. Pr = red, Se = yellow, O = red, Mn = blue.*
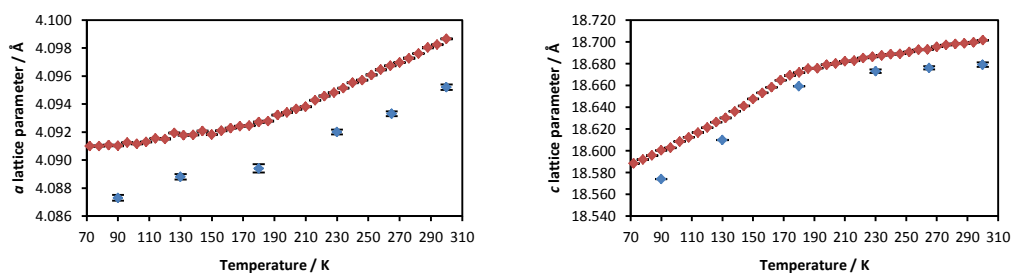

Figure 6.14: *Comparison of lattice parameters derived from single crystal X-ray diffraction (blue) and powder diffraction (red) reproduced from Free.[9]*

161

Table 6.9: *Selected bond lengths and angles for $Pr_2O_2Se_2Mn_2O$.*

Bond length (Å)	90 K	130 K	180 K	230 K	265 K	300 K
d_{M-M}	2.8902(1)	2.8912(1)	2.8916(2)	2.8934(12)	2.8944(12)	2.8957(1)
d_{M-O}	2.0437(1)	2.0444(1)	2.0447(2)	2.0460(9)	2.0467(9)	2.0476(1)
d_{M-Se}	2.7825(10)	2.7858(9)	2.7916(8)	2.7938(7)	2.7938(7)	2.7947(8)
d_{A-O}	2.3479(4)	2.3491(4)	2.3495(4)	2.3507(4)	2.3509(4)	2.3517(4)
d_{A-Se}	3.3031(10)	3.3059(9)	3.3081(8)	3.3104(7)	3.3123(7)	3.3137(8)
Bond angles (°)						
M-Se-M	62.58(2)	62.52(2)	62.38(2)	62.375(17)	62.396(19)	62.41(2)
Se-M-Se (θ_1)	94.52(4)	94.42(4)	94.18(3)	94.17(3)	94.20(3)	94.22(4)
Se-M-Se (θ_2)	85.48(4)	85.58(4)	85.82(3)	85.83(3)	85.80(3)	85.78(4)
A-O-A (δ_1)	104.027(16)	104.040(15)	104.041(14)	104.032(13)	104.008(13)	103.997(14)
A-O-A (δ_2)	121.01(4)	120.99(3)	120.98(3)	121.00(3)	121.06(3)	121.08(3)

6.6 Structural changes of $A_2O_2Se_2Mn_2O$ (A= La & Pr) at low temperature

Multiple data sets were collected with varying temperature on single crystals of $A_2O_2Se_2Mn_2O$ for both (A = La & Pr) to probe changes in the structure at low temperature. Since full analysis of the low temperature incommensurate structure has not yet been possible, we discuss here inferences from changes in the average structure based on subcell reflections only. Data sets for $Pr_2O_2Se_2Mn_2O$ were all collected in one experiment at 6 temperatures from 90 K to 300 K making comparisons straightforward. For $La_2O_2Se_2Mn_2O$ the data were collected on several instruments and it is well known there are often significant systematic errors in the determination of lattice parameters due to errors in assigned crystal to detector distance. $La_2O_2Se_2Mn_2O$ lattice parameters were therefore set to values derived from neutron powder diffraction data collected on HRPD by Free[9]. To achieve this an Einstein type function for the form of equation 6.2 was fitted to the powder cells between 12 K and 282 K, and used to calculate cell parameters at each temperature.

$$a_T = \exp(\ln(a_0) + \sum_n (c_n \theta_n)/\left[\exp\left(\frac{\theta_n}{T}\right) - 1\right]) \qquad \text{eqn 6.2}$$

where: a_T = cell parameter at temperature T, a_0 = cell parameter at 0 K, c_n = an empirically derived coefficient, θ_n = Einstein temperature.

Figures 6.11 and 6.14 suggest that structural changes occur below T_C = ~ 170 K and ~ 100 K for A = Pr and La respectively. Figure 6.14 and 6.15 plot refined factional coordinates and derived bond lengths for the two systems. We will focus on the A = Pr example where we have the most consistent set of data; the A = La material shows similar trends. For both systems a relatively smooth decrease in the A z-coordinate is observed over the temperature ranges investigated, whilst the Se z coordinate changes significantly at low temperature. Selected bond distances and angles are also included in figures 6.15/6.16 and defined in figure 6.17. For each material Mn-O, Mn-Mn, Pr-O and Pr-Se distances show a smooth variation with temperature; the first two just mirroring trends in the a cell parameter. In contrast the Mn-Se bond contracts dramatically on cooling below 170 K, with the Se moving towards the M_2O plane.

The bond angles extracted for the two materials show similar effects. If we consider the ~90° Se-Mn-Se bond angles of the $MnSe_4O_2$ octahedra, on cooling to low temperature θ_1 (along a/b axes) increases from 94.22(4)° to 94.52(4)° and θ_2 (along c axis) decreases from 85.78(4)° to 85.48(4)°. This corresponds to a compression of the octahedra along the c axis. This leads to a small but significant decrease in thickness of the $MnSe_4O_2$ slabs. If we break the structure down into Se-Se slabs (i.e. the $MnSe_4O_2$ layers), Se-Pr slabs and Pr-Pr slabs (i.e. the Pr_4O edge

sharing layers) the % changes in thickness are ~0.72, ~0.74 and ~0.06 % between 300 K and 90 K.

The majority of the structural contraction therefore seems associated with essentially unchanged Pr_4O blocks compressing the Se containing layers by moving closer together. This would be consistent with the low temperature distortion being related to distortions of the $MnSe_4O_2$ octahedra, perhaps allowing at least local ordering of the O2 oxygen site, and consequently subtle movements of the equatorial Se atoms. There is some evidence for ordering of O2 from the U_{33} plot in figure 6.18. U_{33} decreases with increasing temperature and therefore suggesting O2 moves closer to the plane on average at higher temperatures.
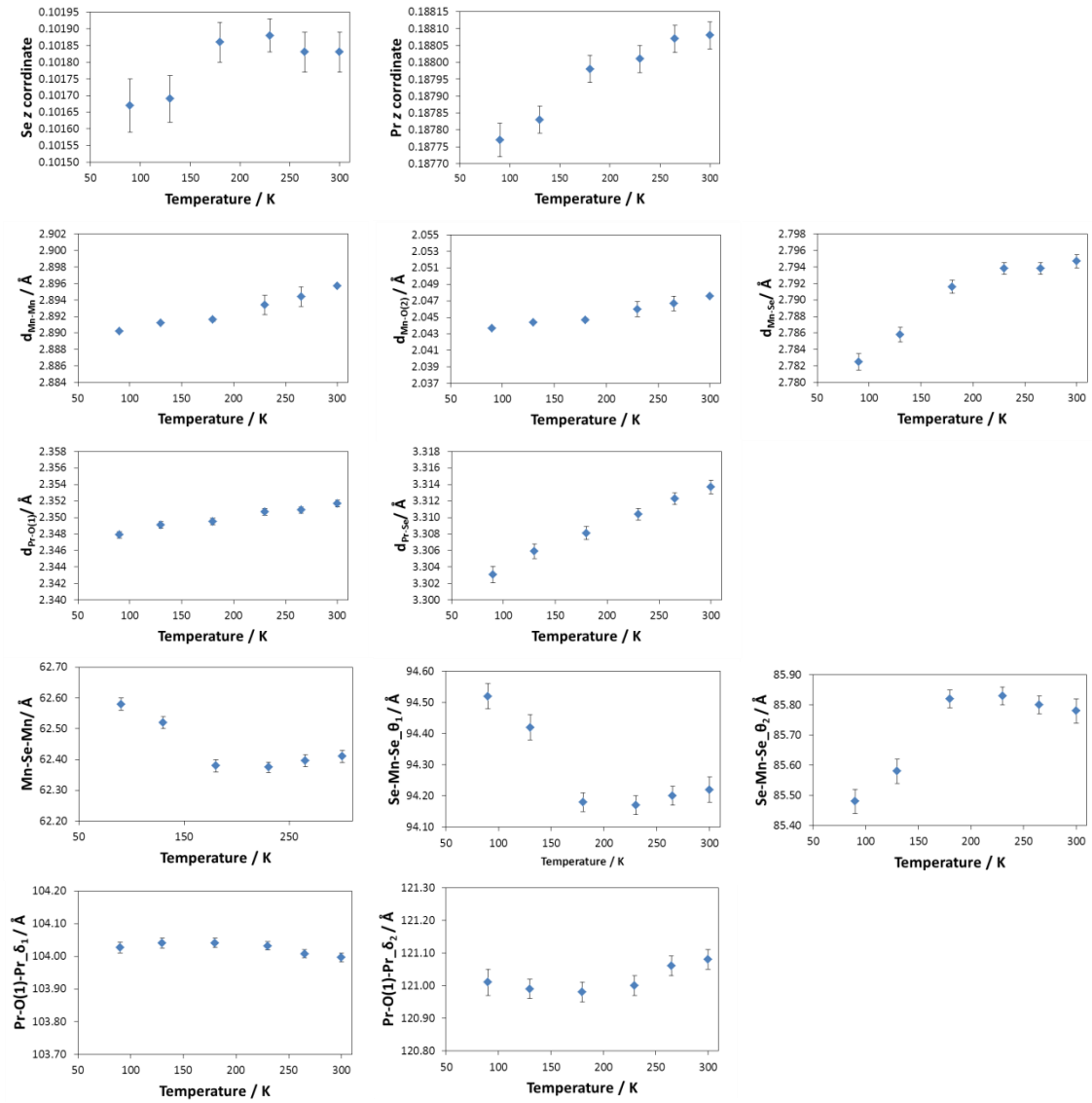
Figure 6.15: *Refined atomic coordinates for $Pr_2O_2Se_2Mn_2O$ between 300 K and 90 K, along with selected bond lengths and angle.*
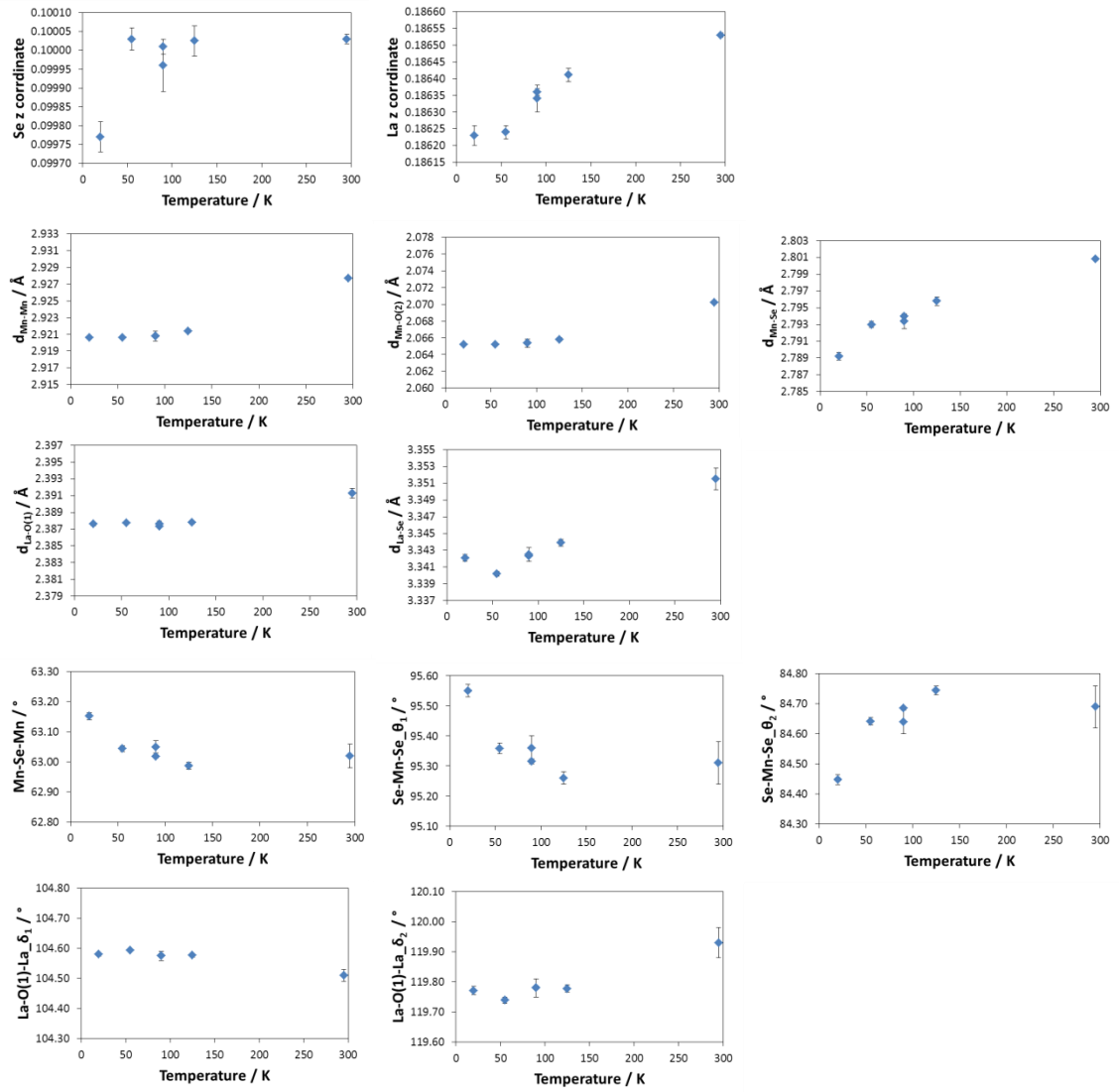
Figure 6.16: *Refined atomic coordinates for La$_2$O$_2$Se$_2$Mn$_2$O between 293 K and 20 K, along with selected bond lengths and angle.*
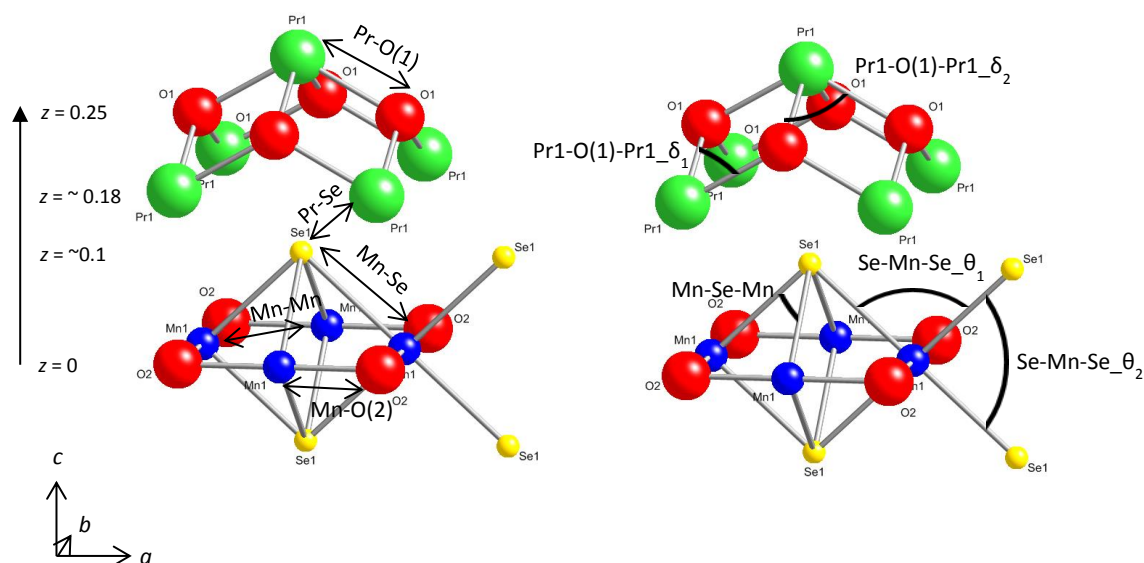
Figure 6.17: *Bond length and angle definitions.*
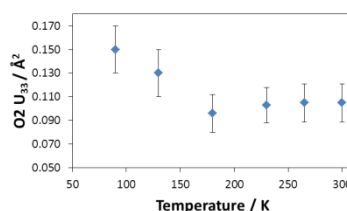
Figure 6.18: *Refined O2 U_{33} parameter for $Pr_2O_2Se_2Mn_2O$ between 300 K and 90 K.*

6.7 Conclusions

Single crystals of $La_2O_2Se_2Fe_2O$, $La_2O_2Se_2Mn_2O$ and $Pr_2O_2Se_2Mn_2O$ have been studied using variable temperature X-ray diffraction. For $La_2O_2Se_2Fe_2O$ no phase change is observed between room temperature and 35 K.

For $La_2O_2Se_2Mn_2O$ weak additional satellite reflections are observed at low temperature using a laboratory instrument, consistent with X-ray and neutron powder diffraction. Synchrotron X-ray diffraction allowed the determination of 2 modulation vectors, and the diffraction pattern has been indexed to a (3+2)d incommensurately modulated structure with q_1 = (−0.3653 0 0) and q_2 = (0 −0.3653 0) with the amplitude of the modulation being relatively weak. High dynamic range synchrotron data for the incommensurate phase were only obtained in the last few weeks of this project in an attempt to gain more insight, but full analysis hasn't yet been completed. Single crystals of $Pr_2O_2Se_2Mn_2O$ were studied using laboratory instruments and no satellite reflections were observed. Weak satellite reflections indicated from powder diffraction measurements suggest higher intensity sources and detectors able to acquire data over a large dynamic range may reveal a similar modulated structure to the La material.

Analysis of bond lengths and angles for $A_2O_2Se_2Mn_2O$ (A = La & Pr) suggest that the materials undergo a similar structural transition at low temperature, which gives a significant contraction of the $MnSe_4O_2$ octahedra along [001] in the average structure. A full modulated description of the low temperature phase hasn't yet been determined.

References

1.   Mayer, J. M., Schneemeyer, L. F., Siegrist, T., Waszczak, J. V., and Dover, B. v., *Angew. Chem. Int. Ed. Engl.*, 1992, **31**, 1645-1647

2.   Fuwa, Y., Wakeshima, M., and Hinatsu, Y., *Journal of physics. Condensed matter : an Institute of Physics journal*, 2010, **22**, 346003

3.   Fuwa, Y., Wakeshima, M., and Hinatsu, Y., *Solid State Communications*, 2010, **150**, 1698-1701

4.   Ni, N., Climent-Pascual, E., Jia, S., Huang, Q., and Cava, R. J., *Physical Review B*, 2010, **82**, 214419

5.   Free, D. G., Withers, N. D., Hickey, P. J., and Evans, J. S. O., *Chemistry of Materials*, 2011, **23**, 1625-1635

6.   Mayer, J. M., Schneemeyer, L. F., Siegrist, T., Waszczak, J. V., and Vandover, B., *Angewandte Chemie-International Edition in English*, 1992, **31**, 1645-1647

7.   Fuwa, Y., Wakeshima, M., and Hinatsu, Y., *Journal of Physics-Condensed Matter*, 2010, **22**, 346003

8.   Wang, C., Tan, M. Q., Feng, C. M., Ma, Z. F., Jiang, S. A., Xu, Z. A., Cao, G. H., Matsubayashi, K., and Uwatoko, Y., *Journal of the American Chemical Society*, 2010, **132**, 7069-7073

9.   Free, D., *PhD thesis: Synthesis and Properties of New Oxychalcogenide materials*, Durham University, 2010

10.   CRYSTALS, Betteridge, P. W., Carruthers, J. R., Cooper, R. I., Prout, K., Watkin, D. J. (2003). J. Appl. Cryst. 36, 1487-1487

11.   *SMART APEX II, Bruker AXS, Madison, WI USA*,

12.   *Jana2006. The crystallographic computing system, Petricek,V., Dusek,M. & Palatinus,L., 2006*,

13.   van Smaalen, S., Campbell, B. J., and Stokes, H. T., *Acta Crystallographica Section A*, 2013, **69**, 75-90

14.   Twinsolve v1.92, Svenson, 2013

Chapter 7: Synthesis and Characterisation of LaInS$_2$O

7.1 Introduction

Relatively few *p*-type transparent conducting compounds are known; rare examples include CuMO_2 (*M* = Al, Ga, In), SrCu$_2$O$_2$ and LaOCuQ (*Q* = S, Se).[1-5] The lack of transparent *p*-type semiconductors restricts the fabrication of *pn* junctions for device application, and there is a need to discover new materials. Potential candidates include In^{3+} containing compounds, which, as d^{10} cations, should contain similar d-energy levels to the Cu$^+$ cations found in LaOCuQ. A material with LaInS$_2$O composition was reported by Kabbour *et al*. in 2004 but the structure of this phase is unknown.[6] Kabbour *et al*. prepared LaInS$_2$O by heating a mixture of La$_2$S$_3$, La$_2$O$_3$ and In$_2$S$_3$ in a 1:2:3 molar ratio in an evacuated sealed quartz tube to 800 °C for 12 hours. Attempts to directly grow single crystals were unsuccessful, and reheating the polycrystalline phase with iodine to favour crystallisation resulted in crystals of In$_2$S$_3$ and La$_5$In$_3$S$_9$O$_3$.[6] In this chapter we report the structure solution of LaInS$_2$O from powder diffraction data.

7.2 Synthesis

Polycrystalline LaInS$_2$O was synthesised using the method outlined in section 2.2.7 La$_2$O$_3$, In and S powders were ground together in a 1:2:4 molar ratio, and placed in an alumina crucible within an evacuated quartz ampoule along with Al powder to act as a getter, forming Al$_2$O$_3$ during the reaction. The resulting product was a bright yellow polycrystalline powder, which was analysed using XRPD. Out attempts to grow single crystals with LaInS$_2$O composition from slow cooling from a CsI flux were also unsuccessful, yielding in crystals of In$_2$S$_3$ and La$_5$In$_3$S$_9$O$_3$.

7.3 Indexing

A XRPD pattern was collected on a laboratory diffractometer using Cu K$\alpha_{1,2}$ radiation over the two theta range 10 to 120° (0.02° step size with 8 seconds per step, 6 mm variable divergent slits). This diffraction pattern was indexed using Topas to an orthorhombic unit cell, with *a* = 3.9849 Å, *b* = 20.5411 Å and *c* = 14.8435 Å. A Pawley refinement using *P*222 symmetry gave refined cell parameters of *a* = 3.9863(1) Å, *b* = 20.5498(8) Å and *c* = 14.8473(6) Å; as can be seen in figure 7.1, an excellent fit to the observed diffraction profile was obtained.
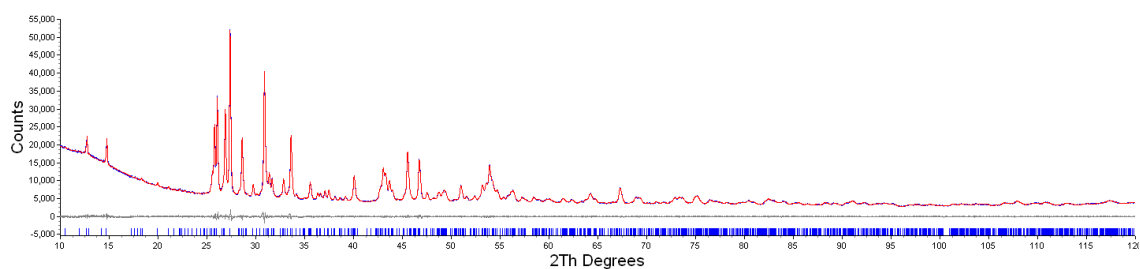
Figure 7.1: *Pawley fit of LaInS$_2$O in P222. R$_{wp}$ = 1.746 %, R$_p$ = 1.298 %, gof = 1.533. AJT174, d7_02965.*

In order to carry out ab initio structure solution a synchrotron powder diffraction pattern was collected using the 11-BM beamline at the Argonne national laboratory. Data were collected in transmission geometry with the sample contained in a 0.8 mm Kapton capillary using a wavelength of 0.413850 Å. In order to reduce the average absorption of the sample LaInS$_2$O was diluted with amorphous SiO$_2$ in a 1:10 molar ratio. Pawley refinement confirmed the orthorhombic cell, figure 7.2.
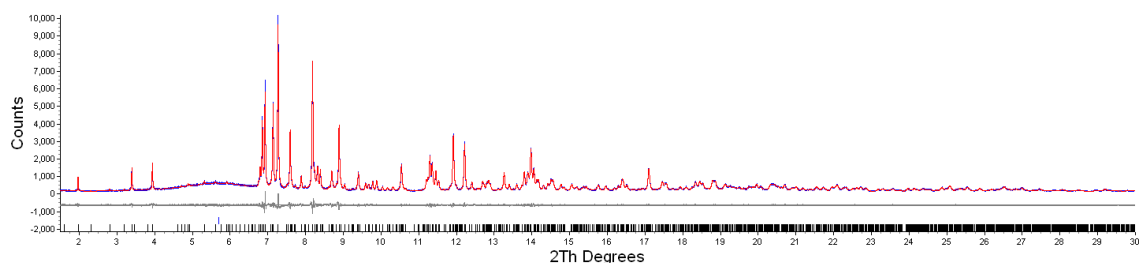
Figure 7.2: *Pawley fit of LaInS$_2$O using synchrotron powder diffraction data with λ=0.41385 Å. Blue vertical tick mark indicates an additional phase to model the amorphous SiO$_2$. R$_{wp}$ = 4.520 %, R$_p$ = 3.634 %, gof = 1.033. AJT192, 11bmb_8963.xye.*

7.4 Structure solution

Analysis of systemic absences suggests 2$_1$ screw axes parallel to *x*, *y* and *z*, consistent with space group *P*2$_1$2$_1$2$_1$. A sample of LaInS$_2$O was tested for second harmonic generation (SHG) using the method outlined in section 2.9.3, at the university of Houston by Prof Shiv Halasyamani. Frequency doubling was observed, consistent with lack of inversion centre and *P*2$_1$2$_1$2$_1$ symmetry. A good fit to the diffraction profile can be obtained using this space group, figure 7.3, with refined cell parameters *a* = 3.98574(4) Å, *b* = 20.5467(3) Å and *c* = 14.8446(2) Å.
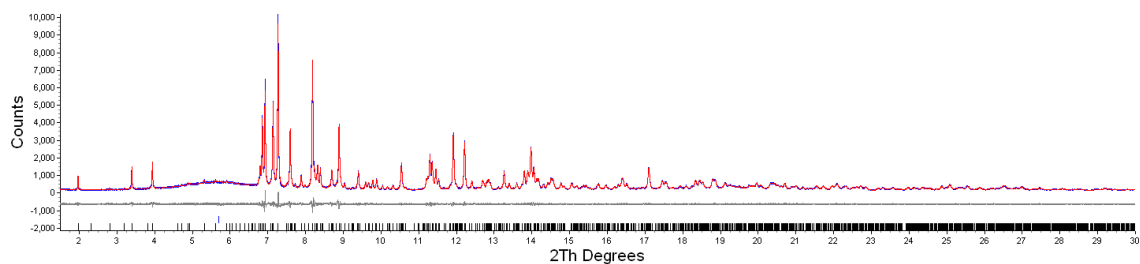
Figure 7.3: *Pawley fit of synchrotron powder diffraction data in space group P2$_1$2$_1$2$_1$. R$_{wp}$ = 4.514 %, R$_p$ = 3.633 %, gof = 1.032. AJT192, 11bmb_8963.xye.*

From the unit cell volume and comparison with compositionally related materials such as LaGaS$_2$O (density = 5.24 g cm^{-3}) the expected cell content was La$_{12}$In$_{12}$S$_{24}$O$_{12}$, resulting in a calculated density of ~5.5 g cm^{-3}. Attempts to solve the structure using either direct methods in EXPO2013 or charge flipping using Topas were unsuccessful.[7, 8] Structure solution was therefore performed using a direct space simulated annealing methodology in Topas over a restricted two theta range of 1.5-20°. General positions in *P*2$_1$2$_1$2$_1$ have a site multiplicity of 4, (this space group has no special positions, but the origin is fixed by three orthogonal 2$_1$ screw axes), therefore 3 La sites and 3 In were introduced to the unit cell. A full Voigt peak shape was fixed at the values determined from Pawley refinement. All 6 atomic sites were allowed to freely refine, and upon convergence were moved randomly by up to 5 Å. One million iterations were run and the atomic positions of the best fit output, figure 7.4. These metal sites seemed to have sensible distances between them, suggesting a sensible partial structure. More significantly, the La sites appeared to have a geometry which would allow units of edge sharing La$_4$O tetrahedra, a geometry found in other lanthanum indium oxysulfides.[6, 9]
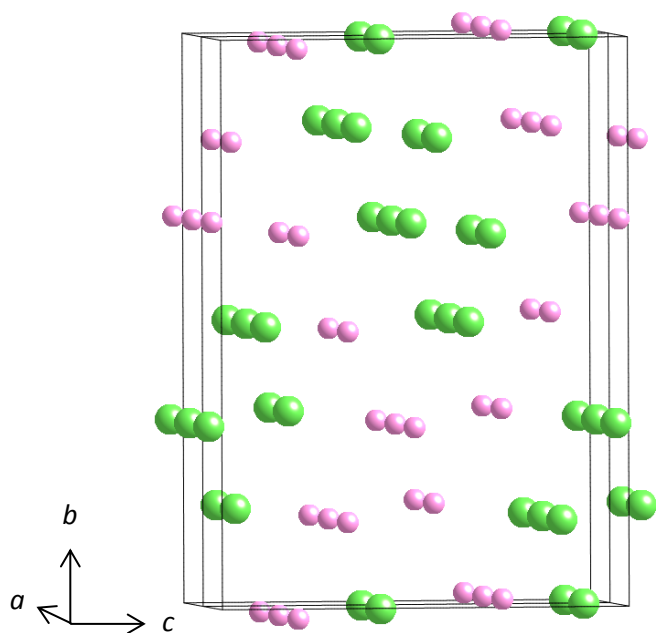
Figure 7.4: *La and In sites identified using a simulated annealing methodology. Green = La, pink = In.*

Six sulfur atoms were added to the asymmetric unit and simulated annealing continued with the metal positions fixed. This resulted in S atoms located at sensible bond distances from metal sites, figure 7.5. Isotropic thermal parameters were then refined for all sites in the model and 3 oxygen sites located though Fourier maps.
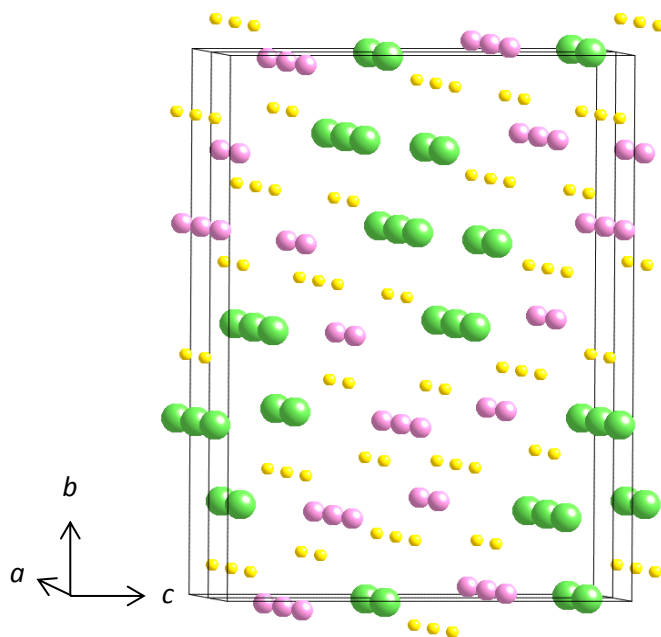
Figure 7.5: *La and In and S sites identified using simulated annealing methodology. Green = La, pink = In, yellow = sulfur.*

7.5 Rietveld refinement and structural description

Final Rietveld refinements were carried out over a larger 2-theta range against the synchrotron XRPD data, 84 independent parameters were refined including, 3 unit cell parameters, a zero point correction, 10 background parameters of a Chebyshev polynomial, 45 atomic coordinates, 3 isotropic thermal parameters (one La site, one for In sites and one for all anion sites), 1 scale factor, 4 refining parameters of a full Voigt peak shape. In order to model the amorphous contribution to the scattering due to SiO$_2$ a single reflection using 4 refining peak shape parameters of a Split PearsonVII model was introduced, along with a single refining position and intensity. A cylindrical absorption parameter was initially refined and then fixed for the final cycle of refinements. Figure 7.6 shows a good fit to the observed diffraction profile; the final structural model is given in table 7.1.
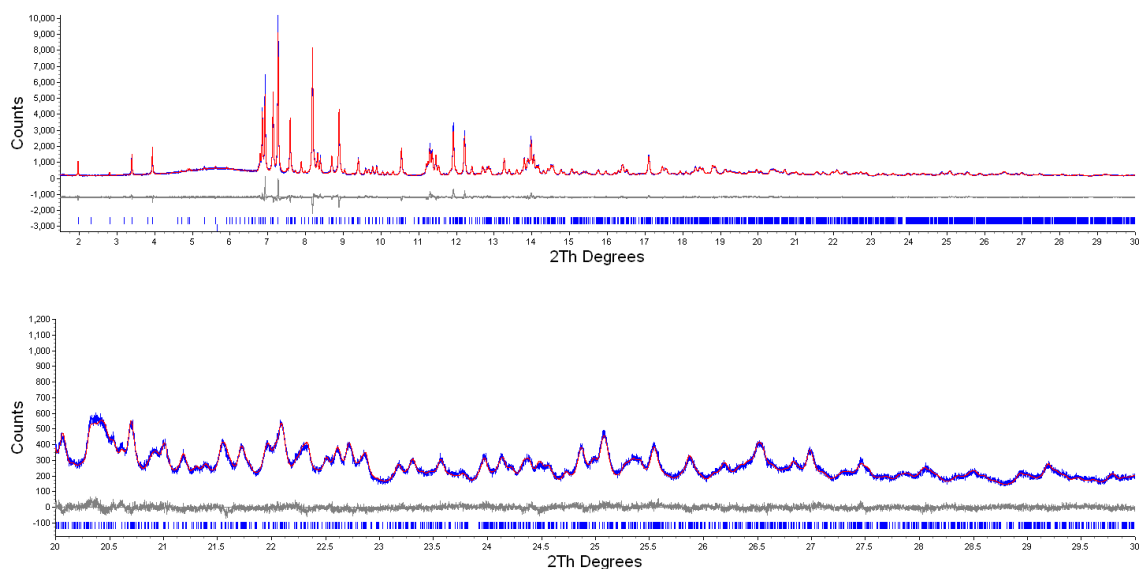
Figure 7.6: *Rietveld refinement profile for LaInS$_2$O. Unit cell parameters a = 3.98578(2) Å, b = 20.5476(1) Å, c = 14.8450(1) Å, space group P2$_1$2$_1$2$_1$. R$_{wp}$ = 6.370 %, R$_p$ =5.232 %, R$_{Bragg}$ = 2.934 %, gof = 1.416. AJT192, 11bmb_8963.xye.*

Table 7.1: *Results of Rietveld analysis of X-ray data of LaInS$_2$O at room temperature. Unit cell parameters a = 3.98578(2) Å, b = 20.5477(1) Å, c = 14.8450(1) Å, space group P2$_1$2$_1$2$_1$. R$_{wp}$ = 6.370 %, R$_p$ =5.232 %, R$_{Bragg}$ = 2.934 %, gof = 1.416. AJT192, 11bmb_8963.xye. BVS= bond valence sum.*

Site label	Wyckoff site	x	y	z	B / Å^2	BVS
La1	4a	0.2656(9)	-0.00689(6)	0.09821(7)	0.26(2)	2.7
La2	4a	0.747(1)	0.15600(6)	0.67582(8)	0.26(2)	3.9
La3	4a	0.257(1)	0.82454(6)	-0.04366(8)	0.26(2)	3.0
In1	4a	0.750(2)	0.32154(8)	0.0350(1)	0.69(2)	3.0
In2	4a	0.240(1)	0.65220(7)	0.2984(1)	0.69(2)	3.2
In3	4a	0.264(1)	0.51390(7)	0.6778(1)	0.69(2)	2.9
S1	4a	0.763(6)	0.8868(2)	0.5477(3)	0.84(5)	2.1
S2	4a	0.752(7)	0.0497(2)	0.4580(3)	0.84(5)	2.0
S3	4a	0.244(7)	0.7463(3)	0.6064(3)	0.84(5)	1.7
S4	4a	0.762(6)	0.4174(2)	0.7371(4)	0.84(5)	1.8
S5	4a	0.216(3)	0.2668(2)	0.6884(4)	0.84(5)	2.3
S6	4a	0.782(3)	0.5982(3)	0.6618(4)	0.84(5)	1.8
O1	4a	0.725(8)	0.6377(6)	0.8789(7)	0.84(5)	2.5
O2	4a	0.278(9)	0.4644(5)	0.3149(7)	0.84(5)	2.4
O3	4a	0.274(9)	0.2797(6)	0.4586(8)	0.84(5)	2.1

The structure of LaInS$_2$O (figure 7.7) contains blocks of edge sharing InS$_6$ distorted octahedra which form infinite slabs along [100]. These InS$_6$ units are connected via corners and edges with InS$_5$O distorted octahedra, which themselves edge-share to produce infinite chains along [100]. The oxygen sites within the InS$_5$O octahedra form part of a block constructed of La$_4$O and La$_3$InO tetrahedra which share through 4 common edges. These form an infinite ribbon along [100] 6 tetrahedra in width. The 6 x tetrahedral ribbon is structurally similar to the 4 x tetrahedral ribbon encountered in the A_4O$_4$TiSe$_4$ structure of Chapter 4. The InS$_5$O and TiSe$_4$O$_2$ terminate tetrahedral ribbons in a similar way in the two structures. There are 3 crystallographically independent La^{3+} ions in the structure which have either LaS$_4$O$_4$ or LaS$_5$O$_3$ 4+4 square antiprismatic coordination environments, figure 7.8. Due to the finite width of the tetrahedral ribbons one oxygen is replaced by sulfur around La1 relative to the La^{3+} coordination environment found in LaOFeAs. LaInS$_2$O thus contains similar A^{3+} coordination environments to those discussed in Chapter 4 for A_4O$_4$TiSe$_4$. There are 3 crystallographically independent indium sites within the structure all with 6 fold coordination in either InS$_6$ or InS$_5$O environments. The InS$_6$ octahedra (In1 & In2) form blocks of 4 polyhedra in the *bc* plane.

One free vertex on each In(1)S$_6$ bonds to In(3)S$_5$O, while the In(2)S$_6$ octahedra share edges with adjacent In(3)S$_5$O polyhedra with the In2 site significantly displaced towards the In(3)S$_5$O unit. Selected bond lengths are given in table 7.2. Bond valence sums, table 7.1, are in line with expected values. The slightly high value for some sites probably reflects the difficulty of accurately locating oxygen from powder X-ray data.
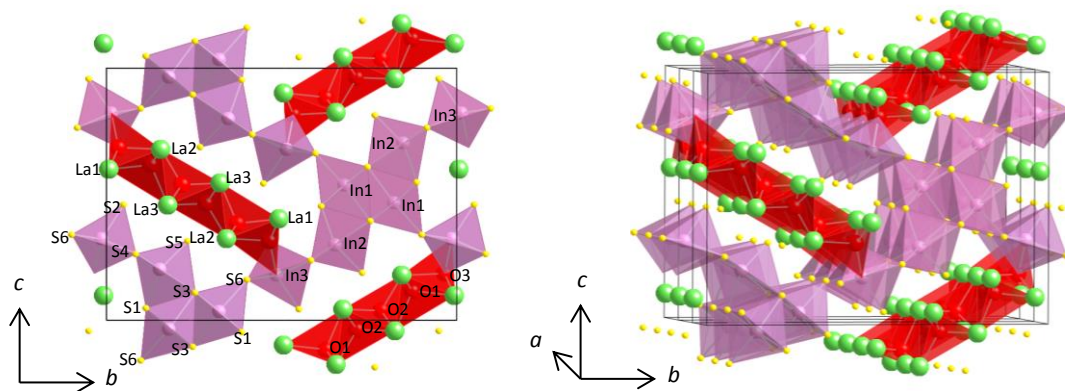

Figure 7.7: *Structure of LaInS$_2$O. La = green, In = purple, S = yellow, O = red.*
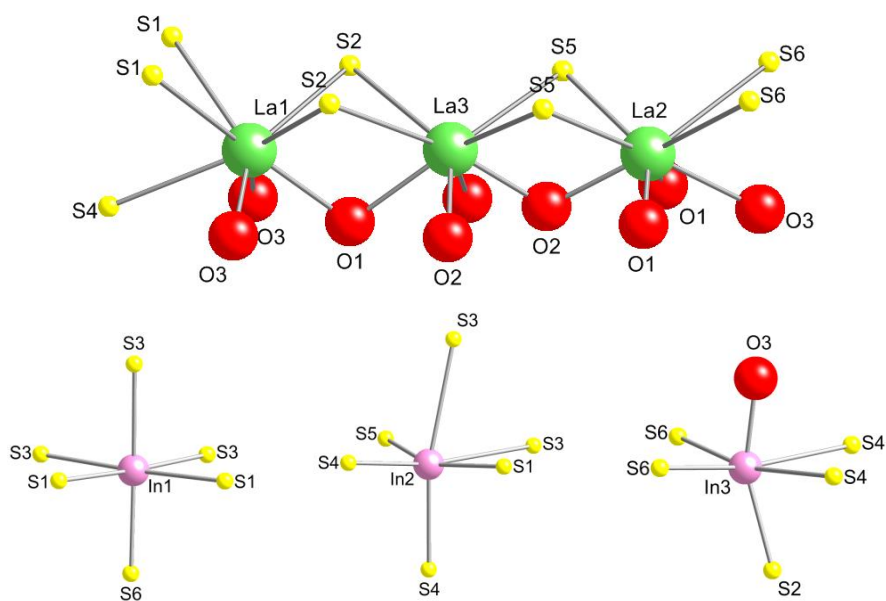
Figure 7.8: *Local coordination environments of metal sites in LaInS$_2$O. La = green, In = purple, S = yellow, O = red.*

Table 7.2: *Selected bond distances for LaInS$_2$O*

Bond	Distance / Å	Bond	Distance / Å	Bond	Distance / Å
In1-S1	2.660(2)	In2-S1	2.4237(5)	In3-S2	2.4030(5)
In1-S1	2.735(2)	In2-S3	3.202(2)	In3-S4	2.939(2)
In1-S3	2.6078(6)	In2-S3	3.222(2)	In3-S4	2.953(2)
In1-S3	2.635(2)	In2-S4	2.612(2)	In3-S6	2.599(1)
In1-S3	2.671(2)	In2-S4	2.620(2)	In3-S6	2.707(1)
In1-S6	2.5052(6)	In2-S5	2.3386(5)	In3-O3	2.091(1)
La1-S1	3.192(1)	La2-S5	2.952(1)	La3-S2	3.242(2)
La1-S1	3.329(2)	La2-S5	3.115(1)	La3-S2	3.284(2)
La1-S2	2.967(2)	La2-S6	3.275(1)	La3-S5	3.095(1)
La1-S2	3.060(2)	La2-S6	3.416(1)	La3-S5	3.230(1)
La1-S4	3.0590(5)	La2-O1	2.084(3)	La3-O1	2.569(1)
La1-O1	2.713(1)	La2-O1	2.287(3)	La3-O2	2.146(1)
La1-O3	2.307(3)	La2-O2	2.395(1)	La3-O2	2.439(3)
La1-O3	2.589(3)	La2-O3	2.480(1)	La3-O2	2.629(3)

Two other indium containing lanthanum oxysulfides have been reported in the literature: La$_5$In$_3$O$_3$S$_9$[6] and La$_{10}$In$_6$S$_{17}$O$_6$[9], both of which contain ribbons of La$_4$O edge shared tetrahedra 3 units in width. The ribbons run parallel to each other in the structure and are separated by layers of InS$_x$ with indium found in both tetrahedral and octahedral environments, figure 7.9. Thus LaInS$_2$O represents a different packing arrangement of the rare-earth containing ribbons, packing in a herringbone-like fashion, and separated solely by octahedrally coordinated indium. It is also the only system to date featuring mixed O/S coordination of In.
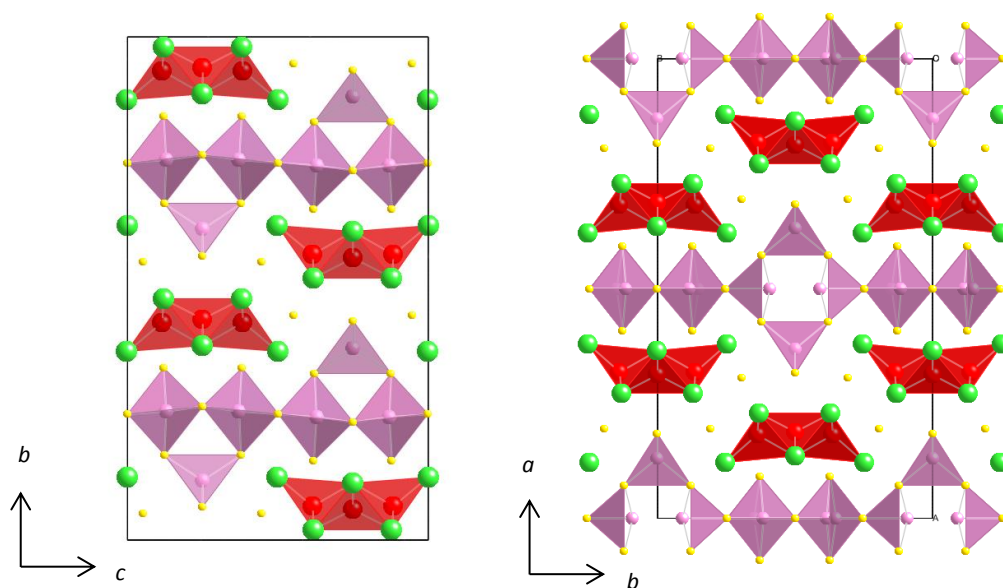
Figure 7.9: *Structures of a) La$_5$In$_3$O$_3$S$_9$ and b) La$_{10}$In$_6$S$_{17}$O$_6$, La = green, In = purple, S = yellow, O = red.*

7.6 Conclusions

A new route to preparing high purity polycrystalline samples of LaInS$_2$O has been reported. The structure of LaInS$_2$O was solved using a simulated annealing methodology from X-ray powder diffraction data. The structure contains ribbons of La$_4$O and La$_3$InO edge sharing tetrahedra, which are 6 tetrahedra in width. These ribbons are connected to octahedrally coordinated indium, which in turn share corners and edges to slabs of edge sharing InS$_6$ octahedra.

References

1. Kudo, A., Yanagi, H., Hosono, H., and Kawazoe, H., *Applied Physics Letters*, 1998, **73**, 220-222

2. Kawazoe, H., Yasukawa, M., Hyodo, H., Kurita, M., Yanagi, H., and Hosono, H., *Nature*, 1997, **389**, 939-942

3. Yanagi, H., Inoue, S., Ueda, K., Kawazoe, H., Hosono, H., and Hamada, N., *Journal of Applied Physics*, 2000, **88**, 4159-4163

4. Yanagi, H., Kawazoe, H., Kudo, A., Yasukawa, M., and Hosono, H., *Journal of Electroceramics*, 2000, **4**, 407-414

5. Ueda, K., Inoue, S., Hirose, S., Kawazoe, H., and Hosono, H., *Applied Physics Letters*, 2000, **77**, 2701-2703

6. Kabbour, H., Cario, L., Moelo, Y., and Meerschaut, A., *Journal of Solid State Chemistry*, 2004, **177**, 1053-1059

7. Altomare, A., Cuocci, C., Giacovazzo, C., Moliterni, A., Rizzi, R., Corriero, N., and Falcicchio, A., *Journal of Applied Crystallography*, 2013, **46**, 1231-1235

8. Coelho, A. A., TOPAS Academic: General Profile and Structure Analysis Software for Powder Diffraction Data, 2012.

9. Gastaldi, L., Carre, D., and Pardo, M. P., *Acta Crystallographica Section B-Structural Science*, 1982, **38**, 2365-2367

Chapter 8: Calibration of Oxford Cryosystems Cryostream© for Powder Diffraction

8.1 Experimental setup

Temperature calibration of a new nitrogen-flow cooling (and heating) system for capillary geometry powder measurements, an Oxford Cryosystems Cryostream© 700 compact, was carried out during this project. This apparatus was used during the work described in Chapter 4. Although the manufacturer-stated temperature accuracy is 0.1 K,[1] the true sample temperature can often differ significantly from that set, and therefore it is important to calibrate the cooling device in the actual instrument geometry.

The Cryostream operates by pulling liquid nitrogen from an unpressurised Dewar into the coldhead of the device, where it is heated to form a vapour. The vapour is pumped through a gas regulator (which controls the gas flow rate), and through a exchanger before being heated to the required sample temperature, figure 8.1. The gas flow rate used is typically 5 litres/minute, but this can be increased to 10 litres/minute for faster cooling rates or if a set temperature of less than 90 K is required. The device was controlled using Oxford Cryosystems 'Cryopad' software.[2] An AD51 dry air unit was used to supply dry air to shroud the cryogenic nitrogen gas stream, this prevents atmospheric moisture from freezing on the sample.
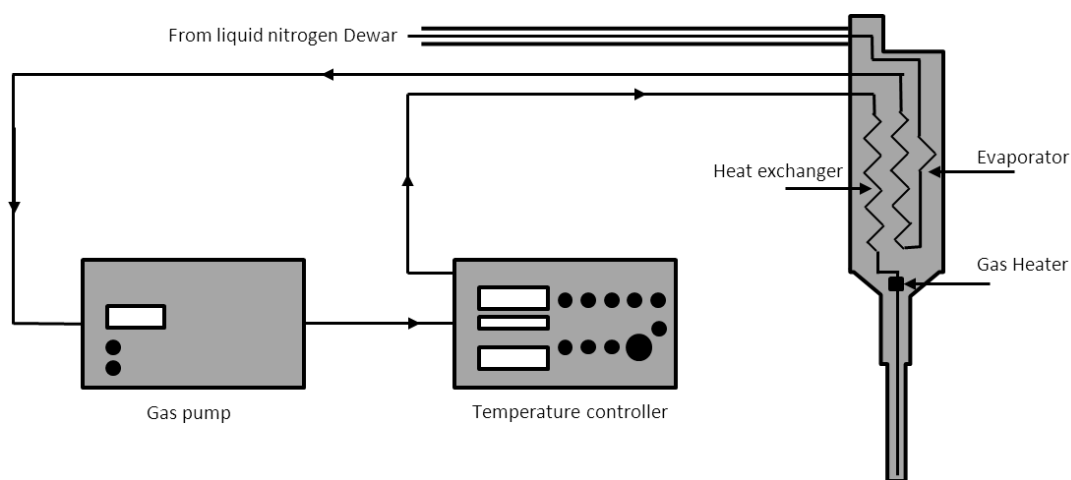
Figure 8.1: Schematic diagram of Oxford Cryosystems Cryostream© setup.[1]

For this system it is well known that the gas temperature increases rapidly after leaving the nozzle. The manufacturer states that the set temperature matches the temperature of the sample when it is positioned 5 to 10 mm from the end of the nozzle.[1] In the instrumental setup

for powder diffraction however, ~15mm of sample is illuminated by the X-ray beam potentially leading to significant temperature discrepancies.

There are two main ways of temperature calibration for a cryogenic cooling system such as this. The first is to calibrate with samples that undergo known phase transitions or changes of state. The second is to calibrate with samples with well determined thermal expansion behaviour over a wide temperature range, and use the measured cell volume to infer the temperature. This problem with this method is that any systematic errors in volume determination can lead to large errors in the estimated temperature. We therefore chose the second method but with two samples used simultaneously for calibration, one with a high (Al) and one with a low (Si) thermal expansion. The difference in thermal expansion between these two compounds can then be used to determine temperature (figure 8.2). Evaluating differences in expansion in this way eliminates systematic errors due to factors such as absorption or instrument misalignment which affect peak positions.
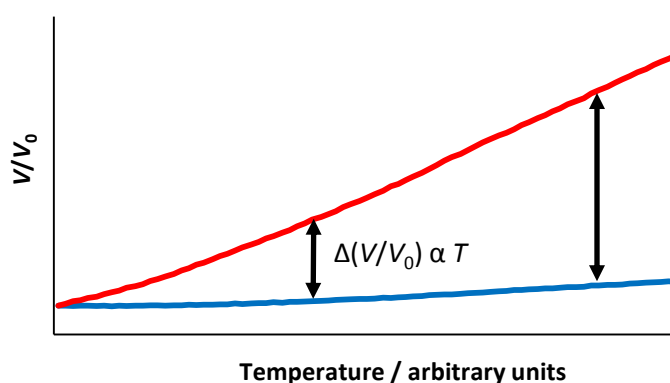
Figure 8.2: Schematic representation of using the difference in thermal expansion between two materials to determine temperature.

To perform the calibration a flame-sealed 0.5 mm diameter borosilicate capillary, 35 mm in length containing a 1:1 by mass mixture of Si (Alfa) and Al (Alfa) powders. The diffractometer (d7) setup is described in section 2.6.1.1. The Cryostream unit was mounted parallel to the capillary at the edge of the beam, as shown in figure 8.3, positioned such that the end of its nozzle was aligned with the beam stop, (as close to the X-ray beam as possible). In this setup the capillary intrudes the nozzle by a few mm. The 35 mm capillary was fixed inside a 10 mm length glass capillary rod with 'superglue', which would remain stable over the entire temperature range of the experiment. The rod was then mounted in a standard goniometer head. Data were collected upon ramping from 80 K to 500 K at 30 K hr^{-1}, while collecting 10 minute scans from 20-140° with step size 0.02°. Each diffraction pattern therefore represents a ~5 K range; a total of 100 diffraction patterns were recorded.
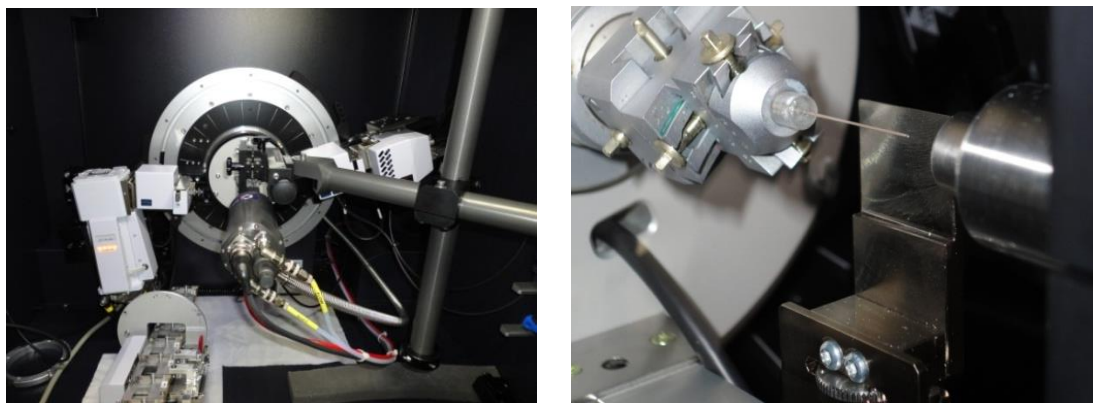
Figure 8.3: *Experimental setup of nitrogen flow cooling device perpendicular to diffractometer axis, note the nozzle has been pulled back for right photo.*

8.2 Data analysis

To check data quality unit cell parameters were extracted from Rietveld analysis of the powder diffraction patterns at set temperatures from 80 to 500 K using sequential refinements in Topas. Figure 8.4 shows that the mixture of Si and Al undergoes thermal expansion of differing magnitudes suitable for applying the method described in 8.1.
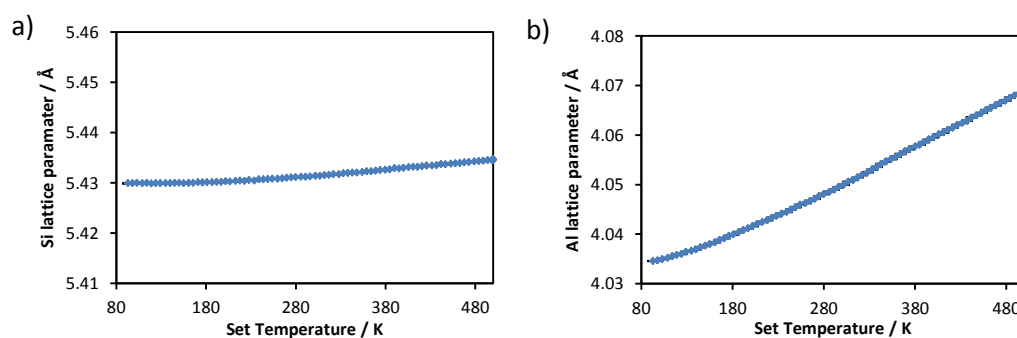
Figures 8.4: *a) silicon lattice parameter, b) aluminium lattice parameter derived from Rietveld analysis of d7_00059.*

In order to extract experimental temperatures directly from the data using the approach of figure 8.1, we adopted the parametric Rietveld refinement methodology described by Evans and Stinton.[3] This can be set up to eliminate systematic errors in the data and effectively extract sample temperatures directly from a single combined refinement of all data sets. In this method instead of freely refining cell parameters from each data set, cell parameters are calculated according to the know thermal expansion of the phase and the experimental set temperature. Any discrepancy in the calculated and predicted peak position (after instrument 2θ calibrations have been applied as described below) is a measure of the difference in the set

and actual sample temperature. By appropriate parameterisation this temperature difference ΔT, can be refined.

For each phase lattice parameters were calculated in the refinement process by Einstein functions of the form:

$$a_T = \exp\left(\ln(a_0) + \sum_n (c_n \theta_n) / \left[\exp\left(\frac{\theta_n}{T}\right) - 1\right]\right) \qquad \text{eqn 8.1}$$

where: a_T = cell parameter at temperature T, a_0 = cell parameter at 0 K, c_n = an empirically derived coefficient, θ_n = Einstein temperature. T was expressed as $T_{set} + \Delta T$ where ΔT is a refinable parameter.

For Al, appropriate values for a_0, c_n, and θ_n were obtained from fitting published thermal expansion behaviour from Wang and Reeber,[4] along with the 4 K lattice parameter reported by Kroeger,[5] with a two term Einstein expression of the form of equation 8.1. To give equations to model the thermal expansion behaviour over the temperature range accessible using the Crycostream system, literature data from 4 to 550K were fitted. Coefficients extracted are given in table 8.1. For Si, lattice parameters were taken for NIST640C Si from Swenson.[3, 6, 7] These data were fitted with a three-term Einstein expression from 4 to 600K, the coefficients of this fit are also given in table 8.1. The calculated fits are shown in figure 8.5, where it can be seen from the difference curve (right hand vertical axis) that the equations model the reported literature data well up to 550 and 600 K for Al and Si respectively. Note the fit is slightly worse for Al due to the greater thermal expansion and the fit is over fewer data points, but reproduces cell parameters to within 0.0001 Å.

Table 8.1: Coefficients used to describe the temperature dependence of the cell parameters of Al and Si using equation 8.1.

	Al	Si
a_0 / Å	4.03257(4)	5.42999(1)
c_1 / K^{-1}	2.19967(2)x10^{-5}	-8.5(2)x10^{-7}
θ_1 / K	200(200)	185(3)
c_2 / K^{-1}	7.97758(1)x10^{-6}	4.95(2)x10^{-6}
θ_2 / K	1100(900)	651(3)
c_3 / K^{-1}	-	3.1(3)x10^{-7}
θ_3 / K	-	1500
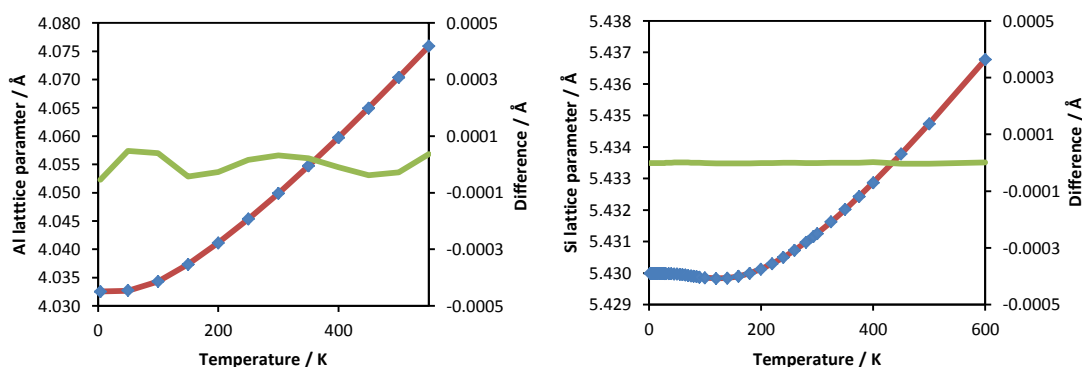
Figure 8.5: *Einstein functions (red) for Al and Si plotted with literature data (blue), difference curve (green) plotted on secondary axis (right).*

A two theta correction was also applied during the Rietveld fitting to account for systematic errors in the lattice parameter determination due to instrument calibration or effects such as absorption. Standard Rietveld analysis was performed on a long (~2 hours, d7_00061) data collection at 295 K, immediately after the variable temperature measurement. The cell parameter for Si was fixed using equation 8.1 and the coefficients from table 8.1, and the Al cell parameter was allowed to refine. A two theta calibration was applied so that the fixed Si lattice parameter predicted perfect experimental peak positions. This two theta calibration was then fixed for the VT refinements. With the correction applied good agreement is seen for both Si (5.43120(5) Å) and Al (4.04944(6) Å) cell parameters at 295 K against the fitted literature data, 5.4311 Å and 4.0495 Å.[4, 7]

To extract ΔT from the diffraction data lattice parameters for Si and Al were both parameterised by equation 8.1 with the a_0 value for Al allowed to refine. T in equation 8.1 was expressed as $T = T_{true} = T_{set} + \Delta T$, and ΔT determined from free refinement from each data set or by simultaneous fitting of coefficients of a ΔT polynomial, as given in equation 8.2 from all the data:

$$\Delta T = a_1 + \left(b_1 \times \frac{T_{set}-T_{mid}}{T_{max}-T_{min}}\right) + \left(c_1 \times \left(\frac{T_{set}-T_{mid}}{T_{max}-T_{min}}\right)^2\right) + \left(d_1 \times \left(\frac{T_{set}-T_{mid}}{T_{max}-T_{min}}\right)^3\right) \text{ Eqn 8.2}$$

Here T_{set} is the programmed temperature and T_{max} and T_{min} are the maximum and minimum temperatures of the experiment, 500 K and 80 K respectively, and T_{mid} is the midpoint of the polynomial (290 K). This polynomial allow accurate sample temperatures to be calculated across the whole diffraction surface.

For the parametric refinements with ΔT refined from all data set using the ΔT polynomial 1010 parameters were refined; 10 global parameters (4 coefficients of the temperature polynomial, 4 parameters to define a TCHZ pseudo Voigt peak shape, 1 parameter to model axial

divergence, a_0 value of aluminium), and 10 parameters for each temperature (2 scale factors, 2 thermal parameters, 6 coefficients of a Chebychev polynomial to model the background), giving an overall R_{wp} = 19.241 %. When ΔT was refined independently from each data set 1106 parameters were refined; 6 global parameters (4 parameters to define a TCHZ peak shape, 1 parameter to model axial divergence, a_0 value of aluminium) and 11 parameters for each temperature (a ΔT value, 2 scale factors, 2 thermal parameters, 6 coefficients of a Chebychev polynomial to model the background), with an R_{wp} = 19.237 %.

The refined coefficients of the ΔT polynomial are given in table 8.2 and there is good correlation between the free and the parameterised ΔT values, figure 8.6.
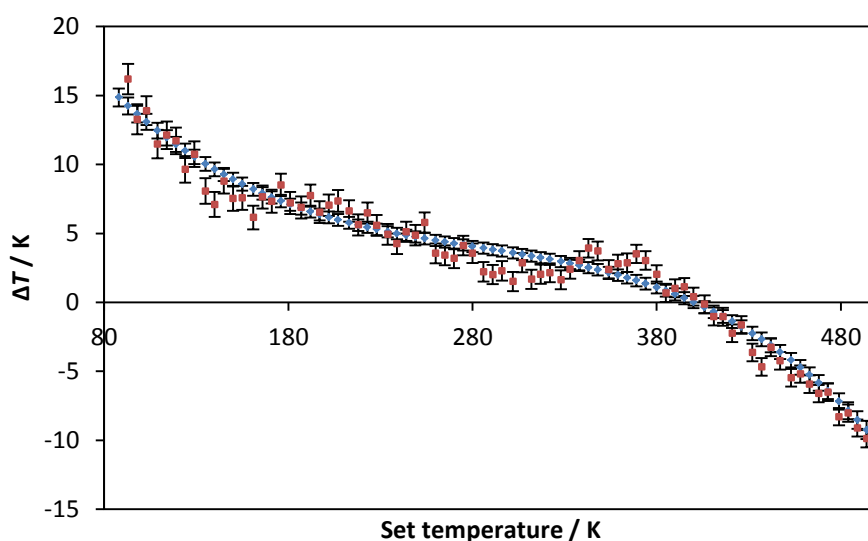
Figure 8.6: *Variation of temperature error with set temperature, red points = free ΔT, blue points = parameterised ΔT.*

Table 8.2: *Coefficients of ΔT polynomial*

a_1	3.8(4) K
b_1	-8.8(6) K
c_1	-4(1) K
d_1	-68(3) K

8.3 Discussion

Figure 8.6 shows there is deviation of the true sample temperature from the set temperature, especially towards the extremes of the accessible temperature range, although the deviation is not substantial. The temperature error (ΔT) is in the direction expected, with the true temperature being warmer than expected at the lowest accessible temperatures and vice

versa at the highest temperatures. Temperature differences up to a maximum error of ~ 15 K were observed at ~ 85 K.

For convenience equation 8.2 can be rewritten as:

$$\Delta T = a_2 + b_2 T_{set} + c_2 T_{set}^2 + d_2 T_{set}^3 \qquad \text{eqn 8.3}$$

The coefficients of this equation are given in table 8.3. A correction term of the form of equation 8.3 should be applied if accurate sample temperatures are required. Our judgement is that using this procedure estimated sample temperatures will be within ~3 K of their true values.

Table 8.3: Coefficients of temperature correction polynomial.

a_2	30(1) K
b_2	-0.24(1)
c_2	7.8(4)x10^{-4} K^{-1}
d_2	-9.2(4)x10^{-7} K^{-2}

References

1. *Oxford Cryosystems, Cyrostream 700 manual*, 2011
2. *Oxford Cryosystems Cryopad v1.500*, 2011
3. Stinton, G. W. and Evans, J. S. O., *Journal of Applied Crystallography*, 2007, **40**, 87-95
4. Wang, K. and Reeber, R. R., *Philosophical Magazine a-Physics of Condensed Matter Structure Defects and Mechanical Properties*, 2000, **80**, 1629-1643
5. Kroeger, F. R. and Swenson, C. A., *Journal of Applied Physics*, 1977, **48**, 853-864
6. *J. P. Cline, Standard Reference Material 640c - Silicon Powder Line Postion and Line Shape Standard for Powder Diffraction, Gaithersburg, Maryland, USA*, 2000
7. Swenson, C. A., *Journal of Physical and Chemical Reference Data*, 1983, **12**, 179-182

Appendix 1

Table of EDX data from 30 points on the surface of a $La_2O_2ZnSe_2$ pellet, 15kV electron beam, referenced to a cobalt standard.

Site	La %	O %	Zn %	Se %	Al %
1	25.18	30.41	15.55	27.65	1.21
2	25.45	30.02	15.58	28.95	0.00
3	24.90	31.19	15.74	28.17	0.00
4	29.15	26.98	14.86	27.38	1.63
5	24.54	30.12	16.25	28.07	1.03
6	24.05	30.56	15.94	28.17	1.29
7	25.27	30.51	15.78	27.08	1.36
8	27.39	29.35	15.53	27.73	0.00
9	27.41	28.62	15.19	27.19	1.58
10	23.68	31.70	15.89	27.64	1.08
11	26.03	29.15	16.81	28.02	0.00
12	25.58	30.88	15.57	27.97	0.00
13	24.87	30.04	15.97	27.99	1.13
14	25.58	30.83	15.67	27.93	0.00
15	26.27	30.57	15.72	27.44	0.00
16	25.40	30.53	15.21	27.63	1.24
17	25.30	30.45	15.75	27.43	1.07
18	25.59	29.44	15.82	27.89	1.25
19	25.55	29.91	16.27	28.27	0.00
20	28.24	28.01	15.83	27.92	0.00
21	27.39	27.96	15.42	27.87	1.36
22	25.73	29.26	15.79	27.80	1.42
23	27.01	29.25	15.58	28.16	0.00
24	25.30	30.37	15.88	28.45	0.00
25	25.89	28.85	15.65	28.31	1.29
26	27.81	27.37	16.10	28.73	0.00
27	25.01	30.77	16.08	28.14	0.00
28	25.46	29.65	16.20	27.61	1.07
29	24.33	32.15	15.92	27.60	0.00
30	28.74	27.20	15.60	28.47	0.00
Average / %	26	30	15.8	27.9	0.6
Standard deviation	1	1	0.4	0.4	0.7

Results from combined X-ray / neutron Rietveld refinement of $La_2O_2ZnSe_2$ at room temperature.

Temperature / K	295 K
Sample	AJT039
Input file	gem52355_ajt_all_cmca_03.inp
	d9_06009.raw
	gem52355_b2_tof.dat
	gem52355_b3_tof.dat
Data file(s)	gem52355_b4_tof.dat
	gem52355_b5_tof.dat
	gem52355_b6_tof.dat
Symmetry	*Cmca*
a (Å)	22.9332(2)
b (Å)	17.80043(6)
c (Å)	5.73241(6)
N^o. variables	162
R_{wp} (%)	5.233
R_p (%)	4.433
χ^2 (%)	6.538
R_{Bragg} X-ray (%)	1.619
R_{Bragg} bank 2 (%)	2.198
R_{Bragg} bank 3 (%)	8.424
R_{Bragg} bank 4 (%)	1.791
R_{Bragg} bank 5 (%)	2.318
R_{Bragg} bank 6 (%)	2.492

162 independent parameters refined including:

26 parameters specific to X-ray data, (18 background parameters of a Chebyshev polynomial, 2 scale factors, 4 refining parameters of a pseudo-Voigt TCHz peak shape, a parameter to model the axial divergence, a sample height parameter).

20 parameters specific to each neutron data bank, (3 parameters to model the tof calibration, 12 background parameters of a Chebyshev polynomial, an absorption parameter, 2 scale factors, 2 peak shape parameters).

33 parameters specific to $La_2O_2ZnSe_2$, (3 unit cell parameters, 20 atomic positions, 10 isotropic thermal parameters).

3 parameters specific to ZnSe, (1 unit cell parameter, 2 isotropic thermal parameters).

Appendix 2

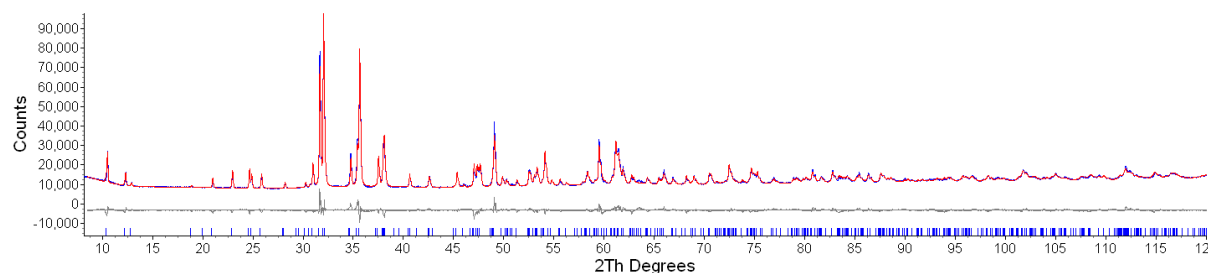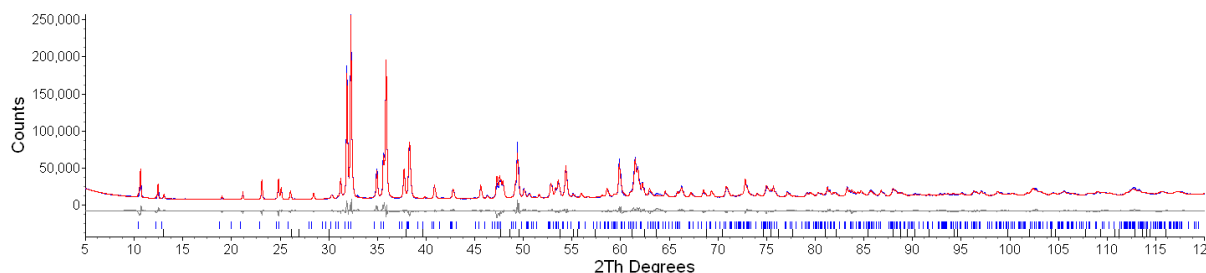**Rietveld refinement of Sm$_4$O$_4$TiSe$_4$ at room temperature**

51 parameters were used to describe the instrumental and structural parameters for Rietveld analysis. The instrumental parameters were 18 Chebychev polynomial coefficients to model the background, a sample height term, 3 scale parameters, 4 terms to model a pseudo-Voigt peak-shape (TCHz) and 1 term to describe axial divergence. The structural parameters refined included Sm$_4$O$_4$TiSe$_4$: 4 cell parameters (a, b, c and β), 8 atomic positions and 6 isotropic thermal parameters; Sm$_2$O$_2$Se: 2 unit cell parameters; SmSe$_2$: 2 lattice parameters. A single thermal parameter was used for all sites in impurity phases.
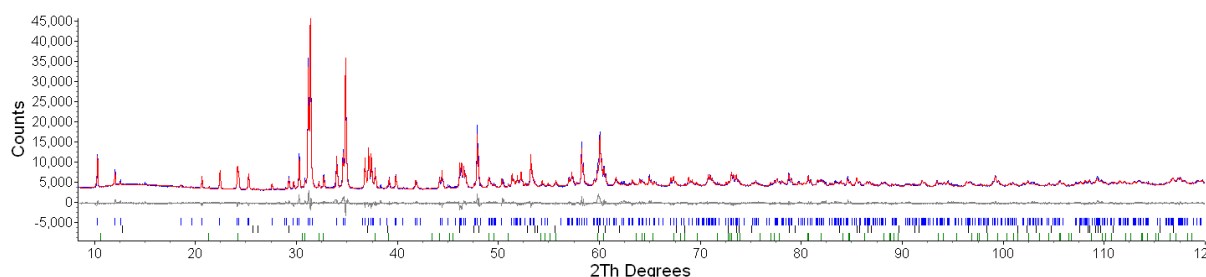
Rietveld refinement profile of room-temperature XRPD data for Sm$_4$O$_4$TiSe$_4$, refined in space group C2/m (observed, calculated, and difference profiles shown in blue, red, and grey, respectively); tick marks show reflection positions for Sm$_4$O$_4$TiSe$_4$ (top), Sm$_2$O$_2$Se (middle, <2 weight %) and SmSe$_2$ (bottom, ~7 %). d7_ 02184, AJT150.

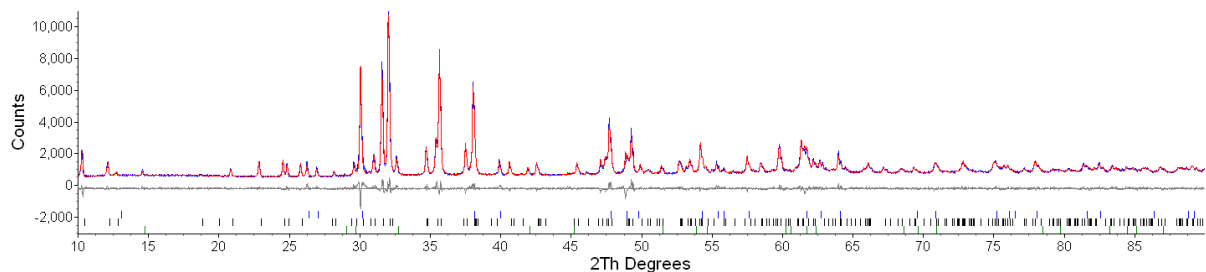**Rietveld refinement of Gd$_4$O$_4$TiSe$_4$ at room temperature**

56 parameters were used to describe the instrumental and structural parameters for Rietveld analysis. The instrumental parameters were 18 Chebychev polynomial coefficients to model the background, a sample height term, 2 scale factors one for Gd$_4$O$_4$TiSe$_4$ and the other for a Si internal standard, 4 terms to model the TCHZ peak-shape for each phase, and 1 term to describe axial divergence. The structural parameters refined included 4 cell parameters (a, b, c and β), 12 atomic positions and 6 isotropic thermal parameters. A single unit cell and thermal parameter for Si was refined, along with 3 refining terms of a spherical harmonic. Three peaks were introduced to model scatter from the cryostat windows.
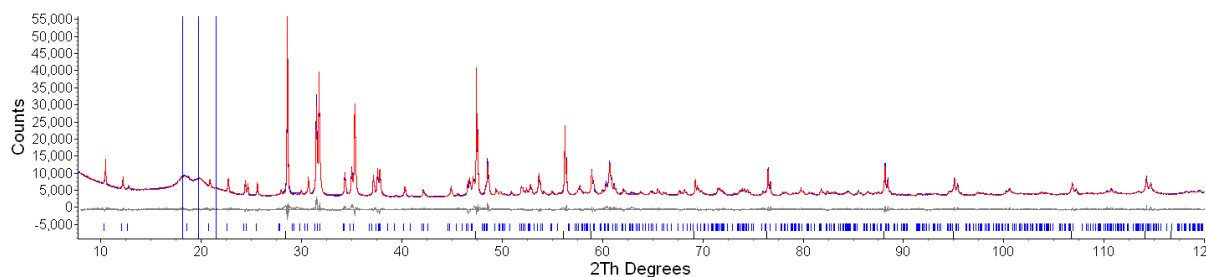
Rietveld refinement profile of room-temperature XRPD data for Gd$_4$O$_4$TiSe$_4$, refined in space group C2/m (observed, calculated, and difference profiles shown in blue, red, and grey, respectively); tick marks show reflection positions for Gd$_4$O$_4$TiSe$_4$ (top), Si internal standard (bottom). d9_06703[58_71], AJT078b.

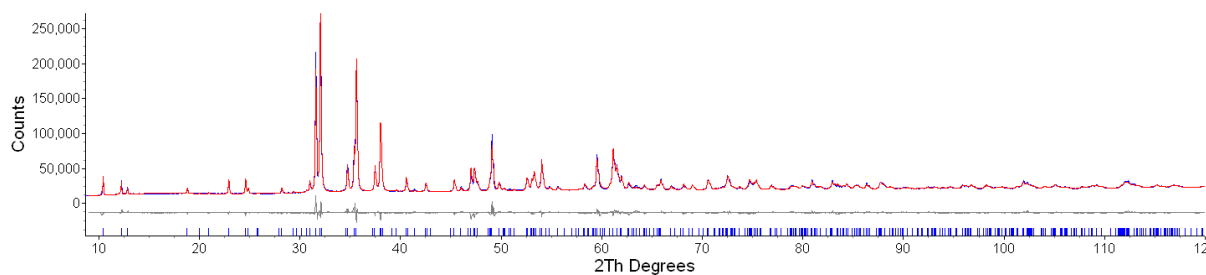## Rietveld refinement of Tb$_4$O$_4$TiSe$_4$ at room temperature

46 parameters were used to describe the instrumental and structural parameters for Rietveld analysis. The instrumental parameters were 18 Chebychev polynomial coefficients to model the background, a sample height term, 2 scale factors one for Tb$_4$O$_4$TiSe$_4$ and the other for Tb$_2$O$_2$Se, 4 terms to model the TCHZ peak-shape and 1 term to describe axial divergence. The structural parameters refined included 4 cell parameters (*a*, *b*, *c* and β), 8 atomic positions, 6 isotropic thermal parameters. 2 cell parameters for the Tb$_2$O$_2$Se impurity phase were also refined.
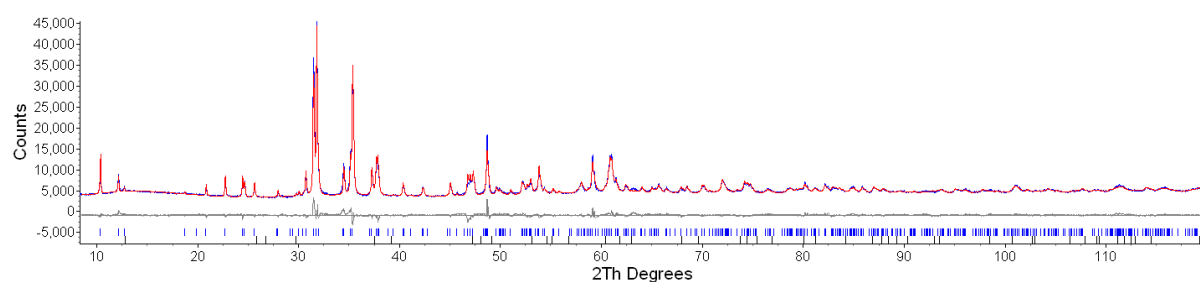
Rietveld refinement profile of room-temperature XRPD data for Tb$_4$O$_4$TiSe, refined in space group C2/m (observed, calculated, and difference profiles shown in blue, red, and grey, respectively); tick marks show reflection positions for Tb$_4$O$_4$TiSe$_4$ (top), Tb$_2$O$_2$Se (bottom, <1 weight %). d7_00873, AJT079.

Rietveld refinement of Dy$_4$O$_4$TiSe$_4$ at room temperature

43 parameters were used to describe the instrumental and structural parameters for Rietveld analysis. The instrumental parameters were 18 Chebychev polynomial coefficients to model the background, a sample height term, 1 scale factor, 4 terms to model the TCHZ peak-shape and 1 term to describe axial divergence. The structural parameters refined were 4 cell parameters (*a*, *b*, *c* and β), 8 atomic positions and 6 isotropic thermal parameters.


Rietveld refinement profile of room-temperature XRPD data for Dy$_4$O$_4$TiSe$_4$ refined in space group C2/m (observed, calculated, and difference profiles shown in blue, red, and grey, respectively); tick marks show reflection positions for Dy$_4$O$_4$TiSe$_4$. d9_06716, AJT082.

Rietveld refinement of Ho$_4$O$_4$TiSe$_4$ at room temperature

46 parameters were used to describe the instrumental and structural parameters for Rietveld analysis. The instrumental parameters were 18 Chebychev polynomial coefficients to model the background, a sample height term, 2 scale factors one for Ho$_4$O$_4$TiSe$_4$ and the other for Ho$_2$O$_2$Se, 4 terms to model the TCHZ peak-shape and 1 term to describe axial divergence. The structural parameters refined were 4 cell parameters (a, b, c and β), 8 atomic positions, 6 isotropic thermal parameters. 2 cell parameters for the Ho$_2$O$_2$Se phase were also refined.

Rietveld refinement profile of room-temperature XRPD data for Ho$_4$O$_4$TiSe$_4$ refined in space group C2/m (observed, calculated, and difference profiles shown in blue, red, and grey, respectively); tick marks show reflection positions for Ho$_4$O$_4$TiSe$_4$ (top), Ho$_2$O$_2$Se (bottom, <1 weight %). d9_06714, AJT093c.

Rietveld refinement of Er$_4$O$_4$TiSe$_4$ at room temperature

59 parameters were used to describe the instrumental and structural parameters for Rietveld analysis. The instrumental parameters were 18 Chebychev polynomial coefficients to model the background, a sample height term, 3 scale factors one for Er$_4$O$_4$TiSe$_4$ and the others for Er$_2$O$_2$Se and TiSe$_2$, 4 terms to model the TCHZ peak-shape and 1 term to describe axial divergence. The structural parameters refined included 4 cell parameters (a, b, c and β), 8 atomic positions, 6 isotropic thermal parameters for A_4O$_4$TiSe$_4$. 2 cell parameters and a single isotropic thermal parameter was used for the Er$_2$O$_2$Se phase; and 2 unit cell parameters and 9 refining terms of a spherical harmonic preferred orientation correction for TiSe$_2$.

Rietveld refinement profile of room-temperature XRPD data for Er$_4$O$_4$TiSe$_4$ refined in space group C2/m (observed, calculated, and difference profiles shown in blue, red, and grey, respectively); tick marks show reflection positions for Er$_2$O$_2$Se (top ~20 weight %), Er$_4$O$_4$TiSe$_4$ (middle), TiSe$_2$ (bottom, ~5 weight %). d7_01000, AJT075b.

Rietveld refinement of $Y_4O_4TiSe_4$ at room temperature

43 parameters were used to describe the instrumental and structural parameters for Rietveld analysis. The instrumental parameters were 18 Chebychev polynomial coefficients to model the background, a sample height term, 1 scale factor, 4 terms to model the TCHZ peak-shape and 1 term to describe axial divergence. The structural parameters refined were 4 cell parameters (a, b, c and β), 8 atomic positions and 6 isotropic thermal parameters.

Rietveld refinement profile of room-temperature XRPD data for $Y_4O_4TiSe_4$ refined in space group $C2/m$ (observed, calculated, and difference profiles shown in blue, red, and grey, respectively); tick marks show reflection positions for $Y_4O_4TiSe_4$. d7_00477, AJT081.

Rapid cooling profile for $Gd_4O4TiSe_4$
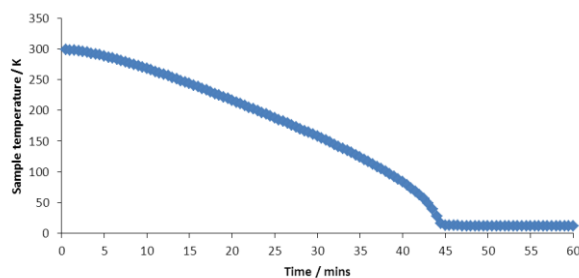
Rapid cooling temperature profile for $Gd_4O_4TiSe_4$. The sample reaches base temperature (12 K) in approximately 44 minutes.

DFT calculation for Gd$_4$O$_4$TiSe$_4$
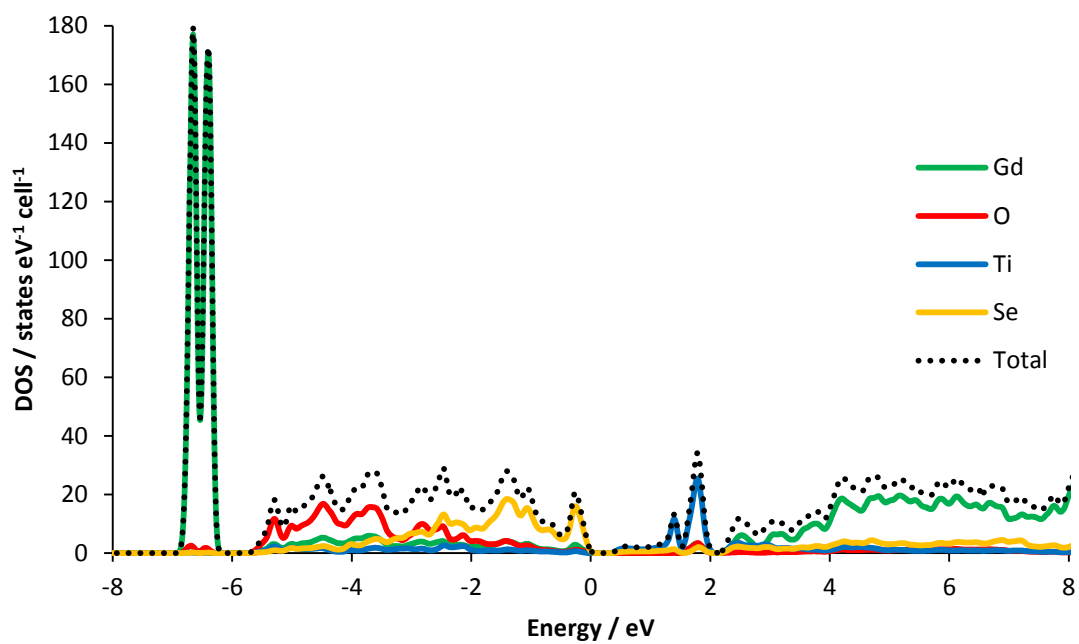
Projected density of states with contributions from Gd, O, Ti, Se in green, red, blue and yellow respectively, and the total density of states in black. Calculations preformed using LDA function with optimised geometry. 0.362 eV indirect band gap predicted.

Field dependent magnetisation of $A_4O_4TiSe_4$ materials
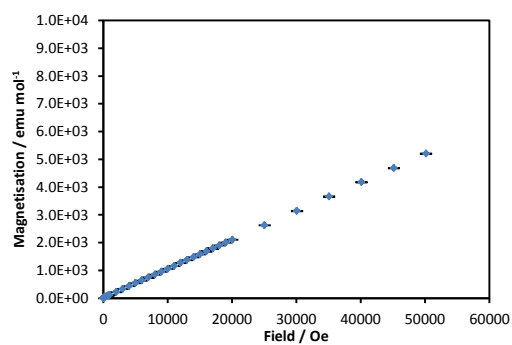
$Gd_4O_4TiSe_4$ field sweep at 292 K
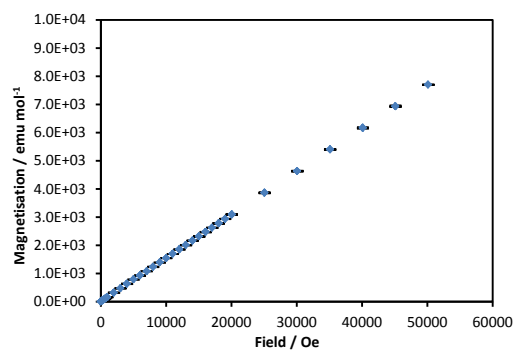
$Tb_4O_4TiSe_4$ field sweep at 292 K
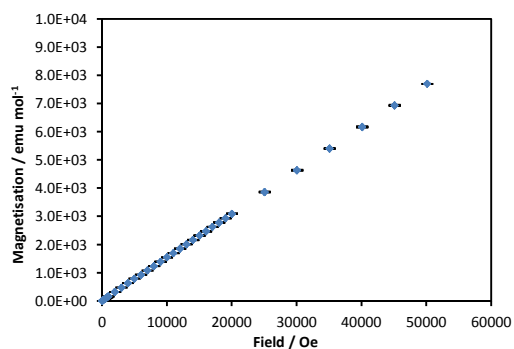
$Dy_4O_4TiSe_4$ field sweep at 292 K
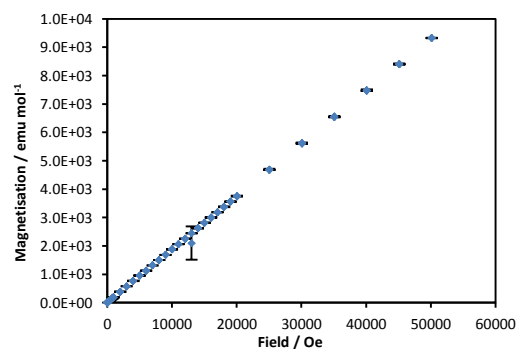
$Ho_4O_4TiSe_4$ field sweep at 292 K

Appendix 3

Selected bond angles for $Eu_4O_4Se_3$ $P2_1/c$ symmetry at 120 K.

Eu(2)	- O(8)	- Eu(2)	106.0(13)	Eu(1)	- O(10)	- Eu(2)	96.7(13)
Eu(2)	- O(8)	- Eu(3)	107.4(13)	Eu(1)	- O(10)	- Eu(4)	105.0(14)
Eu(2)	- O(8)	- Eu(3)	134.6(11)	Eu(2)	- O(10)	- Eu(4)	115.9(10)
Eu(2)	- O(8)	- Eu(4)	114.4(10)	Eu(2)	- O(10)	- Eu(4)	100.0(13)
Eu(2)	- O(8)	- Eu(4)	97.8(11)	Eu(1)	- O(10)	- Eu(4)	135.1(11)
Eu(3)	- O(8)	- Eu(4)	95.5(11)	Eu(4)	- O(10)	- Eu(4)	104.5(14)
Eu(1)	- O(9)	- Eu(1)	109.0(16)	Eu(1)	- O(11)	- Eu(2)	103.1(16)
Eu(1)	- O(9)	- Eu(3)	120.0(11)	Eu(1)	- O(11)	- Eu(3)	115.8(10)
Eu(1)	- O(9)	- Eu(3)	99.4(15)	Eu(2)	- O(11)	- Eu(3)	104.0(17)
Eu(1)	- O(9)	- Eu(4)	106.0(15)	Eu(1)	- O(11)	- Eu(3)	101.8(17)
Eu(1)	- O(9)	- Eu(4)	122.6(11)	Eu(2)	- O(11)	- Eu(3)	125.9(10)
Eu(3)	- O(9)	- Eu(4)	100.7(15)	Eu(3)	- O(11)	- Eu(3)	107.0(16)

*Crystallographic data from Rietveld refinement of $Eu_4O_4Se_3$*

	x	y	z	Occupancy	B / Å^2
Eu1	0.11454(7)	0.3733(5)	0.40786(5)	1	0.44(1)
Eu2	0.37075(7)	0.1238(5)	0.58226(5)	1	0.42(1)
Eu3	0.11452(7)	-0.1243(5)	0.40900(5)	1	0.45(1)
Eu4	0.37168(7)	-0.3747(5)	0.57962(5)	1	0.48(1)
Se5	0.2316(1)	-0.6254(3)	0.73959(8)	1	0.90(1)
Se6	0.5243(1)	-0.6250(5)	0.74288(9)	1	0.86(1)
Se7	0.1233(1)	-0.1260(3)	0.72126(7)	1	0.86(1)
O8	0.3703(7)	-0.129(2)	0.4876(5)	1	0.06(1)
O9	0.1223(7)	-0.384(2)	0.4967(5)	1	0.06(14)
O10	0.3747(7)	-0.636(2)	0.4806(5)	1	0.06(14)
O11	0.1250(7)	0.107(1)	0.5032(5)	1	0.06(14)

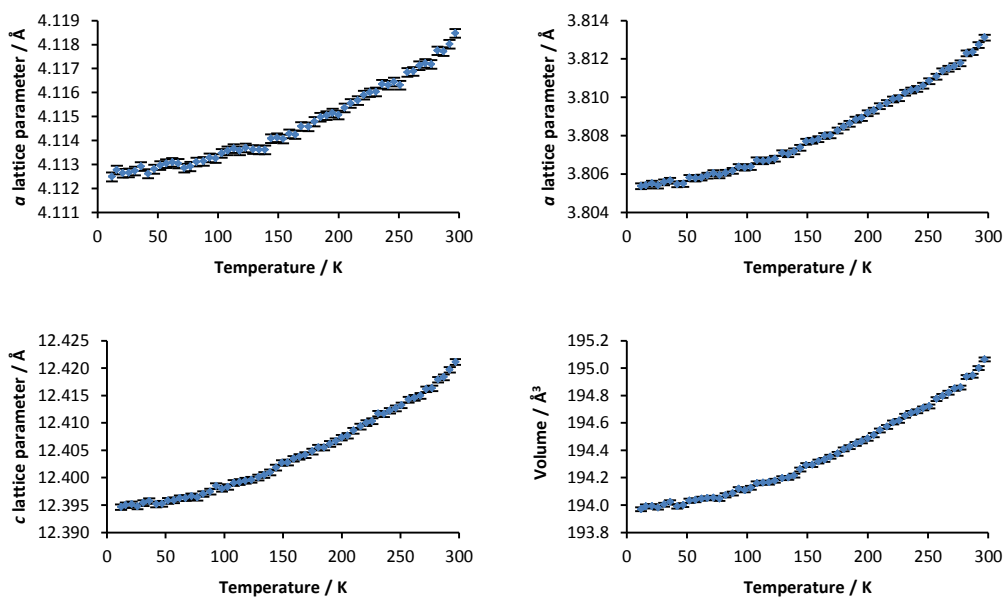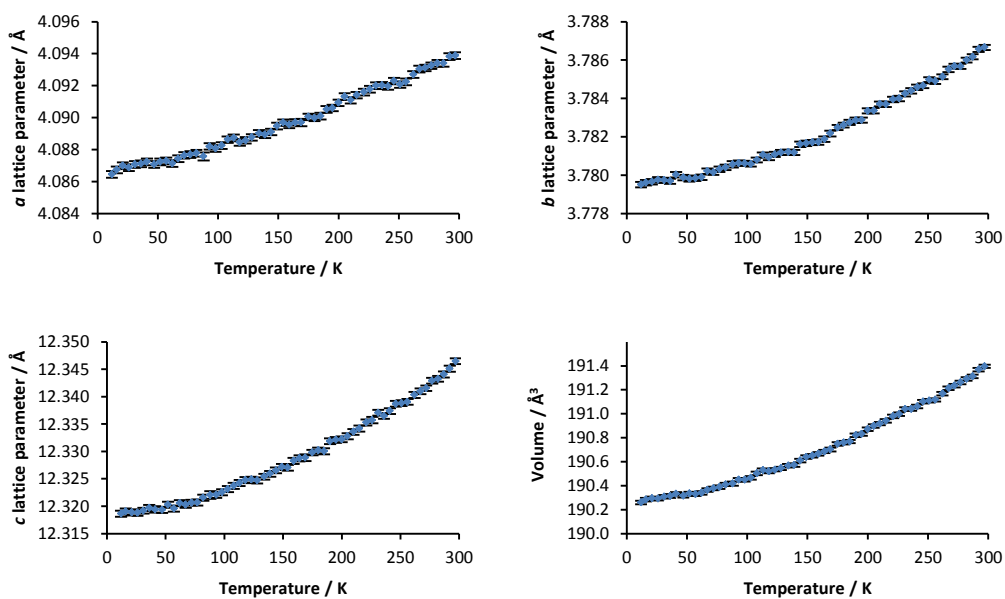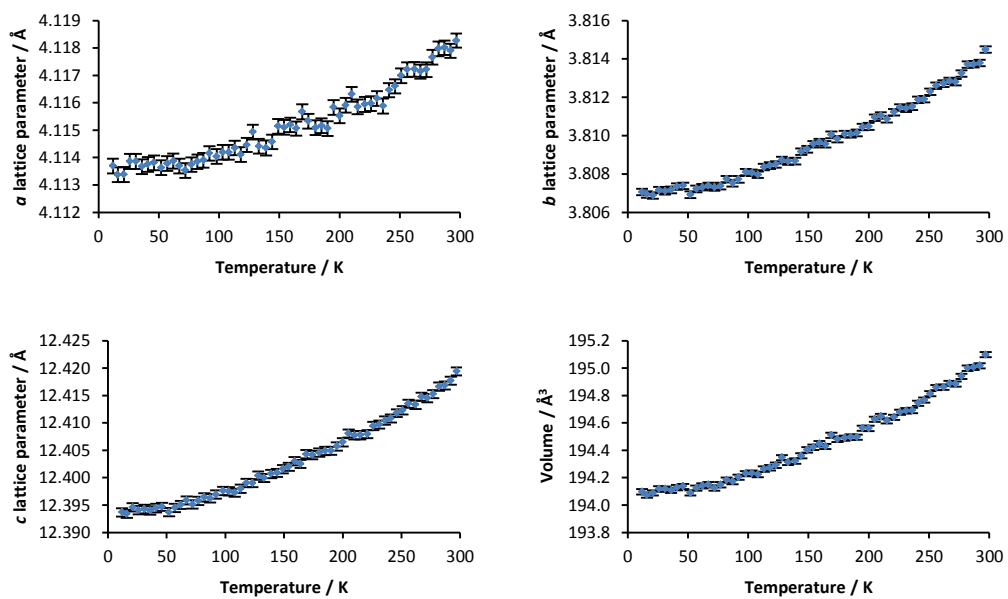Temperature dependence of unit cell parameters for $Nd_4O_4Se_3$, AJT139, d9_07146.
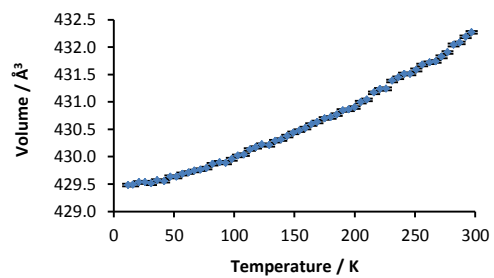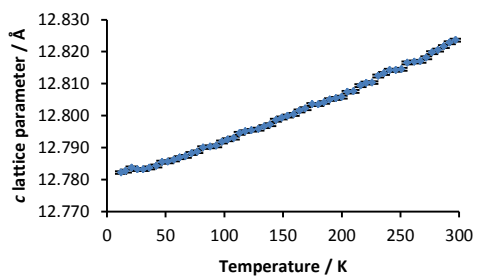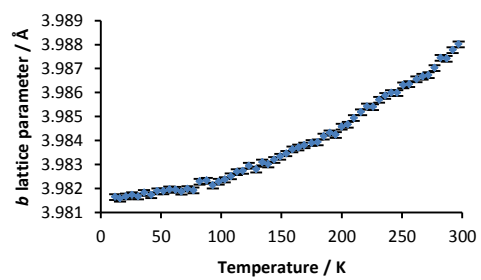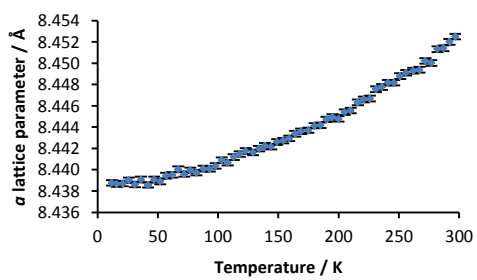
Temperature dependence of unit cell parameters for $Sm_4O_4Se_3$, AJT140, d9_07152.
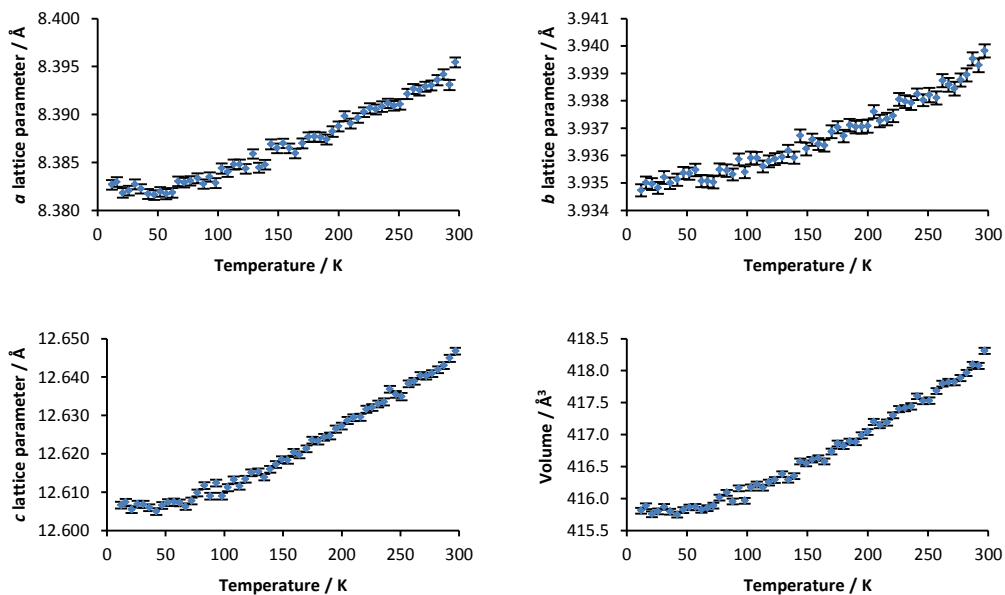
Temperature dependence of unit cell parameters for $Eu_4O_4Se_3$, AJT163b, d9_07105.
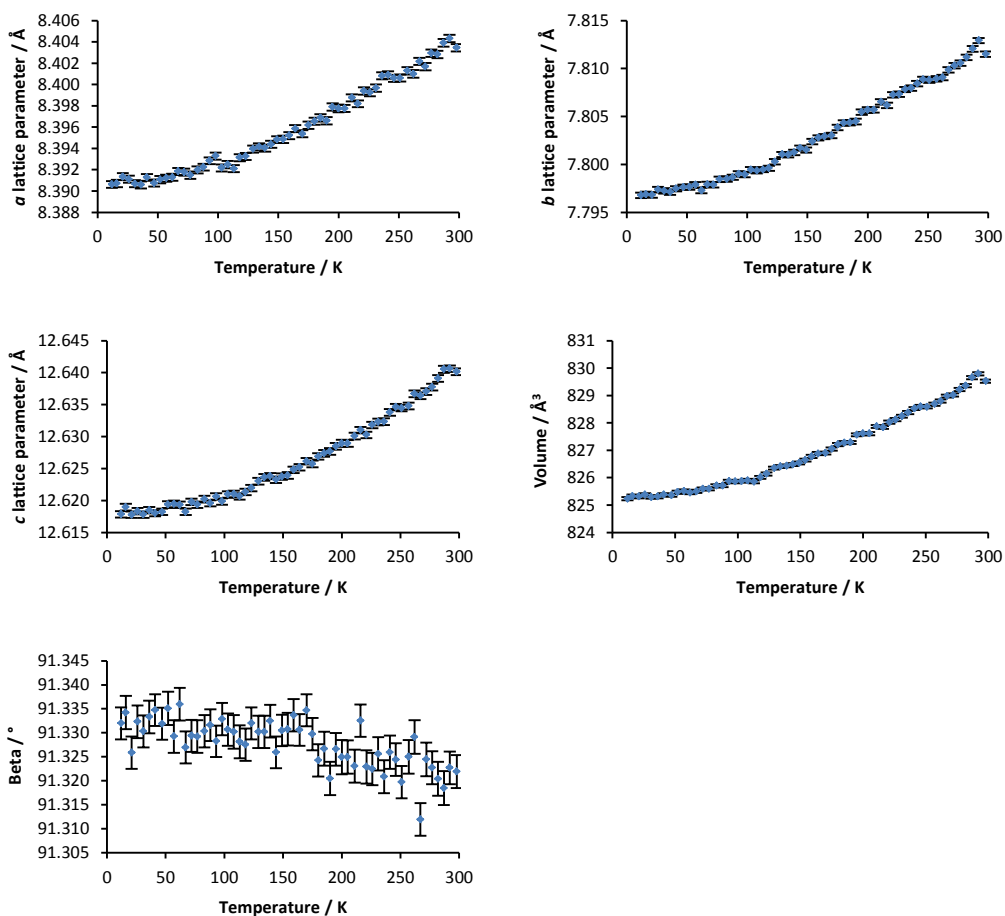
Temperature dependence of unit cell parameters for Gd$_4$O$_4$Se$_3$, AJT180a, d9_07161.
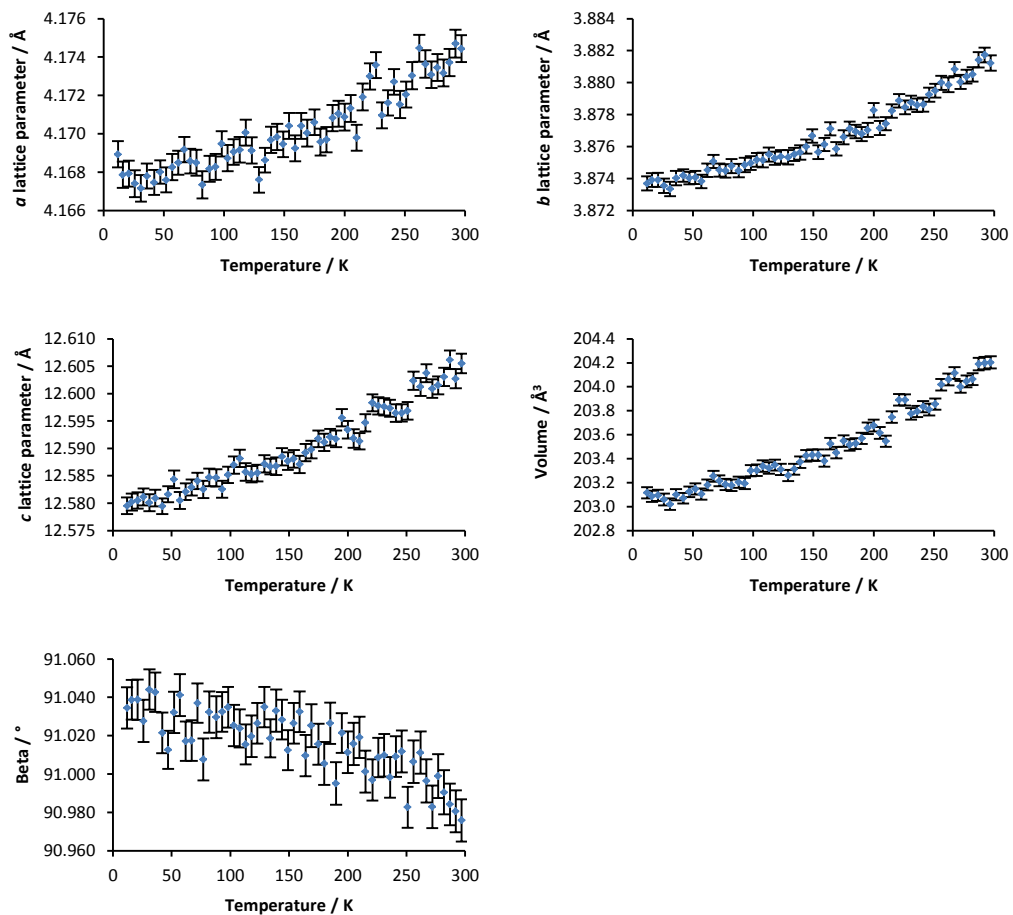
Temperature dependence of unit cell parameters for Tb$_4$O$_4$Se$_3$, AJT190a, d9_07156.
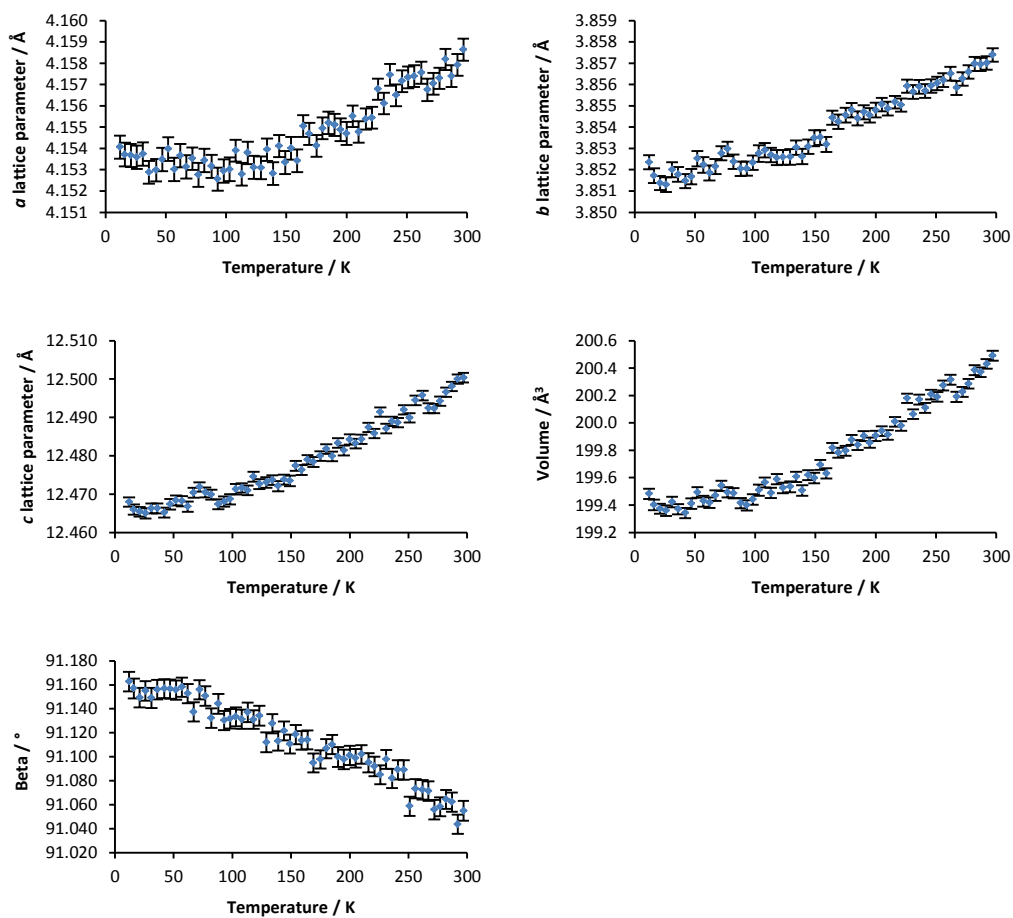
Temperature dependence of unit cell parameters for Dy$_4$O$_4$Se$_3$, AJT181a, d9_07183.
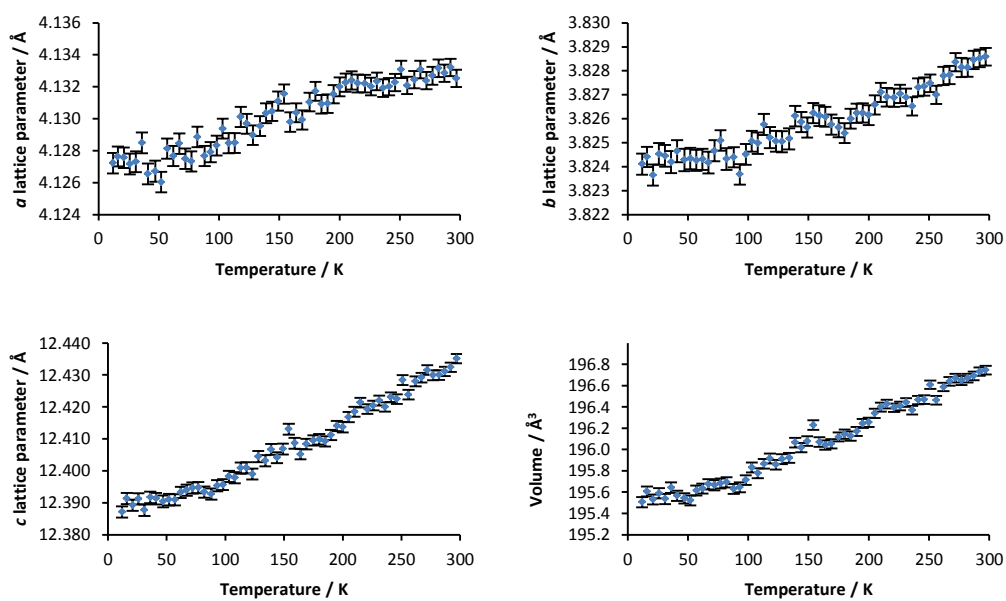
Temperature dependence of unit cell parameters for Ho$_4$O$_4$Se$_3$, AJT159f, d9_07188.

Temperature dependence of unit cell parameters for Er$_4$O$_4$Se$_3$, AJT148c, d9_07193.

Temperature dependence of unit cell parameters for $Y_4O_4Se_3$, AJT179g, d9_07098.

		spreadsheet	SQUID data
	Dy$_4$O$_4$TiSe$_4$	input	Room temperature refinement
		cif	Room temperature CIF
		input	Variable temperature refinement cooling at 15 K hr-1
		spreadsheet	SQUID data
	Ho$_4$O$_4$TiSe$_4$	input	Room temperature refinement
		cif	Room temperature CIF
		input	Variable temperature refinement cooling at 15 K hr-1
		spreadsheet	SQUID data
	Er$_4$O$_4$TiSe$_4$	input	Room temperature refinement
		cif	Room temperature CIF
	Y$_4$O$_4$TiSe$_4$	input	Room temperature refinement
		cif	Room temperature CIF
		input	Variable temperature refinement cooling at 15 K hr-1
	A_4O$_4$TiSe$_4$	spreadsheet	All variable temperature data
		spreadsheet	All conductivity data
Chapter 5	Nd$_4$O$_4$Se$_3$	input	Variable temperature refinement cooling at 15 K hr-1
	Sm$_4$O$_4$Se$_3$	input	Variable temperature refinement cooling at 15 K hr-1
	Eu$_4$O$_4$Se$_3$	dsc	Single crystal refinement
		cif	Single crystal CIF
		input	Room temperature Rietveld refinement (APS)
		input	Room temperature Pawley refinement (APS)
		cif	Room temperature CIF (powder)
		input	Variable temperature refinement cooling at 15 K hr-1
	Gd$_4$O$_4$Se$_3$	input	Room temperature Rietveld refinement
		cif	Room temperature CIF
		input	Variable temperature refinement cooling at 15 K hr-1
		input	Indexing
		ndx	Indexing output
		input	Charge flipping
	Tb$_4$O$_4$Se$_3$	input	Room temperature Rietveld refinement
		cif	Room temperature CIF
		input	Variable temperature refinement cooling at 15 K hr-1
	Dy$_4$O$_4$Se$_3$	input	Room temperature Rietveld refinement
		cif	Room temperature CIF
		input	Variable temperature refinement cooling at 15 K hr-1
	Ho$_4$O$_4$Se$_3$	input	Room temperature Rietveld refinement
		cif	Room temperature CIF
		input	Variable temperature refinement cooling at 15 K hr-1
	Er$_4$O$_4$Se$_3$	input	Room temperature Rietveld refinement
		cif	Room temperature CIF
		input	Variable temperature refinement cooling at 15 K hr-1
	Y$_4$O$_4$Se$_3$	input	Room temperature Rietveld refinement (APS)
		cif	Room temperature CIF
		input	Variable temperature refinement cooling at 15 K hr-1
		input	Charge flipping

	A_4O4Se$_3$	spreadsheet	Combined thermal expansion data
		spreadsheet	Normalised unit cells
Chapter 6	La$_2$O$_2$Se$_2$Fe$_2$O	dsc	293 K refinement
		cif	293 K CIF
		dsc	200 K refinement
		cif	200 K CIF
		dsc	85 K refinement
		cif	85 K CIF
		dsc	35 K refinement
		cif	35 K CIF
	La$_2$O$_2$Se$_2$Mn$_2$O	dsc	293 K refinement
		cif	293 K CIF
		dsc	90 K refinement
		cif	90 K CIF
		dsc	35 K refinement
		cif	35 K CIF
		JANA	125 K refinement (Spring8)
		cif	125 K CIF (Spring8)
		JANA	90 K refinement (Spring8)
		cif	90 K CIF (Spring8)
		JANA	55 K refinement (Spring8)
		cif	55 K CIF (Spring8)
		JANA	20 K refinement (Spring8)
		cif	20 K CIF (Spring8)
	Pr$_2$O$_2$Se$_2$Mn$_2$O	dsc	300 K refinement
		cif	300 K CIF
		dsc	265 K refinement
		cif	265 K CIF
		dsc	230 K refinement
		cif	230 K CIF
		dsc	180 K refinement
		cif	180 K CIF
		dsc	130 K refinement
		cif	130 K CIF
		dsc	90 K refinement
		cif	90 K CIF
Chapter 7	LaInS$_2$O	input	Indexing
		ndx	Indexing results
		input	Room temperature Pawley refinement
		input	Room temperature Pawley refinement P222 (APS)
		input	Room temperature Pawley refinement P212121 (APS)
		input	Room temperature Rietveld refinement (APS)
		cif	Room temperature CIF
Chapter 8	Si+Al	input	Surface refinement